frontiers | Research Topics

Deep-sea sampling technology

Edited by
Jiawang Chen, Yuan Lin, Zhilei Sun and Nhan Phan-Thien

Published in
Frontiers in Marine Science

ISSN 1664-8714
ISBN 978-2-8325-2697-2
DOI 10.3389/978-2-8325-2697-2

About Frontiers

Frontiers is more than just an open access publisher of scholarly articles: it is a pioneering approach to the world of academia, radically improving the way scholarly research is managed. The grand vision of Frontiers is a world where all people have an equal opportunity to seek, share and generate knowledge. Frontiers provides immediate and permanent online open access to all its publications, but this alone is not enough to realize our grand goals.

Frontiers journal series

The Frontiers journal series is a multi-tier and interdisciplinary set of open-access, online journals, promising a paradigm shift from the current review, selection and dissemination processes in academic publishing. All Frontiers journals are driven by researchers for researchers; therefore, they constitute a service to the scholarly community. At the same time, the *Frontiers journal series* operates on a revolutionary invention, the tiered publishing system, initially addressing specific communities of scholars, and gradually climbing up to broader public understanding, thus serving the interests of the lay society, too.

Dedication to quality

Each Frontiers article is a landmark of the highest quality, thanks to genuinely collaborative interactions between authors and review editors, who include some of the world's best academicians. Research must be certified by peers before entering a stream of knowledge that may eventually reach the public - and shape society; therefore, Frontiers only applies the most rigorous and unbiased reviews. Frontiers revolutionizes research publishing by freely delivering the most outstanding research, evaluated with no bias from both the academic and social point of view. By applying the most advanced information technologies, Frontiers is catapulting scholarly publishing into a new generation.

What are Frontiers Research Topics?

Frontiers Research Topics are very popular trademarks of the *Frontiers journals series*: they are collections of at least ten articles, all centered on a particular subject. With their unique mix of varied contributions from Original Research to Review Articles, Frontiers Research Topics unify the most influential researchers, the latest key findings and historical advances in a hot research area.

Find out more on how to host your own Frontiers Research Topic or contribute to one as an author by contacting the Frontiers editorial office: frontiersin.org/about/contact

Deep-sea sampling technology

Topic editors
Jiawang Chen — Zhejiang University, China
Yuan Lin — Zhejiang University, China
Zhilei Sun — Qingdao Institute of Marine Geology (QIMG), China
Nhan Phan-Thien — National University of Singapore, Singapore

Citation
Chen, J., Lin, Y., Sun, Z., Phan-Thien, N., eds. (2023). *Deep-sea sampling technology*. Lausanne: Frontiers Media SA. doi: 10.3389/978-2-8325-2697-2

Table of contents

frontiers | Frontiers in Marine Science

TYPE Editorial
PUBLISHED 31 May 2023
DOI 10.3389/fmars.2023.1182211

OPEN ACCESS

EDITED AND REVIEWED BY
Juan Jose Munoz-Perez,
University of Cádiz, Spain

*CORRESPONDENCE
Jiawang Chen
arwang@zju.edu.cn

RECEIVED 08 March 2023
ACCEPTED 23 May 2023
PUBLISHED 31 May 2023

CITATION
Lin Y, Chen J, Sun Z and Phan-Thien N (2023) Editorial: Deep-sea sampling technology.
Front. Mar. Sci. 10:1182211.
doi: 10.3389/fmars.2023.1182211

Editorial: Deep-sea sampling technology

Yuan Lin[1], Jiawang Chen[1]*, Zhilei Sun[2] and Nhan Phan-Thien[3]

[1]Institute of Ocean Engineering and Technology, Ocean College, Zhejiang University, Hangzhou, China, [2]The Key Laboratory of Gas Hydrate, Ministry of Natural Resources, Qingdao Institute of Marine Geology, Qingdao, China, [3]Faculty of Engineering, National University of Singapore, Singapore, Singapore

KEYWORDS

deep-sea sampling, high fidelity sampling, *in-situ* monitoring, pressure-retaining transfer, *in-situ* observation

Editorial on the Research Topic
Deep-sea sampling technology

With the increasing demand for the marine scientific research and the harvesting of deep-sea resources, such as crude oil, natural gas hydrate and polymetallic nodules, the investigation of deep-sea environment has become increasingly important. It is essential to develop high-accuracy and reliable deep-sea detection technologies, including *in-situ* multidisciplinary observation, and high-fidelity sampling of fluids, sediments and benthos. In this Research Topic, we have collected several progresses made in recent years.

For *in-situ* observation technologies, Ge et al. developed and tested an instrument for the long-term monitoring of the seabed strata deformation for gas hydrate exploitation. The instrument was composed of multiple MEMS (Micro-Electro-Mechanical System) sensors which were placed in the sensor chamber. Corrugated pipes were used as soft joints connecting the sensor chamber, which could bend and twist if slides or deformation have occurred in the strata. The instrument can be deployed through the ROV (Remote Operated Vehicle) and working at the maximum sea-depth of 3000 m. Wang et al. developed a lander loaded with an imaging system to monitoring the dynamics of SPM (Suspended Particle Matter), which played an important role in material transport, deposition, resuspension and the function of benthic communities' processes in deep sea. They were able to capture the *in-situ* digital video images at the water depth of 1450 m in South China sea, based on which they defined an image signal that was the ratio between the area of the SPM and that of the total image, to characterize the SPM concentration. Liu et al. developed an *in-situ* observation system for microscopic targets in the deep sea, which was successfully deployed by the ROV on the seabed in South China Sea with a depth over 770 m. The system integrated microscopic imaging and Raman detection techniques, by which compositional analysis of shell fragments, seabed rock samples, and live sea stars were successively performed. The system illustrated a considerable potential of combining Raman spectroscopy and microscopic imaging in marine research. Guo et al. designed a double decelerating lander for *in-situ* detection and monitoring at the water depth of 6000 m. In order to avoid damage of the OBS (Ocean Bottom Seismometer) due to the impact when the lander, which is released and then touched the seabed during the deploying process, the double decelerating unit were developed as a safeguard for OBS to ensure a low impact rate. The lander was successfully deployed at the water depth of

2240 m and 1790 m, respectively, in South China sea, with the temperature, salinity, Eh (redox potential), turbidity, underwater acoustic environment, and OBS data being successfully monitored

For sampling technologies, Liu et al. developed an active deep-sea low damage pressure-retaining samplers for organisms. They used a HSMPS (Hydraulic Suction Macro-biological Pressure-retaining Sampler) to capture less damaged hadal snailfish samples *via* pumping. They realized active sampling of deep-sea organisms by controlling the flow rate of the pump, designing a pressure compensation mechanism to compensate for the pressure drop in the recovery process of the sampler, and using thermal insulation materials to realize the low-temperature environment inside the sampler. They also suggested a low damage of the sampler capture process of deep-sea organisms by controlling the flow rate in the range of 131 L/min to 174 L/min. Guo et al. proposed and tested a pressure-retaining separation and transfer system for the sediment and the overlying seawater to investigation of methane leakage and the sediment-water interface at the ambient pressure of 30 MPa. The device has the ability to transfer respectively the overlying water by compressing the internal volume and the sediment by secondary sampling. Fang et al. designed a gas-tight water sampler by displacement sampling method, by which the prefilled deionized water is replaced by the water sample. Factors such as indirect displacement, shape and diameter of sampling inlet, Coanda distance, sampling rate and other factors on the displacement effect were investigated. The developed sampler was tested in South China sea at the water-depth reaching 3000 m, and the purity of the collected water sample reached 100%. Wang et al. conducted a concise survey on the isobaric sampling apparatus and essential techniques for deep-sea macro-organisms, and provided an overview of the history and utilization of isobaric samplers for deep-sea creatures developed by researchers worldwide over the past century. They further summarized the key technologies of isobaric samplers, encompassing pressure compensation, insulation, and sealing.

We learn that considerable progress has been made on deep-sea sampling and *in-situ* observation technology at the water depth of about 3000 m. In recently years, mining of deep-sea polymetallic nodules has attracted increasing interest, and intensive survey on the benthonic environment is essential in order to assess the environmental impact due to the mining process. This requires reliable *in-situ* monitoring technologies, as well as time series sampling methods on the sediment, pore water, and benthos, et al., throughout the trail harvesting process at the depth of 6000 m. However, way to achieve such goal is still limited and is expected to be developed in the near future.

Author contributions

YL wrote the first draft of the manuscript. JC and ZS wrote sections of the manuscript. All authors contributed to manuscript revision, read, and approved the submitted version.

Funding

This work was funded by National Key R&D Program of China (grant No. 2022YFC2803903), and Hainan Provincial Natural Science Foundation of China (Grant No. 121MS061).

Conflict of interest

The authors declare that the research was conducted in the absence of any commercial or financial relationships that could be construed as a potential conflict of interest.

Publisher's note

frontiers | Frontiers in Marine Science

TYPE Original Research
PUBLISHED 29 September 2022
DOI 10.3389/fmars.2022.987319

OPEN ACCESS

EDITED BY
Juan Jose Munoz-Perez,
University of Cádiz, Spain

REVIEWED BY
Polina Lemenkova,
Université libre de Bruxelles, Belgium
Yangting Liu,
Ministry of Natural Resources, China

*CORRESPONDENCE
Jiawang Chen
arwang@zju.edu.cn

SPECIALTY SECTION
This article was submitted to Ocean Observation, a section of the journal Frontiers in Marine Science

RECEIVED 06 July 2022
ACCEPTED 12 September 2022
PUBLISHED 29 September 2022

CITATION
Ge Y, Chen J, Zhang P, Cao C, Le X, Ai J, Zhou P and Liang T (2022) A novel technique for seabed strata deformation *in situ* monitoring. *Front. Mar. Sci.* 9:987319. doi: 10.3389/fmars.2022.987319

A novel technique for seabed strata deformation *in situ* monitoring

Yongqiang Ge[1,2], Jiawang Chen[1,2,3]*, Peihao Zhang[1], Chen Cao[1], Xiaoling Le[1], Jingkun Ai[1,2], Peng Zhou[1] and Tao Liang[1]

[1]Ocean College, Zhejiang University, Zhoushan, China, [2]Hainan Institute, Zhejiang University, Sanya, China, [3]The Engineering Research Center of Oceanic Sensing Technology and Equipment, Ministry of Education, Zhoushan, China

Seafloor strata deformation monitoring is important for gas hydrate exploitation and the monitoring and early warning of seabed instabilities. Due to the limitation of *in situ* monitoring technology, existing observations are carried out with geophysical methods to provide basic geomorphological characteristics and stratigraphic structures. However, it is of equal importance to study the *in situ* evolution mechanism of the process of strata deformation, which relies heavily on long-term *in situ* observations. An *in situ* monitoring instrument for seabed strata deformation monitoring is presented. Sufficient theoretical, numerical, and experimental studies were carried out to conduct a mechanical analysis on the entire deployment process of the instrument. The maximum penetration resistance and reaming pressure were calculated during the deployment process, and the stability and feasibility of the deployment method were verified. To validate the maximum penetration resistance obtained and the monitoring performance of the instrument, field tests were conducted on a tidal flat in Changzhi Island. The penetration resistance of the instrument and the strata deformation of the tidal flat were measured and obtained. The results demonstrate the feasibility of the presented instrument.

KEYWORDS

strata deformation monitoring, cavity expansion, penetration resistance, *in-situ* monitoring, field experiment

1 Introduction

Gas hydrate is an ice-like substance comprised of water and low-molecular-weight gases, usually methane, that forms within sediment under a proper condition of high pressure and low temperature (You et al., 2019; Ruppel and Waite, 2020). The decomposition of gas hydrates may reduce the strength of sediments and cause

seafloor instabilities (i.e., seabed subsidence and uplift, strata deformation, and slides) (Nixon and Grozic, 2007; Wang et al., 2017). These instabilities can pose dramatic risks to seabed infrastructure, such as offshore oil platforms, pipelines, and submarine cables, causing significant environmental and economic consequences (Xu et al., 2019). Therefore, seabed instabilities have been the focus of marine geological studies. Studies on seabed strata observations are conventionally carried out through acoustic surveys, including side scan sonar, multibeam echosounder, and various sub-bottom profiling techniques. They can acquire and collect the geomorphological characteristics and stratigraphic structure of the seabed strata (Koch et al., 2015; Paull et al., 2015). However, these acoustic instruments need to be installed on survey platforms (i.e., scientific ship and underwater vehicle) and have a long observation period, preventing long-term continuous monitoring (Xu et al., 2019). Field monitored data are essential for studying the mechanism and process of seabed strata deformation. Thus, it is necessary to develop an *in situ* long-term instrument for seabed deformation monitoring.

At present, with the development of submarine monitoring technologies, *in situ* long-term seafloor deformation measurement methods have been achieved worldwide, utilizing technologies such as high-precision ocean pressure gauges (Phillips et al., 2008; Tsushima et al., 2012) and triaxial accelerometers (Prior et al., 1989; Saito and Yokoyama, 2008). The pressure gauges can be deployed on the seabed and monitor the water pressure changes with seafloor subsidence or uplift. However, most quart pressure gauges undergo a drift at unpredictable rates that are typically equivalent to 20 cm/year (Polster et al., 2009), and it cannot measure horizontal deformation. The single tri-axial accelerometers are spatially restricted and can only measure the deformation of a single point. Moreover, the seabed deformation was calculated through the double-integral method, which has a large accumulative error over time (Wang et al., 2018). On the other hand, the technology of the microelectromechanical system (MEMS) developed rapidly. MEMS accelerometers and inclinometers have been widely used on seafloor subsidence and landslide monitoring (Wang et al., 2020; Ge et al., 2021). Although there are many methods to monitor the seafloor deformation, the random occurrence of seafloor instabilities often leads to high investments in field observation and a low data return rate. The *in situ* monitoring of the seabed deformation is thus still in a relatively preliminary stage and needs further development.

In this paper, an innovative monitoring system was presented to monitor the seabed strata deformation process at different depths. Theoretical, numerical, and experimental studies were carried out to conduct a mechanical analysis on the entire deployment process of the monitoring instrument, proving the feasibility of the deployment and application of the instrument. To validate the deformation monitoring performance of the instrument, the *in situ* deformation monitoring test of a tidal flat was conducted in Changzhi Island. Finally, the discussion and conclusion are presented.

2 Instrument design

2.1 Overview of the instrument

Figure 1 shows the overview diagram of the instrument, which consists of the auxiliary deployment part (ADP) and *in situ* monitoring part (IMP). The APD includes a U-handle, plug, stainless steel casing pipe, and conical drill. The conical drill is connected to the IMP and the casing pipe and can reduce resistance during the deployment process and ensure that the IMP vertically penetrates into the strata. The plug and tight wires connect the casing pipe to the conical drill to prevent them from separating. The IMP is composed of multiple MEMS sensors, sensor chambers, corrugated pipes, watertight cables, and electronic chamber. The MEMS sensors placed in the sensor chamber can withstand the water pressure of 30 MPa. The corrugated pipe is regarded as a soft joint, connects the adjacent sensor chamber, and will bend and twist when slides or deformation occurs in the strata. The watertight cable and the tensioned steel wire are in the corrugated pipe. The watertight cable is responsible for communication and data transmission, and the steel wire rope can bear the axial tension and lateral shear force (to avoid the stress of the watertight cable). The electronic chamber includes data acquisition and control circuit, and battery to realize the timing and synchronous data acquisition, control, and power supply. The specifications of the monitoring instrument are shown in Table 1.

2.2 The *in situ* deployment of the instrument

The direct penetration method (without ADP) is relatively simple, but the flexible joints will deform with large deflections, resulting in the instability and failure of the monitoring instrument during the deployment process. Therefore, in order to ensure the monitoring performance of the monitoring instrument and coupling relationship with the surrounding soil layer, the ADP is used to deploy it into a specific depth of the strata. The deployment processes are shown in Figure 2. The monitoring instrument is deployed with the assistance of an operation ROV (remotely operated vehicle), and the deployment processes are as follows: (a) the ROV carries the monitoring instrument, submerges, and sits on a suitable position on the seabed; (b) the monitoring instrument is penetrated into the seabed sediment segment by segment by the ROV's manipulator; (c) after the monitoring instrument is penetrated to a specific depth, the plug is pulled out, and the casing pipe is separated from the conical drill; and (d) finally, the ROV's manipulator

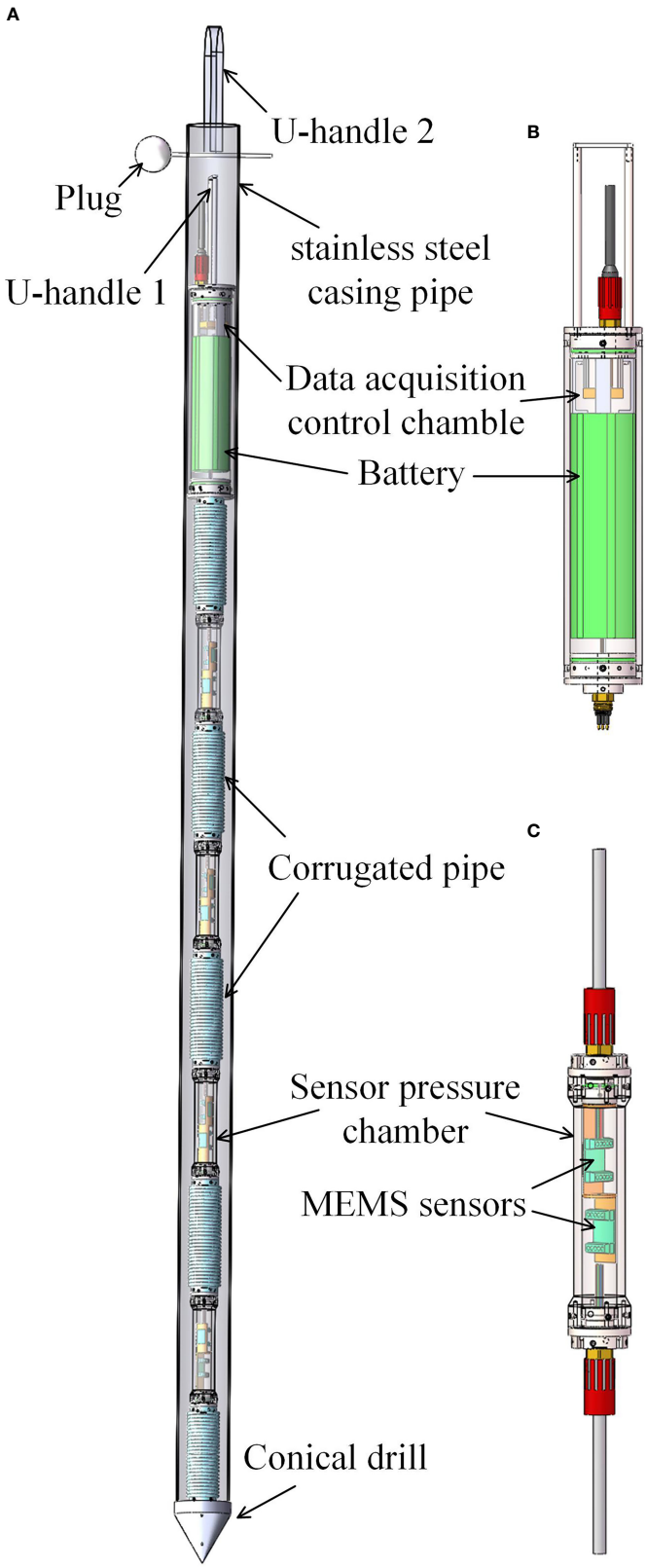

FIGURE 1
The diagram of the monitoring instrument: **(A)** the overview of the instrument; **(B)** the data acquisition chamber; and **(C)** the sensor chamber.

TABLE 1 The specifications of the monitoring instrument.

Parameters	Total length	Diameter	Number of sensing nodes	Monitoring section length	Interval of monitoring point
Value	2.0 m	90 mm	10	1.6 m	400 mm
Parameters	**Static power consumption**	**Work power consumption**	**Battery capacity**		
Value	0.24 W	4.08 W	30 AH		

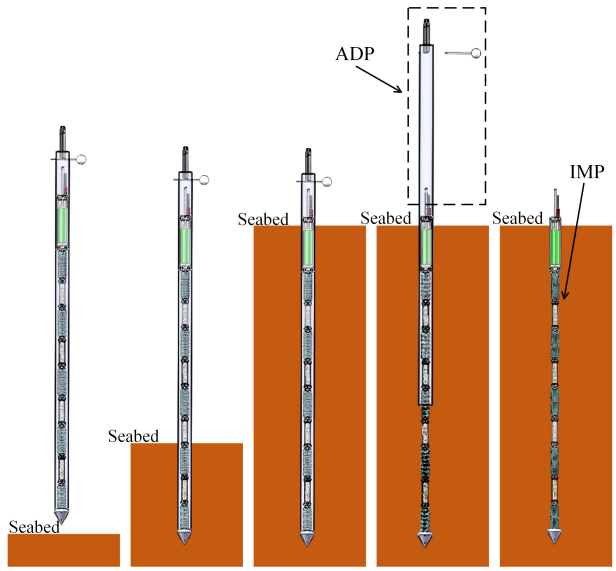

FIGURE 2
The deployment process of the instrument.

holds the U-handle and pulls out the casing pipe, leaving the IMP in the strata to conduct monitoring tasks.

2.3 Design of the acquisition and control system

The IMP integrates a self-capacity lithium battery, a data acquisition and control circuit, and multiple MEMS sensors to realize the long-term *in situ* monitoring of the seabed strata deformation. The output voltage and capacity of the lithium battery is 12 V and 30 AH, respectively. The acquisition and control system is designed with low power consumption, and the static and work power consumption is 0.24 and 4.08 W, respectively. The external crystal periodically turns on the relay the relay to realize the intermittent operation of MEMS sensors.

In order to ensure the stability and reliability of the communication between the acquisition and control system and the sensing nodes and to satisfy the requirement of increasing the sensing node and monitoring range in the future, a communication bus based on RS485 is designed, which can realize the synchronous acquisition of 32 sensing nodes, and the communication distance can reach 1,200 m. The sensors on the RS485 communication bus have a unique physical address, and the acquisition system inquires the data of each sensor in turn and stores it in the Secure Digital Memory Card (SD) card after interpretation and filtering is completed.

3 Mechanics analysis on the deployment process

The penetration process of the instrument in seabed sediment is similar to the pile-sinking process in saturated clay, which can be regarded as similar to the cylindrical/spherical cavity expansion under undrained conditions to study the soil-squeezing effect. The mechanism analysis of the

penetration process in this paper is based on the following assumptions: (1) soil is the ideal elastic–plastic material that is uniform and isotropic; (2) the stress–strain relation of soil in the plastic zone should obey the modified Lade–Duncan yield criterion; (3) the cylindrical and spherical cavity expansions are regarded as an undrained process, and soil is incompressible; and (4) regardless of the self-weight effect of the sensor array, the ultimate expansion radius of the cavity is equal to that of the sensor array.

3.1 Calculation of the side resistance during penetration process

The study of the squeeze of the monitoring instrument during the penetration process is usually idealized and simulated to a series of spherical holes expanding to an equivalent diameter formed by the cylindrical cavity continuum (Tao et al., 2018). As shown in Figure 3, the surrounding soil is damaged, and the damage shape includes the elastic zone and plastic zone. As shown in Figure 3A, the initial radius of the cavity is $R_0(0 \le R_0 \le R_u)$, where R_u is the ultimate radius after cavity expansion, and the corresponding reaming pressure is p_u . Radial displacement after the expansion of soil is u_p . The radius of the elastic–plastic interface is R_p . For the region $r>R_p$, the soil elements obey the generalized Hooke's law. For the region $R_u<r<R_p$, indicating that plastic yield has occurred and the stress–strain relation of soil should obey the modified Lade–Duncan model. The zone, which satisfies $R_0 \le r \le R_u$, indicates the complete damage of soils.

The boundary conditions are given as follows:

$$r = R_0, \sigma_r = p$$
$$r = R_u, \sigma_r = p_u$$
$$r = R_p, \sigma_r = \sigma_p$$

where p is the reaming pressure, σ_r is the radial stress. σ_θ is the circular stress, and σ_p is the radial stress in the elastic–plastic interface.

Strain softening is a significant mechanical characteristic of clay; in fact, during sensor array insertion, soil undergoes large shear deformation, and the damage zone is formed around the sensor array. Soil is squeezed and reaches a plastic flow state in the damage zone. In order to obtain the displacement and stress of soil in the plastic zone, the modified Lade–Duncan Model is introduced (Lade and Duncan, 1975; Ewy, 1999), which can be expressed as

$$\sigma_1 - \eta\sigma_3 - (\eta - 1)\sigma_0 = 0$$

$$\eta = \frac{1}{4}\left[\sqrt[3]{K} - 1 + \sqrt{(\sqrt[3]{K} - 1)^2 - 4}\right]^2$$

$$K = (3 - sin\varphi)^3/(1 + sin\varphi)(1 - sin\varphi)^2$$

where c is the cohesion, φ is the angle of internal friction, and σ_0 is the bond stress, $\sigma_0 = ccot\varphi$.

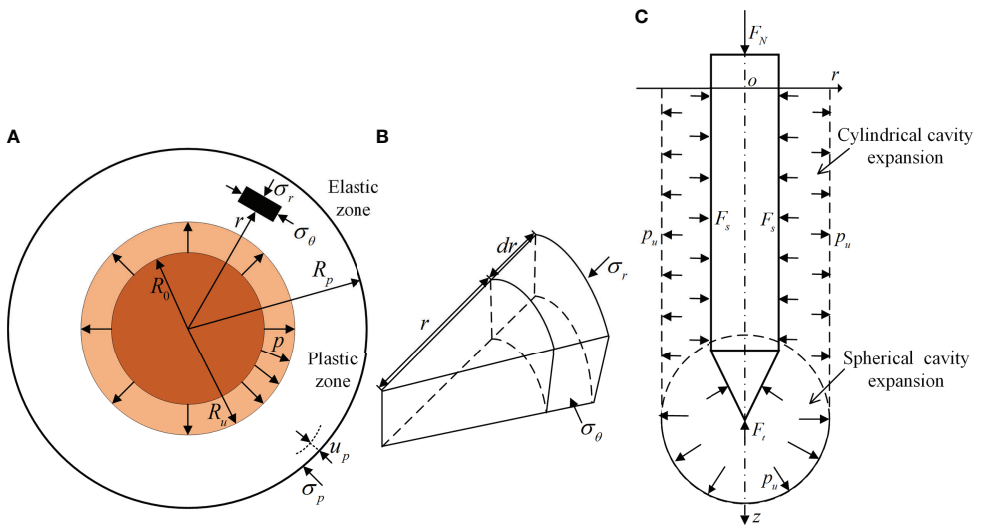

FIGURE 3
(A) Cylindrical cavity expansion model diagram; **(B)** force analysis of soil elements; and **(C)** spherical cavity expansion diagram.

Considering the boundary condition $r=R_u$,$\sigma_r=p_u$ and $r=R_p$, $\sigma_r=\sigma_p$, the stress in the plastic zone can be expressed as

$$\sigma_r = (p_u + \sigma_0)(R_u/r)^{\alpha} - \sigma_0$$

$$\sigma_\theta = (p_u + \sigma_0)(R_u/r)^{\alpha}/\eta - \sigma_0$$

where $\alpha=1-1/\eta$.

The reaming pressure after cavity expansion can be expressed as (Cao, 2020)

$$p_u = \sigma_0\left[2\eta/(\eta+1)\left(\sqrt{E(\eta+1)/2(1+v)(\eta-1)\sigma_0}\right)^{\alpha} - 1\right]$$

Therefore, the side friction resistance of the instrument during penetrating can be expressed as

$$F_S = 2\pi R_u L p_u$$

where R_u is the radius of the instrument, and L is the penetrating depth.

3.2 Calculation of the tip resistance during penetration process

The tip resistance and side friction resistance are independent and unrelated to each other during the monitoring instrument penetration, and the final penetration resistance is the sum of the two. The squeeze effect caused by the conical drill, and soil during the penetration process can be idealized and simulated to a spherical hole expansion in a half-space soil.

When soil reaches the state of plastic, based on the modified Lade–Duncan model and boundary condition ($r=R_u$,$\sigma_r=p_u$), the stress in plastic zone can be calculated as

$$\sigma_r = (p_u + \sigma_0)(R_u/r)^{2\alpha} - \sigma_0$$

$$\sigma_\theta = (p_u + \sigma_0)(R_u/r)^{2\alpha}/\eta - \sigma_0$$

The reaming pressure around the tip can be expressed as (Zhang and Deng, 2003)

$$p_u = \sigma_0\left[3\eta/(\eta+2)\left(\sqrt{2G(\eta+2)/3(\eta-1)\sigma_0}\right)^{2\alpha/3} - 1\right]$$

The multiplication of the reaming pressure and the projected area of the conical drill in the direction of penetration is the tip resistance. The simulated contact surface of the conical drill and soil is a hemispherical surface; thus, the ultimate tip resistance can be expressed as

$$F_t = p_u R_u^2 \pi = R_u^2 \pi \sigma_0\left[3\eta/(\eta+2)\left(\sqrt{2G(\eta+2)/3(\eta-1)\sigma_0}\right)^{2\alpha/3} - 1\right]$$

where R_u is the ultimate pore diameter after the expansion of the hole, which is equal to that of the sensor array, σ_0 is the bond stress, and G is the shear module.

3.3 Stability analysis on deployment process of casing pipe

Table 2 shows the theoretical calculation parameters and results of the side friction resistance and tip resistance. As shown in Figure 3C, during the penetration process, the casing pipe is subjected to the axial force (F_N) of the ROV's manipulator, and the penetration resistance (F_R) due to the soil-squeezing effect. Assuming that the penetrating velocity is uniform, the axial force and the compressive stress of casing pipe can be expressed as

$$F_N = F_R = F_s + F_t$$

$$\sigma_N = \frac{F_N}{\pi\left(r^2 - (r-t)^2\right)}$$

where r and t is the radius and the thickness of the casing pipe, respectively.

Considering the casing pipe as a thin-walled cylinder, the critical compressive stress based on the small deflection theory and large deflection theory can be respectively expressed as (Batdorf et al., 1947)

$$\sigma_{c1} = \frac{Et}{r\sqrt{3(1-\nu^2)}}$$

$$\sigma_{c2} = 0.238\frac{Et}{r}$$

The parameters for stability analysis are shown in Table 3.

3.4 Numerical simulation and results

3.4.1 Finite-element model

Considering that the penetration process of the strata deformation monitoring instrument may cause a large deformation of the mesh in the model, the coupled Eulerian–Lagrangian (CEL) method is applied. Hu et al. (2014) and Zheng et al. (2015) investigated various geotechnical problems using the CEL approach and confirmed its applicability to solve problems involving large deformations. Soil is tracked as it

TABLE 2 The parameters for resistance calculation.

Parameters	Symbol	Value
Cohesion (kPa)	c	2.94
The angle of internal friction (kPa)	φ	30
Young's modulus (MPa)	E	0.81
Poisson's ratio	v	0.32
Bond stress (kPa)	σ_0	5.092
Introduced parameter 1	η	3.825
Introduced parameter 2	K	41.667
Introduced parameter 3	α	0.739
reaming pressure (kPa)	p_u	1.607
Hole radius (mm)	R_u	90
Penetrating depth (m)	L	1.5
Side surface area (m^2)	S_A	0.424
coefficient of friction	f	0.32
Ultimate side resistance (N)	F_s	218.10
Ultimate tip resistance (N)	F_t	541.65

TABLE 3 The parameters for stability analysis during penetration.

Parameter	Symbol	Value
Radius (mm)	r	45
Thickness (mm)	t	3
Young's module (MPa)	E	210,000
Poisson's ratio	v	0.3
Axial stress (MPa)	σ_N	0.926
Critical stress 1 (MPa)	σ_{c1}	8.473×10^3
Critical stress 2 (MPa)	σ_{c2}	6.147×10^8

flows through a Eulerian mesh, fixed in space, by computing the material volume friction in each element. The elements, such as the tube or ADP, are discretized with Lagrangian elements, which can move through the Eulerian mesh without resistance until they encounter Eulerian elements containing soil.

3.4.2 Geometry, material parameters, and constitutive law

The geometry and material parameters are shown in Table 2. In order to model realistic soil, an investigation was conducted through reported cases and field tests (Jiang, 2001; Hu et al., 2009). The material properties of soil in Table 2 are derived from the reported cases and field tests in the Zhoushan Island (Wang et al., 2011). The soil was modeled obeying the Mohr–Coulomb yield criterion. The model is extensively used to model cohesive geological materials, such as soils and rocks (ABAQUS, 2008).

3.4.3 Mesh and boundary conditions

Considering the symmetry of the deployment process, only half-soil was modeled. The diameter and height of the soil zone were 13 D_a and 2 L_p, respectively, to ensure that the soil extension is sufficiently large to avoid a boundary effect in dynamics analysis. The soil zone is separated into two parts: the lower part, filled with soil, and the void upper part (i.e., material-free), which is used to allow soil to heave by containing the extruded soil during the deployment process. A typical mesh grid is shown in Figure 4. The mesh comprised eight-node linear brick element EC3D8R with decreased integration, and a fine mesh region is generated to accommodate the auxiliary deployment device during the entire deployment process. The auxiliary deployment device was simplified as a rigid part and assumed to remain vertical during the entire deployment process. The ADP dynamic deployment was modeled from the soil surface, with a given velocity of 150 mm/s.

3.4.4 Simulation results

Figure 5 shows the results of Mises stress contour in CEL analysis. During the penetration process, the instrument is mainly subjected to two resistances (side friction resistance and tip resistance), the value of which are shown in Figure 6. The tip resistance changes rapidly at the initial penetration, and the total

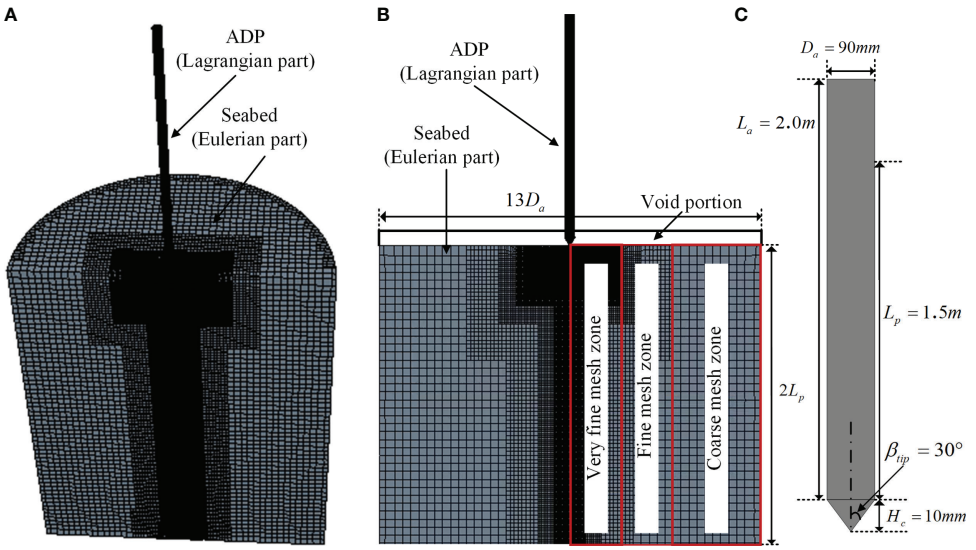

FIGURE 4
Typical mesh and geometry parameters used in coupled Eulerian–Lagrangian (CEL) analysis: **(A)** three-dimensional (3D) mesh; **(B)** side view; and **(C)** the geometry parameters of the auxiliary deployment part (ADP).

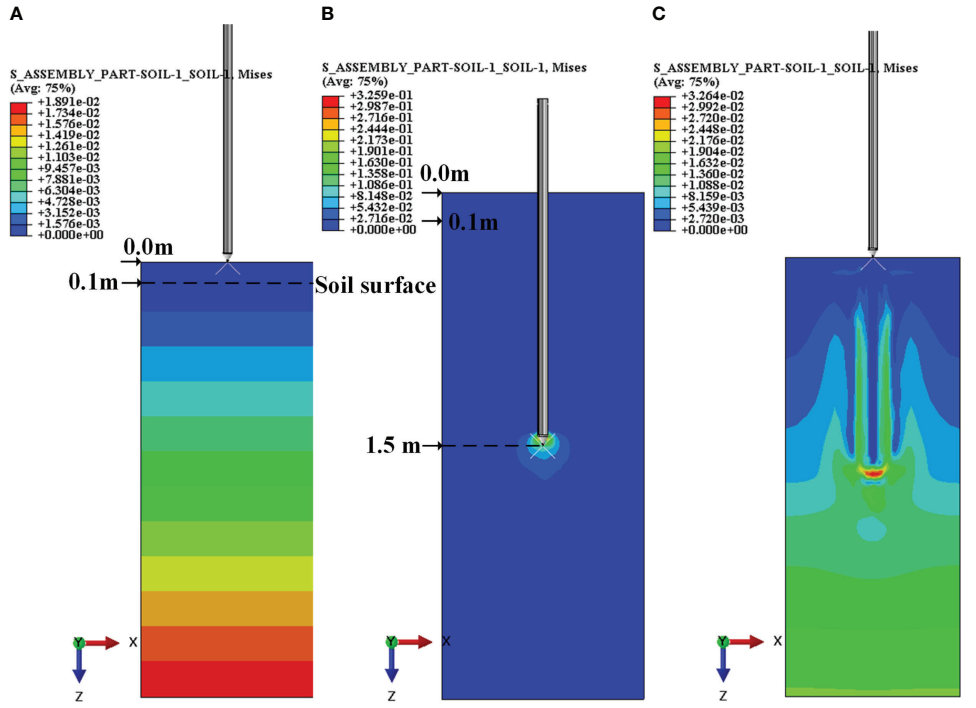

FIGURE 5
Mises stress contour in CEL analysis **(A)** at the initial state; **(B)** at a penetration depth of 1.5 m; and **(C)** after deployment.

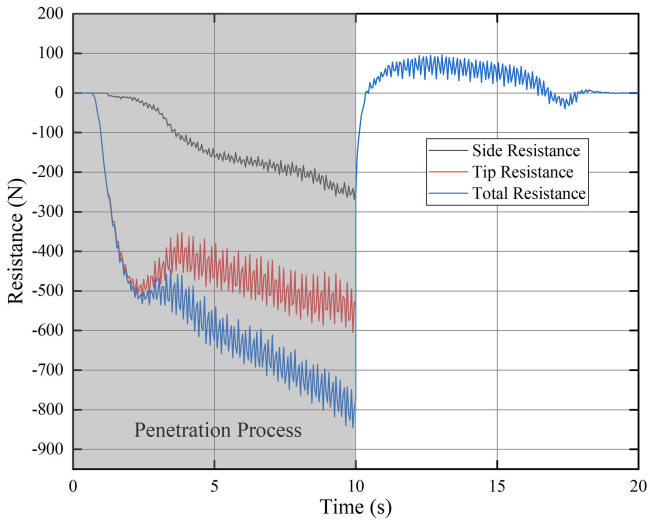

FIGURE 6
The resistance of ADP during the entire deployment process.

resistance is almost equal to the tip resistance. Yang et al. (2020) concluded that if the penetration depth is large enough, the tip resistance will tend to be a stable value. Obviously, the critical depth has not been reached in this case, so the tip resistance increases as the penetration depth increases and eventually reaching 549.32 N. The side friction resistance is mainly due to the soil-squeezing effect, which will increase as the penetration depth increases. The maximum side friction resistance is 251.61 N at the depth of 1.5 m. During the pull-out process of the casing pipe, since the conical drill and IMP remain in the strata, the resistance in this process is only the side friction resistance, which is much smaller than the maximum penetration resistance.

4 Experiment and results

4.1 Mechanical test of indoor deployment process

4.1.1 Design of the experiment

4.1.1.1 Experimental setup

The experimental setup is schematically illustrated in Figure 7. It is comprised of a 3.5-m height experiment platform, a guide rail, a lead screw, a servo motor, a motor controller, a plastic cylindrical tank with well-stirred saturated soft soil, the ADP, and a force sensor. The diameter and depth of the soil tank is 800 and 900 mm, respectively. The length and diameter of the ADP are 1,500 and 90 mm, respectively. The servo motor is installed on the top of the lead screw and can push down or pull up the lead screw along the guide trail at a specific velocity. A high-precision force sensor is placed between the ADP and lead screw to record the stress.

4.1.1.2 Model ADP, soil preparation, and characteristic

The model ADP and solid conical drill was manufactured for the test as shown in Figure 7. The length, diameter and thickness of the ADP is 1, 63, and 1 mm, respectively. The length, diameter and the cone angle of the conical drill is 70 and 65 mm and 30° . The combination of bentonite and fine sand was used to modulate the simulated soil for seabed sediment through the analysis of the physical properties and field sampling data of the seabed sediment (Li and Li, 2010), the mass proportions of which are 70% and 30%, respectively. The soil preparation and characteristic refer to the Wang (2016) reference. Three different properties of soil (flow plastic clay, plastic clay, and try plastic clay) were used in the experiment, as shown in Figure 7.

4.1.1.3 Test procedure

The test processes were as follows: first, some connections and adjustments were completed. The tilt angle of the guide rail and lead screw were adjusted to ensure that the penetration direction of the ADD is perpendicular to the soil bed. Next, the servo motor controller was set up, and the motor as set to make the lead screw move down and keep a velocity of 10 mm/s. Then, the serial port of the host computer was opened to record and save the value of the resistance at a frequency of 1 Hz. Finally, the rotation direction of the motor was changed to pull up the lead screw. The experimental test was repeated three times in order to eliminate the single measurement errors. After each test, the soil bed was stirred with a cement vibrator and stand settlement for 2 days to ensure that soil was fully reconsolidated. The averaged resistance was regarded as the final penetration resistance.

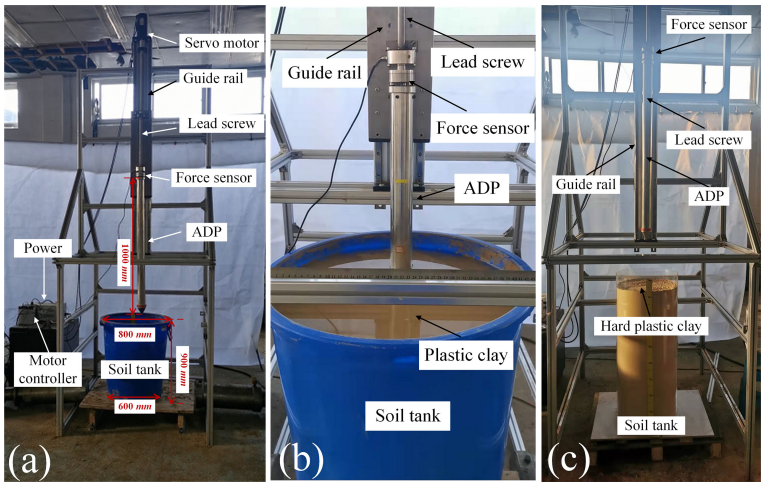

FIGURE 7
Layout of the experiment setup: **(A)** global view of the test bench; **(B)** ADP and plastic clay; and **(C)** ADP and dry plastic clay.

4.1.2 Experiment results and analysis

Three types of soils with different water content were used in tests. The results of maximum penetration force are shown in Table 4, and the forces during penetration are shown in Figure 8. The dry plastic clay is without water in the void; thus, the friction between soil particles is large, resulting in large penetration resistance. The water content of the plastic clay is approximately 25%, similar to the mass ratio in the reference (Wang, 2016). The maximum penetration resistance in plastic clay is close to the numerical results. Flow plastic clay is saturated clay and is covered with water. Excessive water molecules in the voids of soil particles reduce the friction between particles, so the penetration resistance is the smallest.

4.2 Mechanical test of deployment process in tidal flat

4.2.1 Study area

Changzhi Island (122°10′*E*,29°58′*N*) is located in the south of Zhoushan Island in Zhejiang, China, as shown in Figure 9. The Changzhi Island is 7.3 km away from Dinghai district and 350 m away from Zhoushan Island. The coastline is 13.82 km long and covers the land area is 6.30 km^2. The experiment area is the north of Changzhi Island, as shown in Figure 9. The natural experimental conditions on the Changzhi Island are very good. A large range of muddy tidal flat have been formed in Changzhi Island after several sea reclamations, and contains thick soft sediment that has high water content and a large initial void ratio and is mainly flow plastic clay (Xiong et al., 2019).

4.2.2 Tidal flat penetration experiment

Figure 10 presents a diagram of the penetrating experimental setup. The experimental setup and test procedure have been introduced in Section 5.1. In the field tidal flat experiment, the ADP penetrated into the tidal flat with the driving of the servo motor at a velocity of 10 mm/s, and the force sensor and PC recorded the resistance during the entire penetrating process. In order to eliminate the single position error, three repeatable tests were carried out in three adjacent positions (with a distance of 1 m from each other).

4.2.3 Experiment results and analysis

Figure 11 shows the penetration resistance in a tidal flat experiment. The maximum penetration resistance of test 1, test 2, and test 3 are 349, 365, and 378 N, and the averaged maximum penetration resistance is 364 N. Since the sediment layer is

TABLE 4 Results of the penetration tests.

Test No.	Properties of clays	Maximum penetration force (N)
1	Flow plastic	52
2	Plastic clay	335
3	Try plastic clay	1,049

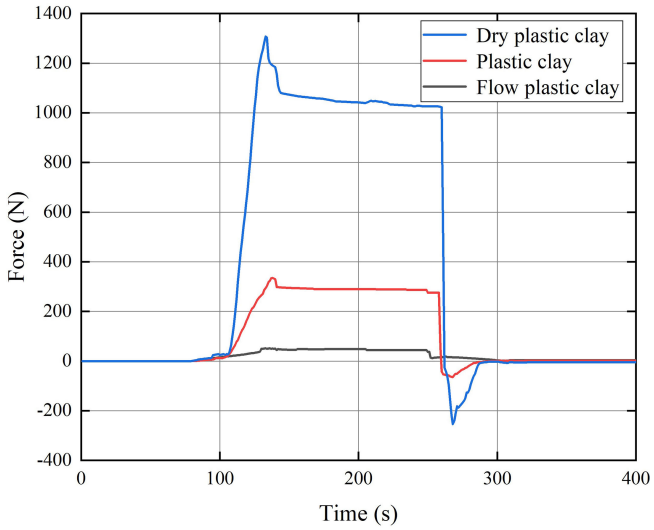

FIGURE 8
Penetration resistance in three types of clay.

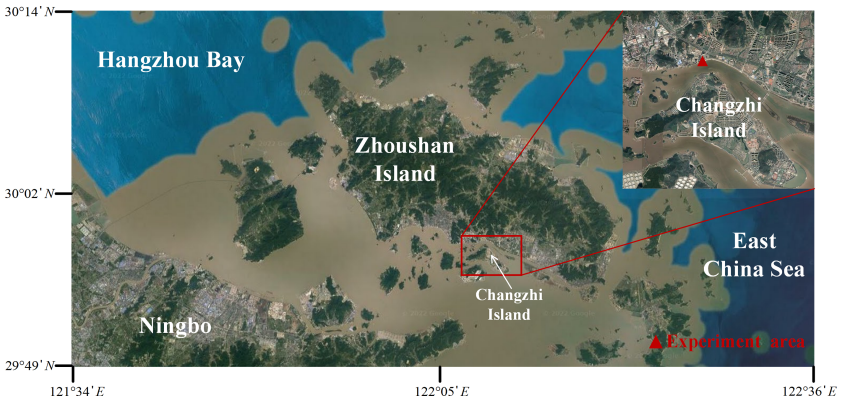

FIGURE 9
The location of the Changzhi Island in Zhoushan Island, China.

relatively uniform, no obvious abrupt changes were recorded in the force sensor. The penetration resistance increases as the penetration depth increases and then gradually decreases after it reaches the maximum penetration depth and remains stable. The pull-out force and penetration force are in opposite directions; thus, the force direction changes abruptly as the pull-out operation is performed. However, the maximum resistance during the pull-out process is much smaller than that in the penetration process. The final weight of the ADP is 10–20 N larger than the initial weight due to the adhesion of mud on the surface and inside.

4.3 *In situ* strata deformation monitoring test, results, and analysis of tidal flat

In order to verify the *in situ* deployment method and the monitoring performance of the strata deformation monitoring instrument, an *in situ* deploying and monitoring experiment was carried out in a tidal flat. The presented instrument operated for five consecutive days. The *in situ* deployment location is in the field experiment site described in Section 5.2. The deployment process is shown in Figure 12. There are five monitoring nodes in the instrument, and each node has two

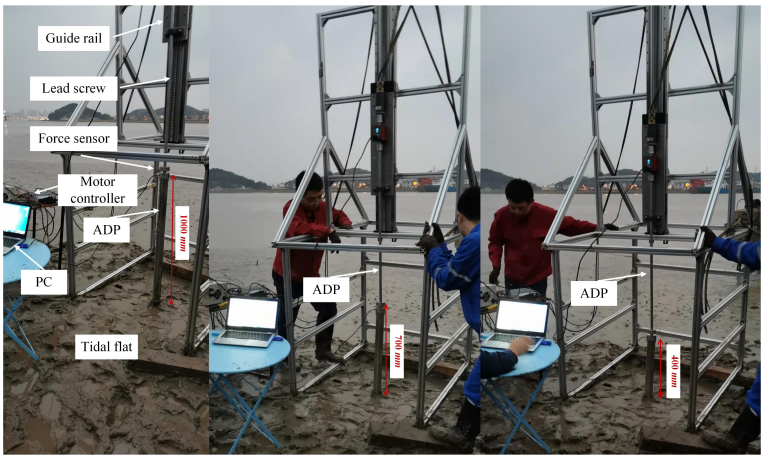

FIGURE 10
Tidal flat penetrating experimental setup.

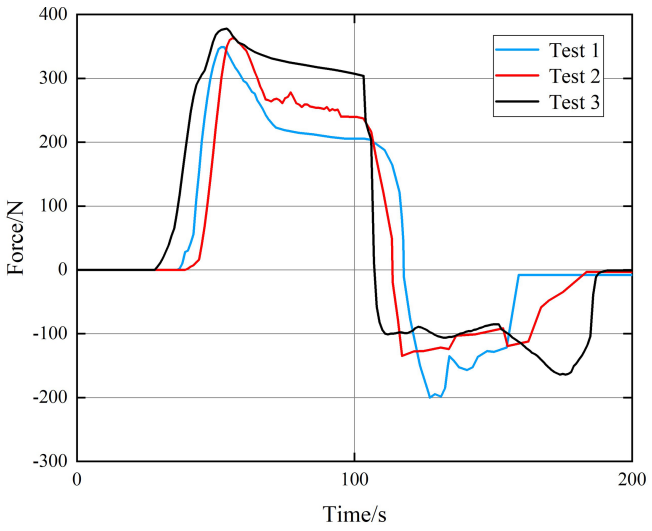

FIGURE 11
Penetration resistance in a tidal flat experiment.

MEMS sensors to monitor the strata deformation in the X and Y directions.

Figure 13 shows the pitch angle of the sensors every 6 h. The initial shape of the IMP is not straight since the sediment layer is soft and the surrounding soil flows and squeezes the IMP as the deployment process is accomplished. The initial deflection angles of the first monitoring node in the direction of X and Y are 11.01 ° nd 12.08 ° respectively. The strata will deform or move under the action of tides, waves, etc. Since the data acquisition period is 6 h, the obtained data cannot reflect the influence of the tide change or specific waves, but it can reflect the cumulative deformation changes of the tidal flat.

Figure 14 shows the deformation of the strata. The maximum and average deformations of the strata are shown in Table 5. The maximum deformation of the first monitoring node is 1.66 cm, and the deformations in the X and Y direction are 1.19 and 1.17 cm, respectively. The deep strata changes very little; on the contrary, the shallow layer changes more frequently due to the influence of the tide and wave. It is worth noting that

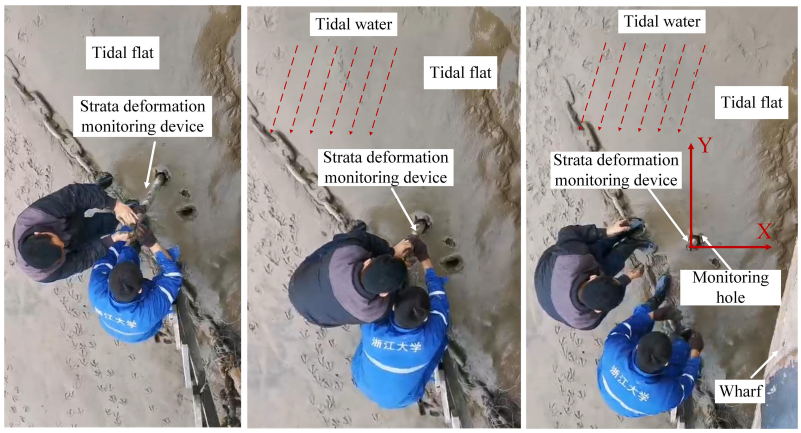

FIGURE 12
Deployment process of the monitoring instrument.

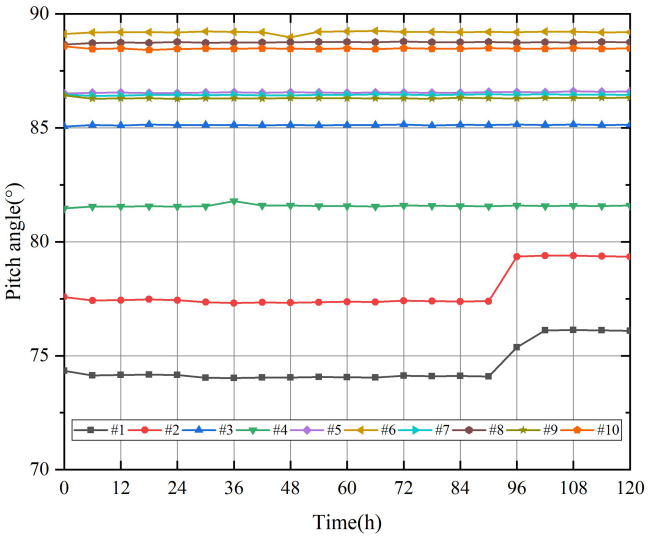

FIGURE 13
Pitch angle of the sensor nodes.

although the average deformation of the forth monitoring node (sensor #7 and #8, at a depth of 1.6 m) is large, the deformation mainly comes from the first monitoring period (2022-1-25-10-00-00 to 2022-1-25-16-00-00). It can be considered that the soil around the IMP was crushed and damaged during deployment and recovered and consolidated after experiencing a tidal change. After that, the monitoring node has a good coupling relationship with soil; thus, the following deformation changes are relatively small.

5. Discussion and conclusion

In this paper, an innovative monitoring instrument was presented for seabed strata deformation monitoring. A sufficient mechanical analysis of the entire deployment process was carried out through theoretical, numerical, and experimental research. Firstly, the reaming pressure and penetration resistance were studied based on the cavity expansion model and modified Lade–Duncan yield criterion. Then, based on the software of

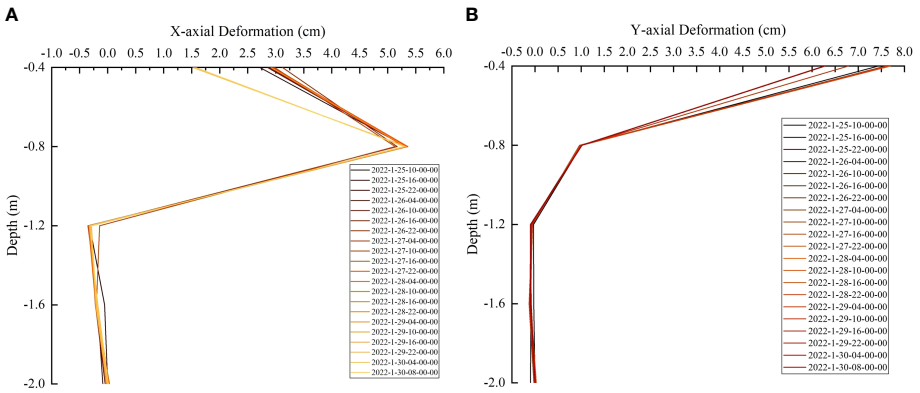

FIGURE 14
Deformation of the monitoring instrument. **(A)** the deformation in X-axis, **(B)** the deformation in Y-axis.

TABLE 5 The maximum and average deformation of the strata.

Direction	X-axial					Y-axial				
Sensor node	#2	#4	#6	#8	#10	#1	#3	#5	#7	#9
max.def (cm)	-1.19	-0.19	-0.03	-0.16	-0.09	-1.17	-0.03	-0.07	-0.10	-0.09
aver.def (cm)	-0.13	-0.02	0.01	-0.14	0	-0.10	-0.01	-0.04	-0.08	0

ABAQUS, the finite-element model was established and the coupled Euler–Lagrangian method was carried out to numerically simulate the entire deployment process, proving the stability and feasibility of the deployment method. A series of indoor and field tests were conducted to validate the maximum penetration resistance obtained and the monitoring ability of the proposed instrument. The experimental results demonstrate the feasibility of the proposed monitoring instrument. The main results of this paper are as follows:

1. The numerical simulation and theoretical results show that when the penetration depth of the instrument is 1.5 m, the maximum penetration resistance is 800.93 and 759.65 N, respectively. Although the penetration resistance calculated in numerical simulation is slightly larger than that in theoretical analysis, the required penetration force can be provided by the manipulators of ROV. The reliability and stability of the *in situ* deployment method with the auxiliary deployment part are verified.
2. The experimental results show that when the penetration depth is 900 mm, the maximum penetration resistance in theoretical analysis and indoor and field tests is 357, 335, and 378 N. Since the field test is located in the tidal flat, the sediment layer is not continuous and the water layer is in the lower layer, the upper layer is harder, and the penetration resistance obtained is the largest. However, the trend of the penetration resistance is similar during the entire deployment process. As the penetration depth increases, the penetration resistance will gradually increase, and the maximum resistance will eventually drop a little and remain stable at the deepest position. The direction of the resistance will change during the pull-out process due to the changes of the pulling force, but the maximum pull-out resistance is smaller than the penetration resistance.
3. The results of the monitoring test of the tidal flat in Changzhi Island show that the deformation of the surface sediment layer is most affected by the tidal and waves. The maximum deformation of the monitoring node in the surface layer (0.4 m) is 1.66 cm, and the average deformation in the direction of X and Y are 0.13 and 0.10 cm, respectively.

Data availability statement

The original contributions presented in the study are included in the article/supplementary material. Further inquiries can be directed to the corresponding author.

Author contributions

Methodology: YG and JC. Formal analysis: CC and YG. Experiment: PenZ, YG, TL, JA, and XL. Data curation, PeiZ, XL and YG. Writing—original draft preparation, YG. Writing—reviewand editing, YG. Visualization, PeiZ and YG. Project administration, JC. Funding acquisition, JC. All authors contributed to the article and approved the submitted version.

Funding

This study was funded by the National Natural Science Foundation of China (41976055), Finance Science and Technology Project of Hainan Province (ZDKJ202019), and Key Research and Development Project of Zhejiang Province (2018C03SAA01010).

Conflict of interest

The authors declare that the research was conducted in the absence of any commercial or financial relationships that could be construed as a potential conflict of interest.

Publisher's note

References

ABAQUS (2008). *ABAQUS 6.6 theory manual* (Washington: ABAQUS Inc).

Batdorf, S. B., Schildcrout, M., and Stein, M. (1947). Critical stress of thin-walled cylinders in axial compression *National Advisory Comittee For Aeronotics* 543, 543–550.

Cao, J. (2020). *Characteristics and numerical simulation of jacked pile driving in saturated clay* (Yanshan, Hubei, China: Yanshan University).

Ewy, R. T. (1999). Wellbore-stability predictions by use of a modified lade criterion. *Spe Drill Completion* 14 (2), 85–91. doi: 10.2118/56862-PA

Ge, Y. Q., Chen, J. W., Cao, C., He, J. M., Zhou, P., Gao, F., et al. (2021). Development and Sea trial of the terrain monitoring device based on MEMS sensing array. *IOP Conf. Ser.: Earth Environ. Sci.* 861 (7), 072008. doi: 10.1088/1755-1315/861/7/072008

Hu, P., Wang, D., Cassidy, M. J., and Stanier, S. A. (2014). Predicting the resistance profile of a spudcan penetrating sand overlying clay. *Can. Geotech J.* 51 (10), 1151–1164. doi: 10.1139/cgj-2013-0374

Hu, R. J., Wu, J. Z., Zhu, L. H., and Ma, F. (2009). Characteristic of surface sediment transport in zhoushan archipelago Sea area, East China Sea (in chinese). *Periodical Ocean Univ. China* 3, 7. doi: 10.16441/j.cnki.hdxb.2009.03.022

Jiang, G. J. (2001). The characteristics of hydro-dynamics and sediments in the strait channels of zhoushan islands area (in chinese). *J. Zhejiang Univ.* 28 (1), 10. doi: 10.3321/j.issn:1008-9497.2001.01.016

Koch, S., Berndt, C., Bialas, J., Haeckel, M., and Greinert, J. (2015). Gas-controlled seafloor doming. *Geology* 43 (7), 571–574. doi: 10.1130/G36596.1

Lade, P. V., and Duncan, J. M. (1975). Elastoplastic stress-strain theory for cohesionless soil. *J. Geotech Eng. Div* 101 (10), 1037–1053. doi: 10.1061/AJGEB6.0000204

Li, L., and Li, S. L. (2010). Simulation and mechanical characteristics of terramechanics of the surface soil on deep-sea bed (in chinese). *Eng. Mech* 11, 213–220. doi: 10.3724/SP.J.1011.2010.01138

Nixon, M. F., and Grozic, J. L. H. (2007). Submarine slope failure due to gas hydrate dissociation. *preliminary quantif: Can. Geotech J.* 44 (3), 314–325. doi: 10.1139/t06-121

Paull, C. K., Caress, D. W., Thomas, H., Lundsten, E., Anderson, K., Gwiazda, R., et al. (2015). Seafloor geomorphic manifestations of gas venting and shallow subbottom gas hydrate occurrences. *Geosphere* 11 (2), 491–513. doi: 10.1130/GES01012.1

Phillips, K. A., Chadwell, C. D., and Hildebrand, J. A. (2008). Vertical deformation measurements on the submerged south flank of kīlauea volcano, hawai'i reveal seafloor motion associated with volcanic collapse. *J. Geophys Res.* 113, 1–15. doi: 10.1029/2007jb005124

Polster, A., Fabian, M., and Villinger, H. (2009). Effective resolution and drift of paroscientific pressure sensors derived from long-term seafloor measurements. *Geochem Geophy Geosys* 10 (8), 1–19. doi: 10.1029/2009GC002532

Prior, D. B., Suhayda, J. N., Lu, N. Z., Bornhold, B. D., Keller, G. H., Wiseman, W. J., et al. (1989). Storm wave reactivation of a submarine landslide. *Nature* 341 (6237), 47–50. doi: 10.1038/341047a0

Ruppel, C. D., and Waite, W. F. (2020). Grand challenge: Timescales and processes of methane hydrate formation and breakdown, with application to geologic systems. *J. Geophys Res.: Solid Earth.* 125, 1–43. doi: 10.1029/2018JB016459

Saito, H., and Yokoyama, T. (2008). "Development of seafloor displacement monitoring system using a 3-component servo-accelerometer," in *Proceedings oceans.* (Kobe, Japan: MTS/IEEE Kobe Techno-Ocean)

Tao, C., Yu, Z., Zheng, J. J., Du, J., and Garg, A. (2018). Improvement of the cavity expansion theory for the measurement of strain softening in over consolidated saturated clay. *Measurement* 119, 156–166. doi: 10.1016/j.measurement.2018.01.069

Tsushima, H., Hino, R., Tanioka, Y., Imamura, F., and Fujimoto, H. (2012). Tsunami waveform inversion incorporating permanent seafloor deformation and its application to tsunami forecasting. *J. Geophys Res. Solid Earth* 117 (B3), 1–20. doi: 10.1029/2011JB008877

Wang, M. (2016). *Key technology research of submarine self-propelled tracked trencher (in chinese)* (Shanghai, China: Shanghai Jiao Tong University).

Wang, Y., Feng, J.-C., Li, X.-S., Zhang, Y., and Han, H. (2017). Experimental investigation on sediment deformation during gas hydrate decomposition for different hydrate reservoir types. *Energy Proc.* 142, 4110–4116. doi: 10.1016/j.egypro.2017.12.333

Wang, Z., Jia, Y., Liu, X., Dong,, Shan, ,.H., and Guo, (2018). In situ observation of storm-wave-induced seabed deformation with a submarine landslide monitoring system. *Bull. Eng. Geol Environ.* 24, 701–709. doi: 10.1007/s10064-017-1130-4

Wang, Z. H., Pan, Y. J., Pan, G. F., and Chen, P. X. (2011). Statistic analysis of physical and mechanical indices of quaternary marine sediments in the western sea area between zhoushan and daishan island (in chinese). *Mar. Sci. Bull.* 30 (5), 557–561. doi: 10.11840/j.issn. 1001-6392.2011.5.013

Wang, Z., Sun, Y., Jia, Y., Shan, Z., and Wen, S. (2020). Wave-induced seafloor instabilities in the subaqueous yellow river delta–initiation and process of sediment failure. *Landslides* 7, 1–14. doi: 10.1007/s10346-020-01399-2

Xiong, Z., Wang, M. Y., Shan, Z. G., Yan, Q., Wang, Y. J., and Li, T. (2019). Physical and chemical characteristics of marine sediments in the offshore of zhoushan (in chinises). *Coast. Eng.* 38 (1), 6. doi: 10.3969/j.issn.1002-3682.2019.01.006

Xu, C., Chen, J., Zhu, H., Liu, H., and Lin, Y. (2019). Experimental research on seafloor mapping and vertical deformation monitoring for gas hydrate zone using nine-axis MEMS sensor tapes. *IEEE J. Oceanic Eng.* 44 (4), 1090–1101. doi: 10.1109/JOE.2018.2859498

Yang, S., Liu, J., Zhang, M., and Wang, Y. (2020). Analytical solution and field test of critical bearing capacity and settlement of pile tip. *Stavební obzor - Civil Eng. J.* 29 (1), 61–73. doi: 10.14311/CEJ.2020.01.0006

You, K., Flemings, P. B., Malinverno, A., Collett, T. S., and Darnell, K. (2019). Mechanisms of methane hydrate formation in geological systems. *Rev. Geophy* 57 (4), 1146–1196. doi: 10.1029/2018RG000638

Zhang, M. Y., and Deng, A. F. (2003). A spherical cavity expansion-sliding friction calculation model on penetration of pressed-in piles. *Rock Soil Mech*. 24, 701–709. doi: 10.1142/S0252959903000104

Zheng, J., Hossain, M. S., and Dong, W. (2015). New design approach for spudcan penetration in nonuniform clay with an interbedded stiff layer. *J. Geotech Geoenviron Eng.* 141 (4), 04015003. doi: 10.1061/(ASCE)GT.1943-5606.0001282

frontiers | Frontiers in Marine Science

TYPE Original Research
PUBLISHED 12 October 2022
DOI 10.3389/fmars.2022.1011029

OPEN ACCESS

EDITED BY
Yuan Lin,
Zhejiang University, China

REVIEWED BY
Bisheng Wu,
Tsinghua University, China
Hu Wang,
Tianjin University, China
Tengfei Fu,
Ministry of Natural Resources of the People's Republic of China, China

*CORRESPONDENCE
Cong Hu
hucong@ouc.edu.cn
Yonggang Jia
yonggang@ouc.edu.cn

SPECIALTY SECTION
This article was submitted to Ocean Observation, a section of the journal Frontiers in Marine Science

RECEIVED 03 August 2022
ACCEPTED 27 September 2022
PUBLISHED 12 October 2022

CITATION
Wang H, Hu C, Feng X, Ji C and Jia Y (2022) *In-situ* long-period monitoring of suspended particulate matter dynamics in deep sea with digital video images.
Front. Mar. Sci. 9:1011029.
doi: 10.3389/fmars.2022.1011029

In-situ long-period monitoring of suspended particulate matter dynamics in deep sea with digital video images

Hui Wang[1], Cong Hu[1,4]*, Xuezhi Feng[1], Chunsheng Ji[1,3] and Yonggang Jia[1,2,4]*

[1]Shandong Provincial Key Laboratory of Marine Environment and Geological Engineering, Ocean University of China, Qingdao, China, [2]Laboratory for Marine Geology, Qingdao National Laboratory for Marine Science and Technology, Qingdao, China, [2]Key Laboratory of Marine Environment and Ecology, Ministry of Education, Ocean University of China, Qingdao, China, [3]Sanya Institute of South China Sea Geology, Guangzhou Marine Geological Survey, China Geological Survey, Sanya, China, [4]Key Laboratory of Marine Environment and Ecology, Ministry of Education, Ocean University of China, Qingdao, China

Suspended particulate matter (SPM) plays an important role in material transport, deposition, resuspension and the function of benthic communities' processes in deep sea. SPM concentration data is usually indirectly measured by optical/acoustic sensors. However, converting these sensors' signal to SPM concentration is associated with a number of uncertainties, which will lead to mis-estimation of the results. Some researchers recommend combining several optical/acoustic sensors to determine SPM concentration. However, due to the lack of corresponding video images, the interpretation of significant mismatch signals recorded by different sensors is subjective. Consequently, a better understanding of long-period SPM dynamics, especially in deep sea, is still a challenge. In this study, we seek to monitor the dynamics of SPM in deep sea, by firstly obtaining *in-situ* digital video images at a water depth of 1450 m on the northern slope of South China Sea in 2020, and secondly developing a digital image processing method to process the *in-situ* monitoring data. In this method, we defined an image signal which was the ratio between the area of the SPM and that of the total image, to characterize the SPM concentration. A linear regression model of the image signal and SPM concentration was established (R^2 = 0.72). K-fold cross-validation showed that the performance of the model was well. We calculated the SPM concentration derived from image signal, and manually classified SPM into three distinct morphological groups. The long-period observation revealed that numerous aggregates existed in deep sea. The change of SPM concentration and morphology under hydrodynamics was synchronous. When current speed equaled to or exceeded 0.15 m/s, there was a significantly increase in SPM concentration and size. However, such increase was episodic. When current speed decreased, they will also decrease. In addition, we compared the image signal with the optical/acoustic backscattering signal, analyzed the mismatch period among these three

signals. We found that the optical backscatter signal can't accurately reflect the SPM concentration during the mismatch period. To our best knowledge, this is the first time that the *in-situ* digital video images were used to analyze the dynamics of SPM in deep sea.

KEYWORDS

deep sea, suspended particulate matter, image processing, *in-situ* observation, measurement, digital video images

1 Introduction

Suspended particulate matter (SPM) refers to a mixture of clay to sand-sized particles that can be detected in suspension, and that consists of minerals from physical-chemical and biogenic origin, living and non-living organic matters (Fettweis et al., 2019). In deep sea, because there is a favorable physical and chemical environment for increased coagulation rates, constituents of the SPM generally are organic-mineral or nonbiological aggregates (Gardner and Walsh, 1990; Thomsen and Gust, 2000; Arı´Stegui et al., 2009; Bochdansky et al., 2010; Verdugo and Santschi, 2010). In addition, the deep-sea environment is extremely complex, the SPM will reaggregate or disaggregate. In terms of ecosystems, the SPM are the basis of food chain, which is closely related to the function of benthic communities (Duineveld et al., 2001; García and Thomsen, 2008; Amaro et al., 2015). Understanding the dynamics of SPM in concentration and morphology is crucial for investigating the process of material transport, deposition, re-suspension and biochemical cycle (Durrieu De Madron et al., 2017; Diercks et al., 2018; Jia et al., 2019; Wang et al., 2022). Hence, it is of great significance to accurately and continuously monitor the long-period variation of SPM in deep sea.

Long-period and high frequency deep-sea SPM concentration data is typically collected indirectly with sensors, which measure either the optical or acoustic backscatter signal (Eittreim, 1984; Rai and Kumar, 2015; Haalboom et al., 2021). Converting these signals to SPM concentration need to establish an inversion model of optical/acoustic backscatter signal with the true SPM concentration by field calibrations (Holdaway et al., 1999; Neukermans et al., 2012). The true SPM concentration is calculated through gravimetric measurements of filtered and dried *in-situ* discrete water samples (Wren et al., 2000; Rai and Kumar, 2015). The optical and acoustic signals depend not only on the SPM concentration, but also on the inherent properties of SPM, such as the SPM size distribution and aggregation (Hatcher et al., 2001; Downing, 2006; Sahin et al., 2019), shape and composition (Ohnemus et al., 2018). Whereas, for *in-situ* long-period observation of deep-sea SPM, the inherent properties of SPM will change under complex hydrodynamic conditions. What's more, it' difficult to obtain water samples from the bottom of deep-sea at different time to calibrate the parameters of the inversion model in real time. This will make the interpretation and quantification of the responses of different signal types complicatedly, and result in mis-estimation of the SPM concentration (Fettweis et al., 2019; Haalboom et al., 2021).

Recently, digital imaging technology and image processing algorithms are rapidly developed, which can be used in SPM measurement. This technology can measure both SPM concentration and morphology. The measuring technology is more intuitive because it directly takes photos. According to different image processing methods, this technology can be grouped into two categories. The direct measurement methods conduct microscopic images on a certain volume of water, calculate the size and shape of each SPM in the image, and then estimate the SPM volume concentration either using empirical or 3D reconstruction methods (Syvitski and Hutton, 1997; Eisma et al., 2001; Graham and Nimmo Smith, 2010; Gray et al., 2010; Rai and Kumar, 2015; Ramalingam and Chandra, 2018). However, these methods are expensive and require precise *in-situ* imaging systems, like Video Plankton Recorder (VPR) (Davis et al., 2005) and Underwater Vision Profiler (UVP) (Gorsky et al., 2000; Picheral et al., 2010). The indirect methods, on the contrary, aim to determine the SPM concentration by analyzing specific image signals, such as the ratio between image hue and saturation (Moirogiorgou et al., 2015), the ratio of blue and red counts (Hoguane et al., 2012), or mean grey level value (Lunven et al., 2003). These methods don't require sophisticated imaging instrument, and only use a digital camera to capture images. Recently such indirect methods were only applied in riverine environment and there was no relevant research in deep-sea environment.

This paper aims to further understand the dynamics of SPM in deep sea, solve the problem of mis-estimation of SPM concentration measurement caused by existing monitoring technologies, and explore the potential application of indirect image analysis in SPM dynamics. We obtained *in-situ* digital video images at a water depth of 1450 m on the northern slope of South China Sea in 2020. An indirect image analysis method was proposed to

analyze the long-period dynamics of SPM in deep sea. This study is organized as follows. Section 2 describes the study area and equipment. Section 3 introduces image analysis methods and defines an image signal which is the ratio between the area of the SPM imaging area and that of the total image, to characterize SPM concentration. Section 4 analyzes and discusses the cross-correlation of different signals, establishes and validates the relationship between image signal and SPM concentration, analyzes the dynamics of SPM in concentration and morphology and reveals the dynamics of SPM under the effect of hydrodynamics. Section 5 and Section 6 gives the future outlook and conclusion respectively.

2 Field observation

2.1 Study area

The South China Sea (SCS) is one of the largest and deepest marginal seas in the western Pacific Ocean (Wang et al., 2021). The northern slope of the SCS is located between the shelf-break and the deep-sea plain of the SCS, with the water depth of 300-3700 m. The sediments on the slope are mainly argillaceous calcareous silty sand and silty clay (Luan et al., 2019). The Shenhu Submarine Canyon Group (SSCG) is one of the obvious submarine landforms in the northern slope of SSC (Su et al., 2020). The SSCG is composed of 17 NW-SE oriented slope-confined submarine canyons and acts as the primary conduits for sediment delivered from the continental shelf and upper slope to deep water sedimentary basins (Su et al., 2020; Li et al., 2022). Our study area is located at the toe of one of the SSCG. As shown in Figure 1, SH2 (19.90°N, 115.27°E) is the monitoring point, the water depth of SH2 is approximately 1450 m. During the cruise, a box corer was used to collect sediment samples in the study area. After the seafloor sediments were collected, we inserted PVC tubes into the box corer to collect short cylindrical sample which was approximately 50 cm long. The physical properties of the sample were measured in the laboratory and the results are shown in Table 1. The results indicated that the surficial sediments have high water content (ω), high saturation (Sr) and large porosity (n). The mean particle size (D_{50}) approximately equals to 0.01 mm, the sediments are fine and cohesive. In addition, X-ray diffraction experiment showed the surficial sediments are dominated by clay minerals and rich in carbon source. The hydrodynamics within the northern slope of South China Sea is characterized by strong diurnal and semidiurnal tides (Zhao, 2014). The complex topography together with the along-slope tidal currents result in the generation of internal tides (Feng et al., 2021). The water flow velocity caused by internal tides in the deep-sea continental slope can reach 0.15 m/s (Xie et al., 2018). These enhanced hydrodynamics influence water mixing near the seafloor, result in sediment and organic matter resuspension and facilitate materials along-slope transport (Liu et al., 2019; Wang et al., 2022).

2.2 Equipment

The lander, shown in Figure 2A, is made of stainless steel. Its size is 3.5 m in length, 3.5 m in width and 2.7 m in height. An imaging system (to obtain video images), a Nortek Vector Acoustic Doppler Velocimetry (ADV) (to record acoustic backscatter signal and velocity), and a RBR turbidimeter (to collect optical backscatter signal), were mounted in the lander. The height above the seabed of the three instruments is 1.13, 0.6

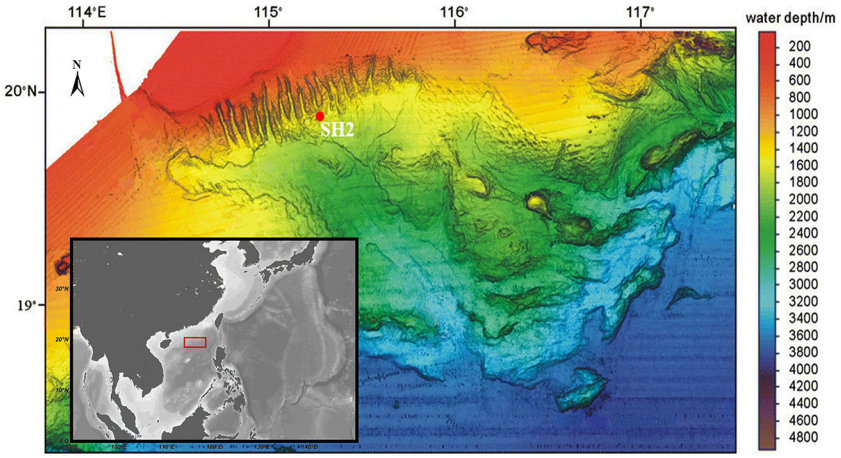

FIGURE 1
Geographical location (lower left inset) and the multi-beam geomorphology shadow map of the Pearl River Canyon system and adjacent area, red dot (SH2) is the monitoring point. Geographical location was mapped by Ocean Data View. The multi-beam geomorphology shadow map was modified from Ding et al. (2013).

TABLE 1 Physical properties of surface sediments in the study area.

Depth (cm)	ω(%)	ρ (g/m^3)	n (%)	D50 (mm)	Sr (%)	ω_l (%)	ω_p (%)
0-10	105.59	1.40	75	0.010	96	98	38
10-20	101.00	1.39	75	0.011	93	98	38
20-30	106.51	1.43	75	0.008	98	98	38
30-40	101.10	1.45	75	0.007	97	98	38
40-50	101.75	1.42	74	0.009	97	98	38

ω is the water content, ρ is the sediment natural density, n is the porosity, D50 is the mean particle size, Sr is the sediment saturation, ω_l is the liquid limit, ω_p is the plastic limit.

and 0.82 m respectively. The imaging system consists of a digital video-camera, a LED light and an underwater battery. To reduce the size of the imaging system, a self-contained high-resolution (1080×1920) Charge Coupled Device (CCD) camera, and a Trans Flash (TF) card were used for video storage. The space that the camera can capture is approximately 0.6 m^3. Illumination is provided by a small, low-power LED light. The total power of the system is about 18 W (3 W for the camera and 15 W for the LED light). Both the camera and the LED have the anti-pressure and anti-corrosion capacities.

2.3 Field work

The lander was deployed from the Dongfanghong3 survey vessel to the seabed on September 3rd in 2020. It was successfully recovered by controlling acoustic releases to discard counterweight on September 23rd in 2020. The digital video-camera's imaging rate was 30 frames per second. The video images were taken in burst for 5 s every 3 min followed by a shutdown to conserve battery and memory. The sampling frequency of the RBR turbidimeter is 1/20 Hz and that of the ADV is 16 Hz. The details of the instrument are summarized in Table 2. Each instrument is equipped with an independent, self-contained battery power supply system, enabling long time-series recordings. The field working picture is shown in Figure 2B.

3 Analysis procedure for the digital video images

In order to effectively extract the image signal of the SPM concentration, a fully-automated image processing program was developed to process the deep-sea SPM video images. The video images were processed with the following four steps: (1) converting color images to grayscale images, (2) removing background, (3) converting grayscale images to binary images, (4) defining the image signal of the SPM concentration based on the processed images. The digital video image processing process is shown in Figure 3, and the specific implementation of each step is described in the following subsections.

3.1 Grayscale processing

Each image after video framing was a RGB image which was stored in a 3D matrix with a dimension of "1080×1920×3" (Figure 3A). "1080×1920" denotes the total pixel number of the image and "3" denotes three channels of each pixel in red, green

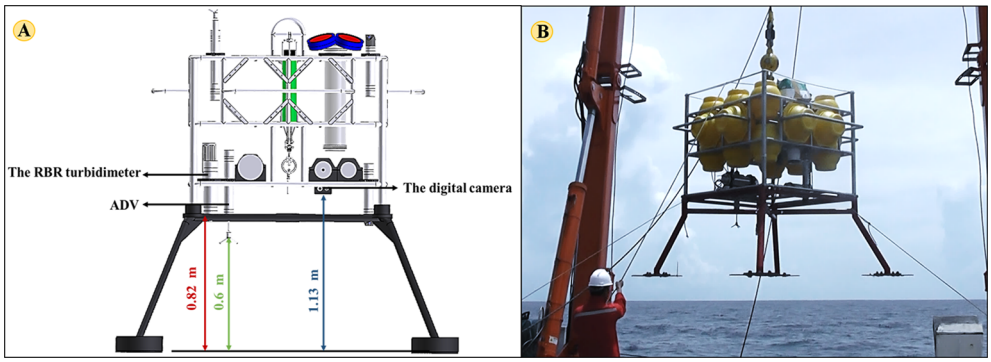

FIGURE 2
(A) Schematic illustration of the lander and instruments; **(B)** the field working picture.

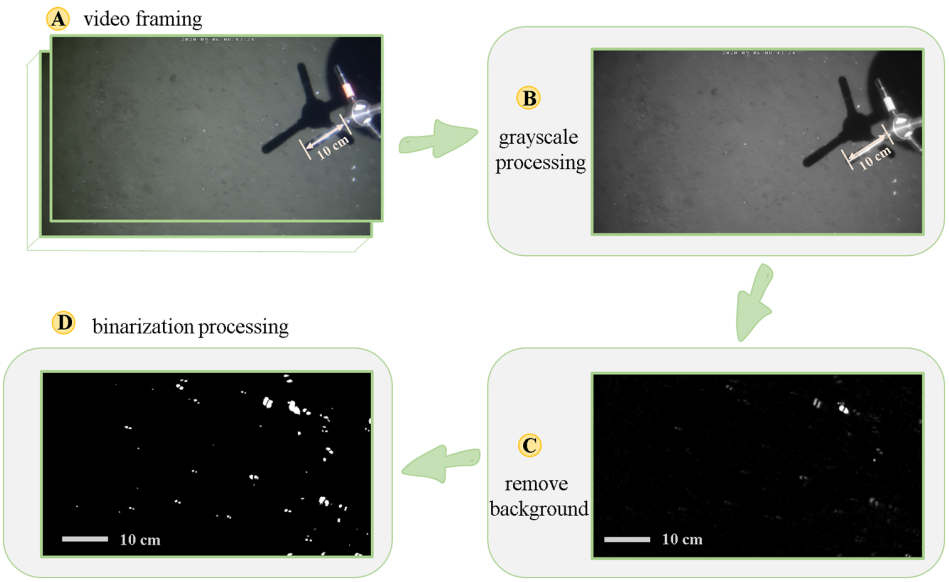

FIGURE 3
Digital video image processing process. **(A)** The original image (video framing); **(B)** grayscale image; **(C)** frame differential image, **(D)** binary image.

and blue. The first operation was to convert RGB images to grayscale images (Figure 3B). The grayscale image consists of a single channel that represents the intensity and brightness of the image (Saravanan, 2010). Converting RGB images to grayscale images will increase the data processing efficiency. Meanwhile, the precision of the results will not be affected. The function for converting RGB image to grayscale image is as follows (Bala and Braun, 2003),

$$Gray(i,j) = 0.2989 * R(i,j) + 0.5870 * G(i,j) + 0.1140 * B(i,j) \quad (1)$$

Where Gray(i,j) is the grayscale value at the point (i,j). R(i, j)、G(i,j)、B(i,j) are the values of R, G, B components at point (i,j) in an image, respectively.

3.2 Background removing

Background removing was to distinguish the SPM information more easily. However, we found that the SPM blended into the seabed background by analyzing Figure 3B. The color feature (brightness, chroma, saturation, etc.) and texture feature of SPM were not clear enough. Hence, it is difficult to remove the background from single frame image using common algorithms, such as the image enhancement algorithm and the top-hat transform (Bai et al., 2012). In this paper, based on the moving object detection algorithm of image sequence, we successfully applied the frame difference method to remove the background (Zhao and Wang, 2007) (Figure 3C). The principle of frame difference method is as follows:

$$D_k(i,j) = |I_k(i,j) - I_{k-1}(i,j)| \quad (2)$$

Where $I_{k-1}(i,j)$ and $I_k(i,j)$ is the k-1 and k-frame images respectively, $D_k(i,j)$ is the difference image.

3.3 Binary processing

The images after removing the background should be converted to binary (black and white) images to extract SPM information. The process needs to define a threshold value. If pixel intensity was higher than the threshold value, they will be converted to white pixel (symbol 1) and the remaining was set to black (symbol 0). As a consequence, a binary image was a logical array with zero (black) and one (white). Setting a suitable threshold value for a large set of images was crucial to the accuracy of the processing results. Numerous automatic methods were developed to find the optimal value of the threshold. For example, Pun (1981) derived the maximum entropy method, which extracted an anisotropy coefficient from the gray-level histogram of an image. This method was closely related to its geometrical shape. Otsu (1979) provided an optimal threshold which was selected by a discriminant criterion to maximize the separability of the resultant classes in gray levels. The comparison of several threshold algorithms for images at different times is shown in Figure 4. The trail results indicated that the SPM information in the binary images segmented by maximum entropy method is generally low, whereas Otsu method is unstable. None of the

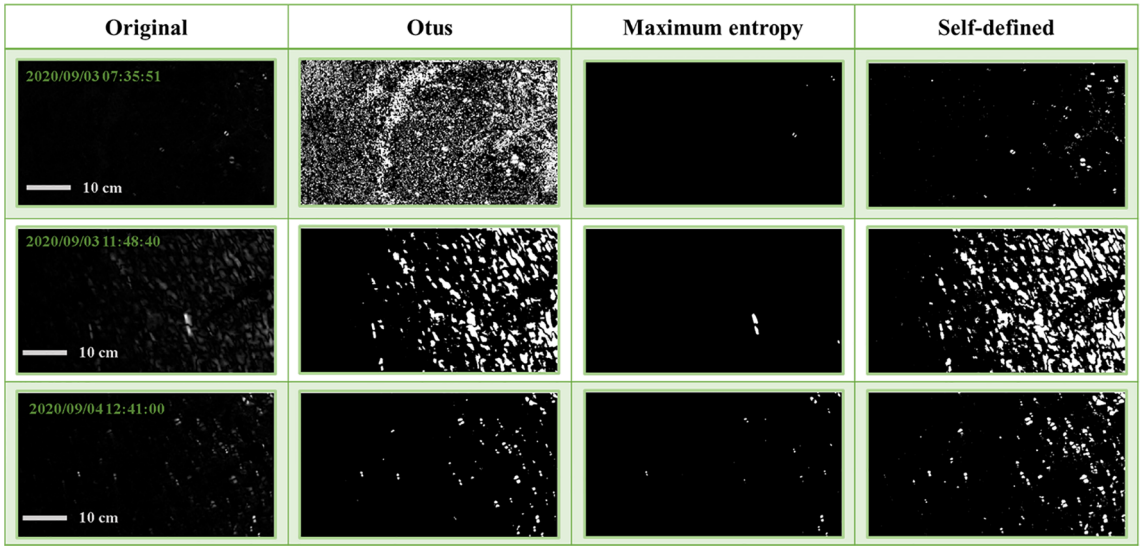

FIGURE 4
Comparison of threshold algorithms for images at different times.

automated thresholding methods were generally robust enough. In order to obtain comparable results, by trial and error, the images in this study were binarized using a constant threshold value (T=2.5), and the trail result was well.

3.4 Image signal definition

The imaging area of white spots are the main signals of the SPM concentration (e. g. the spots in Figure 3D). In this paper, the image signal of the SPM concentration is a ratio between the imaging area of white spots and the total area of each image, as shown in equation (3):

$$C_i = S_{SPM}/S_{all} \tag{3}$$

where C_i is the image signal. S_{SPM} is the imaging area of white spots, S_{all} is the total imaging area.

4 Results and discussion

4.1 Correlation between image and optical/acoustic backscatter signal

In the last decade much work has been done to measure SPM concentration by optical/acoustic backscatter (Fugate and Friedrichs, 2002; Downing, 2006; Sahin et al., 2019). Commonly, the relationship between optical backscatter signal and SPM concentration was almost linear (Haalboom et al., 2021), and the acoustic backscatter signal was logarithmically proportional to the SPM concentration (Rouhnia et al., 2014; Öztürk, 2017; Sahin et al., 2017). In this section, we compared the image signal with the optical/acoustic backscattering signal. The time-series of image signal, optical and acoustic backscatter is shown in Figures 5A–C, respectively. We normalized the time-series of the three signals in order to compare them more intuitively in Figure 5D. The results showed that they had a similar change trend. What's more, it's worth noting that the optical backscatter signal has obviously different change trend from acoustic backscatter and image signal on September 5th at16:26-September 6rd at 00:53, which is called mismatch period (the pale pink rectangle in Figure 5). In the mismatch period, the optical backscatter signal increased by about 15 times larger than the background value, while the acoustic backscatter and image signal didn't change significantly.

In order to quantitatively compare the image signal and optical/backscatter signal, we used normalized cross-correlation algorithm to evaluate the correlation of the three signals in the whole time-series (September 3rd at 00:00-September 6rd at 17:05) and the partial time-series except the mismatch period respectively. The normalized cross-correlation coefficients were calculated using the crosscorr function in Matlab using the equation 4 and equation 5,

$$c_{x,y}(k) = \begin{cases} \frac{1}{n}\sum_{t=1}^{n-k}(x_t - \bar{x})(y_{t+k} - \bar{y}) & where \;\; k = 0, 1, 2\ldots \\ \frac{1}{n}\sum_{t=1}^{n+k}(y_t - \bar{y})(x_{t+k} - \bar{x}) & where \;\; k = 0, -1, -2\ldots \end{cases} \tag{4}$$

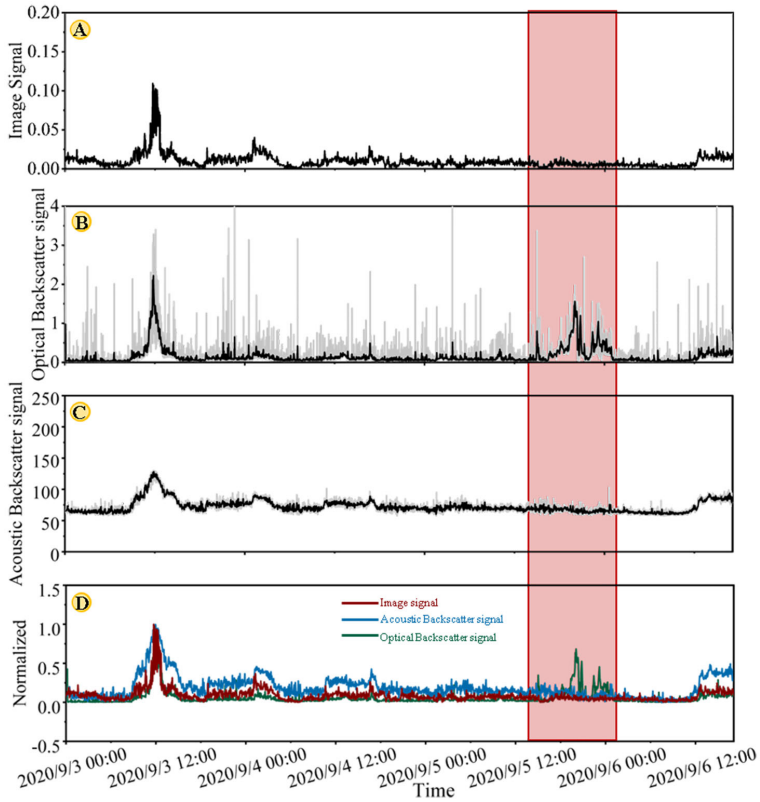

FIGURE 5
Near-bottom (about 1 m) time-series (September 3rd at 00:00-September 6rd at 17:05) at 1450 m water depth. **(A)** image signal recorded by digital video-camera, **(B)** acoustic backscatter signal recorded by ADV, **(C)** optical backscatter signal recorded by RBR turbidity, **(D)** normalized time-series. In panels **(B, C)**, the grey lines represent the actual data, whereas the black lines represent the 3 min averaged values.

$$r_{x,y}(k) = \frac{c_{x,y}(k)}{S_x S_y} \qquad \text{where k} = 0, \pm1, \pm2\ldots \tag{5}$$

where x and y are the variables of the time-series to be compared (i.e., pair-wise comparison of either image signal, optical backscatter signal, or acoustic backscatter signal), t is time, x-bar and y-bar are the means of the x and y series, respectively, Sx and Sy are the standard deviations of x and y, respectively, k is the time lag, n is the sample size, Cx,y is the cross-covariance coefficient, and rx,y is the cross-correlation coefficient. The results are shown in Figure 6, when offset equaled to 0, the normalized cross-correlation was maximum and closed to 1, which meant that the image signal, optical and acoustic backscatter signal were highly correlated.

However, as shown in Figures 6A, C, the correlation of the partial time-series (the green curve) was higher than the whole time-series (the blue curve). Comparing the video images during the mismatch period with the other period, we found that there was no large amount of SPM in the video images during the mismatch period. The sudden increase in optical backscatter during the mismatch period may be induced by the following three reasons: (1) in the mismatch period the majority of suspended particles were fine particles. The RBR turbidimeter was most sensitive to fine particles (Downing, 2006; Haalboom et al., 2021; Sabine et al., 2022). While these fine particles can't contribute significantly to SPM weight (D'sa et al., 2007; Sabine et al., 2022). (2) the RBR turbidimeter only measured the signal of a single point, which may not be a representative of SPM concentration in whole study volume (Rai and Kumar, 2015); (3) biofouling or other type of fouling resulted in a temporary increase of the optical backscatter signal (Delauney et al., 2009; Fettweis et al., 2019). The above analysis showed that the optical backscatter signal can't accurately reflect the SPM concentration during the mismatch period. Therefore, sometimes converting the optical backscatter into SPM concentration by an inversion formula will result in an overestimation of SPM concentration.

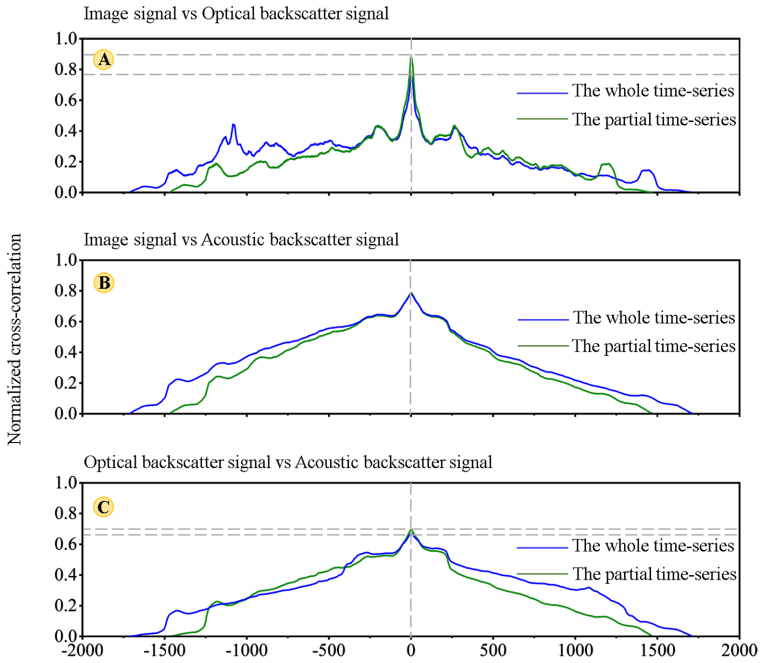

FIGURE 6
Normalized cross-correlation lag-time plots. **(A)** Image signal vs Optical backscatter signal **(B)** Image signal vs Acoustic backscatter signal **(C)** Optical backscatter signal vs Acoustic backscatter signal. On the vertical axis, values close to one indicate a higher correlation. The horizontal axis refers to the lag time between the two timeseries, negative denotes the delay between the first and second signals. The blue curve is cross-correlation analysis of the whole time-series (September 3rd at 00:00-September 6rd at 17:05), while the green curve is cross-correlation analysis of the partial time-series (except September 5rd at 16:26-September 6rd at 00:53).

4.2 Relationship between image signal and SPM concentration

It is difficult to obtain discrete water samples at 1 m above the seabed. Thus, before recovering the lander, we collected seawater at different water depths (50, 100, 150, 200, 300, 400, 500, 600, 800, 1000, 1282, 1332 and 1372 m) by a deploying a SeaBird 911 CTD-Rosette system, and obtained the corresponding optical backscatter signal recorded by the RBR turbidimeter mounted on the CTD at the same time. We calculated the SPM concentration through gravimetric measurements of filtered and dried water samples, and then established the relationship between the optical backscatter signal and the SPM concentration (mg/L). The result is shown in equation (6),

$$Y = 4.03X + 0.71 \tag{6}$$

Where Y is the SPM concentration, X is the optical backscatter signal.

The equation was used in this study to calculate the SPM concentration during September 3rd at 00:00-September 6rd at 17:05. Based on the discussion in Section 4.1, the SPM concentration quantified by optical backscatter signal was overestimated during the mismatch period. Hence, we use the partial time-series to establish the relationship between image signal and the SPM concentration. We conducted linear regression analysis on these time-series. The image signal and the SPM concentration were taken as the independent and dependent variable respectively (Figure 7). The results showed that they had a strong linear relationship. The correlation coefficient R^2 was equal to 0.72. And a linear regression model was obtained: y=55.49 x +0.68.

K-fold cross-validation algorithm was used to evaluate the performance of the linear regression model (Le et al., 2022). Two evaluation indexes, including root-mean-square error (RMSE) and relative error (RE), were used to measure the deviations of the results (Wang et al., 2012; Ciancia et al., 2020; Kwong et al., 2022), which are described by equation (7) and (8).

$$RMSE = \sqrt{\frac{\sum_{i=1}^{n}\left(x_{i,r} - x_{m,r}\right)^2}{n}} \tag{7}$$

$$RE = \frac{\sum_{i=1}^{n}\left|\frac{x_{i,r} - x_{m,r}}{x_{m,r}}\right|}{n} \tag{8}$$

where $x_{i,r}$ is the modeled value of the ith element, $x_{m,r}$ is the SPM concentration of the ith element, and n is the number of test data set.

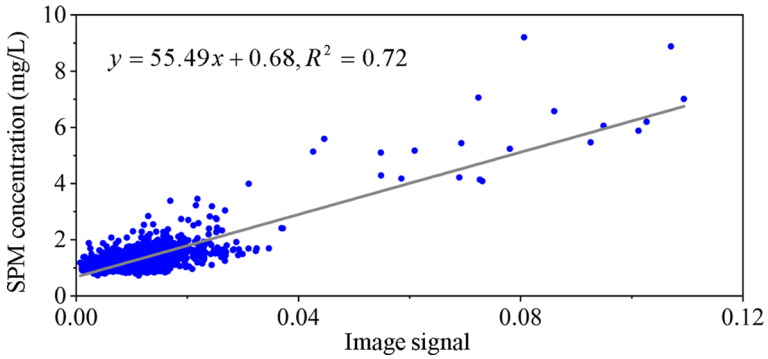

FIGURE 7
The relationship of image signal versus the SPM concentration.

In order to realize the k-fold cross-validation algorithm, we shuffled the sets of "image signal-SPM concentration" data randomly and divided the dataset into 5 groups. For each group, we took this group as a test data set and the remaining groups as a training data set. We fitted the model on the training set and evaluated it on the test set. The performance of the linear regression model was evaluated with the index RESE and RE and the results were summarized in Table 3. The results showed that the RMSE was small and the RE was within ±25%, which indicated high confidence in the model-predicted values. That is to say, the performance of the model was well.

4.3 The dynamics of SPM concentration based on image signal in deep sea

We applied the established linear regression model to whole time-series of image signal to calculate the SPM concentration. The current regime presented in Figures 8A, B showed diurnal and semidiurnal variation in current speed and direction. The current velocity ranged from 0.015 to 0.27 m/s. Figure 8C showed that the background concentration of SPM at the observation station was 1 mg/L. The SPM concentration reached the peak value when current velocity equaled to or exceeded 0.15 m/s. Significant increase in SPM concentration, occurred on September 3rd at 07:26-15:02, September 3rd at 18:01-September 4rd at 05:07, and September 6rd at 11:48-17:05, which were labelled by buff rectangle I, II, III respectively in Figure 8. Particularly, for the period I, the SPM concentration was 1.08 mg/L on September 3rd at 8:00. Then it gradually increased to the maximum (6.62 mg/L) on September 3rd at 11:48. At this time, the current velocity reached to the maximum (0.27 m/s). Subsequently, the SPM concentration gradually decreased to the minimum (0.98 mg/L) on September 3rd at 16:13. Within this more than 8 h interval the SPM concentration increased by 6-7 times larger than the background value (the SPM concentration is 1 mg/L). The SPM concentration variation was coincided with current velocity variation. For the period II, III, the SPM concentration increased by 2 times larger than the background value. The SPM concentration reached to the maximum when the current exceeded 0.15 m/s.

TABLE 2 Details of instrument deployments at the study area.

Instruments	Depth (mab)	Frequency (Hz)	Monitoring time (day)	Monitoring contents
Digital video-camera	1.13 (about 0.6 m^3)		20	Video images
ADV	0.74	16	3.7	Current velocity Acoustic backscatter signal
RBR Turbidimeter	0.62	1/20	20	Optical backscatter signal

TABLE 3 Values of RMSE and RE.

Evaluation indexes	1	2	3	4	5	mean
RMSE	0.13	0.11	0.09	0.13	0.16	0.12
RE	0.21	0.24	0.22	0.25	0.24	0.23

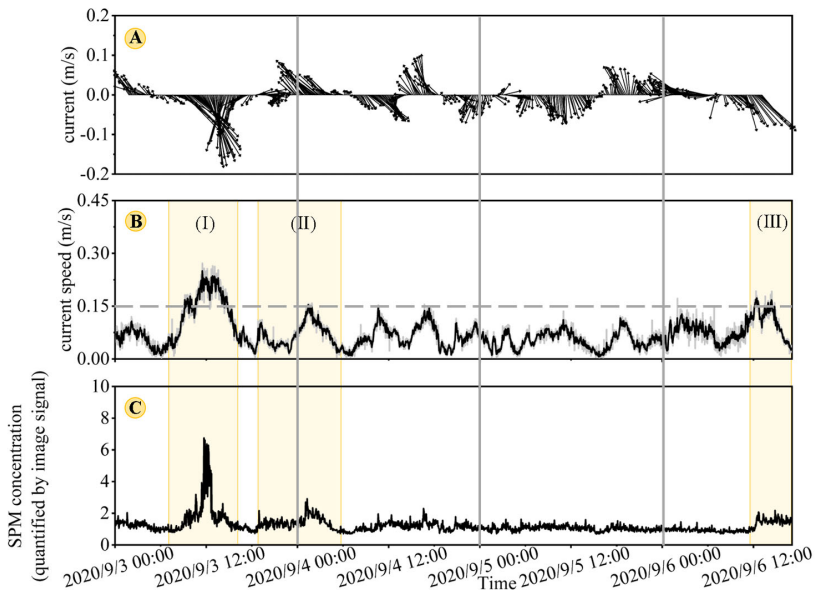

FIGURE 8
Near-bottom (about 1 m) time series on September 3rd at 00:00- September 6rd at 17:05 **(A)** current vector; **(B)** current speed (the gray dashed line indicates the threshold current when sediments resuspension occurred) (Thomsen and Gust, 2000; Xie et al., 2018) **(C)** SPM concentration quantified by image signal.

Combined with the physical properties and composition of the surficial sediment in the study area (described in Section 2.1), we inferred that the current speed is not strong enough to resuspend fine and cohesive sediments during the period of observation, but resuspend the fluffy organic-mineral aggregates which were on top of these more cohesive sediments. This conclusion is consistent with the results that Thomsen and Gust (2000) and Thomsen et al. (2002) developed by doing resuspension experiments with natural deep-sea sediments.

4.4 The dynamics of SPM morphology based on images in deep sea

We can directly observe the morphology of the SPM with digital video images. The observation results indicated that the SPM was mainly large aggregates in images. We manually classified them into three distinct morphological groups according the shape and size of SPM (Figure 9). In the first group, the shape of SPM was ellipse and the size was large (Figure 9A), such SPM mainly existed during September 3rd at 07:26-15:02 (labelled by buff rectangle I in Figure 8). In the second group, the shape of SPM was circular and the size was moderate (Figure 9B), such SPM existed during September 3rd at 18:01-September 4rd at 05:07 (labelled by buff rectangle II in Figure 8), and September 6rd at 11:48-17:05 (labelled by buff rectangle III in Figure 8). At other time, the SPM was dot-shaped and the size was small (Figure 9C), we named them the third group. Trudnowska et al. (2021) classified marine particles into five morphotypes by analyzing the properties of individual particles based on images taken by Underwater Vision Profiler, including circular, elongated, flake-type, fluffy, agglomerated forms of multielement structure. However, in this study, because our imaging system provided a relatively large field of view measuring and can't supply the depth information of each particle, we can't make precise classification based on individual particles. Hence, the way we analyze the SPM morphology is based on SPM relative changes in 2D images with time. Such discussion may be inaccurate, whereas the aim of this study is not to classify the morphology of particle perfectly but to better understand the dynamics of SPM combined with hydrodynamic information.

Haalboom et al. (2021) speculated the type of SPM under different hydrodynamic conditions according to comparing the time-series of optical backscatter signal (recorded by turbidimeter) and acoustic backscatter signal (recorded by 75 k ADCP) in Whittard Canyon at a water depth of 1400 m. They found that when the current speed increased (especially when the current speed increased to 0.4 m/s), the optical backscatter signal increased, whereas the acoustic backscatter decreased. Based on this finding, they inferred that high current velocity would cause larger aggregates break into dispersed smaller particles, whereas moderate current velocity made fine particles aggregate into larger aggregates. However, in their study, the optical and acoustic backscatter signals were recorded at different heights of, 5 and 45 m above the seabed, respectively. And they have no direct observational evidence (like

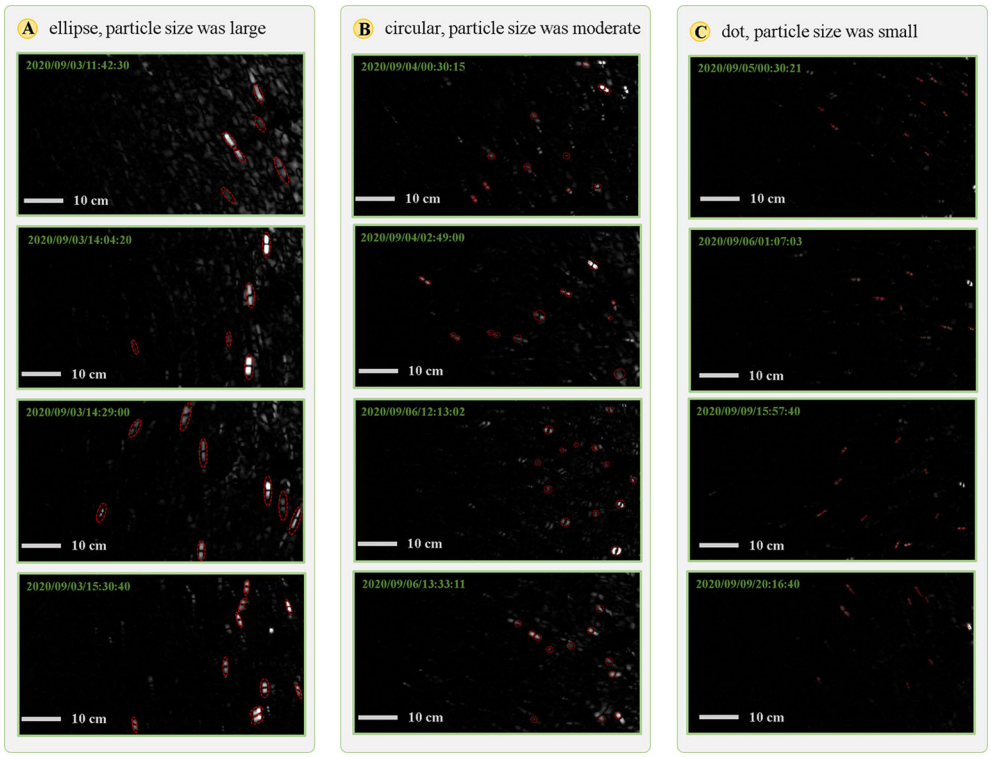

FIGURE 9
The typical images about three morphological groups of the SPM. **(A)** the first group, the shape of SPM was ellipse and the size was large, **(B)** the second group, the shape of SPM was circular and the size was moderate, **(C)** the third group, the SPM was dot-shaped and the size was small.

underwater video images) to verify the conclusion. Different from their study, our digital video images gave us more direct and intuitive evidence to analyze the dynamics of SPM morphology. Our finding was different from theirs. Combined with the hydrodynamic conditions (Figure 8B), we found that high current velocity always correspond to large size of SPM. Particularly, when the current velocity equaled to or exceeded 0.15 m/s, the SPM had the largest size (Figure 9A). Whereas with the decrease of current velocity, the size of SPM was also gradually decreased. Hence, we thought the current speed in our monitoring point was not strong enough to break the large size SPM, and the low current speed made the large size SPM settle down.

5 Future outlook

The digital video camera captures a relatively large field of view, and provides a measuring volume of 0.6 m^3. In such configuration, it is meaningless to define a lower limit of particle size the camera can detect. Despite this, we can roughly estimate the pixel size was 0.35 mm according to the marker of known actual size in the image, and the camera was expected to quantitatively capture particles with ESD (Equivalent Sphere Diameter) >0.7 mm. As a matter of fact, for these particles the camera can't captured, the images as a whole still contain their information in a way of color, texture and so on. Therefore, for the measurement of SPM concentration, the method of this study is to excavate an image signal of SPM concentration by artificially designed image processing algorithms. And the results (discussed in Section 4.1) indicated that the method can effectively work in low SPM concentration in deep-sea environment. The RBR turbidimeter measures optical backscatter signal of particles suspended with particle size >0.88 μm in the water column (Mao et al., 2012). The output voltage is calibrated to turbidity in FTU. The relationship of turbidity and SPM concentration is linear in the range of 0-750 FTU, but it becomes nonlinear for turbidity higher than 750 FTU due to grain shielding effect (Downing, 2006; Mao et al., 2012). In our study, the turbidity values lower than 4 FTU, that is to say, the RBR turbidimeter can work effectively in low SPM concentration deep-sea environment. The acoustic backscatter response of ADV to different particle size is dependent on the operating frequency of the ADV (Ha et al., 2009). The most sensitive diameter of the 6 MHz ADV in this study we used is 80 μm according to scattering theory (Thorne and Hanes, 2002). From laboratory experiments, Li et al. (2019) has shown that 6 MHz ADV works in the range of 0-1000 mg/L.

In general, in the last decades, the optical and acoustic instruments have been widely applied and in deep-sea

environment, and this is the reason why we compare the image signal with optical/acoustic backscatter signal. Yet optical and acoustic approach all have their own drawbacks like the analysis and discussion in Section 4.2. And in this study, the image analysis method has obvious advantages, such as it is more intuitive and contains more information which enables a more multidimensional interpretation of the dynamic changes in SPM. Whether the method can work effectively in higher SPM concentration environments remains to be further explored in the future work. In addition, in other scenes such single signal may cannot reflect all the information in the image, whereas the missing information is likely to be related to the SPM concentration. In the future, the use of convolutional neural networks, data-driven learning, and automatic computer extraction of multidimensional image information may further extend the range of work on image-based measurement of SPM concentration.

6 Conclusion

In this study, we conducted an *in-situ* long-period monitoring of SPM concentration and morphology at a water depth of 1450 m on the northern slope of the South China Sea with digital video images. The results are summarized as follows:

(1) We developed a novel method to process the deep-sea digital video images. In this method, we defined an image signal of SPM concentration. By doing cross-correlation analysis among image, optical and acoustic signals, we made a conclusion that in some period the optical backscatter signal can't accurately reflect the SPM concentration, whereas image signal can overcome this shortcoming.

(2) We calculated the SPM concentration derived from image signal, and manually classified SPM into three distinct morphological groups. Combined with the hydrodynamics, long-period monitoring results revealed that the increase in SPM concentration and size coincided with distinct peak in current velocity, and the decrease in SPM concentration and size corresponded to the decrease in current velocity. Our direct observational evidence helps to make a conclusion that enhanced hydrodynamics resuspend the organic/inorganic matter on the deep-sea seabed, or transport the material from the continental slope to deep sea. Whereas, reduced hydrodynamics make the material settle down.

Data availability statement

The raw data supporting the conclusions of this article will be made available by the authors, without undue reservation.

Author contributions

HW took part in field sampling, developed the digital image processing method, analysed and interpreted the data, wrote the manuscript. CH initiated the central idea, revised the manuscript, discussed the results, contributed to the writing of part of manuscript and approved the submitted version. YJ initiated the central idea, discussed the results, provided advices for the manuscript and approved the submitted version. XF revised the manuscript, took part in field sampling, and provided advices for the manuscript. CJ took part in field sampling, contributed to the analysis of part of data. All authors contributed to the article and approved the submitted version.

Funding

This research was funded by the National Natural Science Foundation of China (No. 41831280), the Marine S&T Fund of Shandong Province for Pilot National Laboratory for Marine Science and Technology (Qingdao) (No. 2021QNLM020003-1) and the National Natural Science Foundation of China (No. 41907227).

Acknowledgments

We thank the Natural Science Foundation of China for the Open Research Cruise of the northern South China Sea (NORC2019-05, NORC2022-05). We appreciate all members for their efforts in the collection of the data in this study.

Conflict of interest

The authors declare that the research was conducted in the absence of any commercial or financial relationships that could be construed as a potential conflict of interest.

Publisher's note

References

Amaro, T., De Stigter, H., Lavaleye, M., and Duineveld, G. (2015). Organic matter enrichment in the whittard channel; its origin and possible effects on benthic megafauna. *Deep Sea Res. Part I: Oceanographic Res. Papers.* 102, 90–100. doi: 10.1016/j.dsr.2015.04.014

Arı´Stegui, J., Gasol, J. M., Duarte, C. M., and Herndld, G. J. (2009). Microbial oceanography of the dark ocean's pelagic realm. *Limnology Oceanography.* 54 (5), 1501–1529. doi: 10.4319/lo.2009.54.5.1501

Bai, X., Zhou, F., and Xue, B. (2012). Image enhancement using multi scale image features extracted by top-hat transform. *Optics Laser Technology.* 44 (2), 328–336. doi: 10.1016/j.optlastec.2011.07.009

Bala, R., and Braun, K. M. (2003). Color-to-grayscale conversion to maintain discriminability. *Color Imaging IX: Processing Hardcopy Applications.* 5293, 196–202. doi: 10.1117/12.532192

Bochdansky, A. B., Van Aken, H. M., and Herndl, G. J. (2010). Role of macroscopic particles in deep-sea oxygen consumption. *Proc. Natl. Acad. Sci. United States America.* 107 (18), 8287–8291. doi: 10.1073/pnas.0913744107

Ciancia, E., Pascucci, S., Tramutoli, V., Campanelli, A., Pergola, N., Lacava, T., et al. (2020). Modeling and multi-temporal characterization of total suspended matter by the combined use of sentinel 2-MSI and landsat 8-OLI data: The pertusillo lake case study (Italy). *Remote Sensing.* 12 (13), 2147. doi: 10.3390/rs12132147

D'sa, E. J., Miller, R. L., and Mckee, B. A. (2007). Suspended particulate matter dynamics in coastal waters from ocean color: Application to the northern gulf of Mexico. *Geophysical Res. Letters.* 34 (23), L23611. doi: 10.1029/2007GL031192

Davis, C. S., Thwaites, F. T., Gallager, S. M., and Hu, Q. (2005). A three-axis fast-tow digital video plankton recorder for rapid surveys of plankton taxa and hydrography. *Limnology Oceanography: Methods* 3 (2), 59–74. doi: 10.4319/lom.2005.3.59

Delauney, L., Compère, C., and Lehaitre, M. (2009). Biofouling protection for marine environmental sensors. *Ocean Science.* 6 (2), 503–511. doi: 10.5194/os-6-503-2010

Diercks, A. R., Dike, C., Asper, V. L., Dimarco, S. F., and Passow, U. (2018). Scales of seafloor sediment resuspension in the northern gulf of Mexico. *Elementa: Sci. Anthropocene.* 6 (1). doi: 10.1525/elementa.285

Ding, W., Li, J., Li, J., Fang, Y., and Yong, T. (2013). Morphotectonics and evolutionary controls on the pearl river canyon system, south China Sea. *Acta Geologica Sinica(English edition).* 34 (3-4), 221–238. doi: 10.1007/s11001-013-9173-9

Downing, J. (2006). Twenty-five years with OBS sensors: the good, the bad, and the ugly. *Continental Shelf Res.* 26 (17–18), 2299–2318. doi: 10.1016/j.csr.2006.07.018

Duineveld, G., Lavaleye, M., Berghuis, E., and De Wilde, P. (2001). Activity and composition of the benthic fauna in the whittard canyon and the adjacent slope. *Oceanologica Acta* 24 (1), 69–83. doi: 10.1016/S0399-1784(00)01129-4

Durrieu De Madron, X., Ramondenc, S., Berline, L., Houpert, L., Bosse, A., Martini, S., et al. (2017). Deep sediment resuspension and thick nepheloid layer generation by open-ocean convection. *J. Geophysical Research: Oceans.* 122 (3), 2291–2318. doi: 10.1002/2016JC012062

Eisma, D., Schuhmacher, T., Boekel, H., Eisma, D., Schuhmacher, T., and Boekel, H. (2001). A camera and image-analysis system for *in situ* observation of flocs in natural waters. *Netherlands J. Sea Res.* 27 (1), 43–56. doi: 10.1016/0077-7579(90)90033-D

Eittreim, S. L. (1984). Methods and observations in the study of deep-sea suspended particulate matter. *Geological Society.* 15 (1), 71–82. doi: 10.1144/gsl.sp.1984.015.01.04

Feng, Y., Tang, Q., Li, J., Sun, J., and Zhan, W. (2021). Internal solitary waves observed on the continental shelf in the northern south China Sea from acoustic backscatter data. *Fronteirs Mar. Science.* 8. doi: 10.3389/fmars.2021.734075

Fettweis, M., Riethmüller, R., Verney, R., Becker, M., Backers, J., Baeye, M., et al. (2019). Uncertainties associated with *in situ* high-frequency long-term observations of suspended particulate matter concentration using optical and acoustic sensors. *Prog. Oceanography.* 178, 102162. doi: 10.1016/j.pocean.2019.102162

Fugate, D. C., and Friedrichs, C. T. (2002). Determining concentration and fall velocity of estuarine particle populations using ADV, OBS and LISST. *Continental Shelf Res.* 22 (11-13), 1867–1886. doi: 10.1016/S0278-4343(02)00043-2

García, R., and Thomsen, L. (2008). Bioavailable organic matter in surface sediments of the nazar´e canyon and adjacent slope (Western Iberian margin). *J. Mar. Systems.* 74 (1–2), 44–59. doi: 10.1016/j.jmarsys.2007.11.004

Gardner, W. D., and Walsh, I. D. (1990). Distribution of macroaggregates and fine-grained particles across a continental-margin and their potential role in fluxes. *Deep Sea Res. Part A. Oceanographic Res. Papers.* 37 (3), 401–411. doi: 10.1016/0198-0149(90)90016-O

Gorsky, G., Picheral, M., and Stemmann, L. (2000). Use of the underwater video profiler for the study of aggregate dynamics in the north Mediterranean. *Estuarine Coast. Shelf Science.* 50 (1), 121–128. doi: 10.1006/ecss.1999.0539

Graham, G. W., and Nimmo Smith, W. (2010). The application of holography to the analysis of size and settling velocity of suspended cohesive sediments. *Limnology Oceanography: Methods* 8 (1), 1–15. doi: 10.4319/lom.2010.8.1

Gray, J. R., Gartner, J. W., Anderson, C. W., Barton, J. S., Gaskin, J., and Pittman, S. A. (2010). Surrogate technologies for monitoring suspended-sediment transport in rivers. *Sedimentology aqueous systems.* 2010, 3–45. doi: 10.1002/9781444317114.ch1

Haalboom, S., Stigter, H. D., Duineveld, G., Haren, H. V., and Mienis, F. (2021). Suspended particulate matter in a submarine canyon (Whittard canyon, bay of Biscay, NE Atlantic ocean): Assessment of commonly used instruments to record turbidity. *Mar. Geology.* 434, 106439. doi: 10.1016/j.margeo.2021.106439

Ha, H. K., Hsu, W. Y., Maa, P. Y., Shao, Y. Y., and Holland, C. W. (2009). Using ADV backscatter strength for measuring suspended cohesive sediment concentration. *Continental Shelf Res.* 10, 1310–1316. doi: 10.1016/j.csr.2009.03.001

Hatcher,A., Hill, P., and Grant, J (2001). Optical backscatter of marine flocs. *J. Sea Res.* 46 (1), 1–12. doi: 10.1016/S1385-1101(01)00066-1

Hoguane, A. M., Green, C. L., and Georgebowers, D. (2012). A note on using a digital camera to measure suspended sediment load in Maputo bay, Mozambique. *Remote Sens. Letters.* 3 (3), 259–266. doi: 10.1080/01431161.2011.566287

Holdaway, G. P., Thorne, P. D., Flatt, D., Jones, S. E., and Prandle, D. (1999). Comparison between ADCP and transmissometer measurements of suspended sediment concentration. *Continental Shelf Res.* 19 (3), 421—441. doi: 10.1016/s0278-4343(98)00097-1

Jia, Y., Tian, Z., Shi, X., Liu, J. P., Chen, J., Liu, X., et al. (2019). Deep-sea sediment resuspension by internal solitary waves in the northern south china Sea. *Sci. Rep.* 9 (1), 1–8. doi: 10.1038/s41598-019-47886-y

Kwong, I. H. Y., Wong, F. K. K., and Fung, T. (2022). Automatic mapping and monitoring of marine water quality parameters in Hong Kong using sentinel-2 image time-series and Google earth engine cloud computing. *Fronteirs Mar. Science.* 9. doi: 10.3389/fmars.2022.871470

Le, K. T., Yuan, Z., Syed, A., Ratelle, D., Orenstein, E. C., Carter, M. L., et al. (2022). Benchmarking and automating the image recognition capability of an *In situ* plankton imaging system. *Fronteirs Mar. Science.* 9. doi: 10.3389/fmars.2022.869088

Li, S., Alves, T. M., Li, W., Wang, X., Rebesco, M., Li, J., et al. (2022). Morphology and evolution of submarine canyons on the northwest south China Sea margin. *Mar. Geology.* 443, 106695. doi: 10.1016/j.margeo.2021.106695

Liu, Q., Xie, X., Shang, X., Chen, G., and Wang, H. (2019). Modal structure and propagation of internal tides in the northeastern south China Sea. *Acta Oceanologica Sinica.* 38, 12–23. doi: 10.1007/s13131-019-1473-1

Li, W., Yang, S., Yang, W., Xiao, Y., Fu, X., and Zhang, S. (2019). Estimating instantaneous concentration of suspended sediment using acoustic backscatter from an ADV. *Int. J. Sediment Res.* 34 (5), 422–431. doi: 10.1016/j.ijsrc.2018.10.012

Luan, X., Ran, W., Wang, K., Shi, Y., and Zhang, H. (2019). New interpretation for the main sediment source of the rapidly deposited sediment drifts on the northern slope of the south China Sea. *J. Asian Earth Sci.* 171, 118–133. doi: 10.1016/j.jseaes.2018.11.004

Lunven, M., Gentien, P., Kononen, K., Le Galla, E., and Danie´Lou, M. M. (2003). In situ video and diffraction analysis of marine particles. *Estuarine Coast. Shelf Science.* 57 (5-6), 1127–1137. doi: 10.1016/S0272-7714(03)00053-2

Mao, Z., Chen, J., Pan, D., Tao, B., and Zhu, Q. (2012). A regional remote sensing algorithm for total suspended matter in the East China Sea. *Remote Sens. Environment.* 124 (124), 819–831. doi: 10.1016/j.rse.2012.06.014

Moirogiorgou, K., Nerantzaki, S., Livanos, G., Antonakakis, M., Nikolaidis, N. P., Petrakis, E. G. M., et al. (2015). "Color characteristics for the evaluation of suspended sediments," in *2015 IEEE International Conference on Imaging Systems and Techniques (IST).* 1–5. doi: 10.1109/IST.2015.7294574

Neukermans, G., Loisel, H., Mériaux, X., Astoreca, R., and Mckee, D. (2012). *In situ* variability of mass-specific beam attenuation and backscattering of marine particles with respect to particle size, density, and composition. *Limnology Oceanography.* 57 (1), 124–144. doi: 10.4319/lo.2011.57.1.014

Ohnemus, D.C., Lam, P.J., and Twining, B.S. (2018). Optical observation of particles and responses to particle composition in the GEOTRACES GP16 section. *Mar. Chem.* 201, 124–136. doi: 10.1016/j.marchem.2017.09.004

Otsu, N. (1979). A threshold selection method from gray-level histograms. *IEEE Trans. systems man cybernetics.* 9 (1), 62–66. doi: 10.1109/TSMC.1979.4310076

Öztürk, M. (2017). Sediment size effects in acoustic doppler velocimeter-derived estimates of suspended sediment concentration. *Water.* 9 (7), 529. doi: 10.3390/w9070529

Picheral, M., Guidi, L., Stemmann, L., Karl, D. M., Iddaoud, G., and Gorsky, G. (2010). The underwater vision profiler 5: an advanced instrument for high spatial resolution studies of particle size spectra and zooplankton. *Limnology Oceanography: Methods* 8 (9), 462–473. doi: 10.4319/lom.2010.8.462

Pun, T. (1981). Entropic thresholding, a new approach. *Comput. Graphics Image Processing.* 16 (3), 210–239. doi: 10.1016/0146-664X(81)90038-1

Rai, A. K., and Kumar, A. (2015). Continuous measurement of suspended sediment concentration: Technological advancement and future outlook. *Measurement.* 76 (2015), 209–227. doi: 10.1016/j.measurement.2015.08.013

Ramalingam, S., and Chandra, V. (2018). Determination of suspended sediments particle size distribution using image capturing method. *Mar. Georesources Geotechnology.* 36 (8), 867–874. doi: 10.1080/1064119X.2017.1392660

Rouhnia, M., Keyvani, A., and Strom, K. (2014). Do changes in the size of mud flocs affect the acoustic backscatter values recorded by a vector ADV? *Continental Shelf Res.* 84, 84–92. doi: 10.1016/j.csr.2014.05.015i

Sabine, H., Timm, S., Peter, U., Iason-Zois, G., Henko, D. S., Benjamin, G., et al. (2022). Monitoring of anthropogenic sediment plumes in the clarion-clipperton zone, NE equatorial pacific ocean. *Front. Mar. Science.* 9. doi: 10.3389/fmars.2022.882155

Sahin, C., Ozturk, M., and Aydogan, B. (2019). Acoustic doppler velocimeter backscatter for suspended sediment measurements: Effects of sediment size and attenuation. *Appl. Ocean Res.* 94, 101975. doi: 10.1016/j.apor.2019.101975

Sahin, C., Verney, R., Sheremet, A., and Voulgaris, G. (2017). Acoustic backscatter by suspended cohesive sediments: field observations, seine estuary, France. *Continental Shelf Res.* 134, 39–51. doi: 10.1016/j.csr.2017.01.003

Saravanan, C. (2010). "Color image to grayscale image conversion," *2010 Second International Conference on Computer Engineering and Applications*. 196–199. doi: 10.1109/ICCEA.2010.192

Su, M., Lin, Z., Wang, C., Kuang, Z., Liang, J., Chen, H., et al. (2020). Geomorphologic and infilling characteristics of the slopeconfined submarine canyons in the pearl river mouth basin, northern south China Sea. *Mar. Geology.* 424, 106166. doi: 10.1016/j.margeo.2020.106166

Syvitski, J. P. M., and Hutton, E. W. H. (1997). FLOC: image analysis of marine suspended particles. *Comput. Geosciences.* 23 (9), 967–974. doi: 10.1016/S0098-3004(97)00060-5

Thomsen, L., and Gust, G. (2000). Sediment erosion thresholds and characteristics of resuspended aggregates on the western European continental margin. *Deep Sea Res. Part I: Oceanographic Res. Papers.* 47 (10), 1881–1897. doi: 10.1016/S0967-0637(00)00003-0

Thomsen, L., Van Weering, T., and Gust, G. (2002). Processes in the benthic boundary layer at the Iberian continental margin and their implication for carbon mineralization. *Prog. Oceanography.* 52 (2–4), 315–329. doi: 10.1016/s0079-6611(02)00013-7

Thorne, P D, and Hanes, D M (2002). A review of acoustic measurement of small-scale sediment processes[J]. *Continental Shelf Res*, 22(4): 603–632. doi: 10.1016/S0278-4343(01)00101-7

Trudnowska,E., Lacour, L., Ardyna, M., Rogge, A., Irisson, J.O., Waite, A.M., et al (2021). Marine snow morphology illuminates the evolution of phytoplankton blooms and determines their subsequent vertical export. *Nature communications*. 12(1), 1–13. doi: 10.1038/s41467-021-22994-4

Verdugo, P., and Santschi, P. H. (2010). Polymer dynamics of DOC networks and gel formation in seawater. *Deep Sea Res. Part II: Topical Stud. Oceanography.* 57 (16), 1486–1493. doi: 10.1016/j.dsr2.2010.03.002

Wang, H., Jia, Y., Ji, C., Jiang, W., and Bian, C. (2022). Internal tide-induced turbulent mixing and suspended sediment transport at the bottom boundary layer of the south China Sea slope. *J. Mar. Systems.* 230, 103723. doi: 10.1016/j.jmarsys.2022.103723

Wang, J., Wu, S., Sun, J., Feng, W., and Li, Q. (2021). Influence of seafloor topography on gas hydrate occurrence across a submarine canyon-incised continental slope in the northern margin of the south china sea. *Mar. Petroleum Geology.* 133, 105279. doi: 10.1016/j.marpetgeo.2021.105279

Wang, L., Zhao, D., Yang, J., and Chen, Y. (2012). Retrieval of total suspended matter from MODIS 250 m imagery in the bohai Sea of China. *J. oceanography.* 68 (5), 719–725. doi: 10.1007/s10872-012-0129-5

Wren, D. G., Barkdoll, B. D., Kuhnle, R. A., Asce, M., and Derrow, R. W. (2000). Field techniques for suspended-sediment measurement. *J. Hydraulic Engineering.* 126 (2), 97–104. doi: 10.1061/(ASCE)0733-9429(2000)126:2(97

Xie, X., Liu, Q., Zhao, Z., Shang, X., Cai, S., Wang, D., et al. (2018). Deep sea currents driven by breaking internal tides on the continental slope. *Geophysical Res. Letters.* 45 (12), 6160–6166. doi: 10.1029/2018GL078372

Zhao, Z. (2014). Internal tide radiation from the Luzon strait. *J. Geophysical Research: Oceans.* 119 (8), 5434–5448. doi: 10.1002/2014JC010014

Zhao, Y., and Wang, Z. (2007). Detecting moving objects by background difference and frame-difference. international symposium on multispectral image processing & pattern recognition. *Int. Soc. Optics Photonics.* 6786, 203–208. doi: doi: 10.1117/12.746469

frontiers | Frontiers in Marine Science

TYPE Original Research
PUBLISHED 14 October 2022
DOI 10.3389/fmars.2022.1018042

OPEN ACCESS

EDITED BY
Zhilei Sun,
Qingdao Institute of Marine Geology (QIMG), China

REVIEWED BY
Yoshihiro Deguchi,
Tokushima University, Japan
Ran Liao,
Tsinghua University, China

*CORRESPONDENCE
Jinjia Guo
opticsc@ouc.edu.cn
Xilin Zhang
ouczhxl@163.com

SPECIALTY SECTION
This article was submitted to Ocean Observation, a section of the journal Frontiers in Marine Science

RECEIVED 12 August 2022
ACCEPTED 22 September 2022
PUBLISHED 14 October 2022

CITATION
Liu Q, Guo J, Lu Y, Wei Z, Liu S, Wu L, Ye W, Zheng R and Zhang X (2022) Underwater Raman microscopy—a novel *in situ* tool for deep-sea microscale target studies. *Front. Mar. Sci.* 9:1018042. doi: 10.3389/fmars.2022.1018042

Underwater Raman microscopy—a novel *in situ* tool for deep-sea microscale target studies

Qingsheng Liu[1], Jinjia Guo[1*], Yuan Lu[1], Zihao Wei[1], Shuang Liu[1], Lulu Wu[1], Wangquan Ye[1], Ronger Zheng[1] and Xilin Zhang[2*]

[1]College of Physics and Optoelectronic Engineering, Ocean University of China, Qingdao, China, [2]Key Laboratory of Gas Hydrate, Ministry of Natural Resources, Qingdao, China

Microscale processes and interactions in the ocean are pervasive. They play a fundamental role in global biogeochemical cycles and have a significant impact on benthic marine ecosystems. However, our understanding of microscale processes and interactions that appeared in the benthic environment is still very limited, particularly for the deep ocean, due to a lack of appropriate *in situ* observation and detection methods. To address this challenge, we have developed an *in situ* observation and detection system for microscopic targets suitable for the deep sea and have successfully deployed the instrument on a remotely operated vehicle (ROV) to achieve *in situ* microscopic Raman detection of targets on the seabed over a depth of 770 m. This is a combined system that integrated microscopic imaging and Raman detection techniques for *in situ* observation and analysis of underwater microscale targets. The complete system consists of an electronics chamber, a detection probe, and a precision external positioning device. Power supply and real-time data transmission are achieved *via* ROV tethers. This allows researchers to operate the instrument in real time to perform microscopic imaging capture and Raman spectroscopy acquisition of interesting targets on the seafloor. The first sea trial of the system was conducted in the South China Sea in 2020, and during the cruise, microscopic image acquisition and *in situ* compositional analysis of shell fragments, seabed rock samples, and live sea stars were successively performed. The system has solved the key technical challenges of deep-sea microscopic imaging, demonstrated the feasibility of deep-sea microscopic imaging, and illustrated the great potential of combining Raman spectroscopy and microscopic imaging in marine research. In this paper, we present the unique design of the instrument and the deep-sea results. With further optimization, the system promises to be a versatile instrument providing a unique perspective for deep-sea geochemical and biochemical studies.

KEYWORDS

deep sea, *in-situ*, micro-imaging, raman spectroscopy, remotely operated vehicle

1 Introduction

Microscale processes and interactions occurring in the marine can significantly influence benthic ecology and play an essential role in the formation and evolution of seabed landscapes at the macrolevel (Murray et al., 2002). Microscale processes and interactions dominated by sediment microbial communities and benthic organisms have already proved to play a fundamental role in global material cycling and energy exchange (Nguyen et al., 2022). In addition, microscale processes under extreme conditions in deep ocean waters, the seafloor, and the deep biosphere provide a way to reveal the processes that led to the origin of life and the potential for life on other planets and their moons (Colman et al., 2017). However, due to the lack of effective *in situ* observation methods, most benthic microscale studies were conducted by sampling (Sogin et al., 2006; Breier et al., 2012). Except for some stable processes that can correctly reproduce in the laboratory, much progress requires unique physical and chemical conditions (e.g., oligotrophic, low temperatures, high pressure, and, in some cases, limited oxygen concentrations). They are only stable in specific environments and cannot be completely simulated in the laboratory (Breier et al., 2010; Liang et al., 2021). For such processes, the best solution is to conduct *in situ* studies in the environment where it occurs. Over the past 20 years, the Global Ocean Observing System (GOOS) has promoted the Deep Ocean Observation Strategy (DOOS), which enhances the need for comprehensive and fine-grained ocean observations at greater depths (Levin et al., 2019). Nowadays, massive sensor arrays and observation networks extending thousands of miles over the seafloor make it possible to acquire real-time environmental data at greater depths and larger scales (Lin and Yang, 2020). In contrast, the development of microscale process detection in the marine environment remains slow, especially for the deep-sea benthic habitat, and only very few works about shallow water applications were reported (Mullen et al., 2016).

The challenges of performing microimaging in the deep sea are apparent: the system must surmount the harsh application environment and simultaneously provide good maneuverability. On the one hand, system vibrations caused by currents and ROV thrusters will be accumulated and amplified by the microscopic imaging system, resulting in dynamic blurring of the images. Thus, the system must operate in a fast imaging mode, which requires high brightness illumination and a fast precision focus to ensure the quality of the microscopic images. On the other hand, instrument operation is a significant challenge for deep-sea microimaging. Solid targets on the seabed are often opaque, complex, and non-homogeneous mixtures requiring micron-scale precision-focusing capabilities. In the laboratory, researchers can manually operate the microscope for microimaging directly. Even in shallow waters, underwater imaging systems can be deployed and adjusted with the help of divers. However, in deep sea, interactive tasks primarily depend on the ROV's robotic arm, which, unlike conventional electrically powered manipulator (Fu et al., 2022; Liu et al., 2022), is hydraulically actuated and therefore its positioning accuracy is usually limited to several centimeters (Aggarwal and Albiez, 2013). This is far from meeting underwater microscopy imaging systems' micron-level positioning accuracy requirements. Therefore, microimaging must incorporate a fast, high-precision auxiliary positioning function to compensate for the inadequate accuracy of the robotic arm. In addition, considering that target characteristics under a microscopic view may differ from macroperception, especially for complex targets without preprocessing, the underwater microimaging system should have additional qualitative recognition capabilities to aid target recognition.

In this paper, we established a deep-sea microscopic imaging system—MICROcean—and presented the first attempt to perform microimaging in the deep sea. The system integrates a high-speed optical zoom lens and an external auxiliary mechanical positioner to compensate for the ROV manipulator accuracy. In addition, it employs co-axial illumination to provide dynamic and uniform light to the imaging area during the optical zoom. Meanwhile, it integrates underwater Raman spectroscopy to provide analysis and recognize ability. Here, we presented the novel design of the instrument and demonstrated some typical applications to illustrate the detection capability of the device.

2 Materials and methods

2.1 Description of system

As shown in Figure 1A, MICROcean adopts a modular design, and its internal components are divided into three functional units (electronics module, probe, and positioner) and packaged in separate compartments. Among them, the probe and positioner are fixed together as the actuating detection section and the electronic compartment as the detection and control section. Different chambers are connected by watertight cables or oil-filled cables for power supply and communication. During underwater deployment, the electronic cabin was fixed inside the sampling basket to the front of the ROV, and the manipulator carried the positioner and probe to detect the interesting targets, as Figure 1B illustrated.

2.1.1 Optical layout

In the MICROcean, a long working distance objective (Mitutoyo M Plan Apo 5X, NA 0.14) was selected as the standard configuration to achieve non-invasive observations of underwater microscale targets. It provides a long working

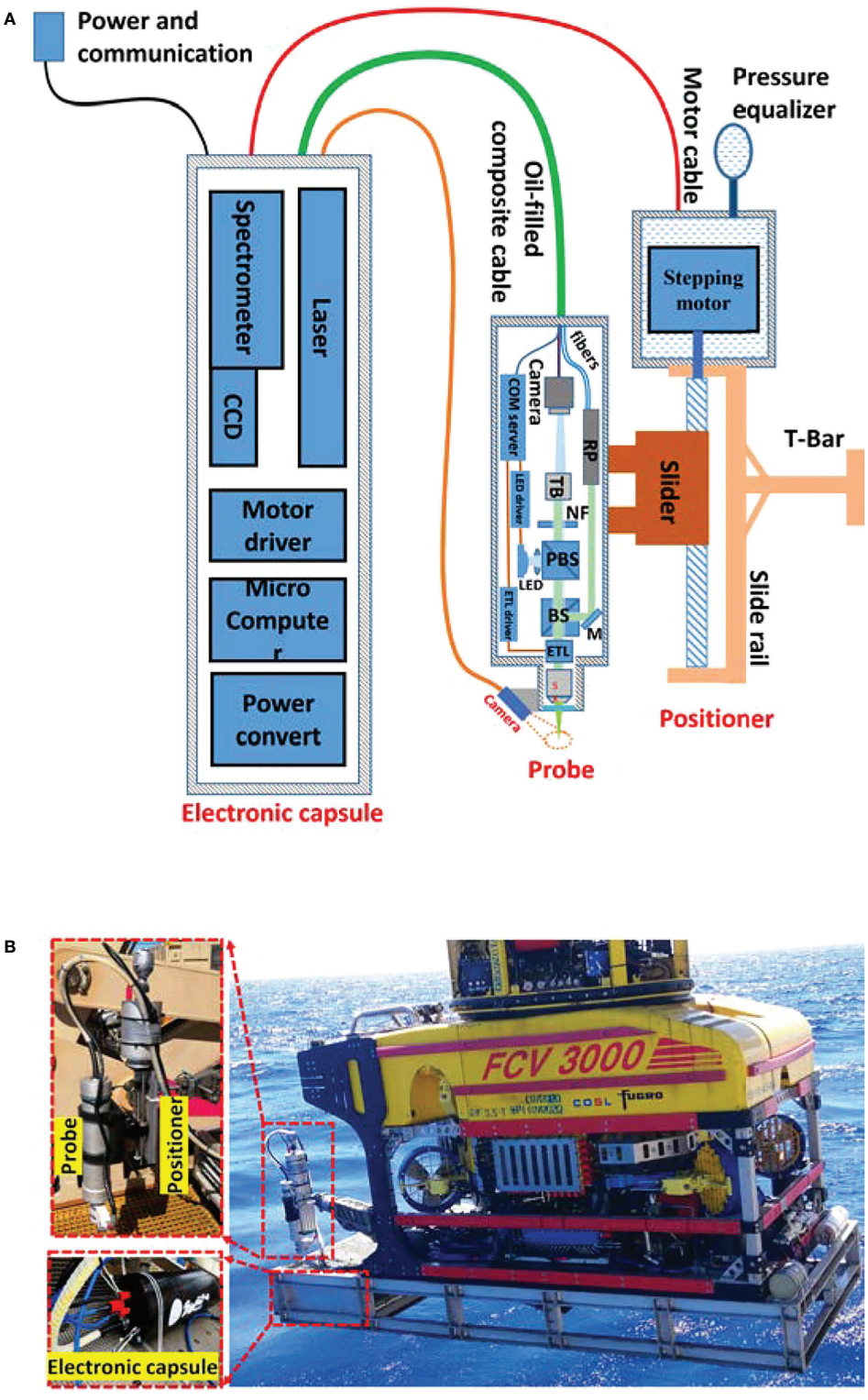

FIGURE 1
System composition and its deployment in the sea trial. **(A)** The schematic diagram of MICROcean. **(B)** The deployment of the MICROcean in the sea trail.

distance of 34 mm in air. After considering the refractive index of seawater and the effect of the optical inspection window, the actual working distance in seawater was approximately 40 mm (from the optic window to the targets). Such a distance is sufficient for the non-invasive observation of most targets and provides an adequate margin for system zooming. In addition, a focus tunable lens (Optotune EL-10-30-C Vis) was introduced into the microscope to dynamically change the system's working distance to provide fast focusing. The MICROcean system also incorporates a Raman spectroscopy module to assist the recognition of microscale targets. Raman spectroscopy is a standard tool to help microscopic identification in the laboratory, and its potential in assisting underwater microimaging has already been proven in our previous work (Liu et al., 2022). As shown in Figure 2, the microimaging and Raman modules are co-axially coupled in the probe using a 50:50 standard beam splitter. They share the same microscope objective and electronic zoom lens to ensure coincidence between the imaging plane and the Raman detection plane.

Under the electronic zoom mode, the microscope imaging plane will move as the tunable lens diopter changes. Hence, the traditional external illuminate method with a fixed lighting field is not suitable again. Thus, in the MICROcean system, we used a co-axial illumination structure, where the illuminator was coupled to the imaging light path by a polarizing beam splitting prism. Here, the camera and the illumination LEDs jointly consisted of an orthogonally polarized imaging structure, which can reduce the loss of the imaging beam at this point and suppress stray light interference between the mirrors in the system's optical path. The illuminator contained six lighting chips that were packaged in one bead. Every chip had its special wavebands, namely, red, yellow, green, blue, ultraviolet, and white, to meet the illumination needs of different water types (Liu et al., 2018). In addition, a fly-eye lens with a 5° divergence angle was used to homogenize the light field and avoid the LED beads imaged in the microimaging plane. When operating, the original light from the LED was separated by the polarizing beam splitter into P- and S-polarization, where the P-polarized component passed through the beam splitter along the incidence direction and was eventually absorbed by the light block. In contrast, the S-polarized component was reflected and coupled into the imaging light path. Then, it was redistributed by the standard prism and went through the tunable lens, objective lens, inspect window, seawater medium, and finally illuminated the target. The rough surface of the target depolarized the reflection ray (Lythgoe, 1972; Schechner and Karpel, 2005). Both the P- and S-polarized reflections were transmitted along the previous path and separated at the polarizing splitter. Only the P-polarization can enter the following imaging parts and focus on the camera as an image. The polarizing splitter will block the remaining S-polarized reflection to improve the contrast. The LED illuminator provided 100 levels for the light changes from the maximum to the darkness.

To get a better spectral performance in long work distance, the Raman module employed a 532-nm continuous wave laser as the excitation source. It can provide a tunable laser output in the range of 0–240 mW to meet the detection needs of different targets. Meanwhile, a wide range spectrometer, which can cover the Raman detection range of 0–4,500 cm^{-1} with a spectral resolution about 10 cm^{-1}, was selected for spectral detection. Both the laser and the spectrometer were mounted in the electronics cabin and connected to the Raman probe *via* two optical fibers, which were sealed in oil-filled composite cables. In the progress of Raman detection, the laser from the input fiber was collimated by the Raman probe, reflected by a broadband dielectric mirror and standard beam splitter, then coupled into the imaging path. The coupled laser went through the tunable lens, objective lens, optical window, seawater, and finally focused

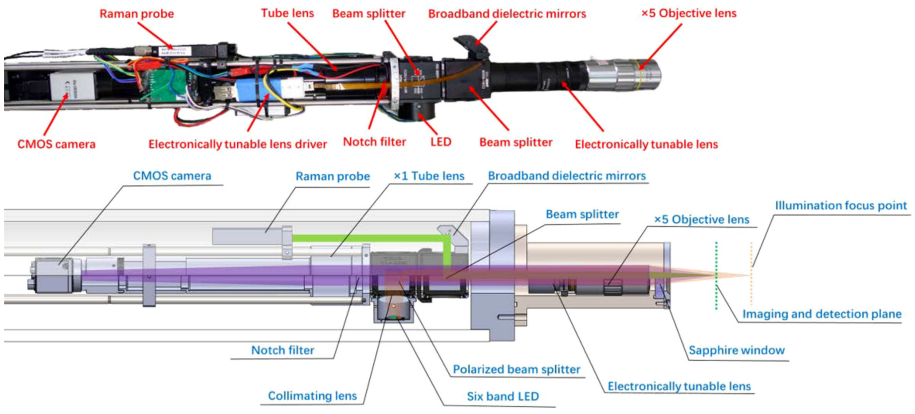

FIGURE 2
The optical layout of the microimaging and Raman detection in MICROcean.

on the target. Similarly, the Raman scatting went back and transmitted into the Raman probe, where the signal was abstracted and delivered through the output fiber to the spectrometer for further analysis.

2.1.2 The positioning and focusing

Compared with macroimaging, microimaging has a shallow depth of focus whose typical value is limited in the range of several microns to tens of microns and requires precise position. In contrast, the positioning accuracy of robotic arms is usually on the order of centimeters, which is far from satisfying the requirements. Two available methods can address the problem, one is adding the precise auxiliary positioner, and the other one is optical zoom adjust (Fahrbach et al., 2013; Bradbury, 2014). The front method changes the distance between the microscope and the target to achieve an appropriate position to capture images. It neither changes the system's magnification nor introduces additional imaging aberration. Meanwhile, it is easy to employ and can extend to a long range. However, due to the properties of the mechanics, it moves slowly and will produce significant errors when the direction of the motion is changed. On the contrary, the latter can obtain a clear image by adjusting the optical parameters rather than moving the position. Hence, it can achieve fast and accurate focus. But for an optimized system, the changes in optical parameters will increase the aberration and changes magnification. Meanwhile, its adjustment range is also limited to a small scale. No method can simultaneously meet the needs of an accurate and fast focusing over a wide range during deep-sea microimaging. Hence, this system proposes a hybrid focusing strategy that fuses the optical zoom adjust and mechanical positioner. It breaks the focus tasks into three steps, namely, roughly move, coarse modify, and fast fine adapts action. In the roughly move step, the ROV's manipulator brings the positioner and probe over the detection target. As this progress usually needs to drive a long distance, the movement error from the manipulator is tolerable. Then, the mechanical positioner is responsible for carrying the probe for coarse adjustment and locating the imaging plane to the target. Finally, the tunable lens fast zooms in available range to track the targets and capture clear images.

The main body of the positioner is a linear actuator driven by a servo motor and screw rod. Under the control command, the motor drives the screw rod rotation and promotes the slider plate to a specific position. Benefiting from the closed-loop controller, the positioner step accuracy can reach 2 μm over a trip range of 30 cm. The optical zoom relies on the tunable lens, which can dynamically change its diopter according to the drive voltage. The test results showed that the ETL diopter changed from −1.5 to 3.5, and the work distance of the MICROcean changed 24 mm underwater, with a maximum focus error of 90 μm. During the focusing process, the gray-level gradient function was used to determine the sharpness of the image and combined with the hill climbing algorithm for auto-focus tracking. Meanwhile, a continuous slice imaging function along the gradient direction was integrated into the control software to cope with the problem of the inability to stabilize the focus when tracking dynamic targets. In addition, at the front of the probe, we added a macrocamera to supply a transitional view from the ROV's wide-angle camera to the microscopy. The macrocamera also provided a rough reference for the first two levels of positioning.

2.1.3 Control and communication

The control and communication of the whole system mainly depended on the center-embedded computer located in the electronic cabin. It connected all the peripheral equipment and established a communication channel to the deck server through the ROV umbilical cable. In the electronic chamber, the embedded computer, electronic controller, and power drivers were regularly installed on an aluminum bench, which was fixed on the front cap. Among them, the high-power items such as the servo motor driver and power converter removed the cooling fins and directly contacted the bench to accelerate the heat exchange with the seawater.

To improve adaptation, the system developed two operation modes: remote process mode and local process mode. In the remote mode, the embedded computer and the ROV nodes consisted of a transparent network. All the information from the peripheral equipment was packaged and sent to the deck server for further processing. Since all the complex data process tasks are transmitted to the powerful deck server in this mode, it can operate some more advanced real-time algorithms to offer a better user experience. However, this mode must transmit the amount of original data requiring a wide network band and stable connection. In the local process model, the embedded computer plays the communication center and the processing center at the same time. It needs to respond to the commands from the deck server, control the equipment for data sampling, process original data, and send the results to the endpoint. In this mode, the MICROcean is an independent system that can automatically work with the default parameters, and all the results will be saved in local storage; hence, it can work with low-speed networks. However, limited by the embedded computer's weak performance, the system can only operate at a low sampling rate.

2.2. Microimaging performance and calibration

For infinity-corrected microscopy, the inserted plane optic elements such as the beam splitter and the notch filter will not change the imaging quality, as the light has the same optical path in those elements. But when it comes to the tunable lens, the

situation became complex. The tunable lens has a variable diopter, which can affect the work distance, magnification, and imaging quality. It is hard to calculate the changes while the specific structure and parameters of the objective lens are unknown. Here, we performed an imaging test using the USAF1951 targets to evaluate the imaging performance under the different diopters. The tunable lens can dynamically change the diopter from −1.5 to 3.5 as the drive current increases from 0 to 300 mA with a linear relationship (Chen et al., 2021; Optotune, 2022). The transformational relation between the current and diopter can present in the following form:

$$D_c = \frac{I_c}{I_{\max}}(D_{\max} - D_{\min}) + D_{\min} \quad (1)$$

In the equation, I_c is the drive current, D_c represents the diopter, I_{max} indicates the max drive current (300 mA), and the D_{max} and D_{min} mean the maximum diopter and minimum diopter in the turnable range, respectively. The ETL offers 300 tunable levels of the drive current, and we evenly selected 16 points with the current increment of 20 mA. For each point, we carefully moved the target to obtain the clearest image and record the target position. The imaging results are shown in Figure 3. Generally, a 5× microscope objective with matching tube lens can provide standard five times system magnification. But when an additional element with non-zero diopter is inserted, the specific system diopter contributed by the objective lens and tube lens will be changed, causing the original magnification to alter. If the diopter of the inserted element is positive, the overall system diopter will increase, resulting in a larger magnification; if the diopter of the inserted element is negative, the overall system diopter will decrease and make the magnification smaller. A large magnification is helpful to improve the imaging resolution. According to the experimental results, it can be clearly observed that as the driving current increased, both the system magnification and the imaging quality had a different degree of improvement. When the drive current was zero, which corresponded to the diopter of ETL of −1.5, the system amplification was about 3.7 times. When the current raised to 300 mA, the ETL diopter changed to 3.5, and the amplification became 8.1 times. Correspondingly, the imaging area also expanded from 1.04×0.87 mm to 1.87×2.23 mm. The imaging quality was inferior at the beginning 6 points, corresponding to currents of 0–100 mA, where the fly-eye lens' pattern appeared

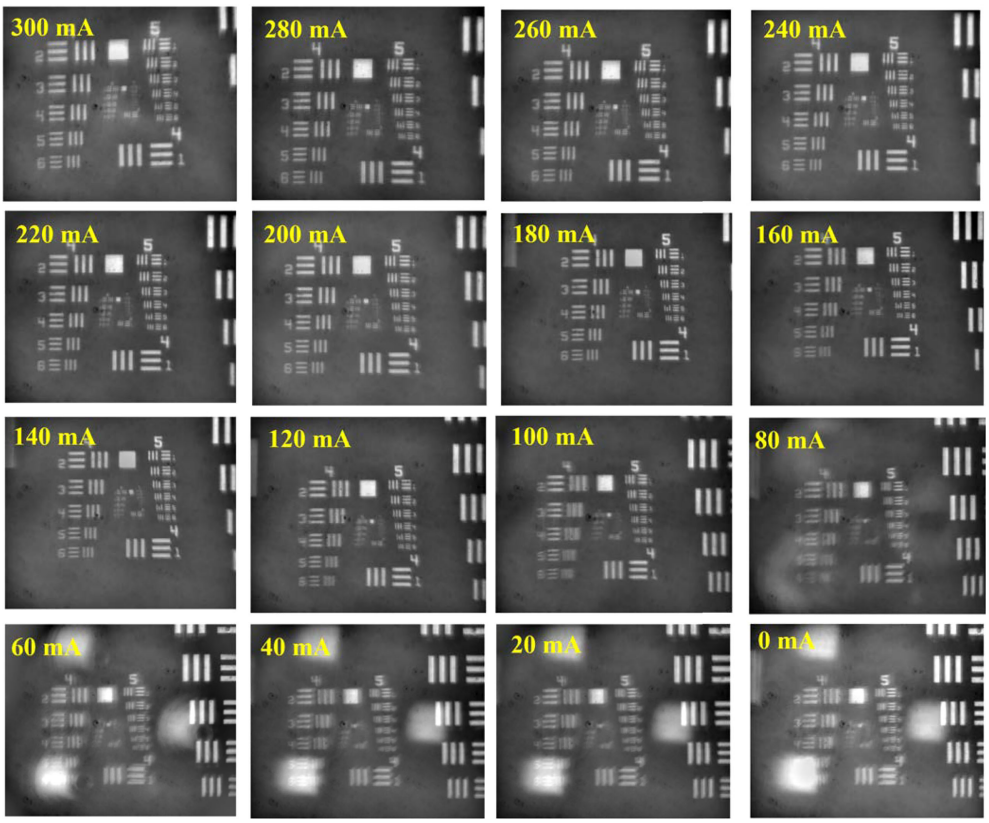

FIGURE 3
The imaging results of MICROcean under different drive currents.

on the image causing uneven illumination and accompanying image blur. When the drive current was above 100 mA, the microimaging became clear and stable, with only slight resolution differences. Furthermore, we selected the image obtained at the middle current between 100 and 300 mA (200 mA) as a sample to analyze. As shown in Figure 4A, there are totally four complete line-pair groups (the fourth, fifth, sixth, and seventh groups) of negative target that appeared in the vision field. Limited by the contrast, the first element in the seventh group already cannot be identified, but all the elements of the sixth group can be recognized as independent elements. Figure 4B illustrates the intensity distribution of the vertical profile of each element in the sixth set of pairs. Such test result means that the system imaging resolution can reach 114.0 line pairs/mm, corresponding to the 4.4-μm resolution.

Due to the notch filter's existence, the laser spot focused on the microimage is invisible. Hence, the system must employ an alignment to map the detection region to the specific position of the microimage. In the alignment progress, a laser observation card (VRC2, Thorlabs), absorbing laser and irradiating the fluorescence, was used to indicate the position and the focus spot size. As shown in Figure 5, the alignment result shows that the laser spot located at the pixel (1,158,802) and its radius occupied about 300 pixels. Although the system magnification will change as the ETL diopter turns, the shared ETL and the objective lens can keep the laser spot always at the same position and occupy about the same pixels. When the system magnification was 5×, the spot diameter was 450 μm. In addition, the Raman detection model was also calibrated using an argon mercury lamp (AvaLight-CAL-Mini) before deployment.

3 Sea trials and deployment

The MICROcean carried out its first sea trials in the South China Sea in August 2020. In this sailing, a deep-sea work class ROV, FCV3000, was used as the underwater carrying platform. It is equipped with "Schilling Titan4" and "Schilling Rig Master," two hydraulic-driven manipulators for interaction. The "Schilling Titan4" has seven degrees of freedom (DOFs), six for movement, and one for end grab. It possesses the ability to reach the target from different multi directions in its workspace, having enough flexibility to finish the complex operation. The "Schilling Rig Master" is a heavy payload manipulator with only five DOFs, four position degrees, and one grab degree. Considering stability, the "Schilling Rig Master" has better payload ability and stiffness, which contribute to restraining the end shaking during the microimaging. Hence, we selected the "Schilling Rig Master" as the prima action hand and the remaining hand, "Schilling Titan4," as an auxiliary to assist in the observation and sampling. As shown in Figure 1B, the electronic capsule was fixed in the front sampling basket, and the manipulator "Schilling Rig Master" grabbed the positioner and probe for imaging and detection. In this deep-sea investigation, the MICROcean reached a maximum depth of 1,100 m and captured thousands of *in situ* microimages and spectroscopic images, including living starfish, shell debris, and stone samples at 700–800 m depths. Next, we present some typical results obtained in the first sea trial.

4 Results and discussion

4.1 Biological target—starfish

Starfish (phylum Echinodermata) are ecologically important and diverse members of marine ecosystems in all of the world's oceans, from the shallow water to the hadal zone (Mu et al., 2018). When the ROV cruised over the sand seabed, a starfish was found crawling over the seabed at 774 m. From the morphological analysis, the starfish belong to the Goniasteridae, *Circeaster pullus*, and is very similar to the species (D2-EX1605-L1-12-21:57:29) found by NOAA in the South Pacific, Johnston Atoll, and the Musicians seamounts during 2015–2017 NOAA, 2022. Both of them were found in the same depth range (600–800 m). As shown in Figure 6A, the starfish has five arms and a polygonal, ordered plate. Abactinal, marginal, and actinal plate surfaces are covered with enlarged, well-spaced granules. Enlarged granules also form a border around plates. Arms elongate tapering, with tips upturned. The further microimaging, top 2 images in Figure 6B, proved that the starfish has at least two large granules in the plate, one with small semicircular bumps along the edge and the other with flat edges and tight connections. At the plate edge, shown in the bottom of Figure 6B, the granules become minor and jumbled, and their shapes change from regular polygons to circles.

The starfish body wall is composed of magnesium calcite ossicles connected by collagenous tissue and muscles. It shows flexibility in stiffness, which is attributed to the mechanical mutability of the collagenous component (Blowes et al., 2017). On the seabed, we analyzed the body wall composition of the star fish using Raman spectroscopy, as shown in Figure 7A. To prevent biological samples damaged by high-energy lasers, the output laser energy was limited to 50 mW, and the exposure times were set to 15 s to depress the noise. The detected results, presented in Figure 7B, revealed that the starfish body wall exhibits a typical biological characteristic, rich in beta-carotenoids. The Raman bands located in 1,520, 1,157, and 1,008 cm^{-1} are the typical carotenoid peaks that can be assigned to C=C (ν_1) stretching, C–C (ν_2) stretching, and C–CH_3 bending, respectively (de Oliveira et al., 2010). The Raman band in 981 cm^{-1} is contributed by the sulfate ion in the seawater (Brewer et al., 2004; Man'kovsky, 2012), and the fluorescence band located at 677 nm is caused by the chlorophyll that may drop from the upper water (Graf, 1989). In addition, the spectra have a unique band at 2,950 cm^{-1}/630 nm, which has never been observed in other targets. This band is so strong that it even changed the shape of the biggest Raman band, which belongs to

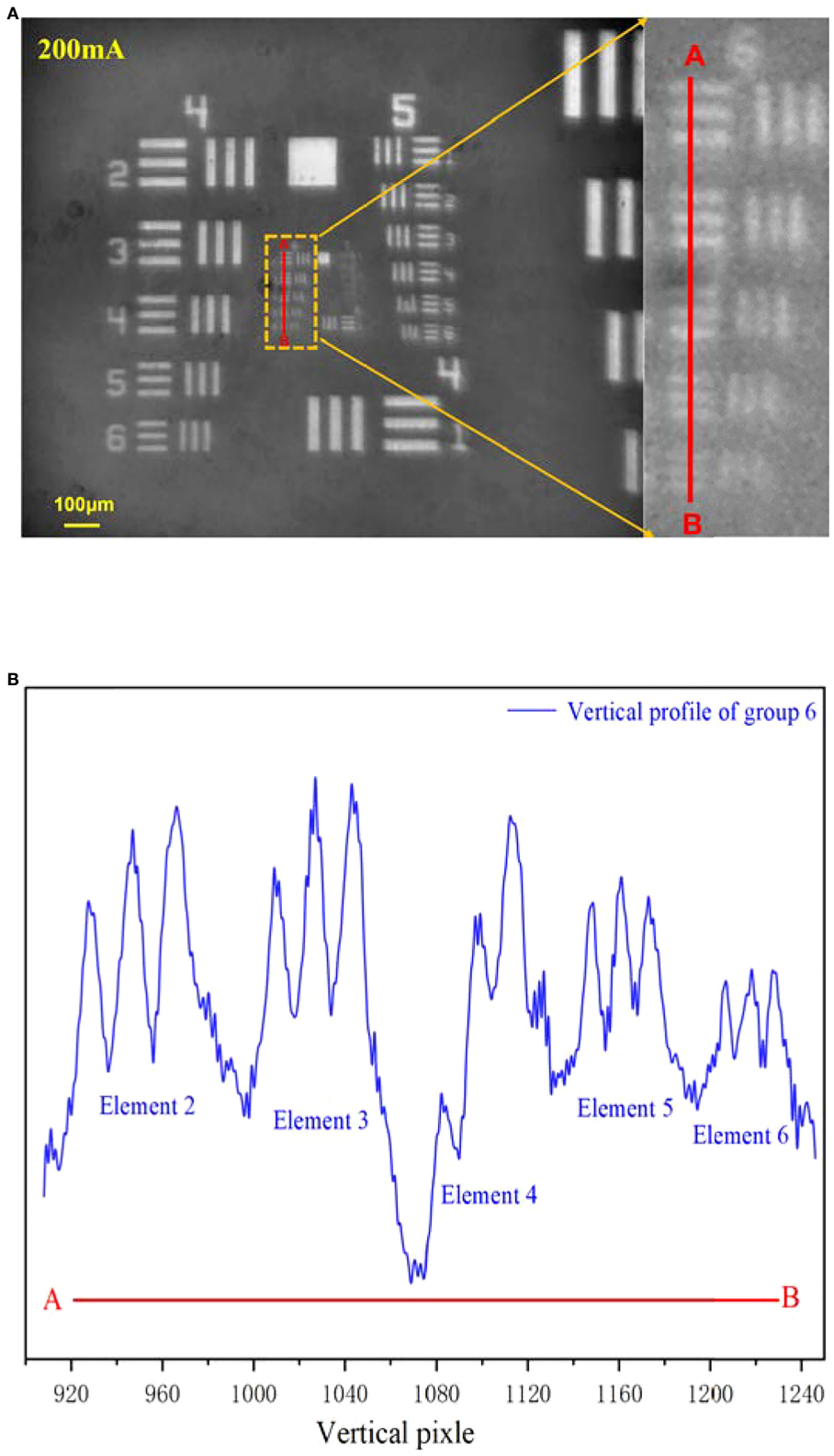

FIGURE 4
The MICROcean imaging resolution at the current of 200 mA. **(A)** The original image and its enlarge image in the sixth line pairs group. **(B)** The vertical intensity profile of group 6.

10.3389/fmars.2022.1018042

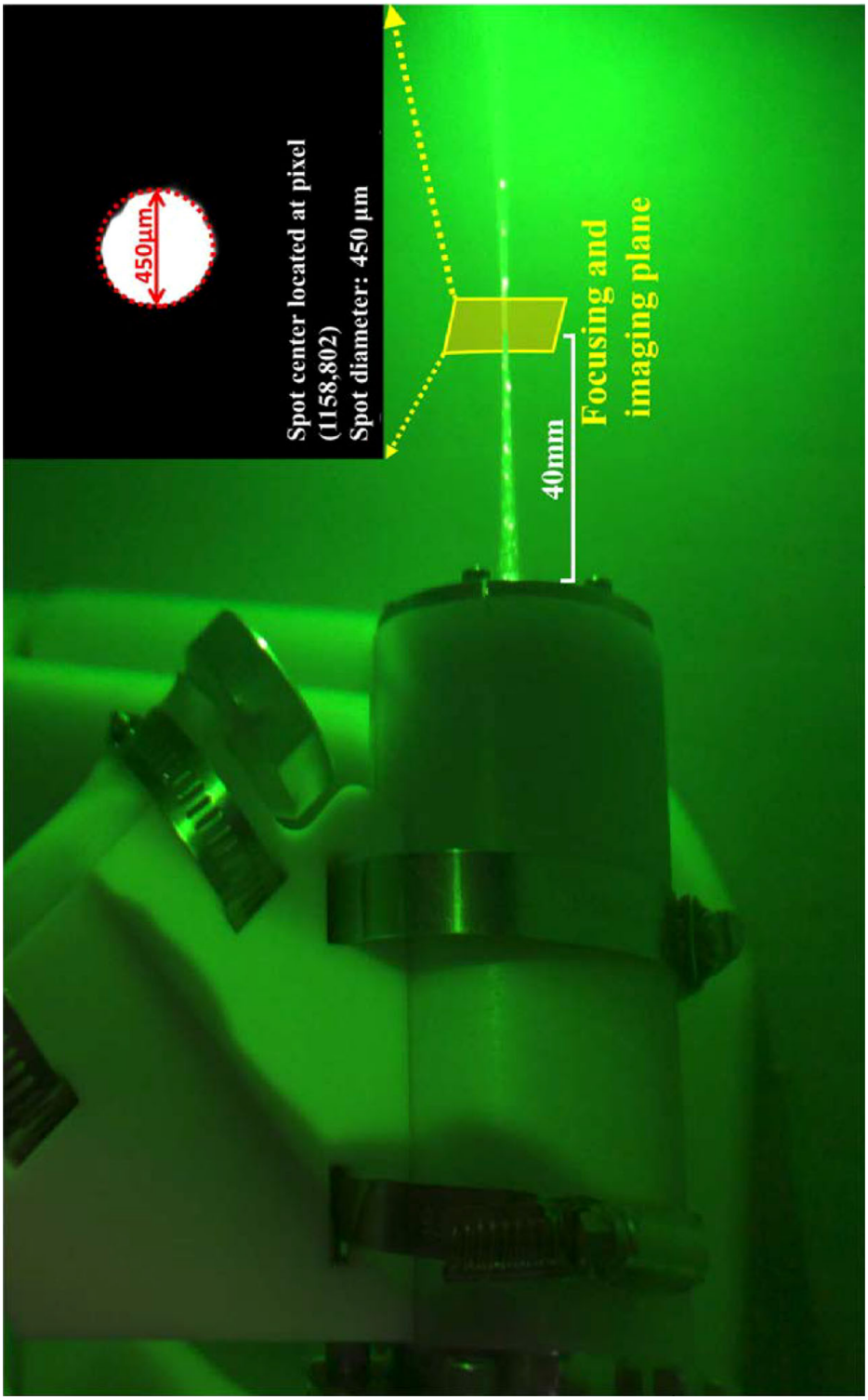

FIGURE 5
The align results of the laser-focused spot and the microimage.

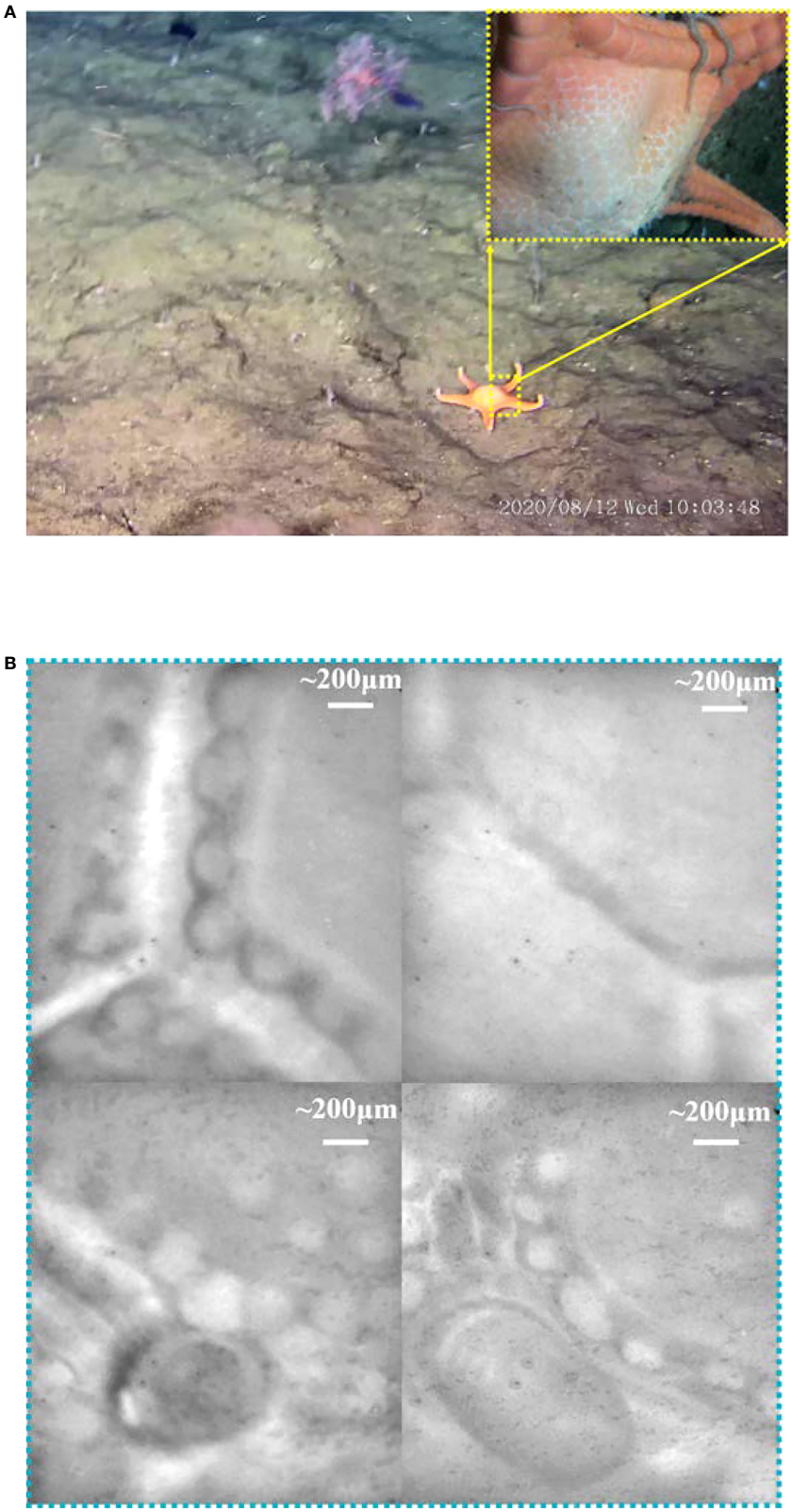

FIGURE 6
The macromorphology and microimaging of the starfish. **(A)** The image obtained by ROV HD camera and probe-side-mounted macrocamera. **(B)** The microimages captured by the microscopy.

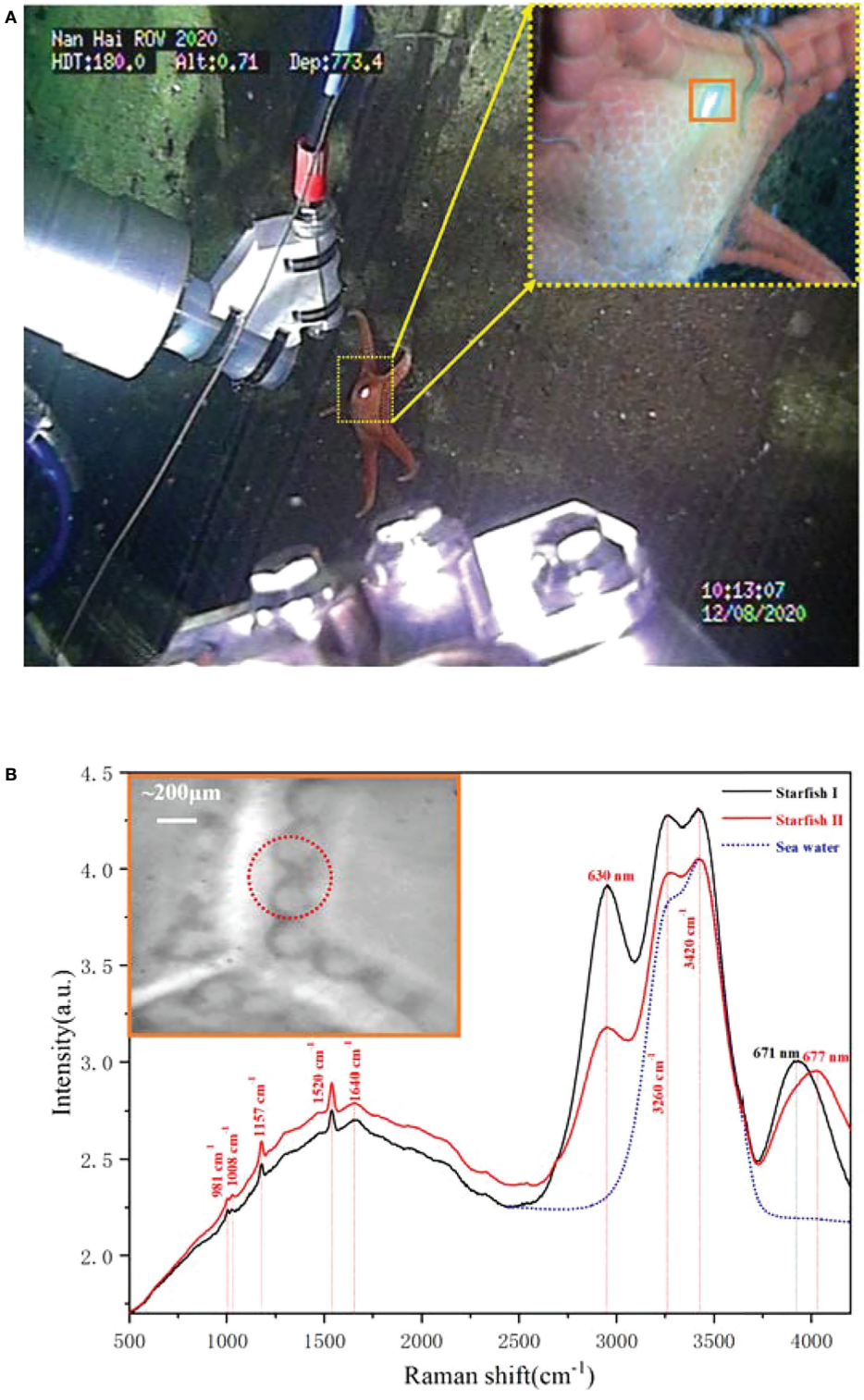

FIGURE 7
The *in situ* Raman detection of the starfish. **(A)** The scenes of *in situ* detection. **(B)** The Raman spectra of the starfish obtained at 773.4 m depth.

the water H–O–H bending mode, and its shoulder peak at 3,260 cm^{-1} already has the same height as the main peak at 3,420 cm^{-1}. By contrast, in these two spectra, starfish I and starfish II, we induct that this fluorescent band may not be caused by pigment, as it does not have any other Raman bands; meanwhile, it is also too strong compared with the carotenoid. Meanwhile, it certainly does not belong to the material in the water because the water is already well mixed and will not have such a big difference in the microscale. The possible origin is that it is caused by the protein and lipids in the collagenous tissue or muscles (Li et al., 2019). In addition, the band located at 671 nm may have the same origin, as it has a similar trend when the band changes.

4.2 Rock target—limestone

Besides the biological targets, we also detected a rock target in the exposed seabed. Unlike the common sandy seabed in this region, this exposed seabed has a dark gray appearance, but its fresh section shows a yellowish color, as shown in Figure 8A. Its structure is loose, has low strength, and is easily broken. For further analysis, we operated the "TITAN 4" manipulator and took a rock sample from the seabed. The microscopic imaging results of the sample's new fracture are shown in Figure 8B. These microimages from different positions of the fracture exhibit very similar features—numerous spherical granularities with 0.1–0.3 mm diameter were glued together by some amorphous cement, and it indicates that the seabed base is a homogeneous matter. According to its microscopic appearance, the rock sample may be some type of granular limestone or sandstone. Furthermore, we performed Raman detection on the rock samples as shown in Figure 9A. For rocks with high damage thresholds, the laser output energy was set to a maximum of 240 mW to get a better excitation effect, and the spectra are collected with an exposure time of 15 s. The *in situ* Raman spectra of the rock sample's new fracture, presented in Figure 9B, indicated that the main component of the sample is calcite. The Raman peaks at 281, 714, and 1,085 cm^{-1} corresponded to the out-of-plane bending vibration, in-plane bending vibration, and symmetric stretching vibration of calcite, respectively (Gunasekaran et al., 2006). The sulfate ion in the seawater contributed to the Raman band at 981 cm^{-1}. The Raman bands located at 1,520 and 1,157 cm^{-1} correspond to the carotenoid C=C (ν_1) stretching and C–C (ν_2) stretching bending, separately. The fluorescence band at 677 nm can be assigned to the chlorophyll. Similar to the previous starfish spectra, the chlorophyll most likely comes from the phytoplankton particles that dropped from the upwater and attached to the seabed (Smith et al., 2008). To determine the difference between the surface and interior of the seabed rocks, we compared the Raman spectra of the new rock sections with the original exposed rocks of the seabed. Figure 9 presents two spectra obtained from the old exposed surface and new fracture, and the major differences between them are fluorescence and carotenoid. Compared to the new section, the surface contained more biological material, causing stronger fluorescence and carotenoid Raman bands. Combining the spectral results and microscopic images of the samples, it was not difficult to infer that the seabed is a granular limestone with calcite as the main component.

4.3 Biomineralization targets—shell

At the seabed crevices, we found numerous shell fragments as shown in Figure 10A, but no living shelled benthic organisms were found in this area. They were more likely transported by bottom currents and retained in the seabed crevices. Further macroscopic imaging by the probe-side-mounted camera showed that these shells were mainly from brachiopod detritus, including *Agulthasia*, *Magellania*, and *Discinisca*. These brachiopods are common on the continental shelf, with only a few occurring at shelf breaks associated with the presence of deep-water corals (Brand et al., 2003). Although they can be found from the littoral waters (generally subtidal) through to the abyssal zone, their fragile shell makes it difficult to obtain complete samples of deep water. Further detection shows that the shell's spectra are really simple, except for the seawater bands and a big florescence bump over the whole range, and only a symmetric stretching band of carbonate is observed in Figure 5. It indicates that the shell is already completely bleached, without any organic matter left. Limited by the microvision field, we can only observe the partial part of the shells, and the crushed shell also indicated that the brachiopod in the shell was already dead for a long time.

5 Conclusion

To solve the problem of *in situ* observation of deep-sea microscale targets, an ROV-based deep-sea microimaging system, MICROcean, was developed. It adapted hybrid positioning method, using mechanical position and optical zoom to overcome the challenge of employing precise focus in the deep sea. Meanwhile, it further coupled a Raman detection model to assist the target identification. In the next sea trials, the system successfully obtained thousands of microimages and Raman spectra of deep-sea benthic target, such as starfish, rocks, and brachiopod shells, at 770 m. This is the first attempt to perform *in situ* microscopic observation of benthic targets in the deep sea; it extends the existing observation

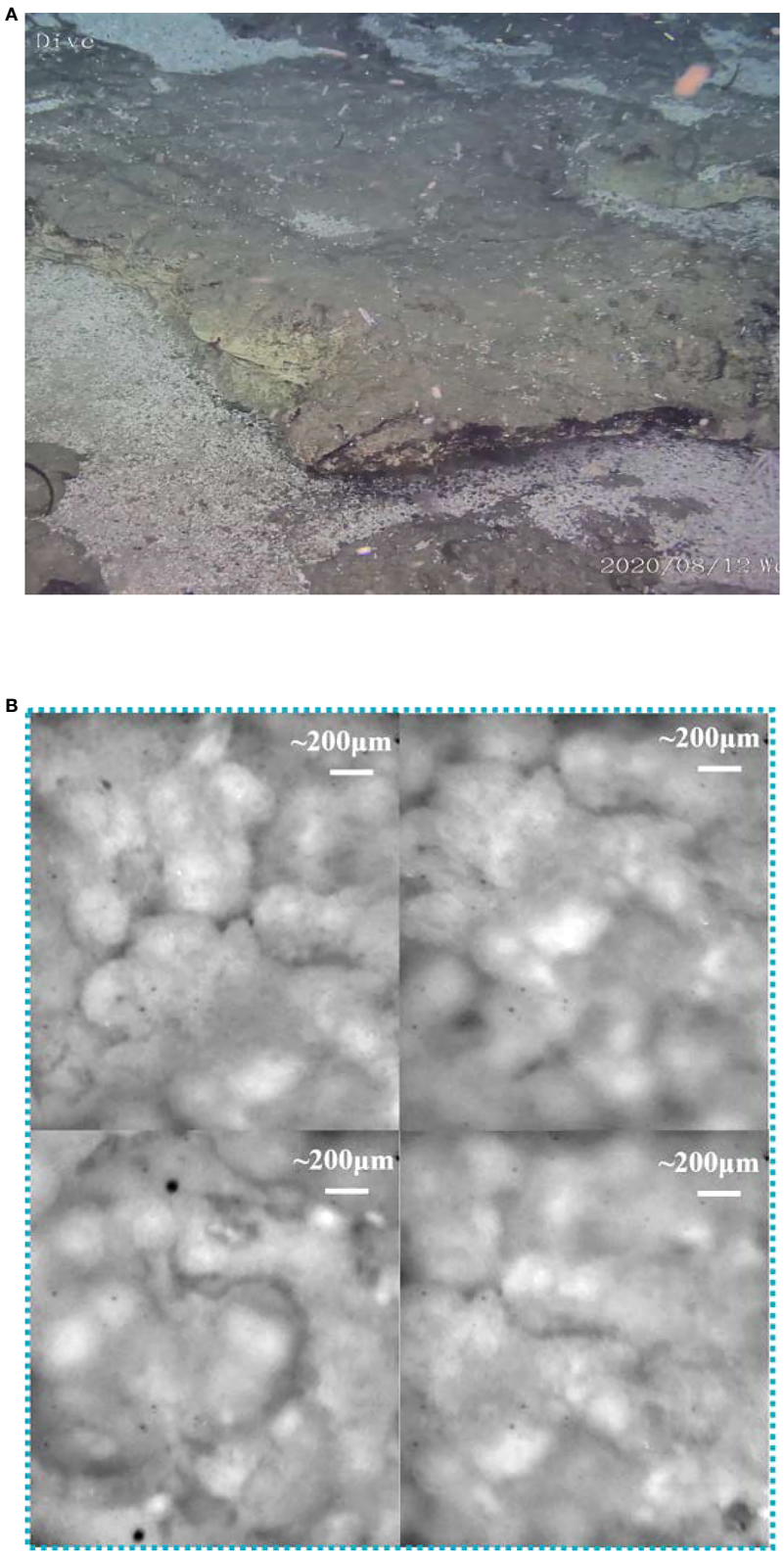

FIGURE 8
The macroimage of the seabed rock sample and its microimaging results. **(A)** The macroimages of the seabed obtained by ROV HD camera. **(B)** The microimaging results of the rock sample.

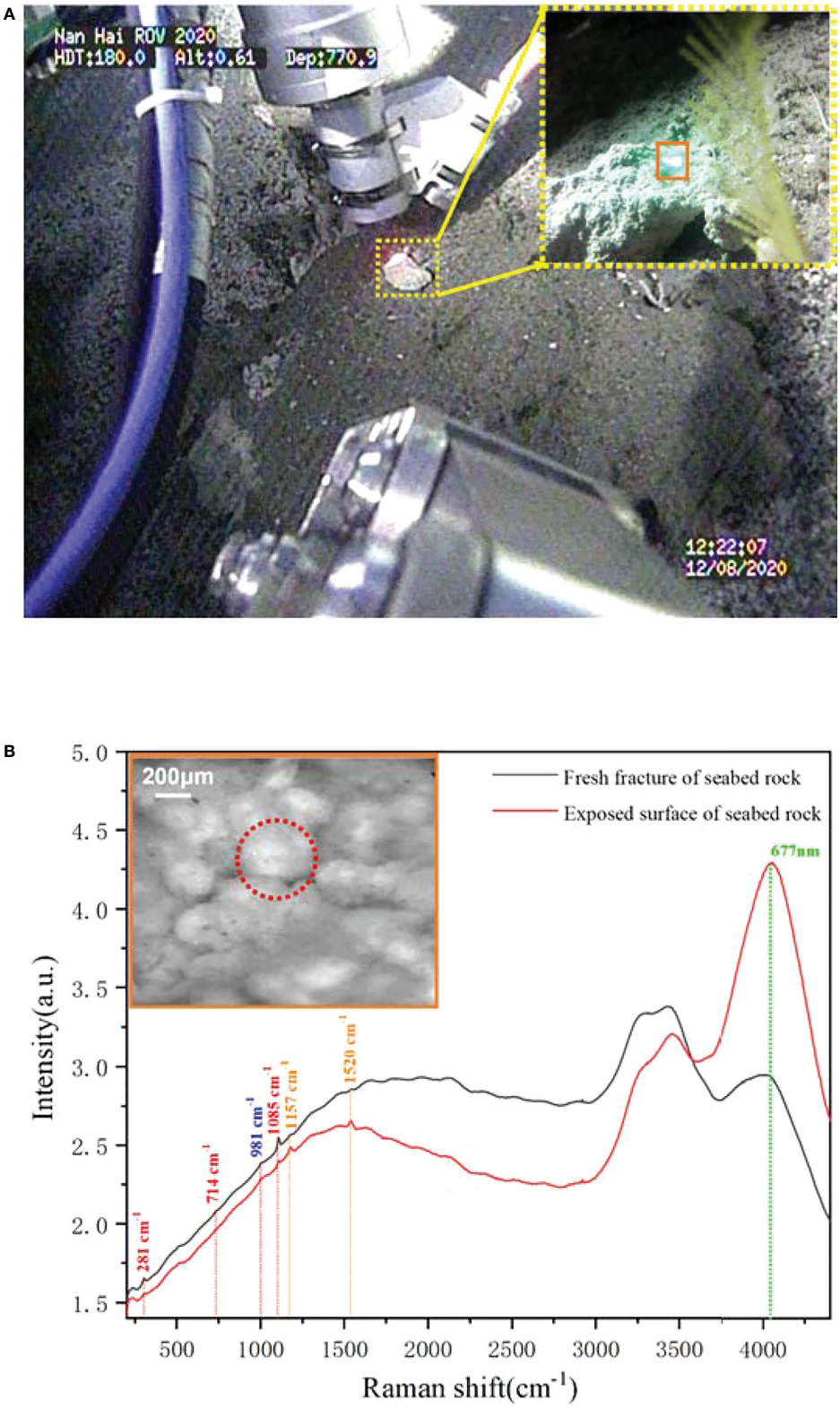

FIGURE 9
The *in situ* Raman detection and microimaging of the rock sample. **(A)** The scenario of underwater imaging and detection. **(B)** The Raman spectra obtained from the benthic rock sample.

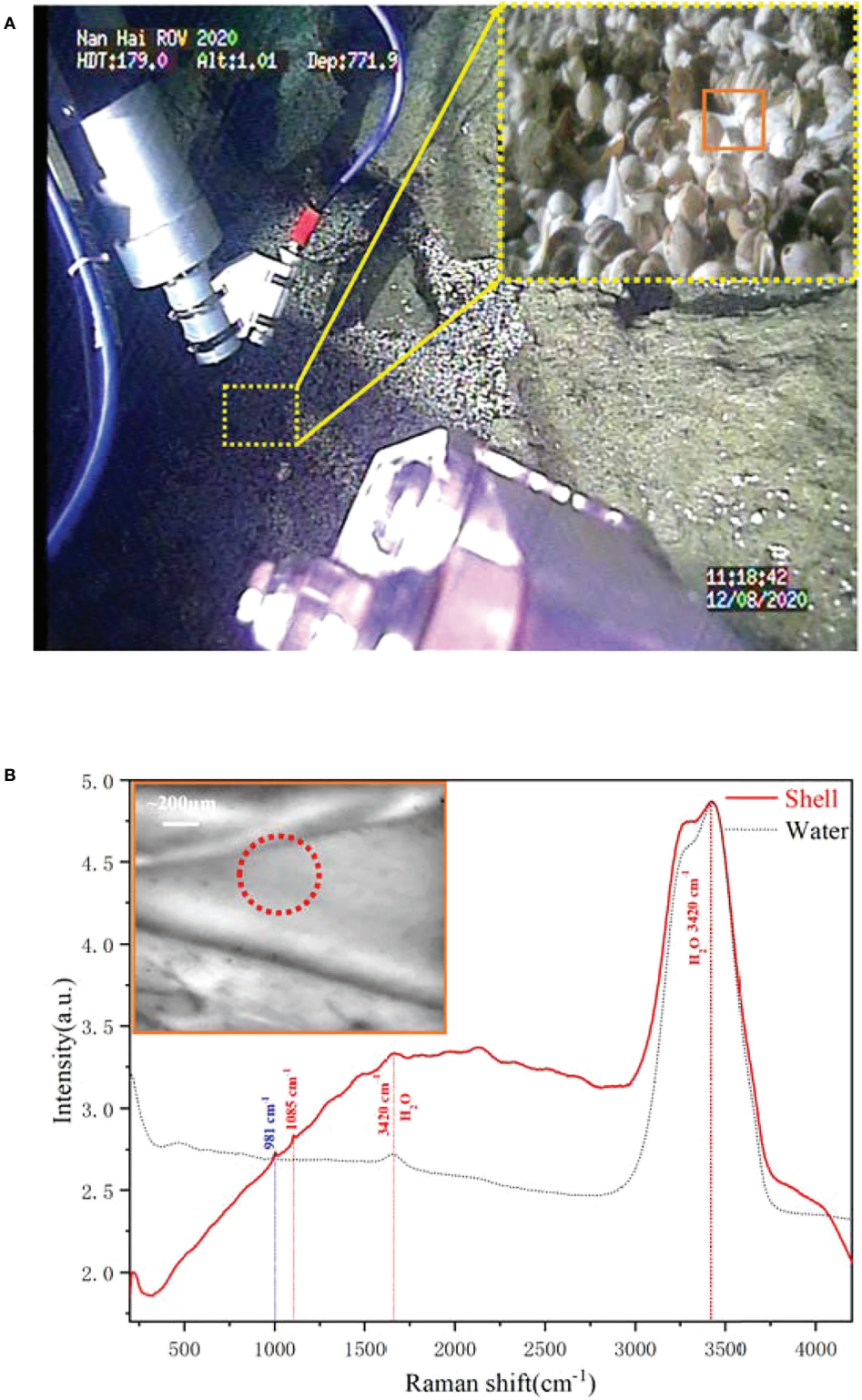

FIGURE 10
The *in situ* Raman detection and microimaging of deep-sea brachiopods shell. **(A)** The scenario of deep-sea *in situ* imaging and detection. **(B)** The Raman spectra of deep sea brachiopods shell.

methods and provides new perspectives for deep-sea investigations. This system demonstrates the feasibility of microscopic imaging in the deep sea and shows its great potential in deep-sea investigation. Next, we will optimize and improve the system for some problems that have not yet been adequately solved, such as low contrast and attenuation in resolution, and promote it to become a common technique for underwater investigation.

Data availability statement

The original contributions presented in the study are included in the article/Supplementary Material. Further inquiries can be directed to the corresponding authors.

Author contributions

QL and JG proposed the conception and built the system. YL provided the solution for microscope imaging. ZW and WY built the software. SL and LW performed the calibration and laboratory test. RZ provided technical guidance for the system setup. XZ planned experiments and led the sea trials. All authors contributed to manuscript revision, read, and approved the submitted version.

Funding

This research was funded by Shandong Special Fund of Pilot National Laboratory for Marine Science and Technology (Qingdao) (No. 2021QNLM020002), Provincial Key Research and Development Program of Shandong, China (2019GHZ010, 2019JZZY010417), and Fundamental Research Funds for the Central Universities (201961006).

Acknowledgments

We would like to thank the captain and crew of the research vehicle "Zhangjian" and the ROV pilots for their skilled operation support in the sea trial.

Conflict of interest

The authors declare that the research was conducted in the absence of any commercial or financial relationships that could be construed as a potential conflict of interest.

The handling editor ZS declared a past co-authorship with the author JG.

Publisher's note

References

Aggarwal, A., and Albiez, J. (2013). "Autonomous trajectory planning and following for industrial underwater manipulators," in *2013 OCEANS-San Diego (New York: IEEE)*, 1–7.

Blowes, L. M., Egertová, M., Liu, Y., Davis, G. R., Terrill, N. J., Gupta, H. S., et al. (2017). Body wall structure in the starfish asterias rubens. *J. Anat.* 231, 325–341. doi: 10.1111/joa.12646

Bradbury, S. (2014). *The evolution of the microscope* (Amsterdam: Elsevier).

Brand, U., Logan, A., Hiller, N., and Richardson, J. (2003). Geochemistry of modern brachiopods: applications and implications for oceanography and paleoceanography. *Chem. Geol.* 198, 305–334. doi: 10.1016/S0009-2541(03)00032-9

Breier, J., Gomez-Ibanez, D., Reddington, E., Huber, J., and Emerson, D. (2012). A precision multi-sampler for deep-sea hydrothermal microbial mat studies. *Deep Sea Res. Part I: Oceanographic Res. Papers* 70, 83–90. doi: 10.1016/j.dsr.2012.10.006

Breier, J., White, S., and German, C. (2010). Mineral–microbe interactions in deep-sea hydrothermal systems: a challenge for raman spectroscopy. *Philos. Trans. R. Soc. A: Mathematical Phys. Eng. Sci.* 368, 3067–3086. doi: 10.1098/rsta.2010.0024

Brewer, P. G., Malby, G., Pasteris, J. D., White, S. N., Peltzer, E. T., Wopenka, B., et al. (2004). Development of a laser raman spectrometer for deep-ocean science. *Deep Sea Res. Part I: Oceanographic Res. Papers* 51, 739–753. doi: 0.1016/j.dsr.2003.11.005

Chen, L., Ghilardi, M., Busfield, J. J., and Carpi, F. (2021). Electrically tunable lenses: a review. *Front. Robotics AI* 166. doi: 10.3389/frobt.2021.678046

Colman, D. R., Poudel, S., Stamps, B. W., Boyd, E. S., and Spear, J. R. (2017). The deep, hot biosphere: Twenty-five years of retrospection. *Proc. Natl. Acad. Sci.* 114, 6895–6903. doi: 10.1073/pnas.1701266114

de Oliveira, V. E., Castro, H. V., Edwards, H. G., and de Oliveira, L. F. C. (2010). Carotenes and carotenoids in natural biological samples: a raman spectroscopic analysis. *J. Raman Spectrosc.* 41, 642–650. doi: 10.1002/jrs.2493

Fahrbach, F. O., Voigt, F. F., Schmid, B., Helmchen, F., and Huisken, J. (2013). Rapid 3d light-sheet microscopy with a tunable lens. *Optics Express* 21, 21010–21026. doi: 10.1364/OE.21.021010

Fu, J., Poletti, M., Liu, Q., Iovene, E., Su, H., Ferrigno, G., et al (2022). Teleoperation Control of an Underactuated Bionic Hand: Comparison between Wearable and Vision-Tracking-Based Methods. *Robotics* 11:61. doi: 10.3390/robotics11030061

Graf, G. (1989). Benthic-pelagic coupling in a deep-sea benthic community. *Nature* 341, 437–439. doi: 10.1038/341437a0

Gunasekaran, S., Anbalagan, G., and Pandi, S. (2006). Raman and infrared spectra of carbonates of calcite structure. *J. Raman Spectrosc.* 37, 892–899. doi: 10.1002/jrs.1518

Levin, L. A., Bett, B. J., Gates, A. R., Heimbach, P., Howe, B. M., Janssen, F., et al. (2019). Global observing needs in the deep ocean. *Front. Mar. Sci.* 6, 241. doi: 10.3389/fmars.2019.00241

Liang, J., Feng, J.-C., Zhang, S., Cai, Y., Yang, Z., Ni, T., et al. (2021). Role of deep-sea equipment in promoting the forefront of studies on life in extreme environments. *Iscience* 24, 103299. doi: 10.1016/j.isci.2021.103299

Lin, M., and Yang, C. (2020). Ocean observation technologies: A review. *Chin. J. Mechanical Eng.* 33, 1–18. doi: 10.1186/s10033-020-00449-z

Liu, Q., Guo, J., Lu, Y., Liu, S., Nie, M., Wei, Z., et al. (2022). Microimage coupled raman optical probes for benthic solid target detection. *J. Raman Spectrosc*. doi: 10.1002/jrs.6411

Liu, F., Han, P., Wei, Y., Yang, K., Huang, S., Li, X., et al. (2018). Deeply seeing through highly turbid water by active polarization imaging. *Optics Lett.* 43, 4903–4906. doi: 10.1364/OL.43.004903

Liu, X., Li, X., Su, H., Zhao, Y., and Ge, S. S. (2022). The opening workspace control strategy of a novel manipulator-driven emission source microscopy system. *ISA transactions (early access)* 53, 1604–1613.. doi: 10.1016/j.isatra.2022.09.002

Li, X., Zhang, D., Bai, Y., Wang, W., Liang, J., and Cheng, J.-X. (2019). Fingerprinting a living cell by raman integrated mid-infrared photothermal microscopy. *Analytical Chem.* 91, 10750–10756. doi: 10.1021/acs.analchem.9b02286

Lythgoe, J. N. (1972). "The adaptation of visual pigments to the photic environment," in *Photochemistry of vision* (Springer) (Amsterdam: Elsevier) 566–603.

Man'kovsky, V. (2012). Spectral contributions of the components of seawater to the beam attenuation coefficient in surface waters of the mediterranean sea. *Phys. Oceanography* 21, 305–319. doi: 10.1007/s11110-012-9124-z

Mu, W., Liu, J., and Zhang, H. (2018). The first complete mitochondrial genome of the mariana trench freyastera benthophila (asteroidea: Brisingida: Brisingidae) allows insights into the deep-sea adaptive evolution of brisingida. *Ecol. Evol.* 8, 10673–10686. doi: 10.1002/ece3.4427

Mullen, A. D., Treibitz, T., Roberts, P. L., Kelly, E. L., Horwitz, R., Smith, J. E., et al. (2016). Underwater microscopy for *in situ* studies of benthic ecosystems. *Nat. Commun.* 7, 1–9. doi: 10.1038/ncomms12093

Murray, J. M., Meadows, A., and Meadows, P. S. (2002). Biogeomorphological implications of microscale interactions between sediment geotechnics and marine benthos: a review. *Geomorphology* 47, 15–30. doi: 10.1016/S0169-555X(02)00138-1

Nguyen, T. T., Zakem, E. J., Ebrahimi, A., Schwartzman, J., Caglar, T., Amarnath, K., et al. (2022). Microbes contribute to setting the ocean carbon flux by altering the fate of sinking particulates. *Nat. Commun.* 13, 1–9. doi: 10.1038/s41467-022-29297-2

NOAA (2022) *Data from: Noaa ocean exploration benthic deepwater animal identification guide*. Available at: http://oceanexplorer.noaa.gov/okeanos/animalguide/animalguide.html

Optotune (2022) *Data from: Optotune el-10-30 datasheet*. Available at: https://www.optotune.com/el-10-30-c-lens

Schechner, Y. Y., and Karpel, N. (2005). Recovery of underwater visibility and structure by polarization analysis. *IEEE J. Oceanic Eng.* 30, 570–587. doi: 10.1109/JOE.2005.850871

Smith, C. R., Mincks, S., and DeMaster, D. J. (2008). The foodbancs project: introduction and sinking fluxes of organic carbon, chlorophyll-a and phytodetritus on the western antarctic peninsula continental shelf. *Deep Sea Res. Part II: Topical Stud. Oceanography* 55, 2404–2414. doi: 10.1016/j.dsr2.2008.06.001

Sogin, M. L., Morrison, H. G., Huber, J. A., Welch, D. M., Huse, S. M., Neal, P. R., et al. (2006). Microbial diversity in the deep sea and the underexplored "rare biosphere". *Proc. Natl. Acad. Sci.* 103, 12115–12120. doi: 10.1073/pnas.0605127103

frontiers | Frontiers in Marine Science

TYPE Original Research
PUBLISHED 21 October 2022
DOI 10.3389/fmars.2022.1028052

OPEN ACCESS

EDITED BY
Yuan Lin,
Zhejiang University, China

REVIEWED BY
Paul Yancey,
Whitman College, United States
Junichi Miyazaki,
Japan Agency for Marine-Earth Science and Technology (JAMSTEC), Japan
Haocai Huang,
Zhejiang University, China

*CORRESPONDENCE
Yongping Jin
jinyongping@hnust.edu.cn

SPECIALTY SECTION
This article was submitted to Ocean Observation, a section of the journal Frontiers in Marine Science

RECEIVED 25 August 2022
ACCEPTED 10 October 2022
PUBLISHED 21 October 2022

CITATION
Liu G, Jin Y, Peng Y, Liu D and Wan B (2022) A novel active deep-sea low-damage pressure-retaining organisms sampler.
Front. Mar. Sci. 9:1028052.
doi: 10.3389/fmars.2022.1028052

A novel active deep-sea low-damage pressure-retaining organisms sampler

Guangping Liu, Yongping Jin*, Youduo Peng, Deshun Liu and Buyan Wan

National-Local Joint Engineering Laboratory of Marine Mineral Resources Exploration Equipment and Safety Technology, Hunan University of Science and Technology, Xiangtan Hunan, China

Capturing less damaged organisms samples is the basis for research on the biological communities, living environments, biological life compositions, and biological tissue structures of organisms livinin the deep seabed. The hadal snailfish is pressure-tolerant, cold-tolerant, and easily damaged. This research used a hydraulic suction macro-biological pressure-retaining sampler (HSMPS) to capture less damaged hadal snailfish samples *via* pumping. As the hadal snailfish is sucked into the macro-organism pressure-maintaining sampler, it inevitably collides with the suction pipe in the diversion area (SPDA) and the inner wall of the pressure-maintaining cylinder in the pressure-maintaining area (PCPA). Therefore, a finite element analysis model of a hadal snailfish with a real geometric shape was constructed by obtaining the material mechanical properties of different parts of the fish on the seabed through static compression tests, and the dynamic modeling and response analysis of the hadal snailfish during the capture process was carried out. Moreover, the dynamic response changes of the stress, strain and acceleration of various tissues and organs of the hadal snailfish during the capture process were determined, thereby providing technical support for the research and development of marine biological sampling equipment.

KEYWORDS

deep sea environment, pressure-retaining sampling, low-damage sampling, dynamic response analysis, Hadal snailfish

Introduction

There are many kinds of biological resources and new biological species in the abyss. Obtaining active samples from the abyss is the premise of scientific research on its environmental changes, life evolution process, macro-organism species distribution, and living conditions. (Jamieson et al., 2010; Ramirez-Llodra et al., 2010; Clark et al., 2016). The deep seabed is characterized by ultra-high pressure and low temperatures; thus, current biological samplers complete the process of collecting benthic organisms in the

abyss and then returning to the surface. Due to the influence of the decrease of the external pressure and the increase of the external temperature of the biological sampler, the collected organisms are killed, which has a significant impact on the proper research of the living conditions of the organisms in this seabed area and the seabed environment (Caron et al., 2015; Edgcomb et al., 2016; Feng et al., 2020).

The hadal snailfish is considered to be the deepest-dwelling vertebrate on earth. Its living environment is extreme and is characterized by high hydrostatic pressure, low temperatures, hypoxia, and high salt. Thus, the hadal snailfish is characterized by pressure resistance, temperature resistance, and easy damage. Some scholars have researched deep-sea pressure and heat preservation sampling, but there has been no report on the dynamic response analysis of deep-sea organisms during the sampling process. However, the dynamic responses of the tissues and organs of deep-sea organisms during the sampling process are the key factors affecting biological activity (Billings et al., 2017; Garel et al., 2019; Peoples et al., 2019; Wang et al., 2020). Because the hadal snailfish lives in the extreme environment of the deep sea, its dynamic response during the capture process cannot be analyzed in a laboratory. The development of advanced numerical and computational techniques makes it possible to perform the dynamic response analysis of the hadal snailfish during its capture. Compared with the experimental method, the numerical method provides a more cost-effective approach to obtaining the eventual outcomes, as well as the behaviors, of different tissues and organs of the hadal snailfish and has been widely used in the study of fish collision problems. As shown in Figure 1, the Fendouzhe manned submersible was carried on the Tan Suo Yi Hao scientific research ship to catch hadal snailfish on the seabed at a depth of 7,731 m. Because there is no pressure-retaining device in this sampling process, the hadal snailfish cannot survive in the recovery process of the sampler. The head of the hadal snailfish sample we caught this time showed signs of injuries, but it was not sure whether these injuries affected the survival of the hadal snailfish. However, Gerringer et al. (2017) pointed out that the pores on the head of hadal snailfish are easily damaged or lost during sampling and recovery and that the fragile skin has been damaged to the extent that the temporal cephalic pores are lost, making it impossible to determine which genus a specimen should be assigned.

For deep-sea organisms sampling, samplers are mainly mounted on remotely operated vehicles and submersibles to collect samples of interest by passive trapping. In deep-sea organisms' low damage sampling, Billings et al. (2017) developed a SyPRID sampler, which operated at a depth of 6000m, using perforated ultra-high molecular weight (UHMW) plastic tubes, supporting a fine mesh in the outer carbon composite tube (tube in tube design), and installing an axial flow pump at the end of the capture filter. They completed sampling at 2160m on the seafloor. With the increasing demand for deep-sea organisms sampling, Phillips et al. (2019) developed a soft robotic arm to protect vulnerable deep-sea organisms samples by controlling a wearable glove gripper (made of materials compatible with the soft and fragile nature of marine organisms) to perform sampling operations in 2300 m water depth. Vogt et al. (2018) used additive manufacturing of flexible materials to obtain a flexible palm grip, improving the operational stability of the soft manipulator by adding interactive "nails" to the soft fingertips for flexible gripping of samples on rigid substrates. At present, organisms sampling for

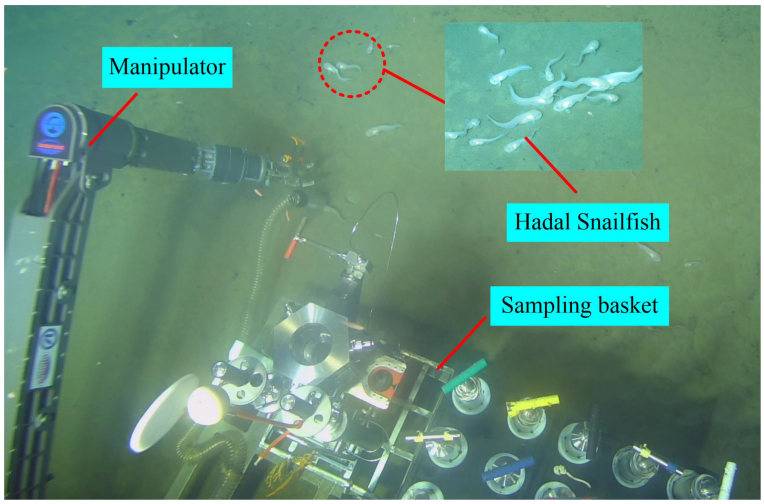

FIGURE 1
Fendouzhe manned submersible catches hadal snailfish.

the seafloor above 3000 m is done using samplers, and although much work has been done on pressure-retaining, the dynamic response of organisms during sampling has not been reported. However, some gelatinous fish are in the deep-sea environment, and it is easy to damage them during the collection process. Marine biologists have tried to catch megafaunal organisms without damaging them for decades, using traditional hard-bodied robotic hands or claws. However, it has only been applied at a depth of about 2000m on the seafloor, can only catch organisms with weak mobility, and is not designed to retain pressure, which is an essential factor affecting the activity of deep-sea organisms. Therefore, we propose a low-damage Pressure-retaining organisms sampling method to meet the demand for high-quality organisms samples for marine scientific research.

This work is based on a hydraulic suction macro-biological pressure sampler (HSMPS), in which a suction pump generates negative pressure to capture benthic organisms. Taking the hadal snailfish as the research object, according to its scanning and anatomical data, a finite element model of the hadal snailfish with real geometry was constructed. The dynamic modeling and response analysis of the capture process of the hadal snailfish were carried out, and the dynamic response changes of the stress, strainand acceleration of various tissues and organs during the capture process were determined. The findings provide technical support for the structural design of deep-sea biological sampling equipment and the life evolution of deep-sea biological communities.

Hydraulic suction macro-biological pressure sampler

Deep-sea organisms live in the high-pressure and low-temperature environment of the seabed for a long time. To obtain *in-situ* biological samples from the seabed, it is necessary to develop a set of marine biological equipment. Marine biological sampling equipment currently solves the problems of pressure and heat preservation, but there is no research on the dynamic response of the deep-sea biological capture process. Some soft and highly fragile organisms live in the deep sea, and it is easy for the sampler to cause damage to these organisms in the sampling process. Therefore, this paper designs a deep-sea low-damage and pressure-keeping biological sampler.

The structure of HSMPS is shown in Figure 2, which includes three parts: diversion area, pressure-maintaining area and pumping area. HSMPS can be carried on manned or unmanned submersibles for operation. The suction pump in the pumping area generates negative pressure, so that the fish-water mixture enters the pressure-maintaining area through the diversion area. The pressure-maintaining area is provided with a

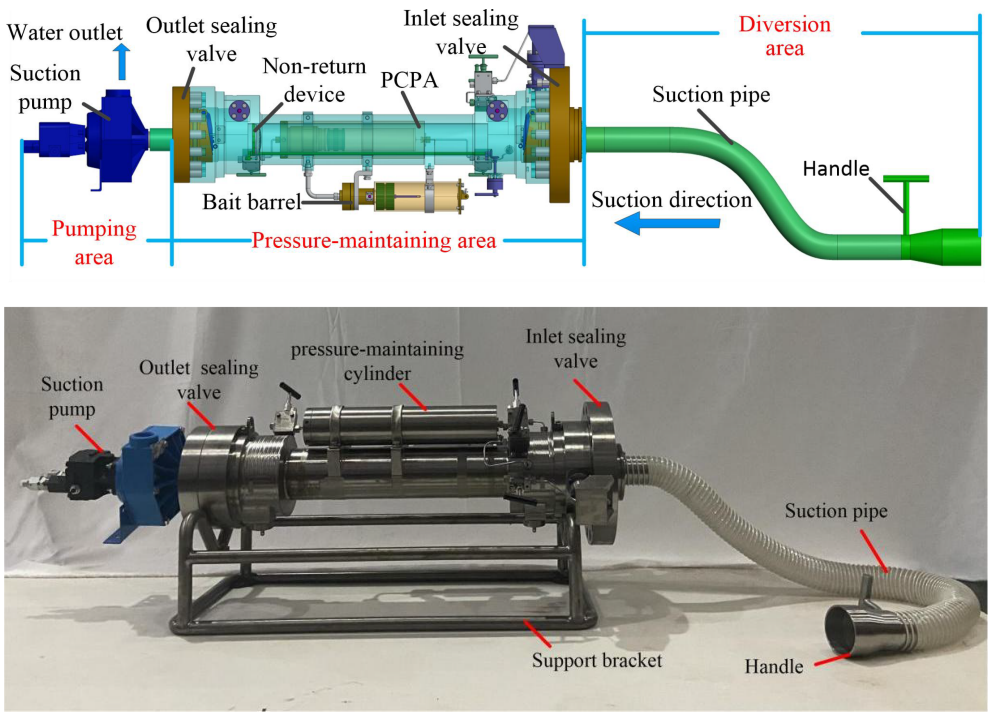

FIGURE 2
Structure of HSMPS.

check valve to prevent the hadal snailfish from being sucked into the pumping area. The pressure-maintaining area includes a pressure-maintaining cylinder, a pressure compensator and a bait cylinder. The function of the pressure-maintaining cylinder is to provide a high-pressure environment for deep-sea organisms. The pressure-maintaining cylinder can bear the pressure of 110MPa, and is made of TC4 titanium alloy, which has the characteristics of high strength, light weight and corrosion resistance. The inner diameter of the pressure-maintaining cylinder is 68mm and the length is 526 mm. During the recovery process of the sampler, the pressure difference between inside and outside will cause the deformation of the pressure-maintaining cylinder, which will lead to the pressure change in the pressure-maintaining cylinder. The function of the pressure compensator is to compensate the pressure drop caused by the expansion and deformation of the pressure-maintaining cylinder. The purpose of bait is to provide nutrients for deep-sea organisms. We will wrap a layer of thermal insulation material on the outer wall of the pressure-maintaining cylinder, so as to prevent the temperature change from affecting the deep-sea organisms in the recovery process of the sampler. The diversion area includes a suction pipe and a handle, the suction pipe is a flexible hose, the suction pipe is connected with the handle through a clamp, and the submarine operator can manipulate the manipulator to grab the handle to capture the benthic organisms, and the inner wall of the suction pipe is made of rubber material. The pump suction area includes a suction pump and a hydraulic pipeline. The suction pump is connected with the hydraulic source on the submersible through the hydraulic pipeline, and the flow rate of the suction pump can be adjusted. Xu et al. (2018) pointed out that when the flow rate of the suction pump is higher than the limit flow rate of fish, the fish can't continue to swim upstream, but the limit flow rate of fish is in the range of 0.6m/s ~ 1.2m/s. However, the excessive suction flow of the suction pump can easily cause damage to the deep-sea organisms, while the too small suction flow can't suck the deep-sea organisms. Therefore, the maximum suction flow of the suction pump is 18m^3/h.

The work of HSMPS is divided into three processes: lowering, capturing, and recycling and the work process of HSMPS is shown in Figure 3. Deep-sea organisms inevitably collide with the suction tube in the diversion area (SPDA) and the inner wall of the pressure-maintaining cylinder in the pressure-maintaining area (PCPA) during the process of being captured, which is very likely to cause damage to deep-sea organisms during the collision. Therefore, we take the hadal snailfish, a species unique to the abyss, as the research object and carry out the dynamics modeling and response analysis of the

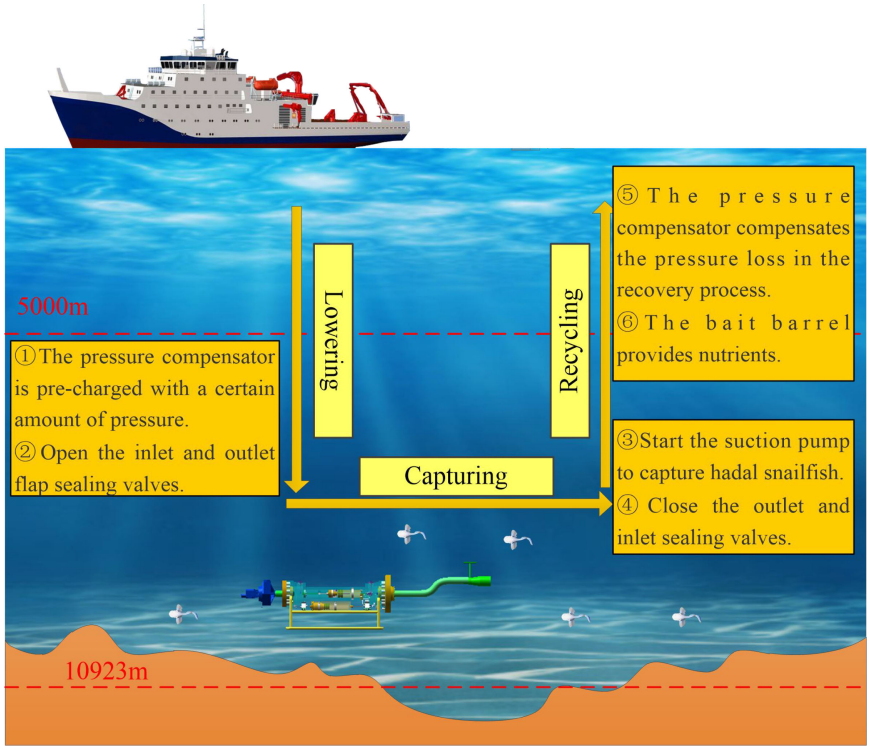

FIGURE 3
Working process of HSMPS.

capture process of the hadal snailfish by establishing the finite element analysis model of the hadal snailfish to determine the dynamic response changes of stress, strain, and acceleration of each tissue and organ of the hadal snailfish during the capture process.

Materials and models

Three-dimensional model of the hadal snailfish

As shown in Figure 4, the model construction of the hadal snailfish was divided into the following four steps: entity data acquisition, 3D model construction, point cloud data processing, and precise surface processing.

Entity data acquisition

According to the scanning and anatomical data of the hadal snailfish, the distribution and geometric data of its various tissues and organs were obtained, as shown in Figures 4A, B. The hadal snailfish sample was captured by the manned submersible Fendouzhe at a depth of 7,731 m in the Western Philippine Basin. Hadal snailfish tissues and organs are composed of bone tissue and soft tissue, among which the bone tissue includes the skull, frontal bone, vertebrae, and fins, while the soft tissue includes the gills, liver, stomach, eggs, back muscles, and skin. The body of the hadal snailfish is elongated with a length between 160 and 200 mm, and the widest part of the body is 45 mm. The front part of the body is sub-cylindrical, the back part is gradually flat and narrow, and the outline of the body has symmetrical geometry. The skin is only a very thin layer of membrane; thus, the physiological tissues in the hadal

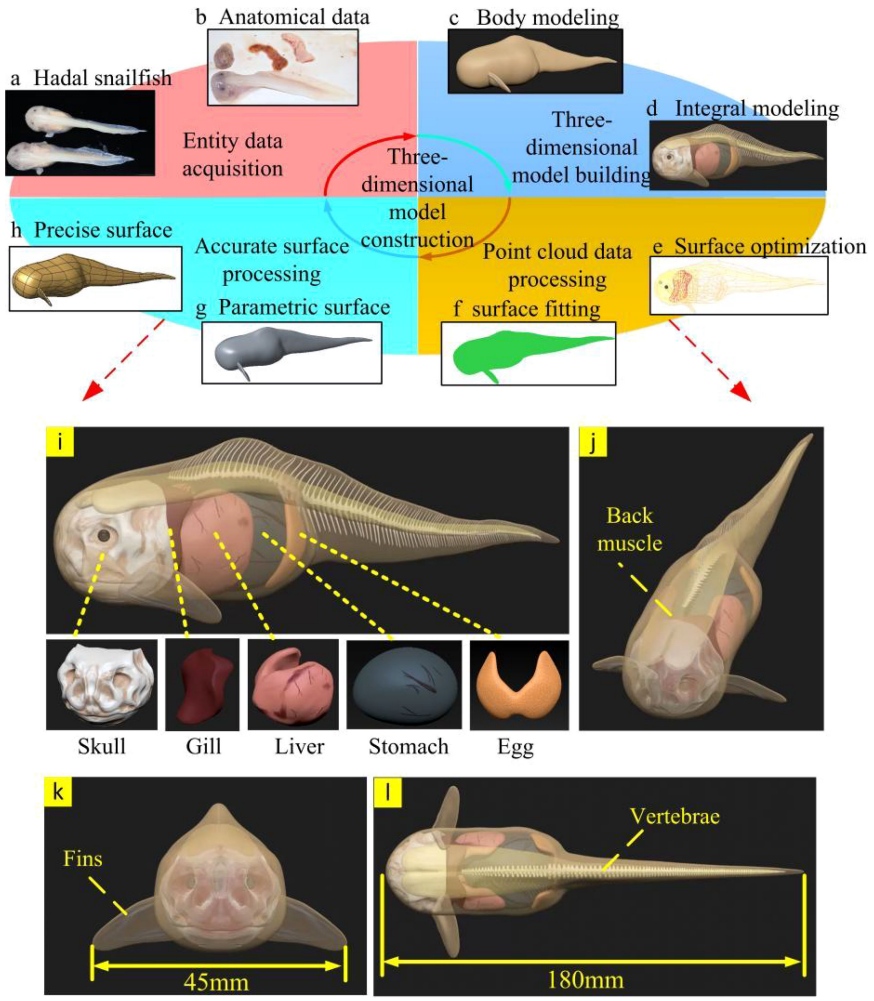

FIGURE 4
Modeling process and structure of tissues and organs of hadal snailfish **(A–H)** construction of a 3D model of hadal snailfish; **(I)** tissue and organ distribution of hadal snailfish; **(J–L)** three views of hadal snailfish.

snailfish can fill with water, the internal and external pressure can be balanced, and there are no scales. The skull of the hadal snailfish, which is wide and flat, is located directly in front of the body, and the skull is not completely closed. To adapt to the high-pressure environment, its bones are very thin and have the ability to bend. The fins of the hadal snailfish are symmetrically distributed on both sides of the body, its gills are located behind the skull, its liver is adjacent to the gills, and behind the liver is the swollen stomach. *Via* anatomical observation, a large number of crustaceans with relatively complete shapes have been found in the stomach contents of hadal snailfish, and its eggs are located behind the stomach. The back muscles and vertebrae are located above the body (Yancey et al., 2014; Linley et al., 2016; Gerringer et al., 2017; Linley et al., 2017; Wang et al., 2019; Orr, 2020).

Three-dimensional model building

Polygon and curved surface modeling are used for most three-dimensional biological modeling. However, these two modeling methods cannot show the details of complex biological models (Nie et al., 2020). ZBrush is a three-dimensional digital engraving software with powerful polygon data processing ability, and can process the details of complex curved surfaces. Therefore, ZBrush software was used to build a three-dimensional model of the hadal snailfish and its different tissues and organs. First, the main outline of the hadal snailfish body was established. The hadal snailfish was 180 mm long and 45 mm wide with a skin thickness of 1 mm. Then, according to the anatomical and scanning data of the hadal snailfish, the contour shapes of different tissues and organs were constructed, converted into a polygonal grid, and subjected to multi-stage subdivision, and the structures of various tissues and organs were more accurately carved out. Finally, the models of different tissues and organs were assembled to generate a three-dimensional model of the hadal snailfish (Figures 4C, D).

Point cloud data processing

Because the generated 3D model of the hadal snailfish had some irregular surfaces, it would have affected the grid division, increased the calculation time, and reduced the calculation efficiency. Therefore, to ensure the anatomical geometric model, the point cloud data of each tissue and organ model of the hadal snailfish obtained from ZBrush was processed by Geomagic studio software (Figures 4E, F).

Accurate surface processing

First, the point cloud was transformed into a polygon that could be manipulated and edited by an accurate surface. Contour lines were then manually built and edited, surface patches were built and repaired, and more contour lines in complex areas of the surface were controlled to ensure the integrity of the surface and make it easier to select mesh nodes during subsequent mesh division. It was checked whether there were any intersections or incorrect parts of the curved surfaces, and modifications ere made accordingly. Finally, the grating was constructed and the curved surface was fitted to obtain the solid geometric model of the hadal snailfish (Figures 4G, H).

Quasi-static compression test

In this paper, we used *Harpadon nehereus* as the experimental sample, a near-benthic fish living within 50m of the seafloor. The *Harpadon nehereus* was first stored in a refrigerator at 4~6°C until the test was performed. The procedure of the quasi-static compression test is shown in Figure 5. Before testing, the *Harpadon nehereus* was removed from the refrigerator and placed in a water bath at room temperature of about 20°C for 10~15min to thaw. Thawed *Harpadon nehereus* heads, bodies, and tails are cut using stainless steel knives at room temperature. The specimen dimensions were measured after cutting, and the cut *Harpadon nehereus* specimens are shown in Figure 5A. A total of 27 specimens were obtained from different parts of the *Harpadon nehereus*, and three sets of tests were performed on different parts with loading rates of 25 mm/min, 50 mm/min, and 100 mm/min, and all experiments were done at room temperature (16-25°C). The experiments were repeated three times for the same part at the same speed to reduce the experimental error. Quasi-static compression test on different parts of fish using electronic universal tensile tester CMT-5105GL. The strain rate at each loading rate varies from 0.039-0.069 s-1, 0.079-0.117 s-1, and 0.145-0.235 s-1 due to the difference in the original spacing of each test sample, and the average value of the test data is taken as the test result at the loading rate, as shown in Figure 5B.

The fish stress-strain curve obtained from the quasi-static compression test is shown in Figure 6. In quasi-static compression experiments, by comparing the stress-strain relationships of soft tissue materials at three different strain rates, it was found that each material exhibited different degrees of strain rate effects, where the stresses in the head and tail at higher strain rates were greater than those at lower strain rates, while the stresses in the fish body at higher strain rates were less than those at lower strain rates, due to the more homogeneous and homogeneous tissue (fewer bones) in the fish body compared to the fish head, and thus the fish tissue was less resistant to compression under high strain rate conditions. The average values under each group of loading rates were calculated and summarized in Table 1. It can be seen that the elastic modulus, strength, and ultimate stress of the fish tail are greater than the values of the fish head and body, due to more fat and softer tissues in the fish body; the fish head tissue is not uniform, with slightly hard bones and soft brain tissue, etc.; the fish tail usually swings more and has good muscle elasticity. By

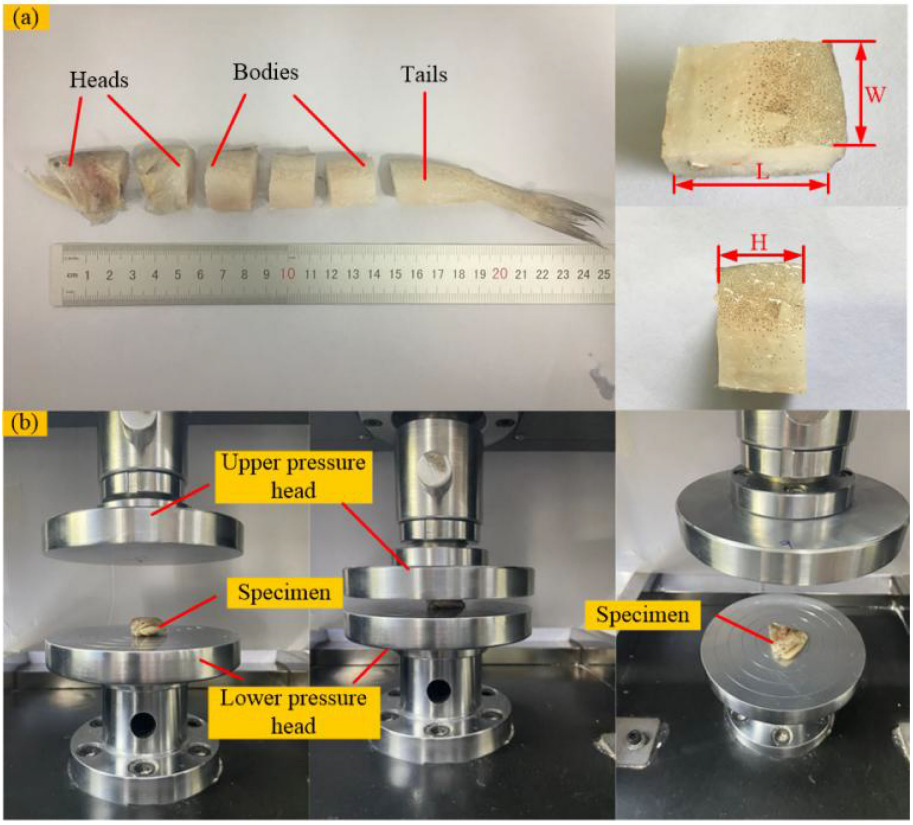

FIGURE 5
Quasi-static compression test **(A)** preparation of test samples of Harpadon nehereus; **(B)** quasi-static compression test of Harpadon nehereus.

comparing with the test results of Chen et al. (2011). and Zhou et al. (2010). the elastic modulus of the fish material obtained in this paper is smaller, with a difference of 0.5 MPa, which is also due to the relatively soft test sample.

Finite element model of the hadal snailfish

As a pre-processing step of the finite element analysis of the hadal snailfish, model meshing was conducted to obtain the finite element analysis model. HyperMesh software was used to mesh the tissues and organs of the hadal snailfish, and a tetrahedral mesh was used to ensure uniform meshing. When capturing the hadal snailfish with the HSMPS, the movement of the fins is complicated. In the simulation, the finite element model of the fins was removed, and the vertebrae were simplified into a spine. The finite element model construction of the hadal snailfish was divided into the following steps. The geometric simplification of the tissues and organs of the hadal snailfish was respectively carried out. Then, 2D grid division was respectively carried out, the quality of the grid was checked, the unqualified grid was readjusted and divided, and a 3D solid grid was finally generated. The resulting grid division of the hadal snailfish is presented in Figure 7 and had 69,203 nodes and 425,660 units. The tissues and organs of the hadal snailfish were connected by common nodes, and normal contact was set between them. The contact type of the tissues and organs was defined as Automatic_singel_surface, and the dynamic and static friction coefficients were both set to 0.2.

The main research objective of this study is the dynamic response of different tissues and organs of the hadal snailfish during collision. Therefore, the possible collision position of the hadal snailfish was simplified, and a flat plate was used instead. The dimensions of the rectangular plate were 68 × 68 × 10 mm (length × width × height). The initial position of the hadal snailfish was located in the center of the flat plate at a distance of 0.1 mm from the plate. The initial velocity of the hadal snailfish was considered to always be along the normal direction of the flat plate. The finite element model of the hadal snailfish colliding with the flat plate is shown in Figure 8. When sucking the hadal snailfish *via* the HSMPS, the pumping speed is very high, which easily causes serious damage to the fish. However, if the pumping speed is too low, the fish can actively swim against the current,

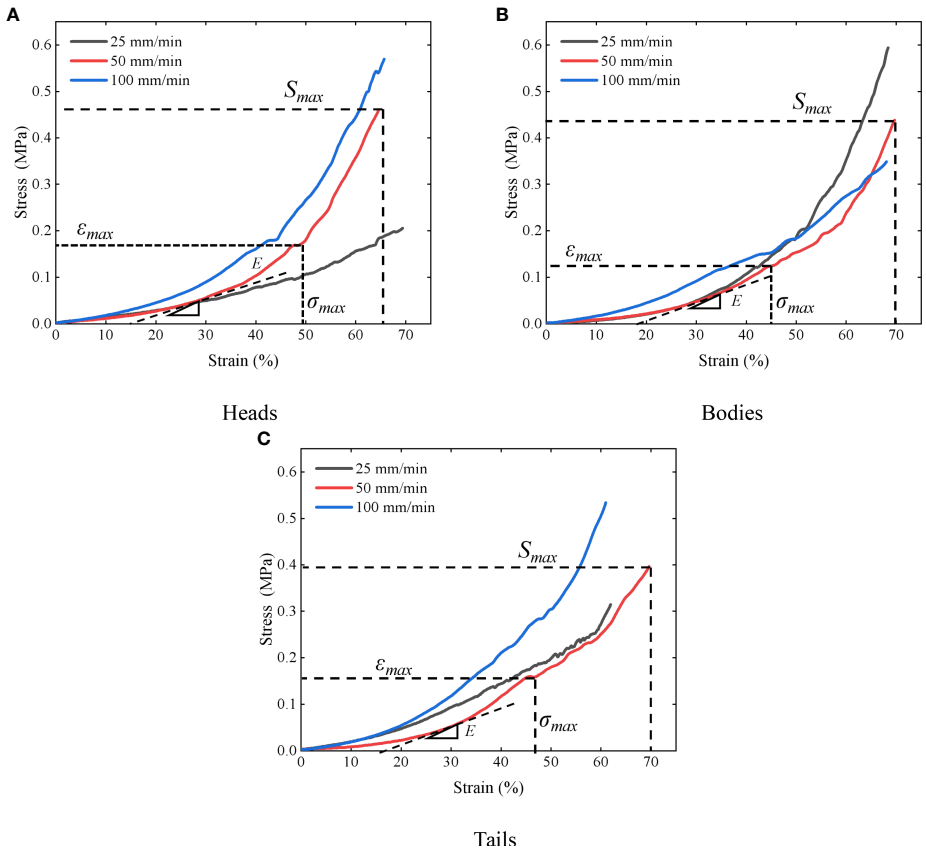

FIGURE 6
Stress-strain curves of different parts of the *Harpadon nehereus* **(A)** heads; **(B)** bodies; **(C)** tails.

resulting in the inability to capture the target. When the pumping speed is higher than the limit flow rate of the fish, the fish cannot continue to swim upstream, and the limit flow rate of the fish is in the range of 0.6-1.2 m/s (Long et al., 2016a, 2016b; Xu et al., 2018). In this study, four pump flows of 7.84 m^3/h (0.6 m/s), 10.45 m^3/h (0.8 m/s), 13.07 m^3/h (1.0 m/s), and 15.68 m^3/h (1.2 m/s) were selected to simulate and analyze the hadal snailfish collision process. The materials of the flat plates were defined as rubber material (SPDA, $\rho = 1.6$ g/cm^3, $E = 5$ MPa, $\mu = 0.47$) and titanium alloy material (PCPA, $\rho = 4.51$ g/cm^3, $E = 110000$ MPa, $\mu = 0.34$). The Lagrange method was used in the calculation of the collision of the hadal snailfish, and the penalty function method was used to solve the contact-collision algorithm. To more accurately obtain the acceleration of the hadal snailfish skull, five feature points on the skull were selected, and their positions were the front (a), top (b), right (c), bottom (d), and left (e). The motion, such as the movement and rotation of the upper and lower surfaces of the plate in three directions, was constrained to six degrees of freedom, and the simulation time was 10 ms. The contact between the hadal snailfish and the plate was defined as Automatic_surface_to_surface, and the friction coefficient was 0.2.

TABLE 1 Material parameters of different parts of the *Harpadon nehereus*.

Parts	Elastic modulus	Compressive strength	Ultimate stress	Ultimate Strain
Heads	0.61MPa	0.20	0.15MPa	46%
Bodies	0.58MPa	0.20	0.14MPa	43%
Tails	0.71MPa	0.28	0.18MPa	42%

Results and discussion

Simulation analysis of the collision process

The history curve of each response and time in the collision process is shown in Figure 9. Figure 9A presents the stress-time curve when the hadal snailfish collided with the PCPA at a speed

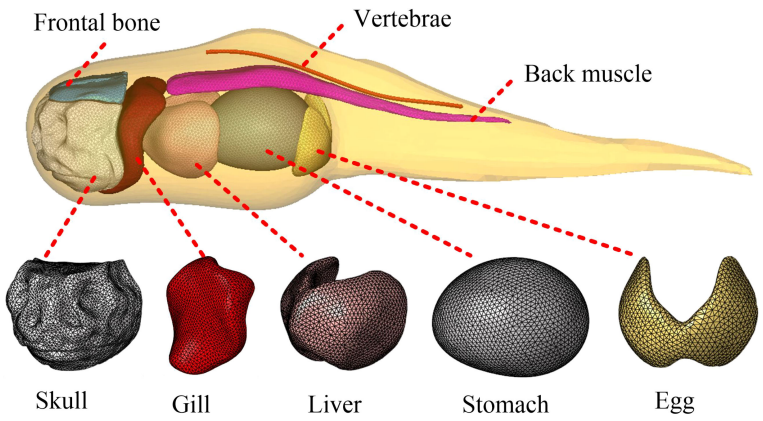

FIGURE 7
Finite element model of hadal snailfish.

of 1 m/s. The stress of the hadal snailfish began to increase after contacting the PCPA, and reached its peak at 1 ms. The stress of the hadal snailfish then gradually decreased from 1-2 ms, which was mainly because of the high rigidity of the PCPA and the rebound of the fish after contacting the PCPA. The stress tended to be stable from 2-10 ms until the end of collision. In the collision process, the maximum stress of hadal snailfish is greater than the ultimate stress ϵ_{max} and full compressive strength S_{max}.therefore, hadal snailfish in the collision PCPA easily cause damage. The strain-time curve is exhibited in Figure 9B. In the initial stage of collision, the hadal snailfish contacted the PCPA to produce deformation, and the strain increased with time. After 1 ms, the hadal snailfish began to rebound when its tissues and organs squeezed each other to produce stress fluctuations. The acceleration-time history curve of each characteristic point of the skull is shown in Figure 9C. In the initial stage of collision, the acceleration of the hadal snailfish skull reached its peak, namely 8*g*, after contacting the PCPA, after which the acceleration gradually decreased and finally tended to be stable. Sun et al. analyzed the process of a fish colliding with an axial pump. *Via* comparative analysis, the simulation results obtained in the present study were found to be basically consistent with the simulation and experimental results of Sun et al. (2020). This indicates that the finite element model

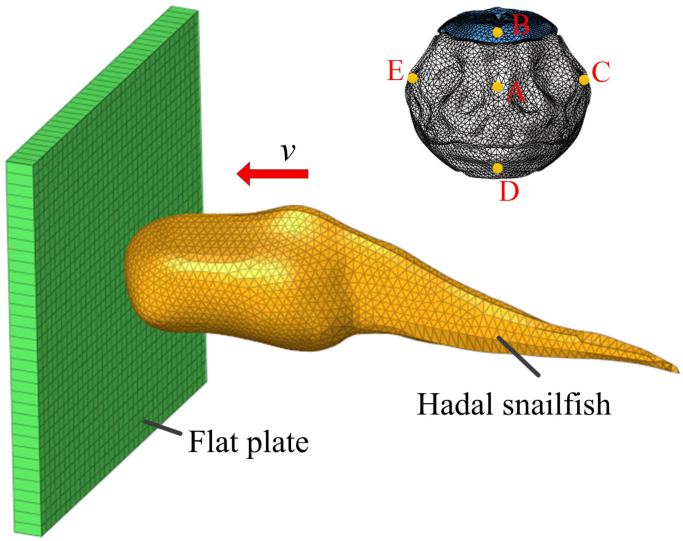

FIGURE 8
Simulation model of hadal snailfish collision.

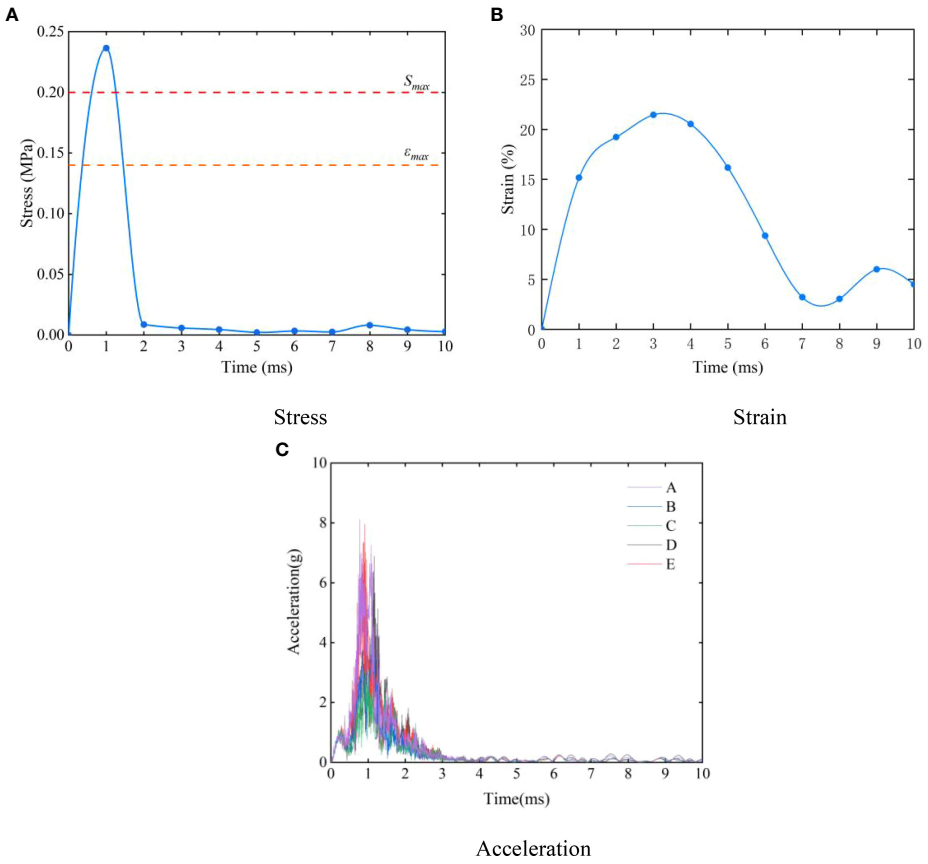

FIGURE 9
History curve of each response and time in collision process **(A)** stress; **(B)** strain; **(C)** acceleration.

of the hadal snailfish constructed in this study can better reflect the mechanical response of the hadal snailfish collision process.

Stress and strain distributions of organs

Figure 10 exhibits the distributions of stress and strain in different tissues and organs during the collision of the hadal snailfish with the PCPA at 1 m/s. Among the hadal snailfish bones, the stress of the skull was the highest, followed by that of the frontal bone, and the stress of the vertebrae was the lowest. The stress of the skull was found to be concentrated at the contact position between the skull and the PCPA, and the maximum stress was 0.236MPa,which was greater than the ultimate stress of the material. Therefore, the skull of the hadal snailfish was the most vulnerable to damage during collision. The stress of the frontal bone was concentrated in the second half of the collision, and the maximum stress was 0.097 MPa. The stress distributions of the skull and frontal bone are shown in Figure 10(a). The strain distributions of the soft tissue are shown in Figure 10(b). During the collision of the soft tissue of the hadal snailfish, the strain of the liver was the highest. Moreover, the strain was concentrated on both sides, mainly *via* the squeezing of the stomach and gills, and the maximum strain was 9.2%; this was found to be the most likely strain to cause damage during the collision. The strain of the stomach was concentrated on the left and right sides, and the maximum strain was 7.9%. The strain of the gills was concentrated in the middle position, and the maximum strain was 4.7%. The strain of the eggs was found to be the lowest with a maximum value of 2.3%. The eggs are located behind the fish body, and they were mainly strained by stomach squeezing. Therefore, the possibility of the eggs being damaged during collision was found to be the lowest.

Results of numerical analysis at the collision speed

The response curves of various tissues and organs at different collision speeds are shown in Figure 11. Figure 11A presents the maximum stress curve of the hadal snailfish during the process of colliding with the PCPA at different speeds. With the increase

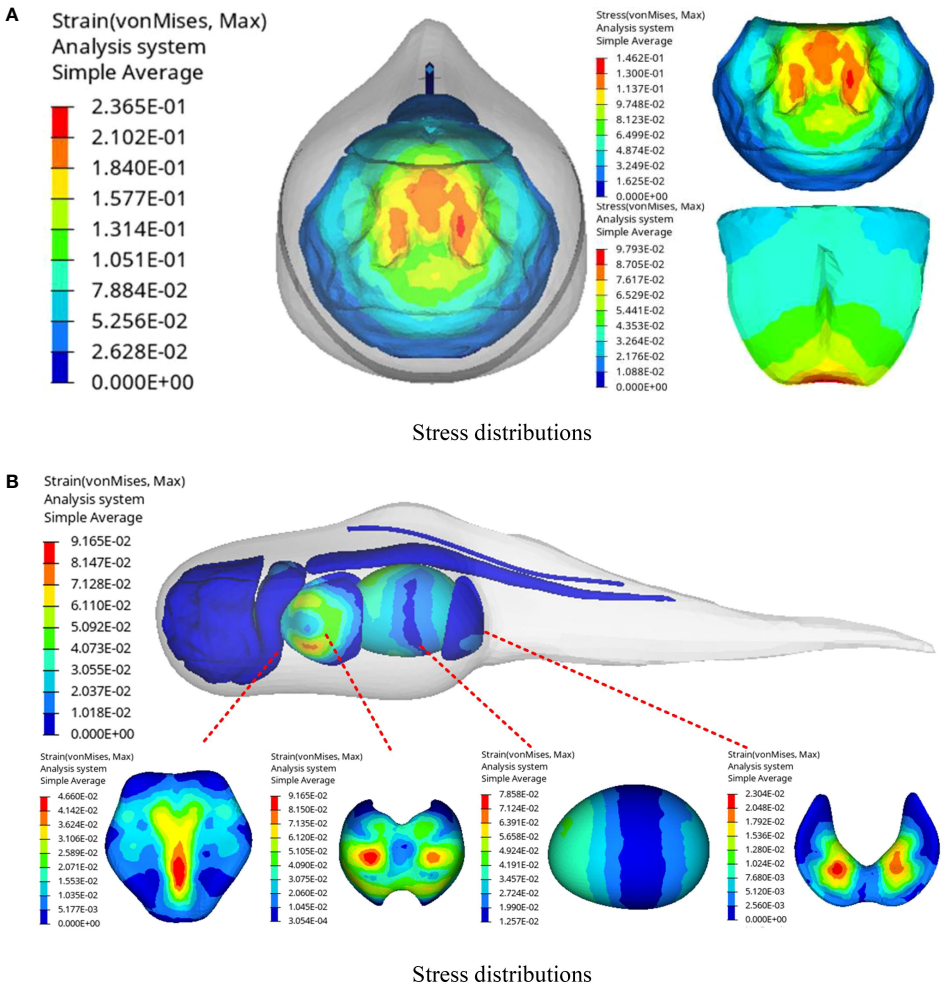

FIGURE 10
Stress and strain distribution of hadal snailfish during collision **(A)** stress distributions; **(B)** strain distributions.

of the speed, the stress of the skull, frontal bone, and vertebrae increased continuously. At the collision speed of 1.2 m/s, the maximum stress was 0.24 MPa, which was 1.2 times the stress at the collision speed of 0.6 m/s. Figure 11B shows the maximum strain curve of the hadal snailfish colliding with the PCPA at different speeds, from which it is evident that the strains of the liver and stomach were found to be higher. At the collision speed of 1.2 m/s, the maximum strain of the liver was 115%, which was 1.63 times the strain at the collision speed of 0.6 m/s. Figure 11C exhibits the acceleration of the skull when the hadal snailfish collided with the PCPA at different speeds. It can be seen from the figure that the acceleration of point A was the highest, mainly because point A was in direct contact with the PCPA during the collision of the skull. Moreover, the acceleration of point C was the same as that of point E, mainly because points C and E were symmetrically distributed on both sides of the skull, and the acceleration of point D was the lowest. At the collision speed of 1.2 m/s, the acceleration of point A was 12.4*g*, which was 3.35 times that at the collision speed of 0.6 m/s. The skull and liver of the hadal snail are easily damaged at high collision speeds. Therefore, while ensuring that the hadal snailfish can be sucked into the HSMPS, the flow rate of the suction pump should be reduced to the greatest extent.

Results of numerical analysis at the collision position

The response curves of various tissues and organs under different collision positions are shown in Figure 12. Figure 12A presents the stress curve of the skull when the hadal snailfish collided with different materials at a speed of 1 m/s. During the process of the hadal snailfish colliding with the PCPA, the stress of the skull reached the maximum at the initial stage of collision,

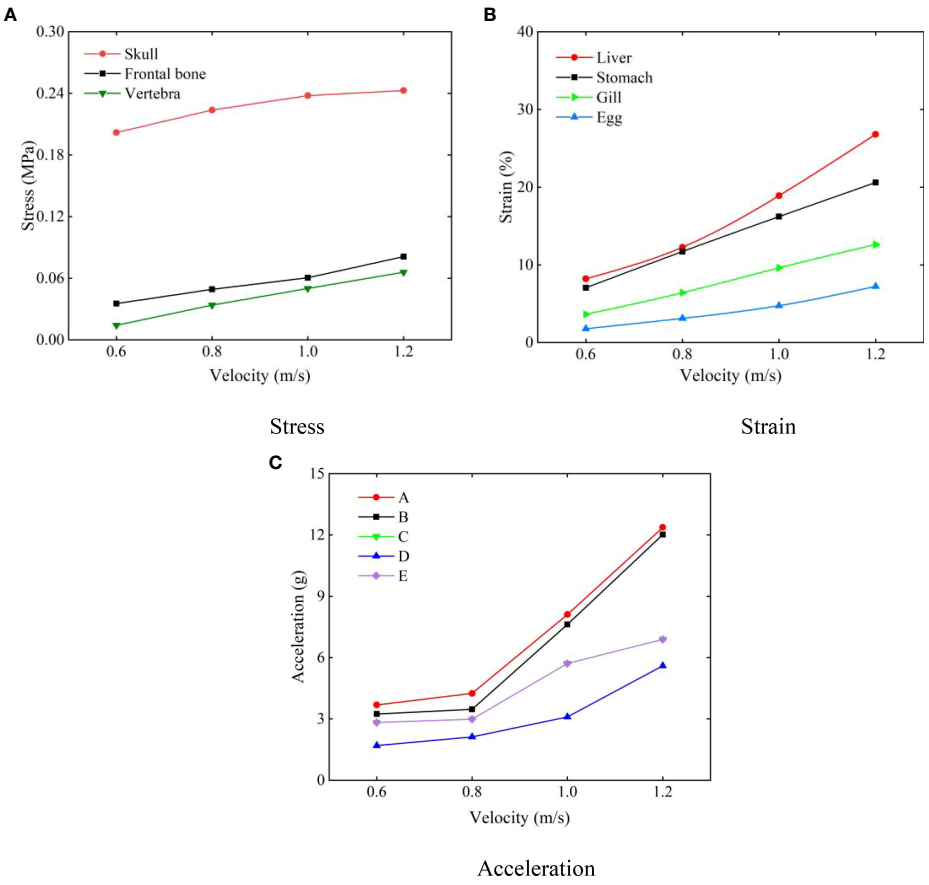

FIGURE 11
Response curves of various tissues and organs at different collision speeds **(A)** stress; **(B)** strain; **(C)** acceleration.

and then tended to be stable until the end of collision. During the process of the hadal snailfish colliding with the SPDA, the stress value of the skull reached the first peak at the initial stage of collision. With the continuation of time, the hadal snailfish continued to collide with the SPDA. Because the SPDA had elasticity, it was found to play a buffering role in the collision of the hadal snailfish, and the speed of the fish decreased. At this time, the maximum stress decreased with time. The hadal snailfish rebounded in 5 ms, and the stress reached the maximum value at this time. After that, the maximum stress of the skull decreased with the continuation of time until the end of collision. When the hadal snailfish collided with PCPA, the maximum stress of the skull was 2.95 times that when the fish collided with the SPDA. Figure 12B presents the strain curve of the liver when the hadal snailfish collided with different materials at a speed of 1 m/s. When the hadal snailfish collided with the PCPA, the stress of the liver fluctuated greatly, and the tissues and organs were squeezed violently during the collision. The maximum strain of the liver when colliding with the PCPA was 2.26 times that when colliding with the SPDA. Figure 12C shows the acceleration of the skull when the hadal snailfish collided with the SPDA at a speed of 1 m/s. When the hadal snailfish collided with PCPA, the acceleration at point A was 2.5 times that when it collided with the SPDA. The response values (stress, strain, acceleration) of different tissues and organs were high when the hadal snailfish collided with the PCPA. Therefore, to reduce the possibility of damage to the hadal snailfish during the suction process, a layer of buffer material can be coated on the inner wall of the HSMPS.

Figure 12 shows that deep-sea organisms are prone to collide with PCPA and cause damage during capture. To minimize the damage, we installed a layer of polyurethane open-cell foam (ρ = 1.05 g/cm^3, E = 8 MPa, μ = 0.47)in the PCPA. Figure 13 shows the stress-time curves when the hadal snailfish collided with PCPA at different velocities. When the hadal snailfish collided with PCPA at 1 m/s, the maximum stress value of the hadal snailfish was 0.148 MPa when there was foam material, while the stress value was 0.236 MPa when there was no foam material, and the stress value of the hadal snailfish was reduced. The maximum stress value of hadal snailfish is less than the

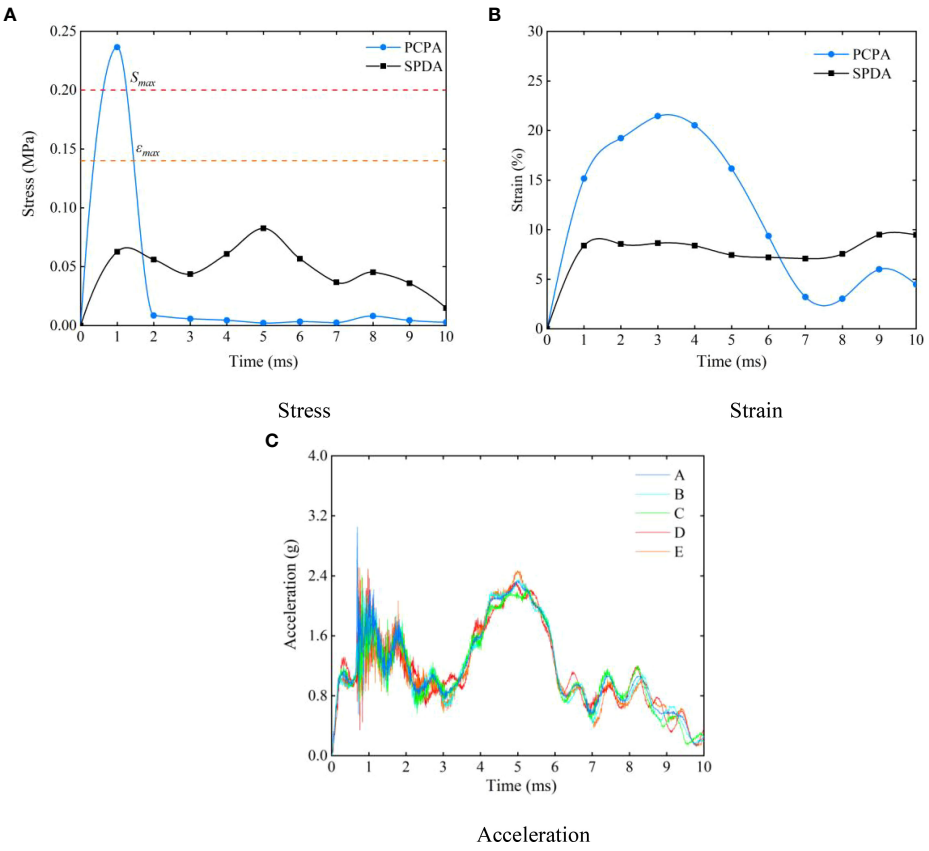

FIGURE 12
Response curves of various tissues and organs under different collision position **(A)** stress; **(B)** strain; **(C)** acceleration.

material's compressive strength. Still, when the collision speed is more significant than 0.8m/s, the maximum stress of hadal snailfish is greater than the ultimate stress of the material, and damage may occur when hadal snailfish collide with PCPA. Therefore, to capture deep-sea biological samples while reducing damage to marine organisms, the flow rate of the suction pump should be adjusted in the range of 131 L/min~174 L/min.

Conclusion and perspectives

Obtaining biological samples *in situ* in the deep sea has become a significant concern for the scientific community. At present, deep-sea biological samplers are mainly carried on landers or deep submersibles. The biological collection is carried out by passive trapping, which has a random nature and may not capture seafloor organisms in one dive. Therefore, we propose a pumping sampling method of deep-sea organisms, which realizes active sampling of deep-sea organisms by controlling the flow rate of the pump, designs a pressure compensation mechanism to compensate for the pressure drop in the recovery process of the sampler, and uses thermal insulation materials to realize the low-temperature environment inside the sampler.

Apart from collecting samples and maintaining them *in situ* conditions, we have also researched the low damage of the sampler capture process of deep-sea organisms. Due to the unique living environment of deep-sea organisms, the laboratory cannot analyze their dynamic response during capture. Therefore, we established a three-dimensional model of deep-sea gelatinous fish and performed quasi-static compression tests on different parts of the seafloor gelatinous fish to obtain a numerical analysis model of marine gelatinous fish, which can be used for impact biomechanics, biomedical and bionomics applications.

We analyzed the influence of different structural parameters of the HSMPS on the tissues and organs of gelatinous fish. The results showed that when gelatinous fish collided with PCPA, the stress of the skull was greater than the ultimate stress and compressive strength of the material, and gelatinous fish might be damaged. We installed a layer of polyurethane open-cell foam in PCPA. The analysis shows that polyurethane open-cell foam can effectively reduce the stress value of gelatinous fish during a collision. When

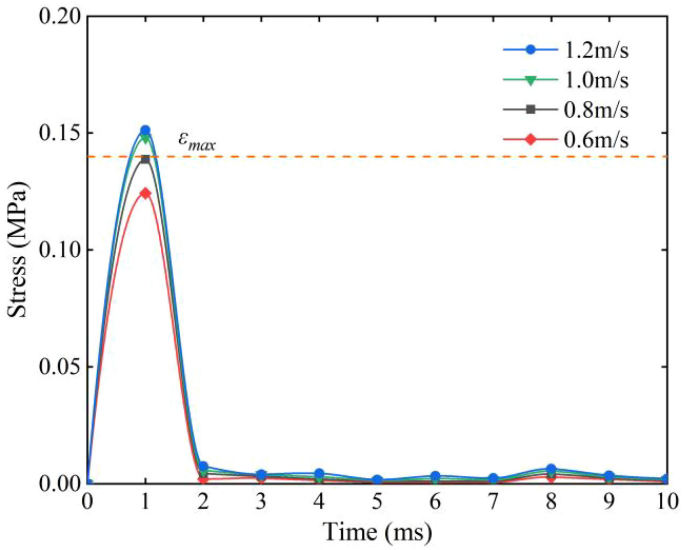

FIGURE 13
Response curves of deep-sea organisms at different collision speeds.

the collision speed of gelatinous fish is less than 0.8m/s, the stress of their skulls is less than the material's ultimate stress and compressive strength. Therefore, we control the pump's flow rate in the range of 131 L/min to 174 L/min to balance the biological damage and escape speed in the deep sea.

The pressure retention and insulation tests proposed in this study have been verified in the laboratory. In our future research, we will design a deep-sea biological sampling-transfer-culture system to put biological samples from deep-sea *in situ* into laboratory culture and analyze the influencing factors affecting marine biological activity to reveal the patterns of different factors on marine biological activity.

Data availability statement

The raw data supporting the conclusions of this article will be made available by the authors, without undue reservation.

Author contributions

GL and YJ wrote the initial draft and coordinated the drafting of the paper, and participated in the experimental design. YP, DL, and BW provided ideas on manuscript writing. All authors contributed to the article and approved the submitted version.

Funding

This work was supported by the National Key Research and Development Program of China (Grant No. 2016YFC0300502) and Postgraduate Scientific Research Innovation Project of Hunan Province (Grant No. CX20210985). It was also supported by Special project for the construction of innovative provinces in Hunan (Grant No. 2020GK1021, 2019SK2271, 2019GK1010, 2019GK1012).

Conflict of interest

The authors declare that the research was conducted in the absence of any commercial or financial relationships that could be construed as a potential conflict of interest.

Publisher's note

All claims expressed in this article are solely those of the authors and do not necessarily represent those of their affiliated organizations, or those of the publisher, the editors and the reviewers. Any product that may be evaluated in this article, or claim that may be made by its manufacturer, is not guaranteed or endorsed by the publisher.

References

Billings, A., Kaiser, C., Young, C. M., Hiebert, L. S., Cole, E., Wagner, J. K., et al. (2017). SyPRID sampler: A large-volume, high-resolution, autonomous, deep-ocean precision plankton sampling system. *Deep Sea Res. Part II: Topical Stud. Oceanog* 137, 297–306. doi: 10.1016/j.dsr2.2016.05.007

Caron, J., Price, J. S., and Rochefort, L. (2015). Physical properties of organic soil: Adapting mineral soil concepts to horticultural growing media and histosol characterization. *Vadose Zone J.* 14 (6), 369–379. doi: 10.2136/vzj2014.10.0146

Chen, M., Jia, L. B., and Yin, X. Z. (2011). Relaxation modulus of caudal fin studied by fractional zener model. *Chin. J. Theor. Appl. Mechanics.* 43 (1), 217–220. doi: 10.6052/0459-1879-2011-1-lxxb2010-145

Clark, M. R., Consalvey, M., and Rowden, A. A. (2016). *Biological sampling in the deep sea* (New Jersey: John Wiley & Sons, Inc).

Edgcomb, V. P., Taylor, C., Pachiadaki, M. G., Honjo, S., Engstrom, I, and Yakimov, M.. (2016). Comparison of Niskin vs. *in situ* approaches for analysis of gene expression in deep Mediterranean Sea water samples. Deep-sea research, Part II. *Topical studies in oceanography* 129, 213–222. doi: 0.1016/j.dsr2.2014.10.020

Feng, J. C., Liang, J. Z., Zhang, S., Yang, Z.F., and Zhu, Z.C.. (2020). Development of deep-Sea biological resources exploitation equipment. *Strategic Study CAE.* 22 (6), 67–75. doi: 10.15302/J-SSCAE-2020.06.009

Garel, M., Bonin, P., Martini, S., Guasco, S., Roumagnac, M., Bhairy, N., et al. (2019). Pressure-retaining sampler and high-pressure systems to study deep-sea microbes under *in situ* conditions. *Front. Microbiol.* 10, 453. doi: 10.3389/fmicb.2019.00453

Gerringer, M. E., Drazen, J. C., Linley, T. D., Summers, A. P., Jamieson, A. J., and Yancey, P. H.. (2017). Distribution, composition and functions of gelatinous tissues in deep-sea fishes. *R. Soc. Open Science.* 4 (12), 171063. doi: 10.1098/rsos.171063

Jamieson, A. J., Fujii, T., Mayor, D. J., Solan, M., and Priede, I. G.. (2010). Hadal trenches: the ecology of the deepest places on earth. *Trends Ecol. Evolution.* 25 (3), 190–197. doi: 10.1016/j.tree.2009.09.009

Linley, T. D., Gerringer, M. E., Yancey, P. H., Drazen, J. C., Weinstock, C. L., and Jamieson, A. J.. (2016). Fishes of the hadal zone including new species, *in situ* observations and depth records of liparidae. *Deep sea Res. Part I: oceanog Res. papers.* 114, 99–110. doi: 10.1016/j.dsr.2016.05.003

Linley, T. D., Lavaleye, M., Maiorano, P., Bergman, M., Capezzuto, F., Cousins, N. J., et al. (2017). Effects of cold-water corals on fish diversity and density (European continental margin: Arctic, NE Atlantic and Mediterranean sea): Data from three baited lander systems. *Deep Sea Res. Part II: Topical Stud. Oceanog* 145, 8–21. doi: 10.1016/j.dsr2.2015.12.003

Long, X., Xu, M., Lyu, Q., and Zou, J. (2016a). Impact of the internal flow in a jet fish pump on the fish. *Ocean Engineering.* 126 (nov.1), 313–320. doi: 10.1016/j.oceaneng.2016.09.027

Long, X., Zhang, J., Wang, Q., Xiao, L., Xu, M., Lyu, Q., et al. (2016b). Experimental investigation on the performance of jet pump cavitation reactor at different area ratios. *Exp. Thermal Fluid Science.* 78, 309–321. doi: 10.1016/j.expthermflusci.2016.06.018

Nie, F. Y., Xie, H., and Li, P. (2020). Research on digitalization method of 3D entity based on zbrush technology. *Comput. Inf. Technol* 28 (06), 16–17. doi: 10.19414/j.cnki.1005-1228.2020.06.006

Orr, J. W. (2020). A new snailfish of the genus careproctus (Cottiformes: Liparidae) from the Beaufort Sea. *Copeia.* 108 (4), 815–819. doi: 10.1643/CI2020089

Peoples, L. M., Norenberg, M., Price, D., McGoldrick, M., Novotny, M., Bochdansky, A., et al. (2019). A full-ocean-depth rated modular lander and pressure-retaining sampler capable of collecting hadal-endemic microbes under *in situ* conditions. *Deep Sea Res. Part I: Oceanog Res. Papers.* 143, 50–57. doi: 10.1016/j.dsr.2018.11.010

Phillips, B. T., Becker, K. P., Kurumaya, S., Galloway, K. C., Whittredge, G., Vogt, D. M., et al. (2019). A dexterous, glove-based teleoperable low-power soft robotic arm for delicate deep-sea biological exploration. *Sci. Rep.* 8 (1), 1–9. doi: 10.1038/s41598-018-33138-y

Ramirez-Llodra, E., Brandt, A., Danovaro, R., De Mol, B., Escobar, E., German, C. R., et al. (2010). Deep, diverse and definitely different: unique attributes of the world's largest ecosystem. *Biogeosciences.* 7 (9), 2851–2899. doi: 10.5194/bg-7-2851-2010

Sun, Z. K., Pan, Q., Zhang, D.S., and Shi, W.D. (2020). *Research on fish damage mechanism of axial flow pump based on CFD-DEM coupling method* (Jiangsu university). doi: 10.16076/j.cnki.cjhd.2020.05.011

Sun, Z. K., Pan, Q., Zhang, D. S., et al. (2020). Study on fish damage mechanism in axial-flow pump based on the CFD-DEM coupling method. *Chin. J. Hydrodynamics.* 35 (5), 631–639.

Vogt, D. M., Becker, K. P., Phillips, B. T., Graule, M. A., Rotjan, R. D., Shank, T. M., et al. (2018). Shipboard design and fabrication of custom 3D-printed soft robotic manipulators for the investigation of delicate deep-sea organisms. *PloS One* 13 (8), e0200386. doi: 10.1371/journal.pone.0200386

Wang, H., Chen, J., Wang, Y., Fang, J., and Fang, Y.. (2020). Research and analysis of pressure-maintaining trapping instrument for macro-organisms in hadal trenches. *J. Mar. Sci. Engineering.* 8 (8), 596. doi: 10.3390/jmse8080596

Wang, K., Shen, Y., Yang, Y., Gan, X., Liu, G., Hu, K., et al. (2019). Morphology and genome of a snailfish from the Mariana trench provide insights into deep-sea adaptation. *Nat. Ecol. evolution.* 3 (5), 823–833. doi: 10.1038/s41559-019-0864-8

Xu, M. S., Yang, X. L., Long, X. P., Lyu, Q., and Ji, B. (2018). Numerical investigation of turbulent flow coherent structures in annular jet pumps using the LES method. *Sci. China Technolog Sci.* 61 (1), 86–97. doi: 10.1007/s11431-017-9047-8

Yancey, P. H., Gerringer, M. E., Drazen, J. C., Rowden, A. A., and Jamieson, A.. (2014). Marine fish may be biochemically constrained from inhabiting the deepest ocean depths. *Proc. Natl. Acad. Sci.* 111 (12), 4461–4465. doi: 10.1073/pnas.1322003111

Zhou, M., Yin, X. Z., and Tong, B. G. (2010). Study of skin and muscle mechanical properties of crucian carp (Carassius auratus). *J. Exp. Mechanics.* 25 (5), 536–545. doi: 10.3788/HPLPB20102208.1731

frontiers | Frontiers in Marine Science

TYPE Review
PUBLISHED 23 November 2022
DOI 10.3389/fmars.2022.1071940

OPEN ACCESS

EDITED BY
Simone Marini,
National Research Council (CNR), Italy

REVIEWED BY
Atmanand M. A.
Indian Institute of Technology Madras, India
Wang Minxiao,
Institute of Oceanology (CAS), China
Haocai Huang,
Zhejiang University, China

*CORRESPONDENCE
Jiawang Chen
arwang@zju.edu.cn

SPECIALTY SECTION
This article was submitted to Ocean Observation, a section of the journal Frontiers in Marine Science

RECEIVED 17 October 2022
ACCEPTED 02 November 2022
PUBLISHED 23 November 2022

CITATION
Wang H, Chen J, Zhou Q, Hu X, Gao Q, Guo J, Wang Y and Li H (2022) Isobaric sampling apparatus and key techniques for deep sea macro-organisms: A brief review. *Front. Mar. Sci.* 9:1071940. doi: 10.3389/fmars.2022.1071940

Isobaric sampling apparatus and key techniques for deep sea macro-organisms: A brief review

Hao Wang, Jiawang Chen *, Qixiao Zhou, Xiaohui Hu, Qiaoling Gao, Jin Guo, Ying Wang and Haonan Li

Ocean College, Zhejiang University, Zhoushan, China

The study of deep-sea fauna is one of the essential themes of marine scientific research. For all that, the biology of deep animals remains largely unknown, such as their behaviors, metabolic characteristics, and mechanisms of adaptation to the deep-sea environment. Obtaining samples in good condition is an essential prerequisite for these investigations. The isobaric samplers were created to keep the organisms as much as possible in the *in-situ* environment during recovery. This report reviews the history and the application of isobaric samplers for deep-sea animals established by researchers worldwide over the past hundred years. Also, the crucial technologies of isobaric samplers are analyzed and summarized, including pressure compensation, insulation, sealing, etc. Finally, prospects for the future development of isobaric sampling technologies from the aspects of high fidelity, function integration, and real-time communication and integration operation. This review can provide a reference for future design and optimization of fidelity samplers for deep-sea animals.

KEYWORDS

isobaric sampling, deep-sea animals, pressure compensation, insulation, sealing

1 Introduction

The deep-sea habitats are characterized by low temperature, high pressure, darkness, and oligotrophy. Despite the harsh environment, the deep sea is still the most biodiverse region on earth (Thurber et al., 2014; Gooday et al., 2020). The systematic study of biological resources and biodiversity of deep-sea ecosystems is of great scientific importance for mankind to reveal the origin of life and the unique environmental adaptation mechanisms of deep-sea organisms (Sandulli et al., 2021). The investigation of deep-sea habitats began in the late 19th century. In the last hundred years, the development of deep-sea exploration techniques and many exciting discoveries have

stimulated worldwide interest in the deep-sea ecosystem (Ramirez-Llodra et al., 2010). Up to the present, our understanding of deep-sea ecosystems is still very limited compared to the complex studies conducted on shallow-sea ecosystems (Jamieson, 2018), which is mainly due to the deficiencies in observation and sampling techniques (Jamieson et al., 2009).

There are currently two methods for conducting experiments on deep-sea bio physiology, i. e., laboratory and *in-situ* methods. Laboratory research entails capturing, recovering and maintaining the macro-organisms. The *in-situ* method deploys scientific instruments to the seafloor to directly observe organisms and measure some physiological parameters. The fact is that both methods have unavoidable limitations, and we cannot claim that either method is superior. Limitations of the laboratory method include the apparent effects in the process of capturing; increased temperature and reduced pressure during recovery (Garel et al., 2019); the influence of artificial light on the animals accustomed to dark environments; restriction of organisms to a container after capture, and the abnormal movement during recovery (e.g., stochastic swaying and vibration) etc. (Smith and Brown, 1983). The *in-situ* method has less impact on the creatures but still does not avoid the effects of the capture process and artificial light sources. The disadvantage of the *in-situ* method is that the availability and complexity of observations and experiments are severely restricted (Smith and Baldwin, 1997).

Nevertheless, both methods have a wide range of applications. *In-situ* methods such as baited cameras are deployed on a lander to reach the seafloor, where a camera records photos or videos of the activity of organisms attracted by the baits (e.g., Cappo et al., 2006; Phillips et al., 2019; Giddens et al., 2021; Jamieson et al., 2021). Towed cameras are mounted on the cables of research vessels to observe organisms at large geographic scales (e.g., Jones et al., 2009; Lembke et al., 2017; Purser et al., 2018). Seafloor Observatories (e.g., White et al., 2003; Favali and Beranzoli, 2009; Aguzzi et al., 2011; Aguzzi et al., 2015) can be deployed on the seafloor for an extended period for continuous observations. Their purpose is to provide scientists with valuable opportunities to study multiple interrelated processes on long-time scales and to conduct comparative studies of processes in different regions (Clark et al., 2016).

Here, we focus on the equipment used to capture and recover organisms. In the past, people have used tools including trawls (e.g. Fanelli et al., 2018; Bosley et al., 2020; De Mendonça and Metaxas, 2021), longlines (e.g. Crespo et al., 2018; Pinho et al., 2020; Prohaska et al., 2021), sledges (Lins and Brandt, 2020; Jóźwiak et al., 2020; Linse and Anderson, 2021), and grabs (e.g. Mortensen et al., 2000; Murton et al., 2012; Przeslawski et al., 2018) to collect animals from the deep sea. Unfortunately, these sampling methods usually cause mechanical damage to organisms and cannot recover organisms while keeping *in-situ* pressure and temperature. With the development of materials science and submersible technology, some innovative, flexible tools can be used to capture animals on the seafloor with the assistance of submersibles without any mechanical damage. However, these apparatuses still do not take adequate measures to maintain the ambient pressure and temperature during recovery (Teoh et al., 2018; Vogt et al., 2018). However, many animals in deep sea could be easily affected by depressurization, such as loss of muscle coordination, abnormal gene expression, destruction of some protein structures, and impairment of enzyme functions (Somero, 1992). The piezophilic megafauna tends to be irreversibly damaged (Fang et al., 2010). Chen et al. (2021) evaluated the response of isobaric and unpressurized samples of deep-sea mussels and their symbionts to depressurization stresses. The results show that depressurization leads to intense DNA fragmentation. This phenomenon was also observed in tubeworms recovered at atmosphere pressure (Dixon et al., 2002). Yan et al. (2022) confirmed the extensive transcriptomic variations in response to pressure during unpressurized sampling. These studies suggest the necessity of pressurized sampling in deep-sea biology studies. It is necessary to take specific measures to isolate the sample container's environment from the external environment during recovery. Isobaric samplers are built for this purpose.

In this review, we first introduce the typical isobaric samplers established for deep-sea animals. Secondly, we analyze the critical technologies of isobaric sampling, including pressure compensation, sealing, insulation, etc. Finally, we summarize the difficulties of isobaric sampling technology and prospect its future development.

2 Development and application of isobaric sampler

The working procedure of deep-sea macro organisms' samplers could be divided into the following four stages:

1. The sampler is deployed from the scientific research ship to the depths.
2. Capture organisms at depths.
3. Close the entrance of animals and seal the pressure vessel.
4. Ascent to the surface, retaining the *in-situ* pressure.

There are many ways to classify these samplers, for example, in terms of deployment methods, whether lowered by a cable on the ship, carried by a submersible, or deployed as a free-fall vehicle. The deployment methods determine the choices of energy supply, communication, control and recovery technologies, etc. From another perspective, how does a sampler capture animal? Is it by a pump, a hook, or baited

trap? The capture method depends on the target species, which determines the structural design of the sampler. In this section, we introduce the typical isobaric samplers in the timeline of the establishment time.

Macdonald and Gilchrist (1969) proposed the first deep-sea animal pressure-retaining sampler (here, we call it the recovery apparatus) (Figure 1). The sampler was built to obtain plankton by filtration at different depths and recover them to the sea surface with constant pressure. The recovery apparatus was connected to the experiment apparatus, and plankton was transferred into the experiment vessel with low-pressure fluctuations. With the optical and polarographic components equipped on the experimental apparatus, the scientist are allowed to study the respiration, activity and survival of plankton. The weight of the recovery apparatus is 180kg, consisting of a stainless-steel pressure vessel (inner diameter, 5.08cm, length, 55.8cm), a global valve (diameter, 2.54cm), a hydraulic accumulator, a depth recorder and pressure transducer. The recovery apparatus is connected to the coring wire on the ship and deployed to the specified depth. The ball valve closed on the seabed by a messenger-actuated device triggering an extension spring coupled to the valve spindle. In November 1968, the prototype of the recovery apparatus was field tested at depths of 1400m and 2000m. The recovered pressures were equal to or greater than (possibly due to temperature rising) the pressure at the sampling depth in all four trials.

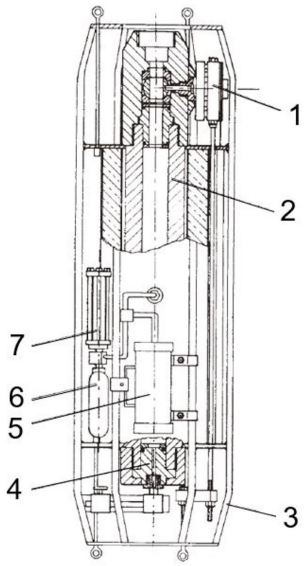

FIGURE 1
Schematic diagram of the recovery apparatus (1: Globe valve;2: recovery pressure vessel;3: frame;4: plug;5: depth recorder;6: hydraulic accumulator;7: pressure transducer housing) (adapted from Macdonald and Gilchrist, 1969).

Brown (1975) established a pressure fish trap to capture deep-sea fish. The pressure vessel of the sampler was made of polyethylene (inner diameter, 30cm, length, 2m) (Figure 2). A trap door that closed inside was used to seal the pressure vessel. The sampler is deployed to the seabed as a free vehicle, the upper plate is connected to a float on the sea surface, and the lower plate is connected to a disposable ballast. The trigger mechanism of the trap door is an elastic cord with a bait at the end. Once the

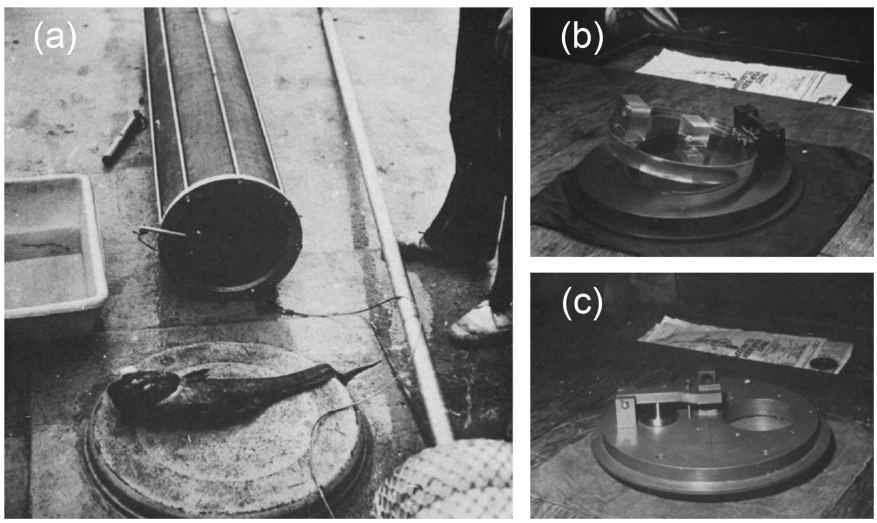

FIGURE 2
Photos of pressure fish trap. **(A)** Fish trap with grenadier or rattail about 60cm long caught in trap at depth of 1200m. **(B)** Pressure fish trap, internal door bottom, lower end plate. **(C)** Pressure fish trap, upper end plate with access port and air vent valve.) (adapted from Brown, 1975).

cord is subjected to a pull of more than 1kg, a pull of 15kg is generated on the cord to pull the fish in, and the door closes. Due to limitations of the material, the pressure fish trap was equipped with a pressure-release valve with a set pressure of 6 atm (0.6 MPa). The sampler successfully obtained pressure-retained live fish samples at a depth of 1200m.

(Yayanos, 1977; Yayanos, 1978; Yayanos, 2009) reported a novel sampler PRAT (pressure-retaining amphipod trap) (Figure 3). The device weighs 21.8kg in air and 16.4kg in water. The system was also deployed as a free vehicle. The disposable ballast is connected to the bottom of a release device, and the top of the release device is connected to the sampling piston through an extension spring. The sampling piston keeps the passage open under the gravity of the ballast. A timer event triggers the release device. After the disposable ballast is released, the sampling piston blocks the passage and the O-rings at both ends of the piston seal the vessel. There are two windows for observation on the side wall. A piston gas accumulator and a "water jacket" insulation sleeve are used to reduce pressure and temperature changes. Different from traditional pressure vessels, the pressure retaining chamber of PRAT is a 24.1×24.1×8.26cm square vessel made of titanium alloy. In June 1977, PRAT was deployed four times at a depth of 5741 to 6049m, and the pressure retaining rate was between 66.3% to 95%. In November 1980, PRAT obtained a living sample of amphipods in the Mariana Trench at a depth of 10900m, with a recovery pressure of 102.6MPa, which was the first time in the world to obtain a living animal in the Mariana Trench.

Macdonald and Gilchrist (1978) reported a novel sampler for amphipods (here we call it the High-pressure Trap) (Figure 4). The High-pressure Trap is a baited benthic trap, which was established to minimize the damage caused by trapping amphipods. The High-pressure Trap includes a globe valve (diameter 2.5cm), a pressure vessel made of stainless steel (diameter over 7.5cm), an enclosing water jacket, a conical plastic window and a hydraulic accumulator. Before a cast of the trap, the pressure vessel was pressurized to a pressure equal to that of operation depth, and then the spindle of the ball valve was connected to the extensible drawbar at the end of the cable. During a deployment to the seafloor, the globe valve is closed due to tension on the cable. After arriving at the seabed, the tension on the cable disappeared, and the globe valve was opened by an extension spring coupled to the spindle of the globe valve. In the same way, when recovering, the tensile force on the cable will close the globe valve again. During the Challenger cruise in 1976, High-pressure Trap was field tested three times at a depth of 1300m and obtained some *tmetonym* cicada. The pressure drop does not exceed 4.3% after recovery.

Phleger et al. (1979) built a hyperbaric fish trap to study the structure and function of biofilms of deep-sea fish when they are swimming (Figure 5). The pressure vessel of the sampler is made of aluminum alloy and contains a flap door for sealing. A piston accumulator was used to compensate for the pressure loss. A plexiglass window is installed on the end plate of the trapper, and a chemiluminescent element is installed inside it, so as to better observe the movement of animals in the trapper. The sampler includes a pressure relief valve with a set pressure of 2250 psi (15.5 MPa) for security. Hyperbaric fish trap reaches the seabed as a free vehicle. On the seafloor, fish were captured in two ways. One is to use a long rope to attract fish, and the hook is connected to a spring in the cabin. When the fish bites the hook, it will trigger a series of events, including the ballast releasing, the spring pulling the fish in, and the flap valve closing. The second is to coat the trapping mechanism near the entrance with chemiluminescent substances to attract fish. The hyperbaric fish trap successfully captured two fishes at 750 m and 1200 m.

The accumulator system of the hyperbaric trap-aquarium includes a nitrogen cylinder, a pressure-reducing regulator and a

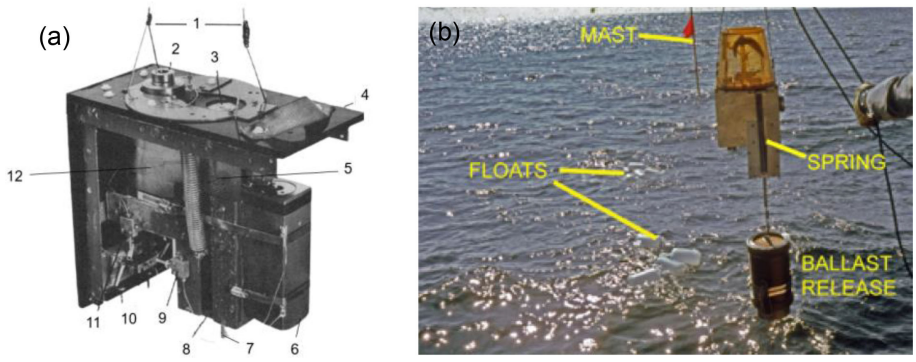

FIGURE 3
Photos of PRAT **(A)** detailed structure of PRAT. 1: The cable connected to the floats;2: Window;3: The piston end;4: Insulating box;5: Springs;6: Accumulator;7: The rod connected to the ballast;8: The stop of piston;9: Valve for charging of nitrogen;10 and 11: Valves connected to high-pressure seawater circulating system; 12: the trap body; **(B)** field test of PRAT (adapted from Yayanos, 1978; Yayanos, 2009).

piston accumulator. The nitrogen cylinder can deliver nitrogen gas to the piston accumulator according to the pressure setting of the pressure relief valve. The pressure vessel was covered with nine layers of pipe-wrapping tape to slow the temperature rise. Unlike other flap-closing mechanisms, the door of this system closes from the outside. Triggered closing action by Derlin burn-wire release, the spring closes the doors at the two ends for sealing. From September 1984 to January 1985, the device was deployed 49 times at depths of 1115m to 1241m, but with only 12 complete operations. The pressure retaining rate was between 13% to 95%.

(Koyama et al., 2002; Koyama, 2010) established a pressure-stat aquarium system for isobaric recovery and maintenance of deep-sea organisms (Figure 7). The sampler consists of a spherical pressure vessel made of stainless steel (outer diameter, 36cm, inner diameter, 34cm) with three round holes in the side wall for installing windows made of acrylic resin. The device weighs 52kg in air and 44kg in water, and the practical volume is 20L. The spherical vessel withstands a maximum internal pressure of 30MPa. A pressure control valve with a set pressure of 20MPa is installed for safety. A gas-filled bladder compensator is installed inside to reduce the pressure drop. The outside of the vessel is covered with an insulating layer. The device was deployed by the ROV to a specific depth and pumped the organisms into the pressure vessel through an inhalation apparatus mounted on the ROV. Then the manipulator of the ROV pulls out the limit pin of the sealing door installed in the chamber, and the compression spring pushes the doors to the inner wall to seal the vessel. In December 2001, the pressure-stat aquarium system captured a deep-sea fish at a depth of 1171m, and the pressure retaining rate was 84%.

Drazen et al. (2005) established a hyperbaric trap respirometer for measuring the breath rate, pressure tolerance and metabolic of fish that respond to different environments (Figure 8). The device consists of a pressure vessel made of 17-4 PH stainless steel (inner diameter, 30.5cm, length, 122cm), thermal insulation (2 layers of 2.5cm thick high-strength foam), and a pre-charged piston accumulator. At the same time, a light-emitting diode, a circulation pump and a camera were installed in the chamber. This device has a total weight of approximately 680kg and is deployed as a free vehicle. The external hook is connected to a high-strength elastic cord coupled with a coil spring when working on the seabed. A fish bite will trigger a sequence of events. First, the coil spring rotates to release the limitation of the flap valve, and the spring slowly pulls the fish into the vessel and closes the flap valve. A hydraulic damper is used to prevent mechanical damage to organisms. The sampler was deployed 7 times at depths of 1430-1500 m, with pressure retaining rates between 93% and 95%.

Shillito et al. (2008) proposed a sampler device PERISCOPE, which is mounted on a submersible (Figure 9). The manipulator on the submersible holds the sampling tube, which is connected to a suction instrument to capture animals. After organisms are sucked into the sampling tube, the submersible places the sampling tube into the pressurized recovery device (PRD). Different from the traditional gas accumulator, the PRD system adopts the high-pressure liquid pressure compensation technology, which can adjust the pressure in real time. In August 2006, PERISCOPE carried out 8 deployments in hydrothermal areas and successfully retained pressure 6 times. The maximum deployment depth in this voyage is 2290m, and the pressure retaining rate is 82%-111%. In 2012, the PERISCOPE sampler took four operations at 2500m and obtained 70 worms with a pressure retaining rate between 68% and 91% (Ravaux et al., 2013).

The pressure vessel is made of 304 stainless steel (inner diameter, 500mm, length, 615mm). A drum in the pressure chamber is divided into three equal parts. Two chambers had no

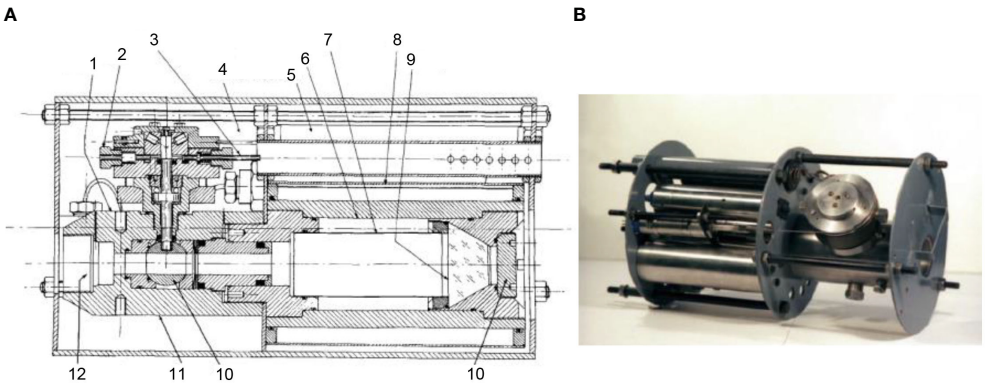

FIGURE 4
Schematic diagram and photo of High-pressure Trap **(A)**: 1: Valve;2: Stop;3: Trigger;4,5: Thermal Insulation;6: Bait chamber;7: Sample chamber;8: Water jacket;9: Viewing window;10: End plate;11: Globe vlave;12: Globe valve body;13: Entrance **(B)** Photo of High-pressure Trap [adapted from Macdonald and Gilchrist, 1978; Macdonald, (2021)].

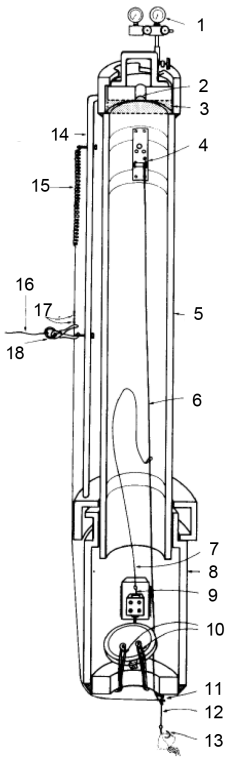

FIGURE 5
Cross section of hyperbaric fish trap (1:Pressure gauges; 2: Window to view fish; 3:Plexiglass; 4:Negator spring(pulls fish in- and closes door after tugging fish releases ballast); 5:Main Al tube; 6:Line between negator spring and fish hook; 7:Line to pin; 8:Large Al tube; 9:Pin; 10:Shock cords to close door; 11:Loops; 12:Taut wire inserted in small hole in end plate; 13:Baited hook; 14:Handling bracket; 15:Spring; 16:Line to baited strings and ballast weights; 17:crimps; 18:Fish-triggered release)(adapted from Phleger et al., 1979) Wilson and Smith (1985) established a hyperbaric trap-aquarium (Figure 6). The device contains an aluminum pressure vessel (inner diameter, 22.9cm, outer diameter, 26.7cm) with an adequate volume of 41.7L.

side walls and were used to place baits. Another chamber has a third cylindrical side wall for sealing. When it closes, the motor drives the drum to rotate, and the side wall of the drum presses the inner wall of the pressure vessel to form a self-tight seal. In addition, there are 4 cylinders with compression springs designed to reduce friction when rotating, providing an initial force to compress the sealing ring. (Wang et al., 2020; Wang et al., 2022) proposed a pressure-retaining trapping instrument (PMTI) that can be applied to the full-ocean depth (Figure 10). The sampler adopts a novel sampling structure, the hollow piston, which automatically forms a seal after sampling, avoiding the design of an additional closing device. This sampler weighs 61.4kg in water, including a pressure vessel made of titanium alloy TC4 (inner diameter, 80mm, outer diameter, 124mm), a piston pressure compensator, a transmission mechanism and an *in-situ* pressurization mechanism. The sampler adopts a semi-active pressure compensation method. After the sampling operation, pure water (about 4.7ml) in a small piston cylinder is injected into the pressure vessel to improve the pressure retaining rate. In August 2021, it was field tested in the China Ocean Scientific Expedition voyage TS-21 and performed four deployments, two of which successfully captured 174 amphipods, and the pressure retaining rate is between 82.7%-84.5%.

This section introduces almost all the typical isobaric samplers for macro organisms. For over one hundred years, people have kept enhancing the isobaric samplers, and we summarize their development trends as follows: (1) The application depth of isobaric samplers is getting deeper, and some of them can operate at full ocean depth. (2) The early pressure-retaining samplers could only collect samples. However, now the samplers are multifunctional, such as measuring some basic biochemical parameters and maintaining the life of organisms for experimental purposes. (3) The development of submersible technology allows us to complete refined sampling operations at specific locations. Compared with the operation of earlier samplers, submersible-equipped samplers tend to have a higher sampling success rate. At the same time, diverse technologies have been integrated and applied to deep-sea biological sampling, such as semi-active and active pressure compensation and insulation technologies, various sealing components, etc. We summarize the technologies applied in these samplers (Table 1) and expect them to be useful to designers.

3 Key techniques

3.1 Pressure compensation technology

The pressure in the vessel reduces during its ascent from the seabed to the surface due to many factors such as metal expansion, seal movement and leakage, etc. To improve the pressure retaining rate, we need to take a practical approach to reduce the pressure drop. Pressure compensation technologies can be divided into three types, passive, semi-active and active. Passive pressure compensation technology uses high-pressure gas to compensate for the pressure loss. Semi-active and active compensation technologies do not rely on pressurized gas entirely but some other methods to improve the pressure in the vessel. There are two ways to increase the pressure in a vessel. One is to compress the volume of the vessel (the volume of water does not change), another is to increase the volume of water in the vessel (the volume of the vessel does not change). Passive and semi-active pressure compensation techniques apply the first principle, and active compensation techniques apply the second.

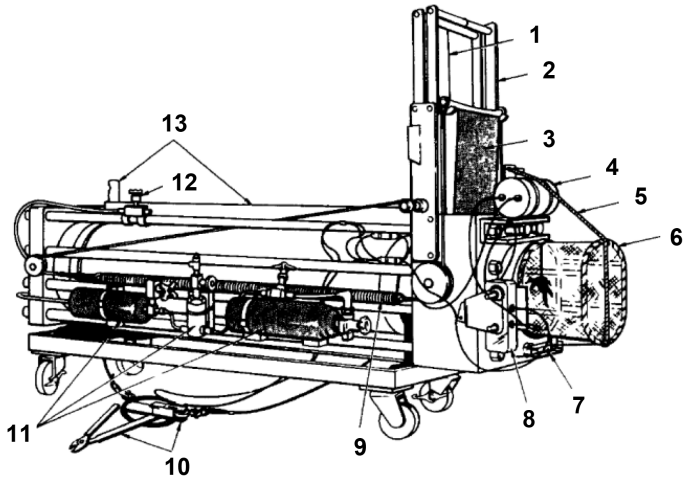

FIGURE 6
Schematic diagram of hyperbaric trap-aquarium (1:Pressure gauges; 2:Window; 3:Plexiglass; 4:Negator spring(pulls fish in- and closes door after tugging fish releases ballast); 5:Main Al tube; 6:Line between negator spring and fish hook; 7:Line to pin; 8:Large Al tube; 9:Pin; 10:Shock cords to close door; 11:Loops; 12:Taut wire; 13:Baited hook; 14:Handling bracket; 15:Spring; 16:Line to baited strings and ballast weights; 17:crimps; 18:Fish-triggered release)(adapted from Phleger et al., 1979).

3.1.1 Passive pressure compensation technology

Passive pressure compensation technology is widely used in the deep-sea pressure-retaining sampler. It is usually achieved by an accumulator filled with high-pressure gas (usually nitrogen). The main principle of this technology is to use the different compression ratios of gas and seawater. When the pressure in the sample chamber decreases, gas volume expansion will be much more significant than that of liquid since the volumetric compression ratio of gas is thousands of times that of liquid. In this way, it can compensate for pressure loss partially. Generally speaking, the pre-charge pressure of the accumulator should be lower than the pressure at the sampling location. Otherwise, the accumulator will lose its function. As a result, the gas accumulator is not sufficient to fully compensate for the pressure loss.

Accumulators can be divided into piston accumulators, diaphragm accumulators and bladder accumulators. Piston accumulator has the advantages of high flow rates, wide application temperature range and high-pressure tolerance (Hiis et al., 2019). The working principle of the latter two types of accumulators is similar and has the advantage of a short response time (usually no more than 25ms). Most of the samplers adopted the bladder accumulator and the piston

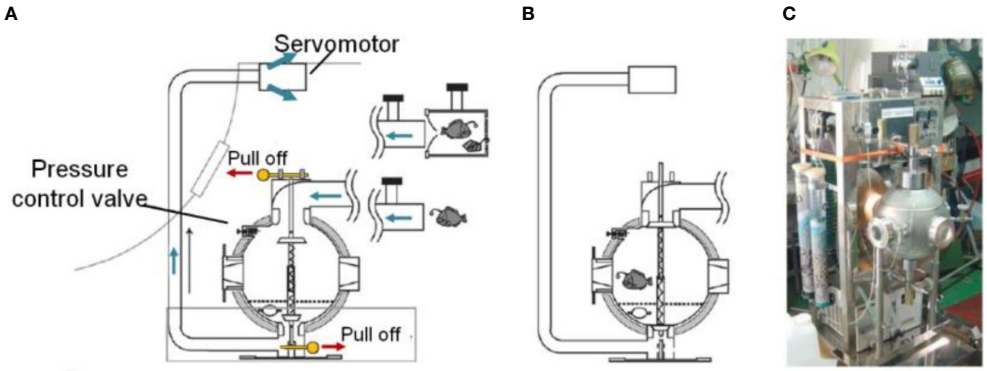

FIGURE 7
Schematic diagram and photo of pressure-stat aquarium **(A)**: Capture procedure of pressure-stat aquarium; **(B)**: Pressure vessel was sealed by the sealing door; **(C)**: Photo of pressure-stat aquarium (adapted from Koyama et al., 2002).

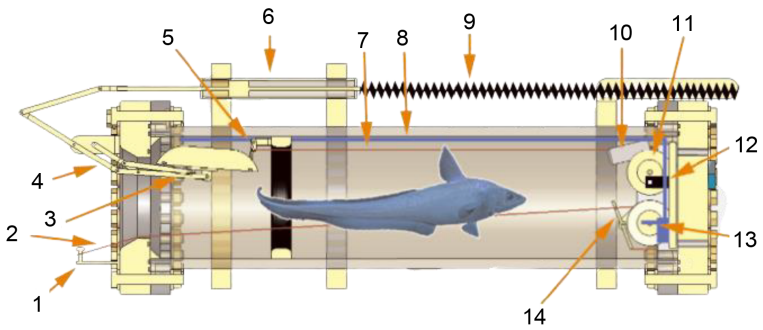

FIGURE 8
Schematic diagram of hyperbaric trap respirometer (1: Pin to hold the release shackle/hook assembly; 2: Retraction line connected to hook; 3: Door; 4: Door linkage system; 5: Door latch; 6: Hydraulic dampening piston; 7: Line to door release plate; 8: Tubing to draw water to pump; 9: Extension springs; 10: Camera with integrated LED lighting; 11: Wheels for coiled constant force springs; 12: Oxygen probe; 13: Water circulation pump; 14: Release trigger for door.)(adapted from Drazen et al., 2005).

accumulator. When the depth exceeds 3500m, piston accumulators are more commonly used (Figure 11).

In general, the accumulator has the advantages of simple structure, lightweight and high efficiency, and it is a suitable choice for pressure compensation components used in isobaric sampling devices. However, there are still some problems in the design and evaluation of accumulators when applied in the deep sea. Firstly, safety is an important issue. With the application depth increases, the interior of the accumulator is filled with high-pressure gas, which is dangerous to operators. Secondly, as the operation depth increases, the compressibility of the gas decreases due to the existence of Van der Waals forces, which leads to a decrease in the volumetric efficiency of the accumulator, and an accumulator with a larger volume is required when the water depth increases. The ideal gas state equation is difficult to satisfy the requirements of application situations with higher pressures, although the equation has high accuracy below 30MPa. Many researchers have established the real gas state equations through theoretical derivation or experiments, but they still cannot accurately describe the gas's properties under high or ultra-high pressure (Span et al., 2000; Mir Rajabi, 2006; Wang et al., 2020). Moreover, despite the simple structure of the accumulator, it is quite difficult to establish a mathematical model for quantitative analysis because this multi-phase system involves mechanics, thermodynamics, pneumatics and hydraulics, etc. Some researchers have established mathematical models to help us optimize the accumulator (Giliomee, 2007; Alatalo et al., 2018).

In addition, to adapt to the deep-sea application situation, many new structures have been designed, such as spring-loaded (Figure 12A) or weight-loaded (Figure 12B) accumulators, in anticipation of using force from spring deformation or gravity of heavy objects to replace high-pressure gas. Some accumulators use two pistons of different sizes to reduce the pressure in the

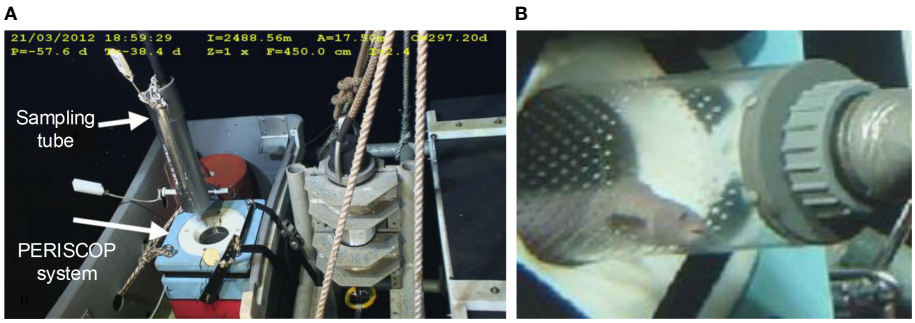

FIGURE 9
Photos of PERISCOPE **(A, B)**: the sampling tube is placed into the pressure vessel of the PERISCOP (adapted from Shillito et al., 2008; Ravaux et al., 2013) Zaharina et al. (2020) proposed a large-scale deep-water trap whose working depth is 1000m.

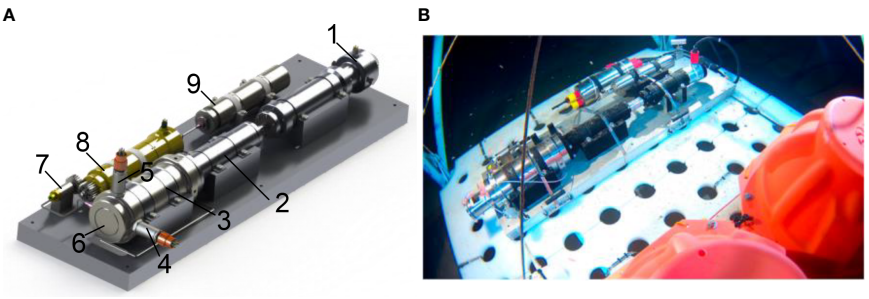

FIGURE 10
Schematic diagram and photo of PMTI **(A)**: 3D model of PMTI (1: sampling motor; 2: screw mechanism; 3: pressure vessel; 4: temperature probe; 5: pressure probe; 6: sampling piston; 7: pressurizing cylinder; 8: pressurizing motor; 9: piston accumulator); **(B)**: PMTI working at seabed) (adapted from Wang et al., 2022).

TABLE 1 Isobaric samplers and the key technologies.

Name of Sampler	Year	Institute and Country	Maximum Pressure Allowed in the Vessel	Capturing method	Close condition and method	Sealing technology	Pressure compensation technology	Temperature Insulation Technology
Recovery Apparatus	1969	University of East Anglia, UK	100MPa	Filter Pump	Human judgment; Extension spring	Globe valve	Bladder type accumulator	N/A
Pressure Fish Trap	1975	Scripps Institution of Oceanography, USA	0.6MPa	Baited Hook	Animals pull the baited hook; Elastic cord	Inner flap door and O-ring	N/A	N/A
PRAT	1977	Scripps Institution of Oceanography, USA	117.2MPa	Baited Trap	Timer; Extension spring	Piston and O-ring	Piston type accumulator	Outer insulation layers
High-pressure Trap	1978	University of Aberdeen, UK	40MPa	Baited Trap	Human judgment; Extensible drawbar and spring	Globe Valve	Bladder type accumulator	Water jacket
Hyperbaric Fish Trap	1979	Scripps Institution of Oceanography, USA	9.6MPa	Baited Hook	Animals pull the baited hook; Negator spring;	Inner flap door and O-ring	Compressed gas cylinder	N/A
Hyperbaric Trap-aquarium	1985	Scripps Institution of Oceanography, USA	14MPa	Baited Trap	Timer; Extensive spring (Derlin release device)	Wedge door and O-ring	Piston type accumulator	Outer insulation layers
Pressure-stat Aquarium System	2002	Marine Science and Technology Center, Japan	20MPa	Suction Pump	Human judgment (based on the vision of ROV); Compressed spring	Inner lids and O-ring	Bladder type accumulator	Outer insulation layers
Hyperbaric Trap Respirometer	2005	Monterey Bay Aquarium Institute, USA	41.4MPa	Baited Hook	Animals pull the baited hook; Extension spring	Inner flap door and O-ring	Piston type accumulator	Outer insulation layers
PERISCOPE	2008	Pierre and Marie Curie University, France	30MPa	Suction Pump	Human judgment (based on the vision of ROV); Manipulator on the ROV	Globe valve	Liquid pressure regulation system	N/A
Deep-water Trap	2020	ITMO University	10MPa	Baited Trap	Human judgment (based on the camera); Deep-water motor	Rotation drum and O-ring	N/A	N/A
PMTI	2020	Zhejiang University, China	125MPa	Baited Trap	Timer; Deep-water motor	Hollow piston and O-ring	Piston type accumulator and liquid compensation components	N/A

N/A, not applicable.

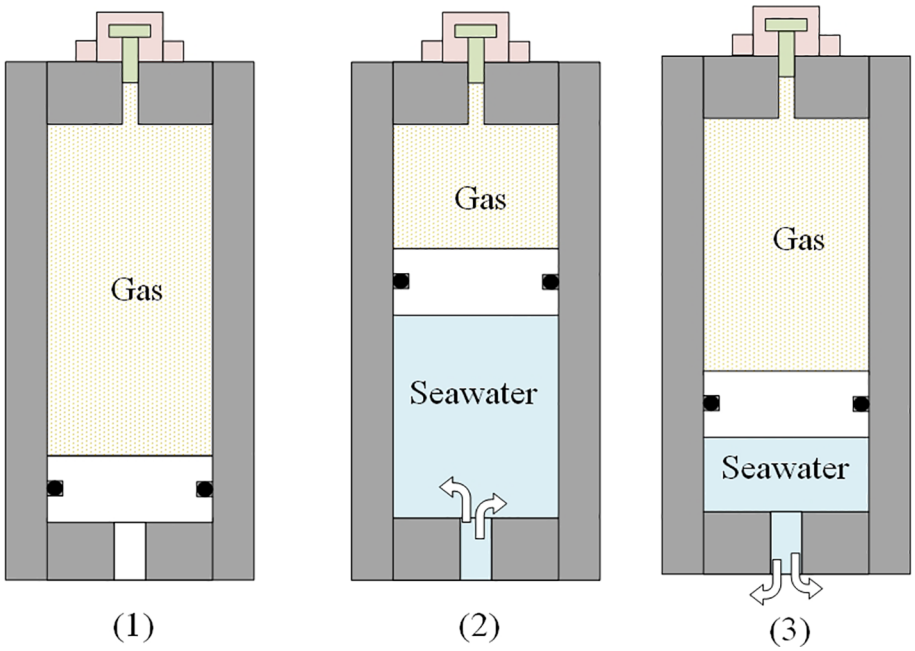

FIGURE 11
working process of a piston accumulator applied in isobaric sampling [(1): pre-charge state; (2): high pressure seawater gets into the accumulator and compresses the gas; (3): the high-pressure gas pushes some of the seawater return to the pressure vessel].

spring chamber, but the volumetric efficiency is lower (Mir Rajabi, 2006) (Figure 12C). These new structures avoid the use of high-pressure gas and significantly improve the safety of deep-sea accumulators. However, they have not yet been used in deep-sea isobaric sampling.

3.1.2 Semi-active pressure compensation technology

Based on the gas accumulator, semi-active pressure compensation uses some measures to improve the pressure retaining rate. For instance, the designer of PMTI equipped a

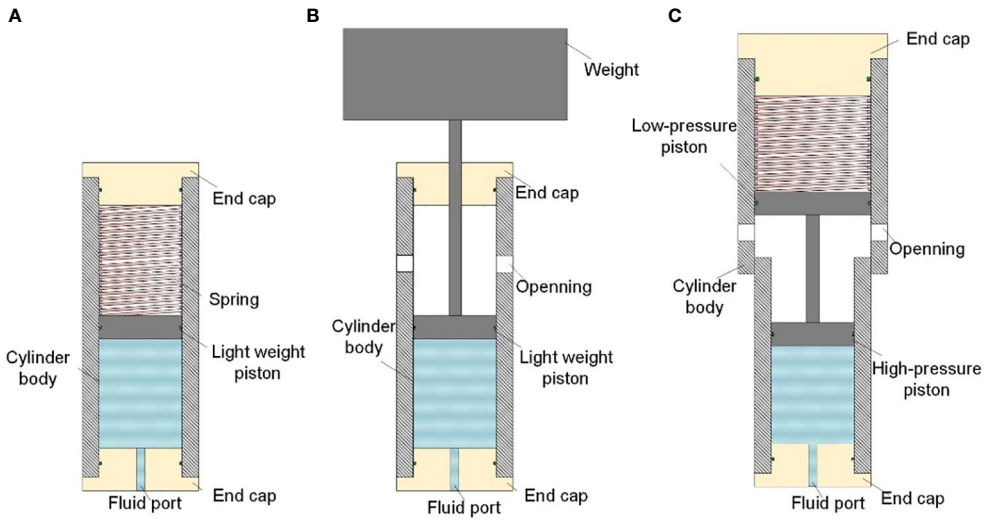

FIGURE 12
New structures of accumulators **(A)**: Spring loaded accumulator; **(B)**: Improved spring-loaded accumulator; **(C)** weight-loaded accumulator.

submarine pressurizing pump connected to the pressure vessel *via* a capillary, mainly considering the effect of seal movement on the pressure drop. The seal can move axially within a specific range in the groove generally. When the sampler is recovered, the seal will be pushed towards the low-pressure side of the groove due to the reduction of external pressure, which increases the volume of the vessel and causes the pressure drop. The submarine pressurizing pump is an electric plunger pump used to establish the initial pressure difference between the vessel and seawater at the sea bed. Besides, it increases the initial contact pressure of the sealing ring and pushes the sealing ring to the low-pressure side of the groove as much as possible. After the sampler is closed on the seabed, the submarine pressurizing pump injects a specific volume of pure water into the vessel (Figure 13). Table 2 compares the pressure retaining performance of PMTI when passive and semi-active technology was adopted. Experiment results show that semi-active compensation method can significantly improve the pressure retaining rate even when water depth exceeds 6000m (Wang et al., 2022).

3.1.3 Active pressure compensation technology

Active pressure compensation technology adopts the liquid compensation method, and there are currently two practical application examples. The first is the PRD compensation device used in the PERISCOP sampling system (Figure 14), which includes a pressure vessel to store the sample, a double-valve mechanical pressure regulator, a reference container, and a reservoir container (with a pressure higher than that of the sampling depth). The reference container is closed at the sampling depth, and recorded the *in-situ* pressure. As the sampler ascends, the pressure regulator compares the pressure in the sample cell and the reference container. Once the pressure in the sample vessel is reduced, the pressure regulator will turn on the passage between the pressure vessel and the high-pressure seawater vessel and repressure the sample vessel until it is equal to the pressure in the reference vessel again.

Another active pressure compensation device is applied to a deep-sea water serial sampler (Figure 15). The pressure compensation device of this sampler is based on an electric reciprocating plunger pump. The plunger pump, equipped with two one-way valves, is used for the inlet of seawater and the pressurizing channel, respectively. Pressure sensors are used to record the pressure of the sampling depth and the pressure value in the sample vessel for the control system to read and compare in real-time. When the pressure drop exceeds 0.5MPa, the booster pump injects water into the pressure vessel. The compensation device proved to have a satisfactory performance within 40MPa.

In general, passive pressure compensation technology is still the most widely applied technology, with a simple structure, low cost, and acceptable pressure-compensation performance. However, because of the use of high-pressure gas, the safety of passive pressure-holding technology is always a hidden problem during offshore operations. In addition, the volumetric efficiency of the gas accumulator decreases significantly as the operating

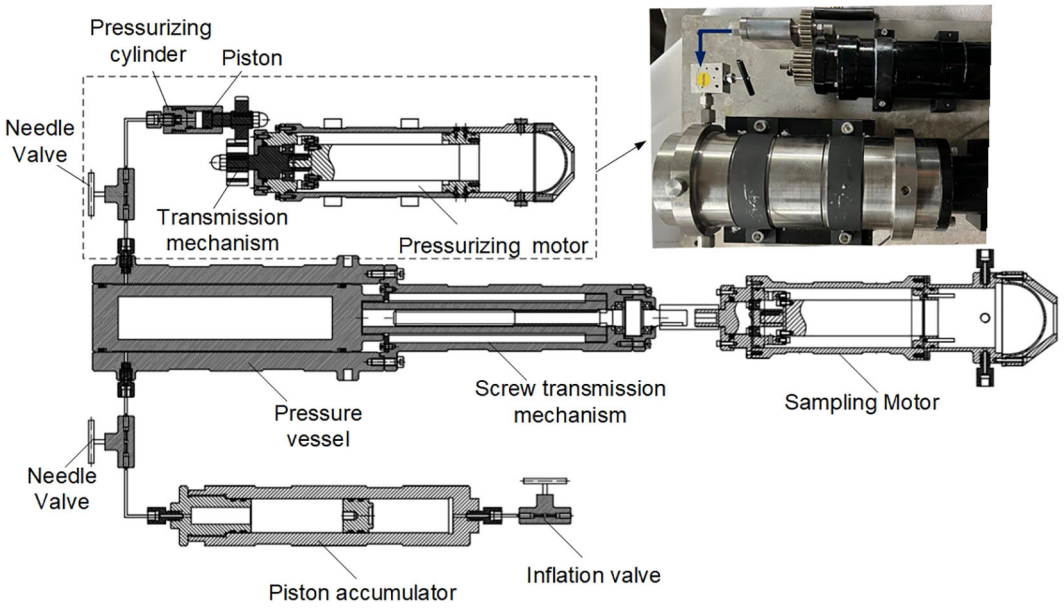

FIGURE 13
The pressurizing device of PMTI.

TABLE 2 Pressure retaining data of hyperbaric chamber of PMTI (data from Wang et al., 2022).

No	Test Pressure	Final Pressure	Pressure retaining rate	Pressure compensation technology adopted in the test
1	60.15	54.67	90.8%	Passive technology
2	60.15	54.35	90.3%	Passive technology
3	60.15	58.61	97.4%	Semi-active technology

depth increases. Currently, semi-active and active pressure compensation technologies are still not commonly used, primarily because the application of these technologies increases the system's complexity and is more expensive. However, semi-active and active techniques are much safer, and we can precisely control the pressure of the sample by adopting these techniques.

3.2 Insulation

According to the World Ocean Atlas published by NOAA in the United States, the ocean's temperature below 2500m is about 2°C-4°C, and it slowly rises to around 30°C on the surface. (https://data.nodc.noaa.gov/woa/WOA18/DATA/temperature/). It is necessary to take appropriate measures to maintain the temperature of the sample if the sampler stays on the surface for several hours. Here we divide the thermal insulation technologies of deep-sea samplers into passive and active thermal insulation.

3.2.1 Passive insulation

There are two methods for passive insulation. The first is to cover the vessel with thermal insulation layers. The second is to install an adiabatic sleeve out of the pressure vessel to form an annular insulation vacuum. Sometimes designers fill this space with water to provide a "water jacket." Most of the samplers mentioned adopted passive insulation techniques. Thermal insulation materials used in deep-sea samplers usually have low thermal conductivity, anti-aging, high-pressure, low water absorption, and corrosion resistance and are lightweight. Commonly used insulation materials include polyurethane, polyvinyl chloride (PVC), polypropylene glass bead composite polyurethane (GSPU), Aerogel, etc. In addition, spraying insulation materials such as ZrO2/CaO, ZrO2-8% Y2O3 epoxy resin, etc., inside and outside the pressure vessel can reduce the radiant heat exchange (Di Girolamo et al., 2010). In some samplers, an insulation sleeve is installed outside the pressure vessel, and the annular space in between is filled with water or other refrigerants. For instance, liquid ammonia is filled in the annular space between the insulation barrel and the sample

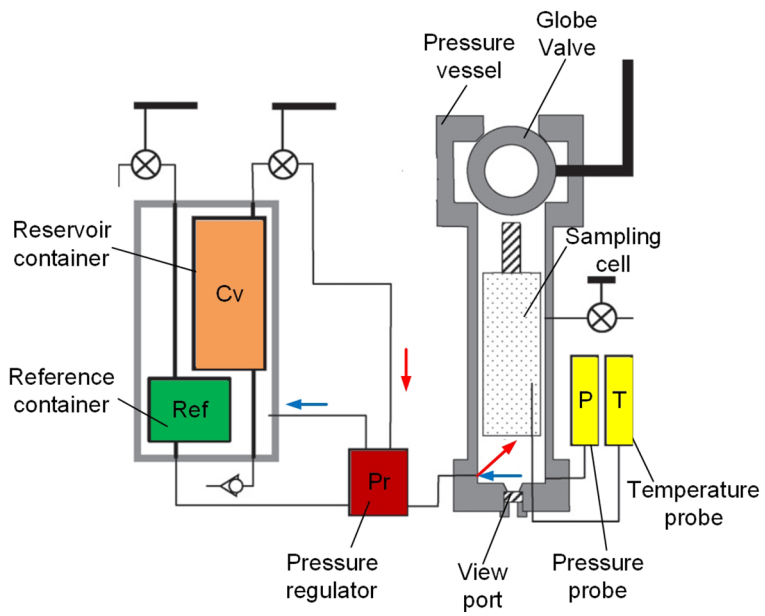

FIGURE 14
PRD of PERISCOP (Adapted from Shillito et al., 2008).

chamber (Zhu et al., 2011). The evaporation of liquid ammonia absorbs heat to keep the sample at a low temperature.

However, the effect of passive insulation is affected by many factors, such as the time staying on the surface, individual differences in materials, etc. and sometimes it does not achieve satisfactory results. For instance, the cod-end sampling system using a closed PVC tube for insulation. When it was recovered to the deck, the temperature increased to 11°C (the temperature of sampling depth is about 5°C and of tropical layer at surface is about 28°C) (Wild et al., 1985).The PERISCOPE system utilizes an insulation box made of syntactic foam to keep the samples cool. The temperature increased about 6°C after a 40min' recovery operation (the temperature of surface water is about 25°C) (Shillito et al., 2008). However, it still is the most widely used insulation technology for deep-ocean samplers because of its simple structure and low cost.

3.2.2 Active insulation

Active insulation automatically adjusts the temperature in the sample chamber, which can keep the temperature within the desired range. Thermoelectric cooling technology is an active thermal insulation technology mainly applied to marine organisms. Wu et al. (2022) proposed an insulated organism sampler containing a pressure-adaptive thermoelectric cooler module and an automatic temperature control system (Figure 16). The cold end of the chilling semiconductor plate directly transmits the cold energy to the water in the sample chamber, while the heat at the hot end is dissipated by convection with seawater during the recovery process. All chilling semiconductor plates are encapsulated in a hose filled with insulating oil, and the pressure of the insulating oil is equal to the external environment pressure because of the elastic deformation of the hose. The device has been tested 4 times at a depth of 1000m-6000m, and the temperature change did not exceed 1°C. In addition, the PTCS system for gas hydrate established by Kawasaki et al. (2006) also applied thermoelectric cooling technology. Sun et al. (2015) proposed a novel gas hydrate sampler by injecting liquid nitrogen into a freezing chamber, and experiments proved that using liquid nitrogen as a freezing medium can improve thermal insulation performance.

Passive insulation technology can satisfy most deep-sea sampling requirements. However, for some special sampling situations, such as hydrothermal ports and deep-sea cold springs, passive insulation may cause excessive temperature changes. In principle, if the sampler stays on the surface for too long, the temperature of the sample will rise to the ambient temperature, which is disastrous for most deep-sea organisms. The advantage of active insulation lies in the temperature inside the sample chamber can be controlled at the *in-situ* temperature as long as there is a sufficient power supply.

3.3 Sealing

A reliable seal is a prerequisite for obtaining pressure-retaining samples. The sealing structures used for deep-sea animal pressure-retaining samplers can be divided into the following categories: ball valve, door sealing, and piston sealing.

Ball valves are widely used in industry and are a highly reliable sealing element. The spool of the ball valve is a sphere with a through hole, which is the passage for animals. When

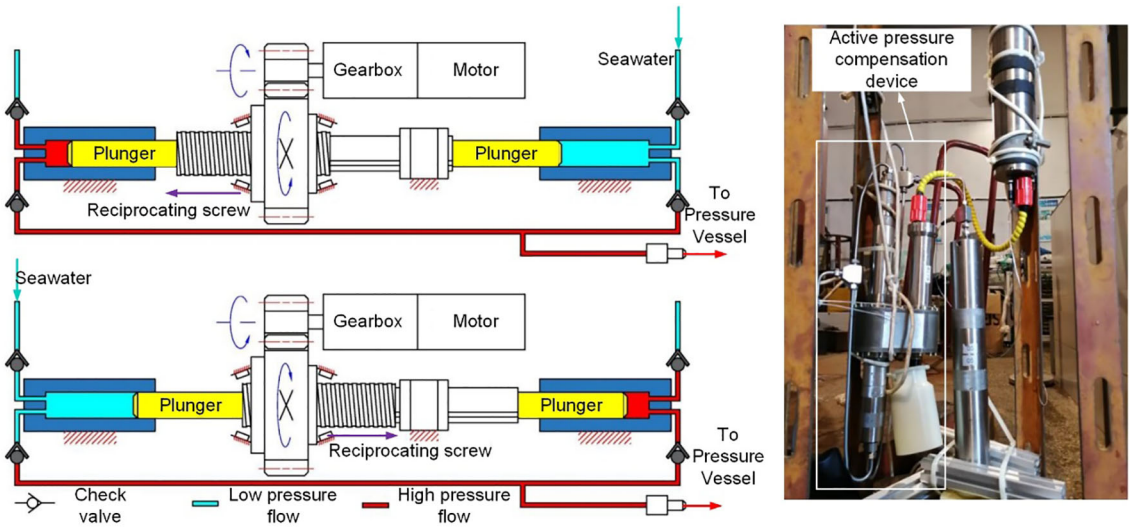

FIGURE 15
Active pressure compensation device (Adapted from Wang, 2020).

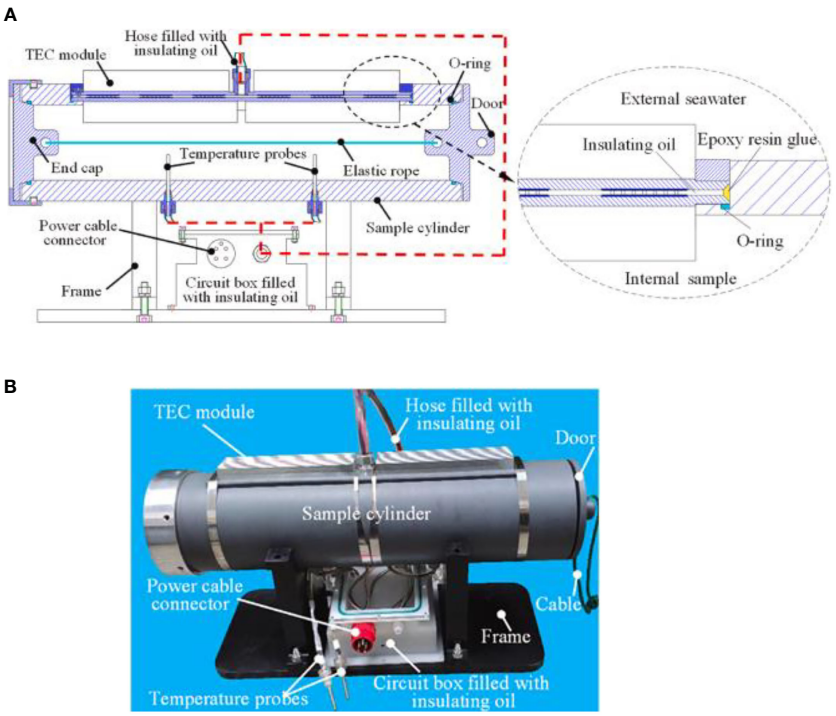

FIGURE 16
Active insulation sampler [**(A)** Schematic diagram of the sampler; **(B)** Photo ofthe sampler]

applied to deep-sea sampling, the disadvantage of the ball valve is its complex structure and heavy weight. The sealing principle of the ball valve determines its inherent geometric properties. The minimum diameter ratio of the ball and the through hole should be greater than 1.42. For example, an inlet with a diameter of 50mm requires a diameter of a sphere greater than 71mm. As the design pressure increases, the seat size will be significantly increased, which leads to the heavy weight of the ball valve. However, in depth is not very deep, and the large through-holes are not required. Using a ball valve is still an efficient and reliable sealing method. Recovery Apparatus, High-pressure trap, PERISCOP adopted ball valves.

Door sealing can be divided into inner and outer door sealing according to the position of the door works. Flap doors are the most commonly used form of door sealing. The flap door is sealed using a plate mounted inside the sample chamber to compress the inner face-mounted seal ring of the pressure chamber. The flap valve is fixed during sampling, and the sample can enter the pressure chamber. Once the release mechanism is triggered, the flap valve flips and compresses the seal ring installed on the end face (usually driven by a spring). Pressure Fish Trap, Hyperbaric Fish Trap, and Hyperbaric Trap Respirometer use flap door. The Pressure-stat Aquarium also adopts internal door sealing. The ROV pulls out the limit pin of the doors, and the two doors inside the vessel are pushed to the end face by springs. Unlike the flap valve, this door performs an axial movement rather than a rotary one. The Deep-water Trap uses an internal rotating drum that is pressed against the inner wall of the pressure vessel by four hydraulic cylinders. As the sampler rises, the pressure difference between the inside and outside increases, and the door is pressed on the sealing ring tighter. Compared with the ball valve seal, the internal door seal has a simpler structure, and its weight is less restricted by the depth and diameter, which makes it easier to be deployed in the deep sea. Nevertheless, the pressure vessel is usually designed with a larger diameter to accommodate the internal doors.

Sealing rings installed on the piston rod press the inner wall of the chamber and thus seal the vessel. Generally, the diameter of the piston is the size of the inlet channel of organisms. The PRAT uses a piston rod with O-rings installed on each end of the rod (Figure 17A). After releasing the counterweight, the piston moves axially under the drive of the spring, and the seal ring is compressed by the inner wall of the pressure vessel to form an initial seal. The ingenious design of PRAT prevents the piston from bearing the axial force caused by the internal pressure, and all the internal pressure acts on the pressure vessel. PIMT uses a specially designed hollow piston with two sealing rings on each end, which is in a long cylindrical shape with a long rectangular slot machined in the middle to keep the sample (Figure 17B). The advantage of piston sealing is its simple structure, which can

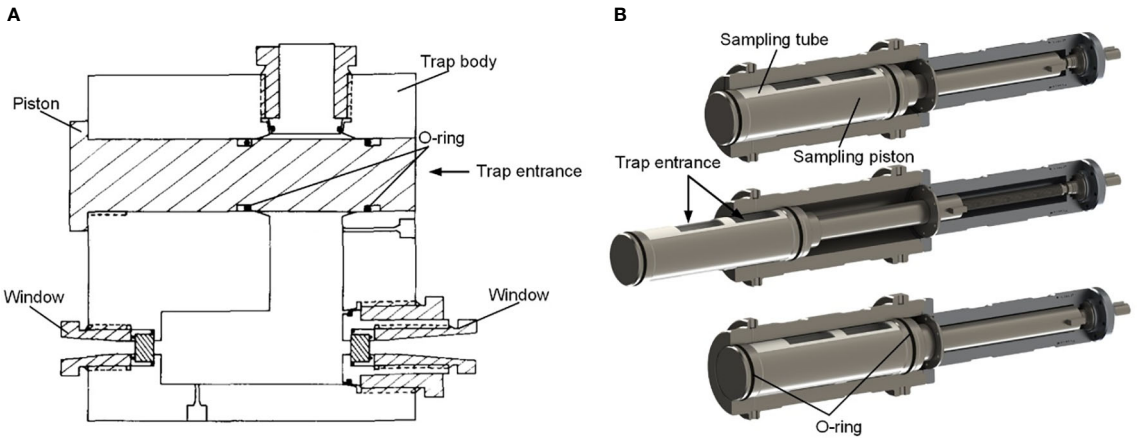

FIGURE 17
Piston sealing structure **(A)**: sealing structure of PRAT [adapted from Yayanos, 1977)]; **(B)**: sealing structure of PIMT [adapted from Wang et al., 2022)].

accomplish sampling and sealing with the exact drive mechanism. In addition, piston-sealing structures will significantly simplify the structure of the device.

In general, as a sealing component, the ball valve is quite reliable. However, as mentioned above, its limitation is that it is cumbersome and inconvenient for offshore deployment. The door sealing structure is simpler and lighter. As the sampler rises, the door presses the seal tighter, so it is a self-tight sealing method. However, its disadvantage is the lack of seal reliability. This is because when the door is triggered, a spring presses the door against the seal on the end face of the vessel. When this seal structure is a flap door, it is driven by a torsion spring. In this case, the seal is not under uniform pressure from the door, so there may be a partial lack of initial contact stress on the sealing ring, resulting in seal failure. The piston seal is light and reliable. This is because the compression between the seal ring and the inner wall of the pressure vessel is fully capable of providing the initial contact pressure for sealing. Therefore, the piston seal is a better choice when other sampling operation requirements are satisfied.

4 Conclusion and prospects

The deep-sea macro organism fidelity samplers are indispensable investigation devices for marine biological research and biological resource development. Although countries worldwide have developed various samplers for over 100 years, it is still not enough. As marine science research goes into the deeper ocean, the requirements for organism samplers are also improving. Integration, intelligence, and diversification are the future development trends of marine sampling equipment. Specific to the deep-sea macro organism fidelity sampler, the purpose is to obtain higher-quality samples, carry out many complex physiological experiments, and obtain reliable data. Therefore, deep-sea macro-organisms sampling technology's development prospects are discussed in the following two aspects.

(1) High fidelity, which means high pressure retaining rate and insulation rate while reducing adverse effects of human factors. It determines the scientific research value of the samples straightly. High fidelity is vital for organisms in unique environments, such as cold springs, hydrothermal fluids, hadals, etc. Therefore, accurate control of sample temperature and pressure will be a significant development direction of macro-organisms sampling equipment. As a result, active pressure compensation and insulation technology will be widely used.

(2) Function integration. It is necessary for marine organism science research to record videos and photos of living things at depth, measure the respiration rate of organisms, and even carry out some simple physiological experiments. Although there have been instruments that can realize one or several functions, they are insufficient. By integrating the fidelity sampler with these optical and electrochemical components, we can compare the physiological parameters of one or several organisms *in situ* and in the laboratory. One of the future development directions of deep-sea organism sampling is how to give more functions to the fidelity sampler.

Author contributions

Contributors HW mainly wrote most chapters of the paper. HW and JC summarized relevant literatures. HW and QZ drafted the manuscript. XH, JG, YW, and HL helped organize the manuscript. All authors contributed to the article and approved the submitted version.

Funding

The study based on the project named "Research on *in-situ* metabolic measurement and high-quality experimental technology in hadal amphipods", which is derived from the "General projects of China National Natural Fund" (grant No 42276191) supporting by the China National Natural Fund Committee.

Conflict of interest

The authors declare that the research was conducted in the absence of any commercial or financial relationships that could be construed as a potential conflict of interest.

The reviewer HH declared a shared affiliation with the authors to the handling Editor at the time of review.

Publisher's note

References

Aguzzi, J., Doya, C., Tecchio, S., De Leo, F. C., Azzurro, E., Costa, C., et al. (2015). Coastal observatories for monitoring of fish behaviour and their responses to environmental changes. *Rev. fish. Biol. fish.* 25 (3), 463–483. doi: 10.1007/s11160-015-9387-9

Aguzzi, J., Mànuel, A., Condal, F., Guillén, J., Nogueras, M., Del Rio, J., et al. (2011). The new seafloor observatory (OBSEA) for remote and long-term coastal ecosystem monitoring. *Sensors* 11 (6), 5850–5872. doi: 10.3390/s110605850

Alatalo, J., Liedes, T., and Pylvänäinen, M. (2018). "Simulation model of a piston type hydro-pneumatic accumulator," in *Proceedings of the 9th EUROSIM congress on modelling and simulation, EUROSIM 2016, the 57th SIMS conference on simulation and modelling SIMS 2016*, vol. 142. (Oulu, Finland: Linköping University Electronic Press), 235–242.

Bosley, K. L., Bosley, K. M., Keller, A. A., and Whitmire, C. E. (2020). Relating groundfish diversity and biomass to deepsea corals and sponges using trawl survey catch data. *Mar. Ecol. Prog. Ser.* 646, 127–143. doi: 10.3354/meps13393

Brown, D. M. (1975). "Four biological samplers: opening-closing midwater trawl, closing vertical tow net, pressure fish trap, free vehicle drop camera," in *Deep Sea research and oceanographic abstracts*, vol. Vol. 22. (Elsevier), 565–567.

Cappo, M., Harvey, E., and Shortis, M. (2006). "Counting and measuring fish with baited video techniques-an overview," in *Australian Society for fish biology workshop proceedings*, vol. Vol. 1. (Tasmania: Australian Society for Fish Biology), 101–114.

Chen, H., Wang, M., Li, M., Lian, C., Zhou, L., Zhang, X., et al. (2021). A glimpse of deep-sea adaptation in chemosynthetic holobionts: Depressurization causes DNA fragmentation and cell death of methanotrophic endosymbionts rather than their deep-sea bathymodiolinae host. *Mol. Ecol.* 30 (10), 2298–2312. doi: 10.1111/mec.15904

Clark, M. R., Consalvey, M., Rowden,, and A., A. (Eds.) (2016). *Biological sampling in the deep sea* (New Jersey, USA: John Wiley & Sons).

Crespo, G. O., Dunn, D. C., Reygondeau, G., Boerder, K., Worm, B., Cheung, W., et al . (2018). The environmental niche of the global high seas pelagic longline fleet. *Sci. Adv.* 4 (8), eaat3681. doi: 10.1126/sciadv.aat36

De Mendonça, S. N., and Metaxas, A. (2021). Comparing the performance of a remotely operated vehicle, a drop camera, and a trawl in capturing deep-sea epifaunal abundance and diversity. *Front. Mar. Sci.* 8, 583. doi: 10.3389/fmars.2021.631354

Di Girolamo, G., Blasi, C., Schioppa, M., and Tapfer, L. (2010). Structure and thermal properties of heat treated plasma sprayed ceria–yttria co-stabilized zirconia coatings. *Ceramics. Int.* 36 (3), 961–968. doi: 10.1016/j.ceramint.2009.10.020

Dixon, D. R., Dixon, L. R., Shillito, B., and Gwynn, J. P. (2002). Background and induced levels of DNA damage in pacific deep-sea vent polychaetes: the case for avoidance. *Cahiers. biologie. Mar.* 43 (3/4), 333–336. doi: 10.21411/CBM.A.13F4BE08

Drazen, J. C., Bird, L. E., and Barry, J. P. (2005). Development of a hyperbaric trap-respirometer for the capture and maintenance of live deep-sea organisms. *Limnol. Oceanogr.: Methods* 3 (11), 488–498. doi: 10.4319/lom.2005.3.488

Fanelli, E., Bianchelli, S., and Danovaro, R. (2018). Deep-sea mobile megafauna of Mediterranean submarine canyons and open slopes: Analysis of spatial and bathymetric gradients. *Prog. Oceanogr.* 168, 23–34. doi: 10.1016/j.pocean.2018.09.010

Fang, J., Zhang, L., and Bazylinski, D. A. (2010). Deep-sea piezosphere and piezophiles: Geomicrobiology and biogeochemistry. *Trends Microbiol.* 18 (9), 413–422. doi: 10.1016/j.tim.2010.06.006

Favali, P., and Beranzoli, L. (2009). EMSO: European multidisciplinary seafloor observatory. *Nucl. Instruments. Methods Phys. Res. Section. A.: Accelerators. Spectrometers. Detectors. Associated. Equip.* 602 (1), 21–27. doi: 10.1016/j.nima.2008.12.214

Garel, M., Bonin, P., Martini, S., Guasco, S., Roumagnac, M., Bhairy, N., et al. (2019). Pressure-retaining sampler and high-pressure systems to study deep-sea microbes under *in situ* conditions. *Front. Microbiol.* 10, 453. doi: 10.3389/fmicb.2019.00453

Giddens, J., Turchik, A., Goodell, W., Rodriguez, M., and Delaney, D. (2021). The national geographic society deep-sea camera system: A low-cost remote video survey instrument to advance biodiversity observation in the deep ocean. *Front. Mar. Sci.* 7, 601411. doi: 10.3389/fmars.2020.601411

Giliomee, C. L. (2007). *Analysis of a four state switchable hydro-pneumatic spring and damper system* (Pretoria, South Africa: University of Pretoria).

Gooday, A. J., Schoenle, A., Dolan, J. R., and Arndt, H. (2020). Protist diversity and function in the dark ocean–challenging the paradigms of deep-sea ecology with special emphasis on foraminiferans and naked protists. *Eur. J. protistol.* 75, 125721. doi: 10.1016/j.ejop.2020.125721

Hiis, E., Stenhjem, M., Pisarev, G. I., and Balakin, B. V. (2019). "Theoretical and experimental study of hydraulic accumulator discharge," in *AIP conference proceedings*, vol. Vol. 2116. (New York, USA: AIP Publishing LLC), 030031.

Jamieson, A. J. (2018). A contemporary perspective on hadal science. *Deep. Sea. Res. Part II.: Topical. Stud. Oceanogr.* 155, 4–10. doi: 10.1016/j.dsr2.2018.01.005

Jamieson, A. J., Fujii, T., Solan, M., Matsumoto, A. K., Bagley, P. M., and Priede, I. G. (2009). Liparid and macrourid fishes of the hadal zone: *In situ* observations of

activity and feeding behaviour. *Proc. R. Soc. B.: Biol. Sci.* 276 (1659), 1037–1045. doi: 10.1098/rspb.2008.1670

Jamieson, A. J., Stewart, H. A., Weston, J. N., and Bongiovanni, C. (2021). Hadal fauna of the south sandwich trench, southern ocean: Baited camera survey from the five deeps expedition. *Deep. Sea. Res. Part II.: Topical. Stud. Oceanogr.* 194, 104987. doi: 10.1016/j.dsr2.2021.104987

Jones, D. O., Bett, B. J., Wynn, R. B., and Masson, D. G. (2009). The use of towed camera platforms in deep-water science. *Underwater. Technol.* 28 (2), 41–50. doi: 10.3723/ut.28.041

Jóźwiak, P., Pabis, K., Brandt, A., and Błażewicz, M. (2020). Epibenthic sled versus giant box corer–comparison of sampling gears for tanaidacean species richness assessment in the abyssal benthic ecosystem. *Prog. Oceanogr.* 181, 102255. doi: 10.1016/j.pocean.2019.102255

Kawasaki, M., Umezu, S., and Yasuda, M. (2006). Pressure temperature core sampler (PTCS). *J. Japanese. Assoc. Petroleum. Technol.* 71 (1), 139–147. doi: 10.3720/japt.71.139

Koyama, S. (2010). Development of high pressure research instrument for keeping of deep-Sea multicellular organisms. *Rev. High Pressure Sci. Technol.* 20 (4), 330-338. doi: 10.4131/jshpreview.20.330

Koyama, S., Miwa, T., Horii, M., Ishikawa, Y., Horikoshi, K., and Aizawa, M. (2002). Pressure-stat aquarium system designed for capturing and maintaining deep-sea organisms. *Deep. Sea. Res. Part I.: Oceanogr. Res. Papers.* 49 (11), 2095–2102. doi: 10.1016/S0967-0637(02)00098-5

Lembke, C., Grasty, S., Silverman, A., Broadbent, H., Butcher, S., and Murawski, S. (2017). The camera-based assessment survey system (C-BASS): a towed camera platform for reef fish abundance surveys and benthic habitat characterization in the gulf of Mexico. *Continental. Shelf. Res.* 151, 62–71. doi: 10.1016/j.csr.2017.10.010

Lins, L., and Brandt, A. (2020). Comparability between box-corer and epibenthic-sledge data on higher taxon level: A case study based on deep-sea samples from the NW pacific. *Prog. Oceanogr.* 182, 102273. doi: 10.1016/j.pocean.2020.102273

Linse, K., and Anderson, M. (2021). *Macrobenthic Mollusca from prince Gustav channel and duse bay, Eastern Antarctic peninsula collected by epibenthic sledge in march 2018* (Southampton, UK: University of Southampton).

Macdonald, A. (1972). High-pressure equipment for use in the laboratory, at sea and at depth. In *Life at High Pressure* (Springer, Cham).

Macdonald, A. (2021). Life at High Pressure. Springer, Berlin. doi: 10.1007/978-3-030-67587-5

Macdonald, A. G., and Gilchrist, I. (1969). Recovery of deep seawater at constant pressure. *Nature* 222 (5188), 71–72. doi: 10.1038/222071a0

Macdonald, A. G., and Gilchrist, I. (1978). Further studies on the pressure tolerance of deep-sea crustacea, with observations using a new high-pressure trap. *Mar. Biol.* 45 (1), 9–21. doi: 10.1007/BF00388973

Mir Rajabi, M. (2006). *The deep water gas charged accumulator and its possible replacements* (Texas, USA: Texas A&M University).

Mortensen, P. B., Roberts, J. M., and Sundt, R. C. (2000). Video-assisted grabbing: a minimally destructive method of sampling azooxanthellate coral banks. *J. Mar. Biol. Assoc. United. Kingdom.* 80 (2), 365–366. doi: 10.1017/S0025315400001983

Murton, B. J., Hühnerbach, V., and Garrard, J. (2012). Exploring ultradeep hydrothermal vents in the Cayman trough by ROV. *Sea. Technol.* 53 (9), 15–18.

Phillips, B. T., Licht, S., Haiat, K. S., Bonney, J., Allder, J., Chaloux, N., et al. (2019). DEEPi: A miniaturized, robust, and economical camera and computer system for deep-sea exploration. *Deep. Sea. Res. Part I.: Oceanogr. Res. Papers.* 153, 103136. doi: 10.1016/j.dsr.2019.103136

Phleger, C. F., McConnaughey, R. R., and Crill, P. (1979)Hyperbaric fish trap operation and deployment in the deep sea. *Deep. Sea. Res. Part A. Oceanogr. Res. Papers.* 26 (12), 1405–1409. doi: 10.1016/0198-0149(79)90008-6

Pinho, M., Medeiros-Leal, W., Sigler, M., Santos, R., Novoa-Pabon, A., Menezes, G., et al. (2020). Azorean demersal longline survey abundance estimates: Procedures and variability. *Regional. Stud. Mar. Sci.* 39, 101443. doi: 10.1016/j.rsma.2020.101443

Prohaska, B. K., Talwar, B. S., and Grubbs, R. D. (2021). Blood biochemical status of deep-sea sharks following longline capture in the gulf of Mexico. *Conserv. Physiol.* 9 (1), coaa113. doi: 10.1093/conphys/coaa113

Przeslawski, R., Berents, P., Clark, M., Edgar, G., Frid, C., Hughes, L., et al. (2018). "Marine sampling field manual for grabs and box corers," in *Field manuals for marine sampling to monitor Australian waters* (Australia: Marine Biodiversity Hub), 172–195.

Purser, A., Marcon, Y., Dreutter, S., Hoge, U., Sablotny, B., Hehemann, L., et al. (2018). Ocean floor observation and bathymetry system (OFOBS): A new towed camera/sonar system for deep-sea habitat surveys. *IEEE J. Oceanic. Eng.* 44 (1), 87–99. doi: 10.1109/JOE.2018.2794095

Ramirez-Llodra, E., Brandt, A., Danovaro, R., De Mol, B., Escobar, E., German, C. R., et al. (2010). Deep, diverse and definitely different: unique attributes of the world's largest ecosystem. *Biogeosciences* 7 (9), 2851–2899. doi: 10.5194/bg-7-2851-2010

Ravaux, J., Hamel, G., Zbinden, M., Tasiemski, A. A., Boutet, I., Léger, N., et al. (2013). Thermal limit for metazoan life in question: *in vivo* heat tolerance of the pompeii worm. *PloS One* 8 (5), e64074. doi: 10.1371/journal.pone.0064074

Sandulli, R., Ingels, J., Zeppilli, D., Sweetman, A. K., Hardy Mincks, S., Mienis, F., et al. (2021). Extreme benthic communities in the age of global change. *Front. Mar. Sci.* 7, 609648. doi: 10.3389/fmars.2020.609648

Shillito, B., Hamel, G., Duchi, C., Cottin, D., Sarrazin, J., Sarradin, P. M., et al. (2008). Live capture of megafauna from 2300 m depth, using a newly designed pressurized recovery device. *Deep. Sea. Res. Part I.: Oceanogr. Res. Papers.* 55 (7), 881–889. doi: 10.1016/j.dsr.2008.03.010

Smith, K.L., and Baldwin, R. J. (1997). "9 laboratory and *in situ* methods for studying deep-Sea fishes," in *Fish physiology*, vol. Vol. 16. (Amsterdam, Netherlands: Academic Press), 351–378.

Smith, K. L., and Brown, N. O. (1983). Oxygen consumption of pelagic juveniles and demersal adults of the deep-sea fish sebastolobus altivelis, measured at depth. *Mar. Biol.* 76 (3), 325–332. doi: 10.1007/BF00393036

Somero, G. N. (1992). Adaptations to high hydrostatic pressure. *Annu. Rev. Physiol.* 54 (1), 557–577. doi: 10.1146/annurev.ph.54.030192.003013

Span, R., Lemmon, E. W., Jacobsen, R. T., Wagner, W., and Yokozeki, A. (2000). A reference equation of state for the thermodynamic properties of nitrogen for temperatures from 63.151 to 1000 K and pressures to 2200 MPa. *J. Phys. Chem. Reference. Data* 29 (6), 1361–1433. doi: 10.1063/1.1349047

Sun, Y., Wang, Y., Lü, X., Jia, R., and Guo, W. (2015). Hole-bottom freezing method for gas hydrate sampling. *J. Natural Gas. Sci. Eng.* 25, 271–283. doi: 10.1016/j.jngse.2015.05.011

Teoh, Z. E., Phillips, B. T., Becker, K. P., Whittredge, G., Weaver, J. C., Hoberman, C., et al. (2018). Rotary-actuated folding polyhedrons for midwater investigation of delicate marine organisms. *Sci. Robotics.* 3 (20), eaat5276. doi: 10.1126/scirobotics.aat5276

Thurber, A. R., Sweetman, A. K., Narayanaswamy, B. E., Jones, D. O., Ingels, J., and Hansman, R. L. (2014). Ecosystem function and services provided by the deep sea. *Biogeosciences* 11 (14), 3941–3963. doi: 10.5194/bg-11-3941-2014

Vogt, D. M., Becker, K. P., Phillips, B. T., Graule, M. A., Rotjan, R. D., Shank, T. M., et al. (2018). Shipboard design and fabrication of custom 3D-printed soft robotic manipulators for the investigation of delicate deep-sea organisms. *PLS. One* 13 (8), e0200386. doi: 10.1371/journal.pone.0200386

Wang, S. (2020). *Research on the mechanism and key technology of accurate pressure-maintaining fluid sampling in full ocean depth*PhD Thesis.

Wang, H., Chen, J., Cao, C., Ge, Y., Fang, J., Zhou, P., et al. (2022). Capturing amphipods in the Mariana trench with a novel pressure retaining sampler. *Deep. Sea. Res. Part I.: Oceanogr. Res. Papers.* 184, 103772. doi: 10.1016/j.dsr.2022.103772

Wang, H., Chen, J., Wang, Y., Fang, J., and Fang, Y. (2020). Research and analysis of pressure-maintaining trapping instrument for macro-organisms in hadal trenches. *J. Mar. Sci. Eng.* 8 (8), 596.

Wang, S., Wu, S., Du, M., Yang, C., and Wang, X. (2020). A new serial sampler for collecting gas-tight samples from seafloor cold seeps and hydrothermal vents. *Deep. Sea. Res. Part I.: Oceanogr. Res. Papers.* (Hangzhou, China; Zhejiang University) 161, 103282. doi: 10.1016/j.dsr.2020.103282

White, S. N., Brewer, P. G., Peltzer, E. T., Kirkwood, W., Pasteris, J. D., and Nakayama, N. (2003). "First expeditionary deployments of the deep ocean raman *in situ* spectrometer," in *AGU fall meeting abstracts* (USA: American Geophysical Union, California), Vol. 2003. OS32A–O0235.

Wild, R. A., Darlington, E., and Herring, P. J. (1985)An acoustically controlled cod-end system for the recovery of deep-sea animals at *in situ* temperatures. *Deep. Sea. Res. Part A. Oceanogr. Res. Papers* 32 (12), 1583–1589 doi: 10.1016/0198-0149(85)90104-9

Wilson, R.R., and Smith, K.L. (1985)Live capture, maintenance and partial decompression of a deep-sea grenadier fish (Coryphaenoides acrolepis) in a hyperbaric trap-aquarium*Deep. Sea. Res. Part A. Oceanogr. Res. Papers.* 32 (12), 1571–1582. doi: 10.1016/0198-0149(85)90103-7

Wu, S. J., Wang, X., Wang, S., Zhang, B., Yang, C. J., and Zhi, H. (2022). Active temperature-preserving deep-sea water sampler configured with a pressure-adaptive thermoelectric cooler module. *Deep. Sea. Res. Part I.: Oceanogr. Res. Papers.* 181, 103701. doi: 10.1016/j.dsr.2022.103701

Yan, G., Lan, Y., Sun, J., Xu, T., Wei, T., and Qian, P. Y. (2022). Comparative transcriptomic analysis of *in situ* and onboard fixed deep-sea limpets reveals sample preparation-related differences. *Iscience* 25 (4), 104092. doi: 10.1016/j.isci.2022.104092

Yayanos, A. A. (1977). Simply actuated closure for a pressure vessel: design for use to trap deep-sea animals. *Rev. Sci. Instruments.* 48 (7), 786–789. doi: 10.1063/1.1135150

Yayanos, A. A. (1978). Recovery and maintenance of live amphipods at a pressure of 580 bars from an ocean depth of 5700 meters. *Science* 200 (4345), 1056–1059. 10.1126/science.200.4345.1056

Yayanos, A. A. (2009). Recovery of live amphipods at over 102 MPa from the challenger deep. *Mar. Technol. Soc. J.* 43 (5), 132–136. doi: 10.4031/MTSJ.43.5.20

Zaharina, E., Abramchuk, M., and Perepelkina, S. Y. (2020). "Development of the hyperbaric chamber for capturing and studying deep-Sea creatures," in *International Russian automation conference* (Cham: Springer), 956–966.

Zhu, H., Liu, Q., Deng, J., Wang, G., Xiao, X., Jiang, Z., et al. (2011). Pressure and temperature preservation techniques for gas-hydrate-bearing sediments sampling. *Energy* 36 (7), 4542–4551. doi: 10.1016/j.energy.2011.03.053

frontiers | Frontiers in Marine Science

TYPE Original Research
PUBLISHED 25 November 2022
DOI 10.3389/fmars.2022.1052802

OPEN ACCESS

EDITED BY
Xianbiao Lin,
Ocean University of China, China

REVIEWED BY
Wei Guo,
Jilin University, China
Miao Li,
Charles Sturt University, Australia

*CORRESPONDENCE
Jiawang Chen
arwang@zju.edu.cn

SPECIALTY SECTION
This article was submitted to Ocean Observation, a section of the journal Frontiers in Marine Science

RECEIVED 24 September 2022
ACCEPTED 14 November 2022
PUBLISHED 25 November 2022

CITATION
Guo J, Zhou Q, Ge Y, Li H, Gao Q, Wang Y, Lin Y and Chen J (2022) Development of a pressure-retaining separation and transfer system for sediment and overlying seawater. *Front. Mar. Sci.* 9:1052802. doi: 10.3389/fmars.2022.1052802

Development of a pressure-retaining separation and transfer system for sediment and overlying seawater

Jin Guo[1,2], Qixiao Zhou[1,2], Yongqiang Ge[1], Haonan Li[1,2], Qiaoling Gao[1], Ying Wang[1,2], Yuan Lin[1] and Jiawang Chen[1,2,3]*

[1]Institute of Ocean Engineering and Technology, Ocean College, Zhejiang University, Zhoushan, China, [2]Hainan Institute, Zhejiang University, Sanya, China, [3]State Key Laboratory of Fluid Power and Mechatronic Systems (Zhejiang University), Hangzhou, China

Methane leakage at the interface between sediment and overlying seawater is an important basis for gas hydrate exploration. Therefore, a transfer device with working pressure of 30MPa and corresponding scheme are proposed to separate and transfer the sediment and overlying water inside the sampler under the condition of pressure-retaining. Based on the pressure relief valve with adjustable threshold pressure, the device transfers the overlying water by compressing the internal volume and transfers the sediment by secondary sampling. The performance of transfer device is studied by simulation and experiment. Based on the coupled Eulerian-Lagrangian approach in the Abaqus, the secondary sampling was investigated, and the penetration resistance and coring rate of the secondary sampling tube are 141N and 86.2%, respectively. By using the hydraulic simulation software AMESim, the pressure fluctuation caused by the movement of the mechanism during the transfer process was studied, and the pressure fluctuation amplitude is within 0.89 MPa. Furthermore, the laboratory transfer tests were carried out under high pressure conditions, and meantime, the simulation results are verified. Under the working condition of 30MPa, the device can maintain a pressure loss of no more than 8.0% (2.4MPa) within two hours, maintain pressure fluctuations during the transfer process within 4.8% (1.44MPa), and ensure that the pressure in the culture kettle decreases by 4.7% relative to the pressure in the sampler after the transfer, which shows the feasibility of the device application.

KEYWORDS

sediment, overlying seawater, pressure-retaining transfer, numerical simulation, laboratory test

1 Introduction

Methane leakage (cold seeps) at sediment seawater interface is an important basis for gas hydrate exploration and subsequent pre-production test (Gornitz and Fung, 1994; Roberts and Aharon, 1994; Suess et al., 1999), which is also an international research hotspot of marine environmental change, but the detection of regional methane leakage is relatively insufficient due to the lack of sampling technology on this interface and corresponding pressure-retaining transfer analysis technology.

For methane *in situ* detection technology, Minato et al. (1999) used a LIDAR system to measure the concentration of methane in the atmosphere by analyzing the initial and return power of the laser to obtain the gas concentration based on the selective absorption of light by gas molecules. Yalong et al. (2011) designed a methane concentration detection system based on TDLAS (diode laser absorption) technology, which emits a laser that is reflected by methane gas clusters, but the system is only suitable for close-range handheld devices. Weil (1993) developed a device that uses infrared light to analyze changes in thermal radiation around a pipeline when methane leaks and the surrounding temperature decreases due to the throttling effect. There are many other technical approaches to measure methane concentration using different technical principles, but there is still no more mature methane detection technique that can be applied to the sediment seawater interface.

In order to study the scientific problems related to natural gas hydrate and seabed geology, the existing sampling technology is developing towards longer cores and high fidelity on the basis of pressure-retaining function. Single pressure-retaining core obtained by subsea drilling rig usually exceeds 2 m (Tréhu, 2006); the length of the sample obtained from the pressure coring barrel (PCB) used in the international deep-sea drilling project is 6 m (Zhu et al., 2011); the sample length obtained by the advanced piston corer used in the international offshore drilling project can reach 9.5 m (Jutzeler et al., 2014); the pressure-retaining cores obtained in the sea trial in 2011 reached 9.5 m by using the long pressure-retaining coring device developed by Zhejiang University (Chen et al., 2013). Moreover, by using a vacuum in the middle of an interlayer, a pressure and temperature preservation system (PTPS) was proposed and applied in the gravity piston sampler developed by Zhejiang University to obtain gas-hydrate-bearing sediments (Li et al., 2006; Zhu et al., 2013). Furthermore, Japan's pressure temperature coring system (PTCS) achieved an active temperature-retaining function by using adiabatic and thermoelectric inner tube cooling (Kawasaki et al., 2006).

After the pressure-retaining sediment sample is obtained, a set of devices is required to transfer the sample to the laboratory for further analysis without obvious pressure drop and disturbance. For the purpose of analyzing the physical and chemical properties of samples, usually only a section of sample needs to be taken from the pressure core. Therefore, a transmission system that can cut and transmit long cores under the working condition of retaining pressure is needed (Rothwell and Rack, 2006; Abegg et al., 2008; Schultheiss et al., 2009; Hao et al., 2013). For example, the hydrate auto-clave coring equipment (HYACE), features not only sampling tools but also a range of pressure core processing equipment (Matsumoto et al., 2011). This device has been used in four major gas hydrate surveys to quantify gas hydrates and accurately measure sediments containing gas hydrates (Amann et al., 1997; Schultheiss et al., 2006). A pressure-retaining transfer system was developed by Zhejiang University to study natural gas hydrate, which includes a mechanical device for continuous sample transfer, e.g., sample grabbing, sample pushing, sample cutting, sample encapsulation, and small sample transfer (Chen et al., 2019; Zhang et al., 2019; Zhu et al., 2022).

In addition, Geotek UK has developed a series of devices for sample transfer analysis. For example, Multi-Sensor Core Logger (MSCL) is a sample undisturbed analysis tool that can quickly acquire high-resolution data from pressure cores or seafloor sediments without damaging the sample structure (Schultheiss and Weaver, 1992; Dickens et al., 2003). On the basis of MSCL, Geotek has further developed the pressure core analysis and transmission system (PCATS), which can cut the high-pressure long columnar sediment into sub samples with a minimum length of 50 mm (Priest et al., 2015; Priest et al., 2019). The Mini-PCATS is a small, simplified version of the PCATS (Liu et al., 2014). By using Mini-PCATS, a core section up to 1.2 m can be removed from the storage chamber and accurately cut into sub-samples, which can be transferred to the sample test unit while maintaining a pressure of up to 35 MPa. However, the existing sampling and transfer analysis technologies lack attention to the interface between sediment and overlying seawater.

In this paper, (1) based on the pressure-retaining sampler for sediment and overlying water, we propose a device and corresponding scheme that can realize multiple separation and transfer of sediment and overlying water under the condition of pressure-retaining, which can effectively reduce the loss of gas components, microbial death and organic component decomposition of samples; (2) by using the pressure relief valves with adjustable threshold pressure and gas-liquid booster pumps, the pressure-retaining transfer device can transfer the overlying water by compressing the internal volume and sediment by secondary sampling; (3) by using the coupled Eulerian-Lagrangian (CEL) approach in the Abaqus, the penetration resistance and coring rate of secondary sampling tube were investigated, (4) the pressure fluctuation caused by the movement of the mechanism during the transfer process is studied based on AMESim; (5) furthermore, the laboratory tests are carried out to test the strength, sealing performance, the ability to maintain pressure stability of the device, and the feasibility of the device application.

2 Mechanical design

As shown in Figure 1, the pressure-retaining transfer device is composed of a push transfer system, a sampler system and a culture system, and any the two systems are sealed through a clamp with O-ring seal. In addition, the transfer device also includes an air compressor, a gas-liquid booster pump, support carts, high-pressure stainless-steel pipes, high-pressure needle valves, and pressure relief valves that can adjust the threshold pressure, etc.

2.1 Push transfer system

As shown in Figure 2, the push transfer system includes two sections of pressure chamber (chamber-A: secondary sampling tube mechanism chamber; chamber-B: putter mechanism chamber). In which, the sealing piston-A (connected with the secondary sampling tube) moves in the pressure chamber-A, and the sealing piston-B (connected with the putter-B) moves in the pressure chamber-B. A hydraulic interface is designed at both ends of the two sections of pressure chambers. Therefore, the reciprocating motion of piston-A (secondary sampling tube) is achieved by injecting water at interface-A1 or interface-A2, and the reciprocating motion of the piston-B (putter-B) is achieved by injecting water at the interface-B1 or the interface-B2. In addition, the push block-B at the other end of the putter-B can reciprocate in the secondary sampling tube to push the sediment the sediment in the secondary sampling pipe into the three-way joint. Furthermore, in order to determine the real-time position of pistons inside the chamber, magnets are installed on all pistons and magnetic induction sensors are installed outside the chamber.

2.2 Culture system

As shown in Figure 3, the culture system includes a culture kettle and putter mechanism, in which the sealing piston-C (connected with the putter-C) moves in the pressure chamber-C. A hydraulic interface is set at both ends of the pressure chamber-C, and the reciprocating motion of the piston-C (putter-C) is achieved by injecting water at the interface-C1 or the interface-C2. There are four hydraulic interfaces on the culture kettle, which are used to fill the culture liquid, monitor the pressure and overpressure overflow. Moreover, a three-way joint is used to connect the culture system to the push transfer system.

2.3 Sampler system for sediment and overlying water

Figure 4 shows the sampler for sediment and overlying water developed by the Zhejiang University team (Guo et al., 2022). The high-pressure needle valve installed on the side wall of the pressure-retaining cylinder and the ball valve installed at the bottom are used to transfer the overlying water and sediment, respectively, under the pressure-retaining condition, and multiple transfer of samples can be completed by controlling the switch of the needle valve and ball valve.

2.4 Transfer process

2.4.1 The process of overlying water transfer and sediment secondary sampling

Figure 5 shows the process of overlying water transfer and sediment secondary sampling, which is divided into the following steps.

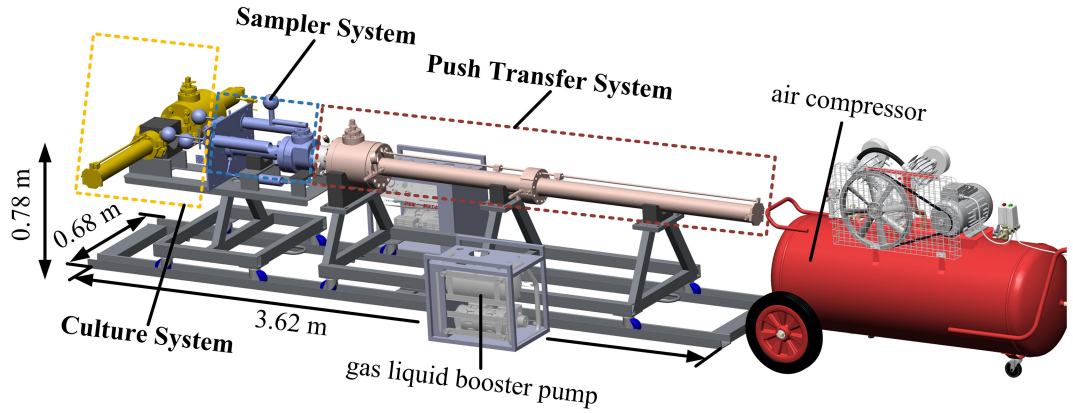

FIGURE 1
Sediment and overlying water pressure-retaining separation and transfer system.

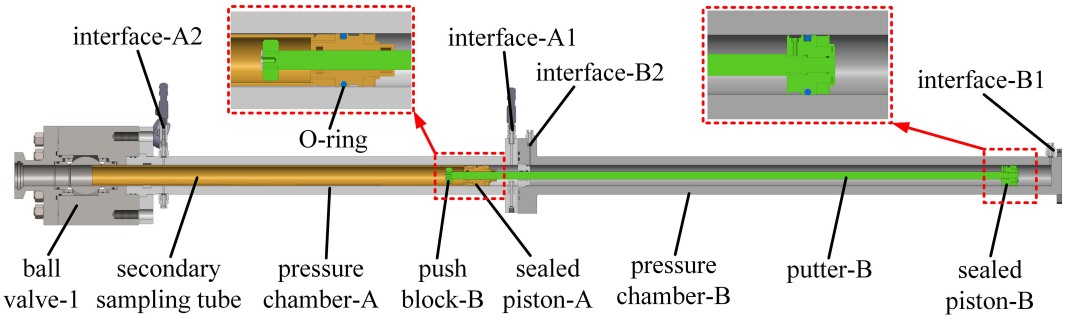

FIGURE 2
Section view of push transfer system.

Step 1: The sampler system is connected with the push transfer system with a clamp, and the pressure chamber-A is pre-filled with deionized water. The installation and current position of all parts are shown in step 1 in Figure 5. The threshold pressure of the pressure relief valve at the interface-A2 is slightly greater than the internal pressure of the sampler, and the threshold pressure of the relief valve at the overlying water transfer interface is consistent with the internal pressure of the sampler. The gas-liquid booster pump is connected to the interface-A1 to pressurize the chamber-A to the same pressure as the internal pressure of the sampler to balance the pressure on both sides of the ball valve-3.

Step 2: The water bag is connected to the overlying water transfer interface, and the sampler ball valve is opened to connect the sampler chamber with the push transfer chamber. When high-pressure deionized water is pumped into the interface-A1, the sealing piston-A moves to the left and compresses the liquid in its left chamber to make the overlying water flow out of the relief valve to the water bag.

Step 3: The threshold pressure of the relief valve at the interface-A2 is adjusted to be equal to the threshold pressure of the relief valve at the overlying water interface. High-pressure deionized water (the specific pressure value will be calculated based on the simulated penetration resistance) is pumped at interface-A1. Seal piston-A (secondary sampling tube) continues to move to the left and compress the liquid in its left chamber to flow out of the relief valve at interface-A2. When the sealing piston-A moves to the leftmost end of its stroke, the secondary sampling tube completes the secondary sampling of sediment in the sampler chamber.

Step 4: The relief valve is connected to interface-A1, and the gas-liquid booster pump is connected to interface-A2 to pump high-pressure deionized water to move the sealing piston-A (secondary sampling tube) to the right and meanwhile compress the liquid in its right chamber to flow out of the relief valve at interface-A1. When seal piston-A moves to the rightmost end of its stroke, ball valve-1 of the push transfer chamber is closed. At this point, the secondary sampling process of the sediment from the sampler to the transfer device has been completed.

2.4.2 The process of transferring sediment to the culture kettle

Figure 6 shows the process of transferring sediment to the culture kettle, which is divided into the following steps.

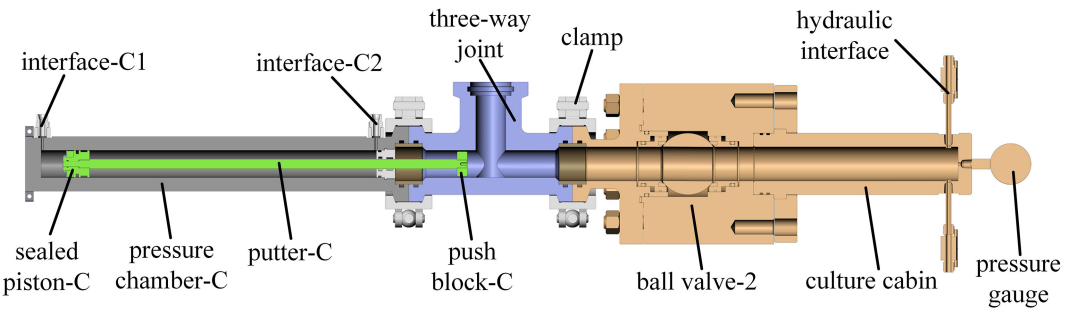

FIGURE 3
Section view of sediment culture system.

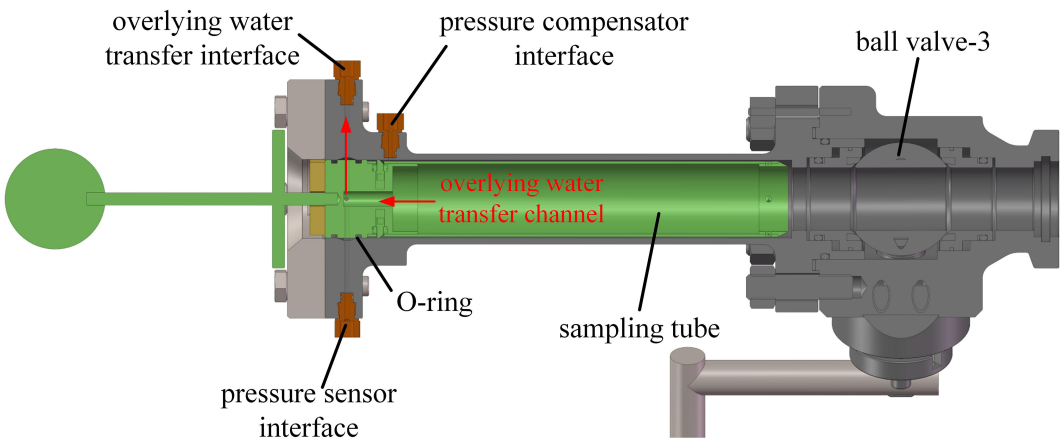

FIGURE 4
Section view of sediment and its overlying seawater sampler.

Step 1: The clamp is used to connect and seal the culture kettle system with the push transfer system, and the culture kettle cabin is pre-filled with microbial culture solution. The installation and current position of all parts are shown in step 1 in the Figure 6. The threshold pressure of the relief valve (connected with the culture kettle) is adjusted to be consistent with the internal pressure of the push transfer cabin, and the gas-liquid booster pump is connected to the side wall interface of the culture kettle to pressurize the culture kettle cabin to the same pressure as the internal pressure of the sampler to balance the pressure on both sides of the ball valve-1.

Step 2: The ball valve-1 is opened to connect the push transfer chamber with the culture kettle cabin. The threshold pressure of the relief valve at the interface-B2 is adjusted to an appropriate value, and the threshold pressure of the relief valve at the interface of the culture kettle is consistent with the internal pressure of the push transfer chamber. High-pressure deionized water is pumped into the interface-B1 to move the sealing piston-B to the left and drive the putter-B to push the sediment in the secondary sampling tube to the three-way joint.

Step 3: The threshold pressure of the relief valve at interface-C2 is adjusted to an appropriate value, and high-pressure deionized water is pumped at interface-C1 to make the sealing piston-C move down and drive the putter-C to push the sediment in the three-way joint into the culture kettle chamber.

Step 4: The relief valve at interface-C2 is moved to interface-C1, and high-pressure nutrient solution is pumped into the side wall interface of the culture kettle to make the putter-C move upward to the top of its stroke.

Step 5: The ball valve-2 and all interfaces on the side wall of the culture kettle are closed. The clamp between the ball valve-2 and the three-way joint is removed, and the culture kettle is transferred to the laboratory for further culture analysis.

3 Method

3.1 Numerical simulation of secondary sampling

In order to ensure that the secondary sampling tube can penetrate the sediment sample in the sampler smoothly with low disturbance, the penetration resistance of the secondary sampling tube needs to be defined by using the coupled Eulerian-Lagrangian (CEL) approach in the commercial package Abaqus/Explicit. Therefore, the pressure to be maintained at interface-A1 (see Figure 2) can be determined. CEL model in Abaqus has advantages in solving mesh distortion in large deformation problems (Konkol, 2015; Ko et al., 2017; Zhen et al., 2017), which has been successfully used to study the behavior of anchors during dynamic installation in non-homogeneous clay (Kim and Hossain, 2017) and optimize the gravity coring (Qin et al., 2016). The Euler mesh used in the CEL approach can be void domain, or part or all of it is occupied by more than one material, and its volume fraction represents the part of the mesh filled with a specific material.

As shown in Figure 7, the diameter and length of the sediment inside the sampler are 56 mm and 150 mm respectively (the volume is 369.5 ml), and 100 mm thick (no material) void field is set at the end of the sediment to provide a place for sediment deformation during secondary sampling. The inner diameter and outer diameter of the secondary sampling tube are 42mm and 48mm, respectively. The computational domain is divided into hexahedral structured mesh, and the mesh size is shown in Table 1. The sampling tube is simplified as a rigid body and is assumed to be vertical and not inclined during the penetration process. In simulation, the soil is modeled as an elasto-perfectly plastic material that obeys the mohr-

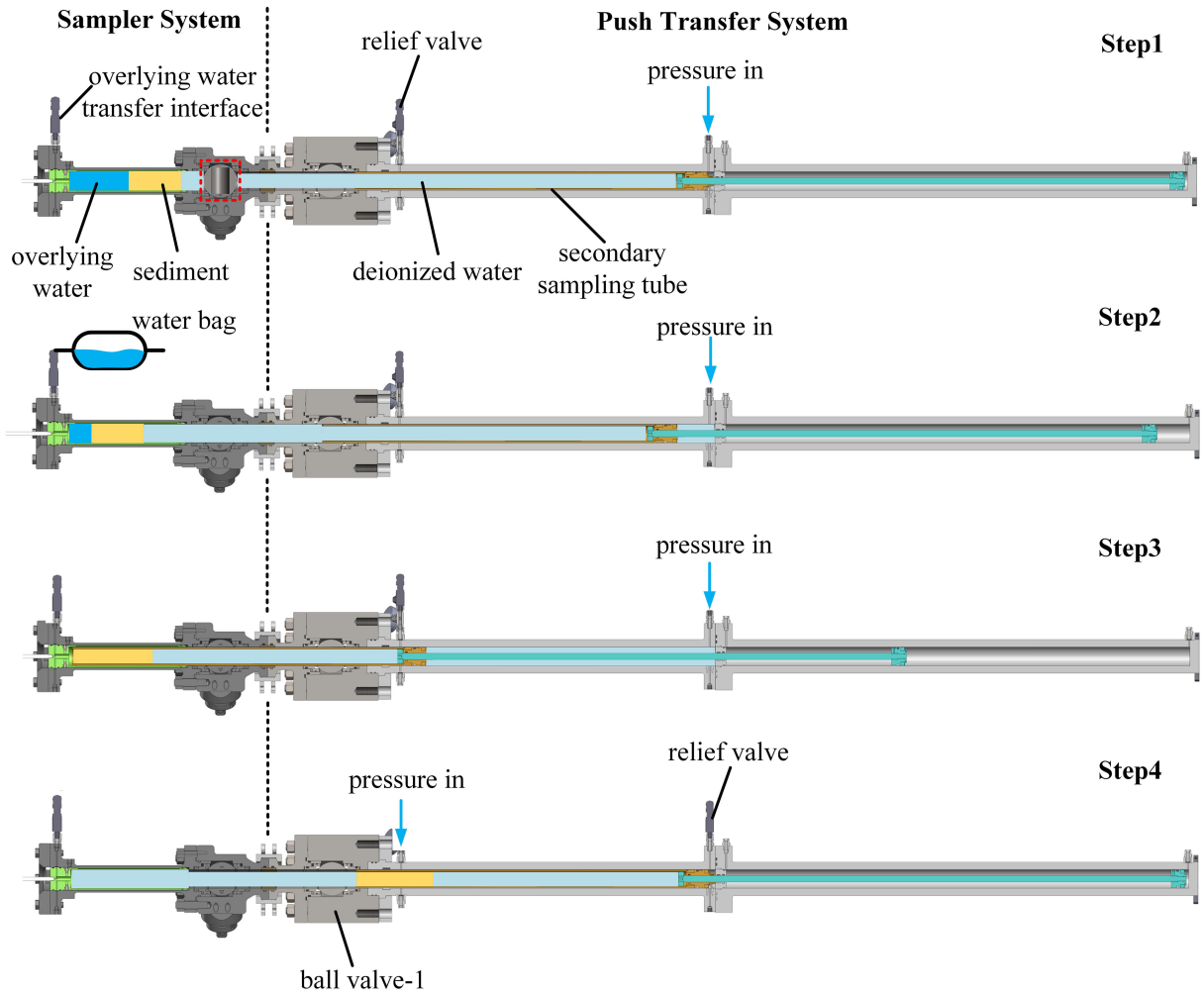

FIGURE 5
Schematic diagram of overlying water transfer and sediment secondary sampling process.

coulomb yield criterion. In the entire soil profile, the elastic behavior is defined by poisson's ratio of 0.4 and young's modulus of 10 MPa and the plastic behavior is defined by a friction angle of 12 degrees and a cohesive force of 15 KPa (Tong et al., 2019).

3.2 Numerical simulation of pressure fluctuation in transfer process

In order to verify that the device can maintain the pressure stability of the sample during transfer process to avoid the death of microorganisms and decomposition of dissolved gas, the pressure fluctuations during sample transfer were simulated in the software AMESim (advanced modelling environment for performing simulation of engineering systems), which is widely used for numerical calculations of hydraulic problems (Zhao et al., 2009; Xuanyin et al., 2010; Ramakrishnan et al., 2012; Zeng et al., 2018).

For the simulation model, the HCD (hydraulic component design) library and the HYD (hydraulic) library are used to build the model, and the spring element is used to simulate the resistance existing in the process of marine sediment transfer. The corresponding chamber pressure change is simulated by variable volume pressure change, and reasonable pipe diameter, pump speed, mass of mass block, leakage coefficient, etc. are set to ensure that they are close to the actual working conditions. As shown in Figure 8A, the reciprocating linear motion of the secondary sampling tube is achieved by using the throttle valve and the waveform signal control channel. Figure 8B shows the simulation model of the process of pushing the sediment with putter-B. In addition, it should be noted that the piston with spring module in Figure A needs to be replaced with the rightmost piston module when the secondary sampling tube moves in different directions. For the process of pressurization, a sinusoidal signal plus a random signal is used to simulate the actual working

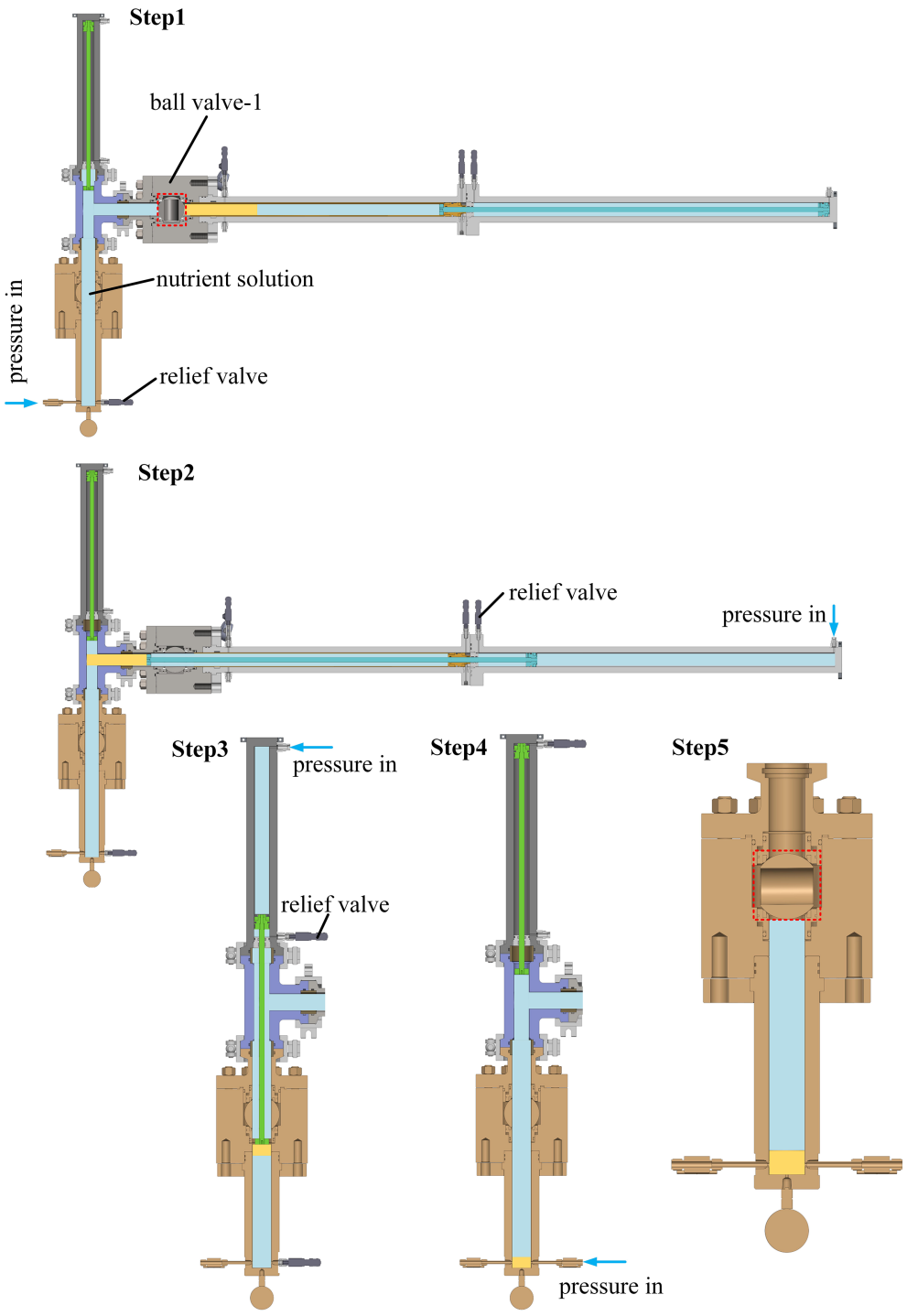

FIGURE 6
Schematic diagram of transferring sediment to culture kettle.

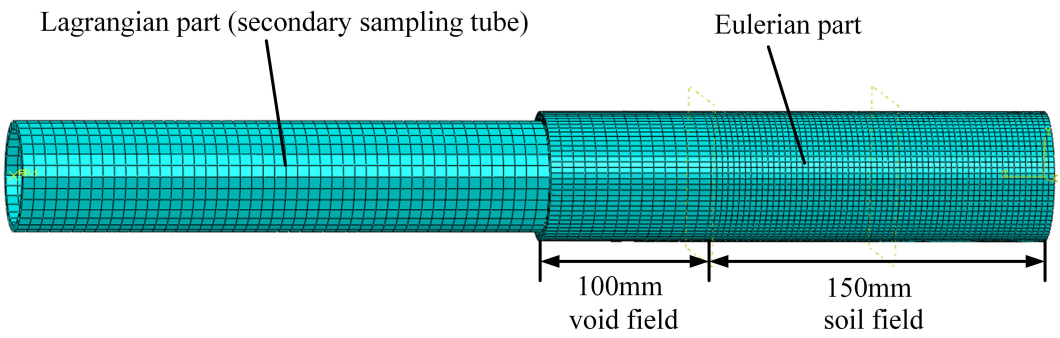

FIGURE 7
Meshes of penetration simulation used in CEL analysis.

TABLE 1 Size and number of meshes used in Abaqus.

Mesh size (mm)	3	2.5	2	1.75
No (s) meshes	23816	36432	68372	104200

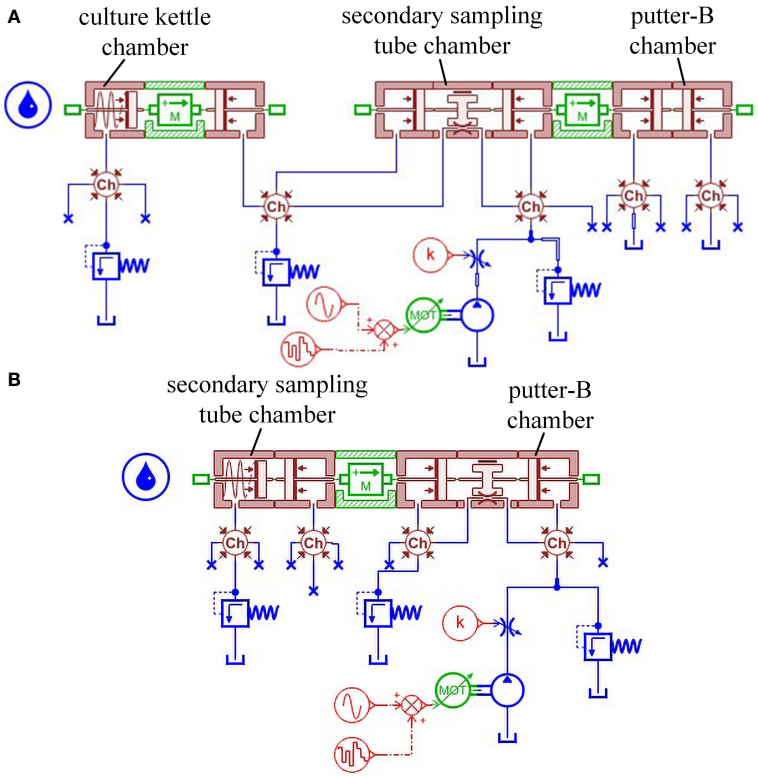

FIGURE 8
Simulation model, **(A)** the movement process of the secondary sampling tube, and **(B)** the movement process of the putter-B.

condition of a single-stroke gas-liquid booster pump. Table 2 lists the settings of key parameters in the simulation.

3.3 Laboratory test

In order to further understand the real performance of the device to maintain pressure stability, and also to verify the simulation results, the transfer test under high pressure is adopted.

3.3.1 Pressure-retaining performance test

As shown in Figure 9, according to *section 2.4 Transfer process*, the sealed chambers formed by the transfer device and the sampler, the transfer device and the sediment culture kettle were constructed respectively to check sealing and pressure-retaining performance. Before the test, the pressure sensor and gas-liquid booster pump are connected with the interface of the transfer device. During the test, the gas liquid booster pump pumps water into the internal chamber of the transfer device to pressurize, and the pressure-retaining performance of the device is reflected by measuring the pressure drop within two hours.

3.3.2 Sample transfer test

Furthermore, according to the operation process in *section 2.4.1. The process of overlying water transfer and sediment secondary sampling* and *2.4.2. The process of transferring sediment to the culture kettle*, the pressure evolution during the transfer process is measured to reflect the performance of the transfer device to maintain pressure stability.

4 Results and discussion

4.1 Numerical simulation results

4.1.1 Secondary sampling process

Based on the penetration force of secondary sampling tube, the mesh independence in numerical simulation is studied. As shown in Figure 10A, the penetration resistance decreases first with the number of meshes increasing from 23816 to 68372. When the number of meshes exceeds 68372, the penetration resistance tends to be stable, that is, the number of meshes is used in the following simulation. In addition, since the sediment inside the sampler is soft, the penetration force of the secondary sampling tube remains at a low level (about 140 N, this value can be used to determine the injection pressure during the transfer process), which is Much lower than the penetration resistance of the shallow sediment sampler (Chen et al., 2020; Guo et al., 2022; Wang et al., 2022). When the penetration depth is close to 150mm, the sediment between the end of the secondary sampling tube and the end of the sampler is compacted and hardened, resulting in the sudden increase of the penetration force. Therefore, during the actual pressure-retaining transfer, a penetration depth of 140 mm can be used to prevent the damage of the secondary sampling tube.

Furthermore, the distribution of sediments in secondary sampling tube is shown in the Figure 10B, the actual sediment volume in the secondary sampling tube is 318.68 ml without soil plug effect, which shows the feasibility of the transfer scheme.

Since the sampling tube is made of thin-wall PC tube, the buckling failure is the primary form of failure during penetration. In structural mechanics, the criterion of buckling failure of slender members under compression is determined by the critical force F_{Pcr}. Therefore, the critical force $F_{Pcr} = 580.5\ N$ of tube, which is greater than penetration force, can be calculated by the equation (1) given by Batdorf et al. (1947), where r is the radius, t is the wall thickness, L is the length and μ is the poisson's ratio, and the K_x in the formula can be obtained by the relationship between it and the variable Z.

$$F_{Pcr} = \frac{\pi(r^2 - (r-t)^2)K_x\pi^2 2r}{L^2 t} \tag{1}$$

TABLE 2 Key parameters in the simulation.

Element	Parameter	Value
BAP11	Rod diameter	18 mm
	Piston diameter	50 mm
	Length of chamber	720 mm
MECMAS21	Mass	2.3 kg
	Coefficient of viscous friction	0.001 N/(m/s)
BHC11	Dead volume	10 cm^3
BAP016	Spring stiffness	1 N/mm
	Spring force at zero displacement	1000 N
BAF01	Clearance on diameter	0.01 mm

BAP11: piston; MECMAS21: mass block; BHC11: variable volume; BAP016: piston with spring; BAF01: leak module.

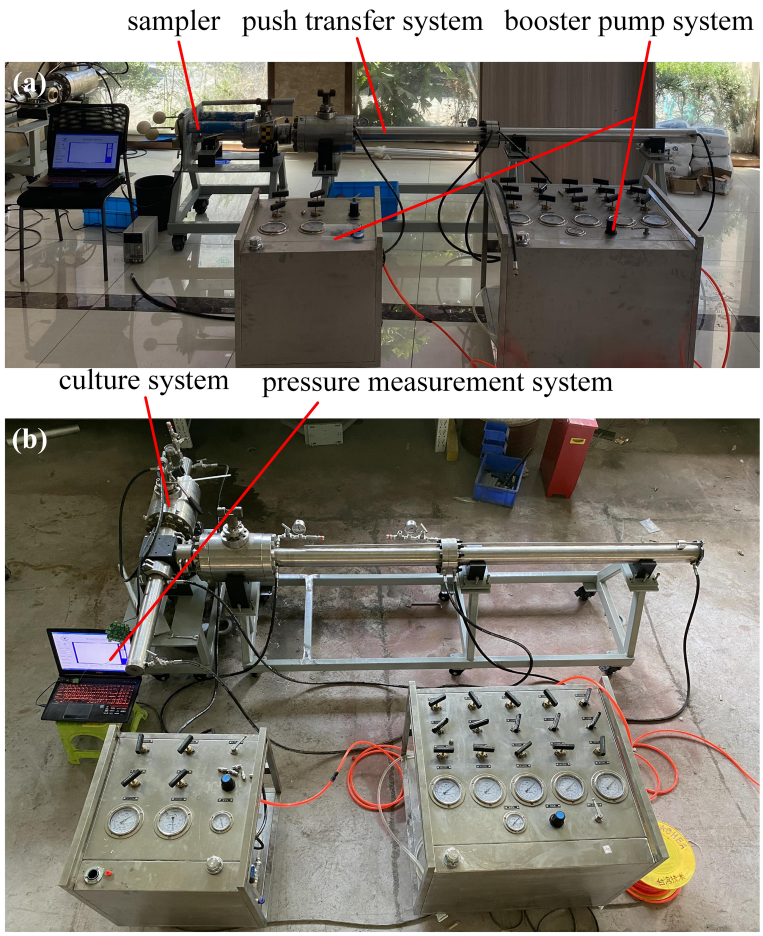

FIGURE 9
Experimental device and construction, **(A)** the transfer device is connected to the sampler and **(B)** the transfer device is connected to the culture kettle.

$$Z = \frac{L^2}{rt}\sqrt{1-\mu^2} \tag{2}$$

4.1.2 Pressure fluctuations in the transfer process

The Figures 11A-C show the simulated pressure evolution of the three key steps (pushing the secondary sampling tube into the sampler, recovering secondary sampling tube, and pushing the putter-B) with the movement of the mechanism under three pressure conditions (10MPa, 20MPa, and 30MPa) respectively. Comparing the Figures 11A-C, it can be seen that the pressure fluctuation amplitudes caused by the actions of the three mechanisms under different pressure conditions are all within 0.89 MPa, which shows that the pressure fluctuation amplitude has no obvious relationship with the pressure of the working conditions and also the mechanism that produces the action. The pressure fluctuations of each process at different pressure conditions can be found in Table 3.

Moreover, in order to identify the factors that affect the pressure fluctuation amplitude, based on the process of pushing the secondary sampling tube into the sampler, the influence of the outlet flow of the booster pump on the pressure fluctuation amplitude was studied. As shown in the Figure 11D, the pressure fluctuation amplitude increases with the increasing outlet flow of the booster pump, which means that a small flow booster pump can be selected to keep the pressure stability during the transfer process.

4.3 Laboratory test

4.3.1 Pressure-retaining performance test

Furthermore, the laboratory test is carried out to verify the feasibility of device application, and also verify the simulation results. Figure 12 shows the internal pressure drop of the two systems within 2 hours, and the pressure decreased from

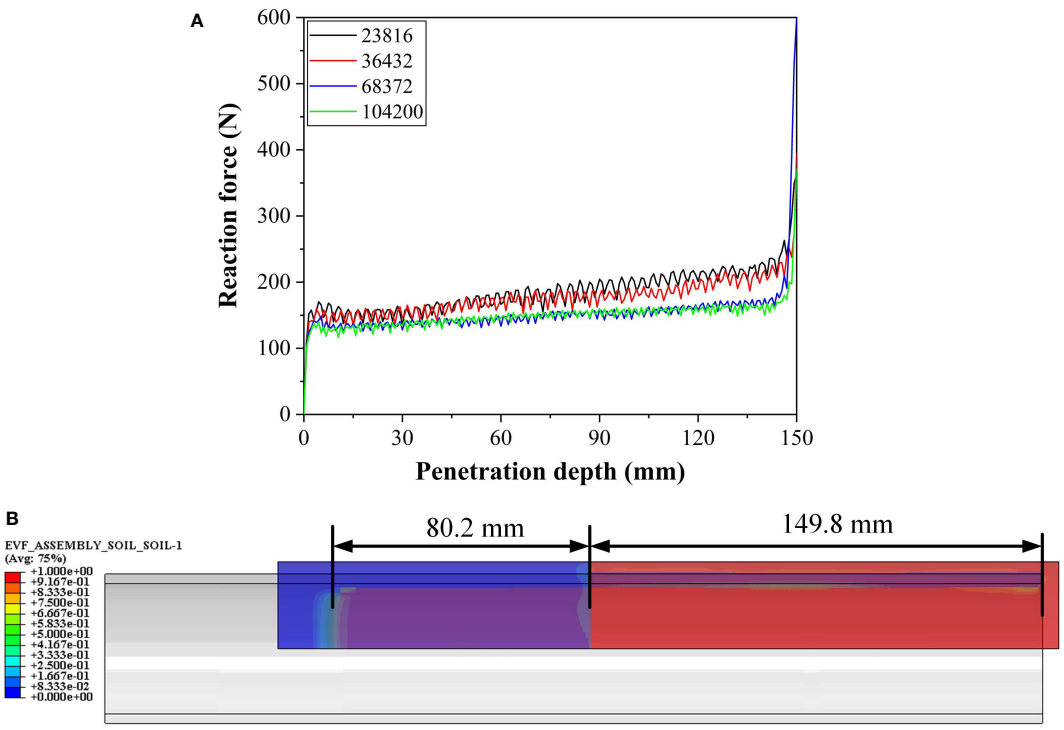

FIGURE 10
(A) Evolution of penetration resistance with penetration depth, and **(B)** profile of soil deformation.

30.60MPa to 28.34MPa (system-1, decreased by 7.4%) and 30.60MPa to 28.18MPa (system-2, decreased by 7.9%), respectively, which shows that the transfer device has sufficient strength and sealing performance compared with other pressure-retaining devices (Abid et al., 2015; Peoples et al., 2019; He et al., 2020). Since the volume of the system-2 chamber is greater than the volume of the system-1 chamber, the pressure drops in system-2 is greater.

4.2.2 Sample transfer test

The Figure 13 shows the experimental pressure evolution of the four key steps (pushing the secondary sampling tube into the sampler, recovering secondary sampling tube, pushing the putter-B, and pushing the putter-C) with the movement of the mechanism under three pressure conditions (10MPa, 20MPa, and 30MPa) respectively. The largest pressure fluctuation occurs in the recovery process of the secondary sampling tube under 30MPa, and the pressure fluctuation amplitude is 29.96MPa to 31.40 MPa (a change of 4.8%, Figure 13B), which is slightly larger than the simulation result (0.89MPa). The pressure fluctuations of each process at different pressure conditions can be found in Table 3.

Since the system is pressurized by a single stroke gas-liquid booster pump, the frequency of pressure fluctuation is related to the working frequency of the gas-liquid booster pump, which can be adjusted by the gas source pressure, and the magnitude of pressure fluctuation is related to the flow degree of the outlet valve of the gas-liquid booster pump. Furthermore, by comparing Figures 13A-D, it can be found that there is no obvious relationship between the pressure fluctuation and the pressure under the test condition and motion mechanism that generates the action, which agrees with the findings from the simulation.

In order to test the ability of the device to transfer samples, a complete transfer operation was carried out by pre-placing 300ml of clay and 300ml of water in the sampler under the working pressure of 30 MPa, as shown in the Figure 14A. Before the test, the threshold pressure of the pressure relief valve of the overlying water chamber is adjusted to 30MPa, and then, the high-pressure water is pumped into the interface-A1 (see Figure 2) to move the secondary sampling tube and compress the overlying water to flow out from the pressure relief valve, as shown in Figure 14B. During the whole process, the pressure inside the transfer system is maintained at about 30MPa.

Then, according to the steps in sections *2.4.1* and *2.4.2*, the pressure-retaining transfer of the sediment from the sampler to the culture kettle is completed, and the transferred sediment is shown in the Figure 14C, which verifies the conclusion obtained from the simulation that the soil plug effect will not occur in the secondary sampling pipe. During the complete pressure-retaining

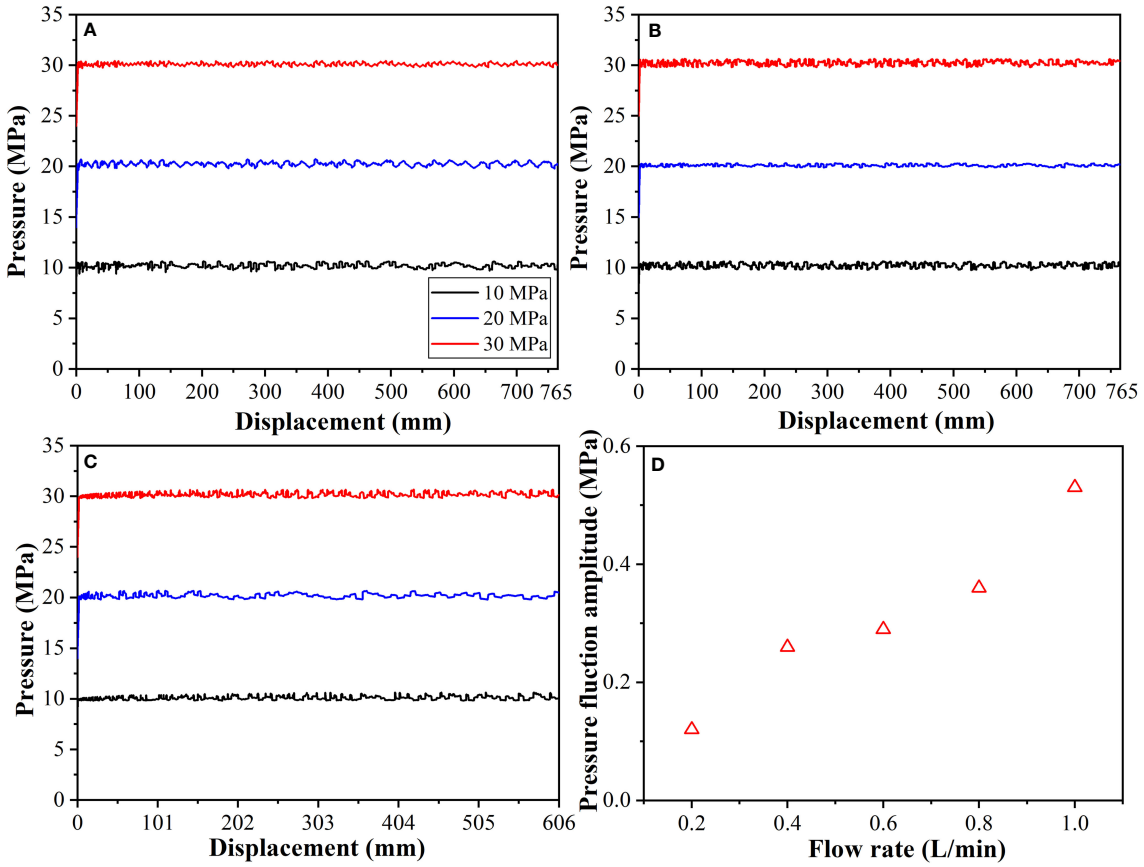

FIGURE 11
Pressure evolution with displacement during the process of **(A)** pushing the secondary sampling tube into the sampler (Step3 in section *2.4.1*), **(B)** recovering secondary sampling tube (Step4 in section *2.4.1*), **(C)** pushing the putter-B (Step2 in section *2.4.2*), and **(D)** pressure fluctuation amplitude at different flow rates.

TABLE 3 Simulated and experimental pressure fluctuations.

Transfer action	Pressure condition/MPa	Simulated result/MPa	Experimental result/MPa
Pushing the secondary sampling tube into the sampler	10	0.71	0.90
	20	0.73	0.89
	30	0.89	1.12
Recovering secondary sampling tube	10	0.76	0.91
	20	0.75	0.89
	30	0.77	1.44
Pushing the putter-B	10	0.72	0.96
	20	0.75	0.96
	30	0.70	1.06
Pushing the putter-C	10	\	0.85
	20	\	1.25
	30	\	1.23

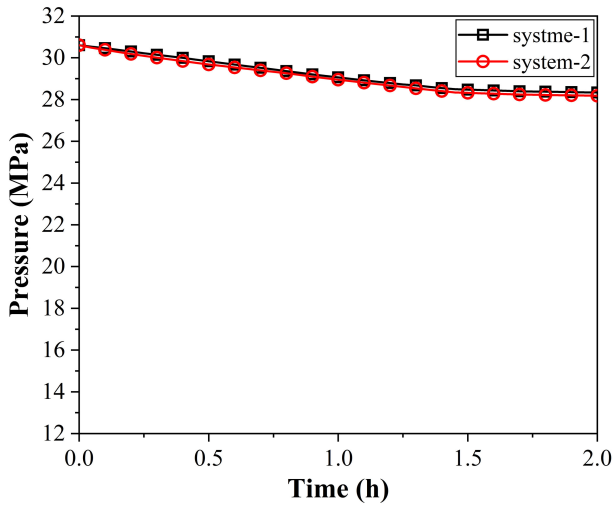

FIGURE 12
Evolution process of internal pressure of system-1 and system-2 within 2 hours. system-1: the transfer device is connected to the sampler, and system-2: the transfer device is connected to the culture kettle.

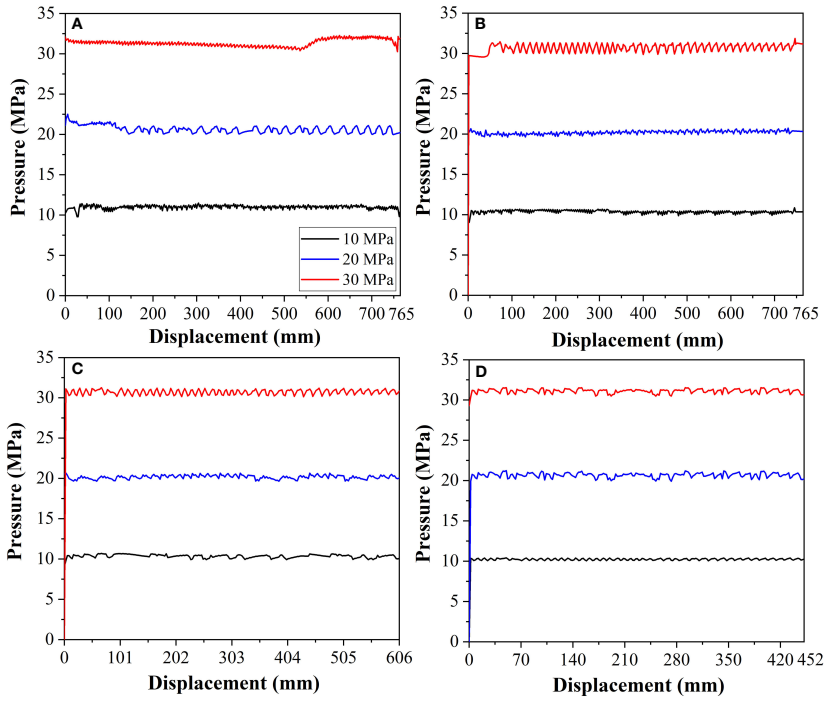

FIGURE 13
Pressure evolution with displacement during the process of **(A)** pushing the secondary sampling tube into the sampler (Step3 in section *2.4.1*), **(B)** recovering secondary sampling tube (Step4 in section *2.4.1*), **(C)** pushing the putter-B (Step2 in section *2.4.2*), and **(D)** pushing the putter-C (Step3 in section *2.4.2*).

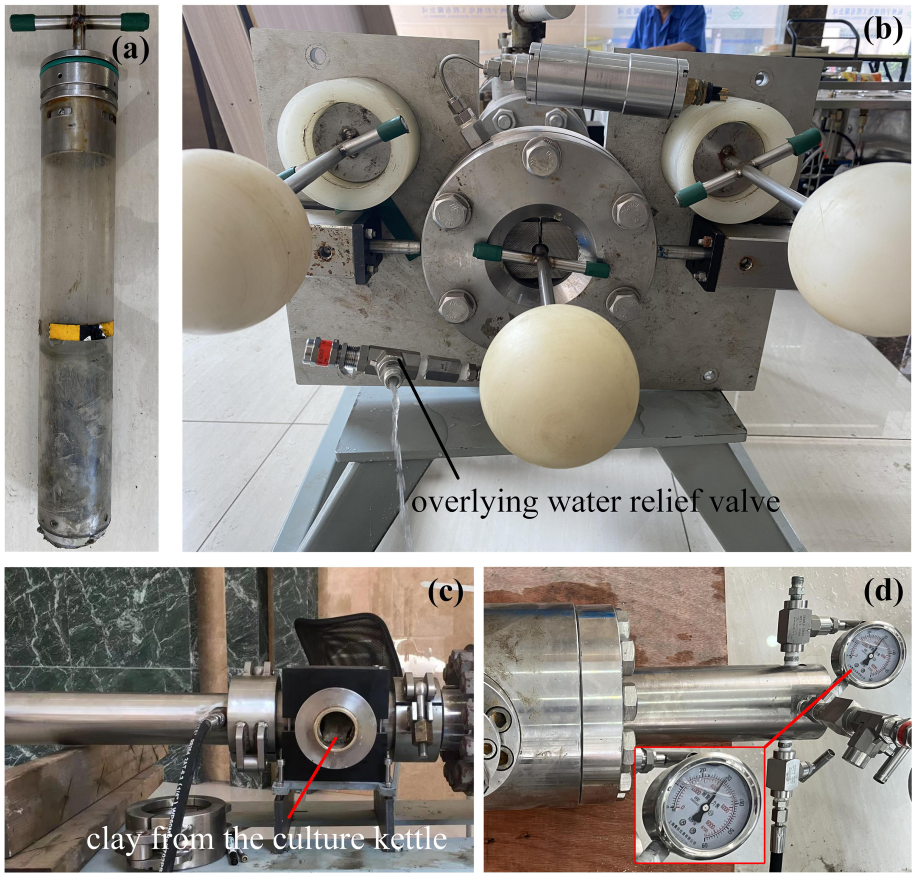

FIGURE 14
(A) sampling tube with clay in the sampler, **(B)** transfer of overlying water under 30MPa working condition, **(C)** the clay in the culture kettle, and **(D)** pressure of culture kettle after transfer.

transfer process, the final pressure Figure 14D of the sample in the culture kettle changed by 4.7% (1.41MPa) compared with the initial pressure in the sampler, which is much lower than the pressure drop of other transfer devices (Tabor et al., 1981; Chen et al., 2019; Garel et al., 2019; Priest et al., 2019).

The results of the laboratory tests demonstrate the rationality of the transfer scheme and the ability of the device to maintain pressure stability during the transfer process. The pressure fluctuation in the transfer process can be improved by adjusting the working frequency of the gas-liquid booster pump and the flow degree of the outlet valve. Additionally, compensators can be installed on the transfer device to further reduce pressure drop and pressure fluctuations.

5 Conclusion

Based on the pressure-retaining sampler for sediment and overlying seawater, the pressure-retaining transfer device with working pressure of 30MPa, composed of a push transfer system, a sampler system and a culture system, and the corresponding scheme are proposed to separate and transfer the sediment and overlying water inside the sampler under the condition of pressure-retaining. Based on the pressure relief valve with adjustable threshold pressure, the transfer device transfers the overlying water by compressing the internal volume and transfers the sediment by secondary sampling, respectively.

By using the numerical method, the secondary sampling is investigated based on the coupled Eulerian-Lagrangian (CEL) approach in the Abaqus, and the penetration resistance and coring rate of the secondary sampling tube are 141N (this value can be used to determine the injection pressure during the transfer process) and 86.2%, respectively. In addition, the pressure fluctuation during transfer process is studied based on the AMESim, and the pressure fluctuation amplitudes caused by the actions of the mechanisms under different pressure conditions are all within 0.89MPa, which shows that the pressure fluctuation amplitude has no obvious relationship with the pressure of the working conditions and the mechanism that produces the action.

Furthermore, the strength, sealing performance and ability to maintain pressure stability of the device were also studied by laboratory test. The device can maintain a pressure loss of no more than 8% within two hours, maintain pressure fluctuations during the transfer process within 4.8% (which agrees well with the findings from simulation), and ensure that the pressure in the culture kettle decreases by 4.7% relative to the pressure in the sampler after the transfer, which shows the feasibility of the device application. The pressure fluctuation during the transfer process can be improved by adjusting the working frequency of the gas-liquid booster pump and the flow degree of the outlet valve. Additionally, compensators can be installed on the transfer device to further reduce pressure drop and pressure fluctuations.

In the next, sea trials will be adopted in the methane leakage area to further study the application performance of the device. In addition, since the transfer process of the device includes a large number of needle valve switching operations, we will replace the needle valve with a solenoid valve in the future. The corresponding control system and the upper computer will also be designed to automatically complete all operations.

Data availability statement

The original contributions presented in the study are included in the article/Supplementary Material. Further inquiries can be directed to the corresponding author.

Author contributions

JG: software, data curation, and writing- original draft preparation, visualization; JC: conceptualization, supervision, and writing- reviewing and editing; QZ: data curation, visualization, and investigation; YG: software, visualization, and investigation; HL: software, visualization, and investigation; QG: methodology, writing- reviewing and editing, and validation; YL: conceptualization, supervision, and writing- reviewing and editing; YW: data curation, writing- original draft preparation, and visualization. All authors contributed to the article and approved the submitted version.

Funding

This work was supported by Key R&D of Zhejiang Province (Grant No. 2021C03183); the Finance Science and Technology Project of Hainan Province (Grant No. ZDKJ202019); the 2020 Research Program of Sanya Yazhou Bay Science and Technology City (Grant No. SKYC-2020-01-001).

Conflict of interest

The authors declare that the research was conducted in the absence of any commercial or financial relationships that could be construed as a potential conflict of interest.

Publisher's note

All claims expressed in this article are solely those of the authors and do not necessarily represent those of their affiliated organizations, or those of the publisher, the editors and the reviewers. Any product that may be evaluated in this article, or claim that may be made by its manufacturer, is not guaranteed or endorsed by the publisher.

References

Abegg, F., Hohnberg, H.-J., Pape, T., Bohrmann, G., and Freitag, J. (2008). Development and application of pressure-core-sampling systems for the investigation of gas-and gas-hydrate-bearing sediments. *Deep Sea Res. Part I Oceanogr. Res. Pap.* 55, 1590–1599. doi: 10.1016/j.dsr.2008.06.006

Abid, K., Spagnoli, G., Teodoriu, C., and Falcone, G. (2015). Review of pressure coring systems for offshore gas hydrates research. *Underw. Technol.* 33, 19–30. doi: 10.3723/ut.33.019

Amann, H., Hohnberg, H. J., and Reinelt, R. (1997). HYACE-a novel autoclave coring equipment for systematic offshore gashydrate sampling, 37–49.

Batdorf, S. B., Schildcrout, M., and Stein, M. (1947). Critical stress of thin-walled cylinders in axial compression. *Tech. Rep. Arch. image Libr* 1344), 0–21.

Chen, J.-W., Fan, W., Bingham, B., Chen, Y., Gu, L.-Y., and Li, S.-L. (2013). A long gravity-piston corer developed for seafloor gas hydrate coring utilizing an *in situ* pressure-retained method. *Energies* 6, 3353–3372. doi: 10.3390/en6073353

Chen, J. W., Gao, Q. L., Liu, H. H., Zhang, H. Q., Xiao, B., and Liu, F. L. (2019). Development of a pressure-retained transfer system of seafloor natural gas hydrates. *Environ. Geotech.* 8, 529–538. doi: 10.1680/jenge.19.00062

Chen, J., Huang, Y., Lin, Y., Zhou, P., Fang, Y., Le, X., et al. (2020). A novel sediment pressure sampling device carried by a hadal-rated lander. *J. Mar. Sci. Eng.* 8, 839. doi: 10.3390/jmse8110839

Dickens, G. R., Schroeder, D., and Hinrichs, K.-U. (2003). "The pressure core sampler (PCS) on ODP leg 201: General operations and gas release," in *Proceedings of the ocean drilling program, initial reports* (TX: Ocean Drilling Program College Station), 1–22.

Garel, M., Bonin, P., Martini, S., Guasco, S., Roumagnac, M., Bhairy, N., et al. (2019). Pressure-retaining sampler and high-pressure systems to study deep-sea microbes under *in situ* conditions. *Front. Microbiol.* 10, 453. doi: 10.3389/fmicb.2019.00453

Gornitz, V., and Fung, I. (1994). Potential distribution of methane hydrates in the world's oceans. *Global Biogeochem. Cycles* 8, 335–347. doi: 10.1029/94GB00766

Guo, J., Wang, Y., Wang, W., Ren, X., Zhou, P., Fang, Y., et al. (2022). Pressure-retaining sampler for sediment including overlying water based on heavy duty ROV-jellyfish. *Appl. Ocean Res.* 128, 103354. doi: 10.1016/j.apor.2022.103354

Hao, Z.-B., Huang, W.-Q., Qin, J.-X., and Wu, X.-Y. (2013). Estimation technique for gas hydrate saturation of pressure core samples. *Chin. J. Geophys.* 56, 3917–3921. doi: 10.6038/cjg20131133

He, S., Peng, Y., Jin, Y., Wan, B., and Liu, G. (2020). Review and analysis of key techniques in marine sediment sampling. *Chin. J. Mech. Eng.* 33. doi: 10.1186/s10033-020-00480-0

Jutzeler, M., White, J. D. L., Talling, P. J., McCanta, M., Morgan, S., Le Friant, A., et al. (2014). Coring disturbances in IODP piston cores with implications for offshore record of volcanic events and the Missoula megafloods. *Geochem. Geophys. Geosyst.* 15, 3572–3590. doi: 10.1002/2014GC005447

Kawasaki, M., Umezu, S., and Yasuda, M. (2006). Pressure temperature core sampler (PTCS). *J. Japanese Assoc. Pet. Technol.* 71, 139–147. doi: 10.3720/japt.71.139

Kim, Y. H., and Hossain, M. S. (2017). Dynamic installation, keying and diving of OMNI-max anchors in clay. *Geotechnique* 67, 78–85. doi: 10.1680/jgeot.16.T.008

Ko, J., Jeong, S., and Kim, J. (2017). Application of a coupled eulerian-Lagrangian technique on constructability problems of site on very soft soil. *Appl. Sci.* 7, 1080. doi: 10.3390/app7101080

Konkol, J. (2015). Numerical estimation of the pile toe and shaft unit resistances during the installation process in sands. *Stud. Geotech. Mech.*), 37–44. doi: 10.1515/sgem-2015-0005

Li, S., Cheng, Y., and Qin, H. (2006). Development of pressure piston corer for exploring natural gas hydrates. *Journal-Zhejiang Univ. Eng. Sci.* 40, 888. doi: 10.3785/j.issn.1008-973X.2006.05.033

Liu, J., Chen, J., Liu, F., Gu, L., Sheng, Y., Zhang, M., et al. (2014). "Development of one pressure core transfer device for one long gravity-piston pressure-retained corer," in *2014 oceans-st. john's* (St. John's, NL, Canada: IEEE), 1–6.

Matsumoto, R., Ryu, B.-J., Lee, S.-R., Lin, S., Wu, S., Sain, K., et al. (2011). Occurrence and exploration of gas hydrate in the marginal seas and continental margin of the Asia and Oceania region. *Mar. Pet. Geol.* 28, 1751–1767. doi: 10.1016/j.marpetgeo.2011.09.009

Minato, A., Joarder, M. D. M. A., Ozawa, S., Kadoya, M., and Sugimoto, N. (1999). Development of a lidar system for measuring methane using a gas correlation method. *Jpn. J. Appl. Phys.* 38, 6130. doi: 10.1143/JJAP.38.6130

Peoples, L. M., Norenberg, M., Price, D., McGoldrick, M., Novotny, M., Bochdansky, A., et al. (2019). A full-ocean-depth rated modular lander and pressure-retaining sampler capable of collecting hadal-endemic microbes under *in situ* conditions. *Deep Sea Res. Part I Oceanogr. Res. Pap.* 143, 50–57. doi: 10.1016/j.dsr.2018.11.010

Priest, J. A., Druce, M., Roberts, J., Schultheiss, P., Nakatsuka, Y., and Suzuki, K. (2015). PCATS triaxial: A new geotechnical apparatus for characterizing pressure cores from the nankai trough, Japan. *Mar. Pet. Geol.* 66, 460–470. doi: 10.1016/j.marpetgeo.2014.12.005

Priest, J. A., Hayley, J. L., Smith, W. E., Schultheiss, P., and Roberts, J. (2019). PCATS triaxial testing: Geomechanical properties of sediments from pressure cores recovered from the bay of Bengal during expedition NGHP-02. *Mar. Pet. Geol.* 108, 424–438. doi: 10.1016/j.marpetgeo.2018.07.005

Qin, H., Cai, Z., Hu, H., Wang, J., Ye, W., and Chen, Y. (2016). Numerical analysis of gravity coring using coupled eulerian-Lagrangian method and a new corer. *Mar. Geores. Geotechnol.* 34, 403–408. doi: 10.1080/1064119X.2014.958880

Ramakrishnan, R., Hiremath, S. S., and Singaperumal, M. (2012). Theoretical investigations on the effect of system parameters in series hydraulic hybrid system with hydrostatic regenerative braking. *J. Mech. Sci. Technol.* 26, 1321–1331. doi: 10.1007/s12206-012-0321-y

Roberts, H. H., and Aharon, P. (1994). Hydrocarbon-derived carbonate buildups of the northern gulf of Mexico continental slope: A review of submersible investigations. *Geo-Marine Lett.* 14, 135–148. doi: 10.1007/BF01203725

Rothwell, R. G., and Rack, F. R. (2006). New techniques in sediment core analysis: an introduction. *Geol. Soc London Spec. Publ.* 267, 1–29. doi: 10.1144/GSL.SP.2006.267.01.01

Schultheiss, P. J., Francis, T. J. G., Holland, M., Roberts, J. A., Amann, H., Parkes, R. J., et al. (2006). Pressure coring, logging and subsampling with the HYACINTH system. *Geol. Soc London Spec. Publ.* 267, 151–163. doi: 10.1144/GSL.SP.2006.267.01.11

Schultheiss, P., Holland, M., and Humphrey, G. (2009). Wireline coring and analysis under pressure: Recent use and future developments of the HYACINTH system. *Sci. Drill.* 7, 44–50. doi: 10.5194/sd-7-44-2009

Schultheiss, P. J., and Weaver, P. P. E. (1992). "Multi-sensor core logging for science and industry," in *OCEANS 92 proceedings M_Mastering the oceans through technology* (Newport, RI, USA: IEEE), 608–613.

Suess, E., Torres, M. E., Bohrmann, G., Collier, R. W., Greinert, J., Linke, P., et al. (1999). Gas hydrate destabilization: Enhanced dewatering, benthic material turnover and large methane plumes at the cascadia convergent margin. *Earth Planet. Sci. Lett.* 170, 1–15. doi: 10.1016/S0012-821X(99)00092-8

Tabor, P. S., Deming, J. W., Ohwada, K., Davis, H., Waxman, M., and Colwell, R. R. (1981). A pressure-retaining deep ocean sampler and transfer system for measurement of microbial activity in the deep sea. *Microb. Ecol.* 7, 51–65. doi: 10.1007/BF02010478

Tong, D., Liao, C., and Chen, J. (2019). Wave-monopile-seabed interaction considering nonlinear pile-soil contact. *Comput. Geotech.* 113, 103076. doi: 10.1016/j.compgeo.2019.04.021

Tréhu, A. M. (2006). Gas hydrates in marine sediments: Lessons from scientific ocean drilling. *Oceanography* 19, 124–142. doi: 10.5670/oceanog.2006.11

Wang, H., Ruan, D.-R., Cao, C., Fang, J.-S., Zhou, P., Fang, Y.-P., et al. (2022). Collection sediment from Mariana trench with a novel pressure-retaining sampler. *Deep Sea Res. Part I Oceanogr. Res. Pap.* 183, 103740. doi: 10.1016/j.dsr.2022.103740

Weil, G. J. (1993). "Non contact, remote sensing of buried water pipeline leaks using infrared thermography," in *Water management in the'90s: A time for innovation* (St. Louis, United States: ASCE), 404–407.

Xuanyin, W., Xiaoxiao, L., and Fushang, L. (2010). Analysis on oscillation in electro-hydraulic regulating system of steam turbine and fault diagnosis based on PSOBP. *Expert Syst. Appl.* 37, 3887–3892. doi: 10.1016/j.eswa.2009.11.029

Yalong, J., Tingli, C., and Yuquan, Z. (2011). Methane monitoring system based on absorption spectroscopy of tunable diode laser. *J. Electron. Meas. Instrum* 25, 265–271. doi: 10.1631/jzus.B1000265

Zeng, X., Li, G., Yin, G., Song, D., Li, S., and Yang, N. (2018). Model predictive control-based dynamic coordinate strategy for hydraulic hub-motor auxiliary system of a heavy commercial vehicle. *Mech. Syst. Signal Process* 101, 97–120. doi: 10.1016/j.ymssp.2017.08.029

Zhang, P., Chen, J., Gao, Q., Xiao, B., Geng, X., and Zhou, P. (2019). Research on a temperature control device for seawater hydraulic systems based on a natural gas hydrate core sample pressure-retaining and transfer device. *Energies* 12), 1–20. doi: 10.3390/en12203990

Zhao, Z., Jia, M., Wang, F., and Wang, S. (2009). Intermittent chaos and sliding window symbol sequence statistics-based early fault diagnosis for hydraulic pump on hydraulic tube tester. *Mech. Syst. Signal Process* 23, 1573–1585. doi: 10.1016/j.ymssp.2009.01.011

Zhen, M., Jinjian, C., and Jianhua, W. (2017). The coupled eulerian-Lagrangian analysis of pile jacking process in saturated soft clay by using modified cam-clay model. *J. Shanghai Jiaotong Univ.* 51, 263. doi: 10.16183/j.cnki.jsjtu.2017.03.002

Zhu, H., Chen, J. W., Ren, Z. Q., Zhang, P. H., Gao, Q.L., Le, X.L., et al. (2022). A new technique for high-fidelity cutting technology for hydrate samples. *J. Zhejiang Univ. Sci. A* 23, 40–54. doi: 10.1631/jzus.A2100188

Zhu, H., Liu, Q., Deng, J., Wang, G., Xiao, X., Jiang, Z., et al. (2011). Pressure and temperature preservation techniques for gas-hydrate-bearing sediments sampling. *Energy* 36, 4542–4551. doi: 10.1016/j.energy.2011.03.053

Zhu, H. Y., Liu, Q. Y., Wong, G. R., Xiao, X. H., Zhu, X. H., Jiang, Z. L., et al. (2013). A pressure and temperature preservation system for gas-hydrate-bearing sediments sampler. *Pet. Sci. Technol.* 31, 652–662. doi: 10.1080/10916466.2010.531352

frontiers | Frontiers in Marine Science

TYPE Original Research
PUBLISHED 12 December 2022
DOI 10.3389/fmars.2022.1075446

OPEN ACCESS

EDITED BY
Zhilei Sun,
Qingdao Institute of Marine Geology (QIMG), China

REVIEWED BY
Yongping Jin,
Hunan University of Science and Technology, China
Cong Hu,
Ocean University of China, China

*CORRESPONDENCE
Haocai Huang
hchuang@zju.edu.cn

SPECIALTY SECTION
This article was submitted to Ocean Observation, a section of the journal Frontiers in Marine Science

RECEIVED 20 October 2022
ACCEPTED 22 November 2022
PUBLISHED 12 December 2022

CITATION
Fang Y, Chen D, Deng Y and Huang H (2022) Analysis of influencing factors on displacement sampling performance of deep-sea gas-tight sampler.
Front. Mar. Sci. 9:1075446.
doi: 10.3389/fmars.2022.1075446

Analysis of influencing factors on displacement sampling performance of deep-sea gas-tight sampler

Yuanli Fang[1], Daohua Chen[2,3], Yinan Deng[2,3] and Haocai Huang[1,4]*

[1]Ocean College, Zhejiang University, Zhoushan, China, [2]Southern Marine Science and Engineering Guangdong Laboratory (Guangzhou), Guangzhou, China, [3]Institute of Experimental Testing, Guangzhou Marine Geological Survey (GMGS), Guangzhou, China, [4]Dalian Maritime University, Shenzhen Research Institute of Dalian Maritime University, Shenzhen, China

The collection and research of deep sea water has always been a hot and key topic in the field of marine research. Collecting seawater samples that can truly reflect the *in-situ* water composition information through a deep-sea sampler is an important technical means in the field of deep-sea exploration. The deep-sea water sampler designed in this subject samples deep-sea water by displacement sampling. According to the jet theory, the method of numerical calculation combined with experiment is adopted, the influence of indirect displacement, shape and diameter of sampling inlet, Coanda distance, sampling rate and other factors on the displacement effect is analyzed in this paper. The results of the study demonstrate that at low speed, multiple displacements can improve the displacement effect. In the high-speed sampling state, a single displacement method should be adopted. The design of making the sampling port as close as possible to the wall of the sampling cavity helps to strengthen the plane jet to improve the displacement efficiency. The displacement efficiency can be slightly improved by using the rectangular sampling inlet and outlet. As the extraction speed increases, the liquid mixing area becomes larger. Through discussion and comparison with similar research at home and abroad, the sampler has good performance and high sampling purity. The analysis of the effect of changes in sample temperature on the sampling displacement efficiency will be performed in the future. The research on the thermal insulation performance of the sampling channel will be put on the agenda.

KEYWORDS

deep sea, marine, seawater sample, displacement4, jet

Introduction

At present, there are two main methods for the study of deep-sea hydrothermal fluids, cold springs and other bottom waters: the first is to measure the physical and chemical quantities *in situ* at the hydrothermal vent; the second is to obtain hydrothermal samples, analysis in the laboratory after return. Through *in situ* measurement, we can obtain long-term and continuous observation data so as to obtain the real dynamic data of seawater physical and chemical data. However, it is still not comparable to laboratory measurements in terms of measurement accuracy and detection parameter range. At present, the sampling of deep sea water is still irreplaceable (Edgcomb et al., 2016). Since the nineteenth century, various institutions at home and abroad have developed a variety of deep-sea water samplers with different functions. Especially in recent years, deep-sea water sampler technology has developed rapidly. ANEMONE-11 with 128 sampling channels was proposed by (Okamura et al., 2013). It is mainly carried on the AUV and used for monitoring the chemical and biological components of water. The WHATS series of three generations of water samplers has developed in Japan, and a new idea of sequence triggering is proposed. The blocking rod and the sheaves on the inlet valve and the outlet valve form a group Space sheave stepping transmission mechanism through a mechanical sliding arm with blocking rods installed at both ends (Saegusa et al., 2006; Junichi et al., 2017). An inexpensive and easy-to-use high-resolution water sampling device for ecological research and water quality analysis was developed at Indiana Wesleyan University (Sattley et al., 2017). A sediment pore water sampler that can prevent samples from being polluted by seawater was invented by Institute of Disaster Prevention, Langfang Hebei and tested in the northern part of the South China Sea (Liu et al., 2018). Compared with the previous water sampler, the displacement sampling method is used in this sampler to collect bottom water samples. The deep-sea water sampler developed in this study belongs to the pass-flow sampler, and the sampling chamber needs to be prefilled with deionized water. On the other hand, this design can equalize the pressure inside and outside of the water sampler during the descent process, so as to avoid leakage or rupture of the sampling chamber due to the huge pressure difference between inside and outside during the descent process. The pass-through structure can also use the sample water to scour the sampling channel to avoid pollution. At the beginning of sampling, the seawater from the outside is continuously sucked into the sampling chamber, and the deionized water is continuously discharged. The process in which the two fluids replace each other is called displacement process. The mixing of deionized water and water samples in the process of displacement affects the displacement effect and the purity of sample collection. It is very important to study the factors affecting the displacement process, optimize the related parameters, improve the displacement efficiency, shorten the necessary time of displacement, and improve the sampling reliability without affecting the sampling effect for the overall performance improvement of water sampler. However, there are few deep-sea samplers using displacement sampling principle at home and abroad. We intends to explore the influence of different parameters on sampling efficiency through numerical simulation and sea trials from the indirect displacement, shape and diameter of sampling inlet, Coanda distance and sampling rate in this paper. The full paper is mainly divided into the following parts: Materials and methods, Results, Discussion, and Conclusions. Jet theory, displacement theory and the design of the water sampler are introduced in Chapter 2. The numerical results of displacement efficiency corresponding to each parameter and the sea trial of the prototype are listed in Chapter 3. Other similar studies at home and abroad are discussed in Chapter 4. Finally, the comprehensive conclusion of the whole study is summarized in Chapter 5.

Materials and methods

The theory of jet and displacement

The displacement process is a very complex fluid motion process. It is the jet movement that has an important influence on the displacement process. The process of the sample from the relatively narrow sampling line into the relatively wide sampling cavity is a kind of jet movement. Jet refers to a moving fluid that is ejected from various discharge ports or mechanically propelled into another surrounding fluid domain. Usually the entire perimeter of the jet is fluid, which is the main difference between it and pipe flow and open channel flow. From the perspective of flow morphology, jets can be divided into laminar jets and turbulent jets, which can be distinguished by the Reynolds number. When $Re > 30$, the state of the jet can be considered as a turbulent jet (Yu, 1993). As the sampling speed increases, the jet motion also produces an evolution from laminar jet to turbulent jet, and the displacement motion is affected by the jet characteristics. In addition, there is a density difference between the external seawater sample and deionized water, so the displacement flow field between the seawater sample and the pre-charged deionized water is a kind of hyperpycnal flow. Depending on the size of the density difference, the inflow will experience greater or lesser buoyancy.

$$Re = \frac{2b_0u_0}{\nu} \tag{1}$$

In the formula, $b_0$is the outlet radius of the jet nozzle, $u_0$is the outlet velocity, and ν is the kinematic viscosity of the fluid.

The critical flow rate at a Reynolds number of 30 is:

$$u_0' = \frac{30\nu}{2b_0} \tag{2}$$

The flow Q is:

$$Q = S \cdot u_0 = \pi b_0^2 \frac{30\nu}{2b_0} = 15\pi b_0 \nu \tag{3}$$

In the formula, S is the cross-sectional area of the nozzle outlet, and it is assumed that the flow velocity on the cross-section is uniform. It can be known that when the kinematic viscosity of the fluid is constant, the critical flow rate is proportional to the radius of the nozzle outlet.

The overall structure of the turbulent jet is very complex. For the convenience of analysis, researchers usually divide the jet into several regions according to different flow characteristics, namely: the initial section, the transition section, and the main section. The shear flow area extending from the nozzle outlet boundary to the inside and outside is called the free shear layer area; the central part is not affected by turbulent mixing and the area where the nozzle velocity is maintained is called the jet core area; along the longitudinal direction The area from the nozzle outlet to the end of the core area is called the initial section of the jet; most of the downstream area of the initial section is a fully developed turbulent mixing area, which is called the main section of the jet; between the initial section and the main section The transition section is usually ignored in the gap because it is too short.

The movement of the buoyant jet is the result of the combined action of the initial momentum and the buoyancy. When the direction of the buoyancy is the same as the direction of the initial momentum, it is called a positive buoyant jet, and if it is the opposite, it is a negative buoyant jet. For the purpose of improving the displacement efficiency, it is desirable to reduce the mixing of incident samples with prefilled water. Preliminary analysis shows that if it is a positive buoyancy jet, the incident sample will enter the ambient fluid faster under the action of buoyancy, that is, pre-charged water. Pure water and intensify mixing. If it is a negatively buoyant jet, the direction of buoyancy is opposite to the direction of initial momentum, the velocity of the incident sample will be slowed down, and delamination may occur, thereby improving the displacement efficiency.

Compared to the previously discussed case, this jet will be subject to the buoyant force produced by the density difference, and the ratio of inertial force to buoyancy force plays a decisive role in the jet motion. The contrast of these two forces, their relative action, can be measured by the densimetric Froude number (Yu, 1993):

$$Fr = \frac{u}{\sqrt{\frac{\rho - \rho_a}{\rho_a} g b_0}} = \frac{u}{\sqrt{g^* b_0}} \tag{4}$$

where u is the characteristic velocity of the jet; b_0 is the characteristic length of the jet, which in this paper is the inlet radius of the jet; ρ is the density of the jet; ρ_a is the density of the surrounding fluid; g is the acceleration of gravity. When Fr is low, the sinking fluid in the negative buoyancy jet will gradually settle in the lower part of the sampling chamber and replace the ambient fluid near the inlet, and at the same time generate a certain amount of mixing with it. When Fr is high, it shows strong jet characteristics, The fluid may strike a reflection near the exit face.

Because the sampling cavity is a limited space and the density of the surrounding fluid changes in real time, it is difficult to describe the displacement process accurately in theory, so it needs to be further discussed through simulation and experiments.

In order to better describe the displacement effect, the indicator of displacement rate is proposed, which is defined as follows:

$$E(t) = \frac{V_{aim}(t)}{V_{vol}} \tag{5}$$

$E(t)$ is the displacement rate, that is, the ratio of the cavity volume of the target sample station, t is the displacement time, V_{vol} is the cavity volume, and $V_{aim}(t)$ is the volume of the sample in the cavity at t. The value of $E(t)$ varies from 0 to 1, which is a function of t and describes the displacement completion degree in the sampling cavity at a certain time point.

Numerical calculation and analysis

Fluent was used for numerical analysis. To describe the flow characteristics of the near-wall flow field, the k-epsilon equation was chosen to solve the model. Enhanced wall treatments are used, and the full buoyancy effect is turned on to emphasize the role of buoyancy in the motion of the flow field. During the solution process, chemical reactions between the sample and the pre-filled water and metal precipitation were ignored. On the other hand, although there is a density difference between the sample and the prefilled water, this density difference is actually very small. In order to facilitate convergence, the Boussinesq assumption can be considered to hold, that is, the density variation due to the inhomogeneity of the substance concentration is small. When solving the N-S equations, the densities in terms other than the gravity term are treated as constants.

The sampling channel is arranged in a U shape, and the two sampling chambers are connected in series. The density of the pre-charged deionized water is 1000kg/m^3 and the density of the sample is 1035kg/m^3. The sampling cavity model is set to be cylindrical, the cavity height is 112.5mm, the diameter is 52mm, the wall thickness is 9mm, the outer diameter of the sampling inlet and outlet is 6.2mm, and the inner diameter is 4mm. The

inflow velocity ranges from 0.044 to 0.2m/s, and the displacement time ranges from 500s to 1000s. The numerical calculation model is shown in Figure 1.

Free jets and clinging wall jets

According to the research of Imperial College London and University of Cambridge, under the same source conditions, the walled jet is stronger than the free jet (Burridge and Hunt, 2017).

We can assume that the force at the source is large enough that the inertial force dominates the buoyancy at the source. The established flow is turbulent and the viscous forces are much smaller than the inertial forces.

$$L_M = \frac{M_0^{3/4}}{B_0^{1/2}}, \quad Q_M = \frac{M_0^{5/4}}{B_0^{1/2}} \tag{6}$$

πM_0 and πB_0 are source fluxes of specific momentum and buoyancy. For the near-field region, the resulting dominant length scale (the jet length) and the dominant volume flux scale may be written respectively by (6). where the subscript M is used to convey that it is the source momentum flux that is dominant in this region of flow.

The dynamics of circular and rectangular jets in cross flow were studied at Louisiana State University and the Illinois Institute of Technology. Numerical methods of finite volume code in-house code chem3D are used to compute such problems (Pokharel and Acharya, 2021).

$$\frac{\partial}{\partial \xi_i}\left(\sqrt{g}\overline{U}^j\right) = 0 \tag{7}$$

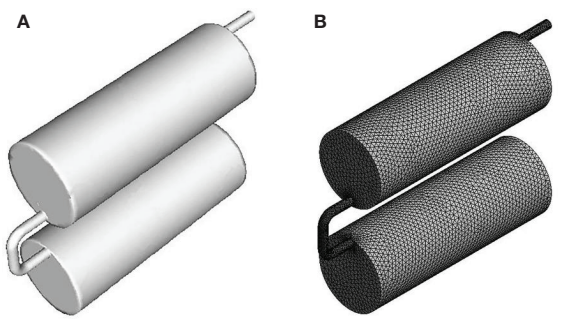

FIGURE 1
numerical calculation model, **(A)** The internal structure of the sampling channel, **(B)** CFD calculation mesh diagram.

$$\frac{\partial}{\partial t}\left(\sqrt{g}\overline{u}_i\right) + \frac{\partial}{\partial \xi_j}\left(\sqrt{g}\overline{U}^j\overline{u}_i\right) = -\frac{\partial}{\partial \xi_j}\left(\sqrt{g}\left(a^j\right)_i\overline{p}\right) + \frac{\partial}{\partial \xi_j}\left(\left(\frac{1}{Re}+\frac{1}{Re}\right)\sqrt{g}g^{jk}\frac{\partial \overline{u}_i}{\partial \xi_k}\right) \tag{8}$$

$$\frac{1}{Re_t} = C_s^2\left(\sqrt{g}\right)^{2/3}\left|\overline{S}\right| \tag{9}$$

$$\overline{S}_{ik} = \frac{1}{2}\left(\left(a^m\right)_k\frac{\partial \overline{u}i}{\partial \xi_m} + \left(a^m\right)_i\frac{\partial \overline{u}_k}{\partial \xi_m}\right) \tag{10}$$

Where $\sqrt{g}\overline{U}^j = \sqrt{g}(a^j)_k\overline{u}_k$ is the contravariant velocity components, $(a^j)_k = \frac{\partial \xi_j}{\partial x_k}$ is the associated metric terms, $\sqrt{g}$ is the Jacobian of the transformation, $|\overline{S}|$ is the magnitude of the strain rate tensor. (6) represents the conservation of mass, (7) represents the conservation of momentum. (8) and (9) represent the relationship of eddy viscosity to the strain rate tensor and Smagorinsky constant.

Liquid stratification

The jet is a flow with opposite momentum and buoyancy, and the vertical velocity of the jet gradually decreases and becomes zero at the maximum penetration height of the jet. After that, the jet reverses direction and forms a falling flow (OF – Out flow); the falling flow and the upward jet (IF – In flow) injected into the ambient fluid from the jet inlet are mixed with each other due to the viscosity and shear of the fluid., forming an entrainment phenomenon. At the same time, the falling flow also mixes with the adjacent ambient fluid (AF – Ambient flow), resulting in a decrease in its density and an increase in its volume. When the falling fluid descends to the bottom, it will form an intrusion that extends horizontally outward (Li, 2021). Therefore, how to minimize the entrainment and mixing between different fluid layers caused by the buoyant jet characteristics of the samples entering the sampling cavity during the sampling process is one of the key research contents.

When the environmental fluid is linearly stratified, the flow behavior of the negative buoyancy jet is not only controlled by *Re* and *Fr*, but also controlled by the stratification parameter *Sp* of the environmental fluid. The definition of *Sp* is: $Sp = \frac{1}{\rho_{a,0}} \cdot \frac{d\rho_{a,Z}}{dZ}$, $\rho_{a,0}$ and $\rho_{a,Z}$ are respectively located in Initial density of ambient fluid at bottom Z=0 and height Z.

If the fluid load Boussinesq is approximated, *Sp* can also be replaced by the temperature stratification parameter S defined as follows, $S = \frac{dT_{a,Z}}{dZ} = \frac{Sp}{\beta}$, where $T_{a,z}$ is the initial temperature of the ambient fluid at height Z. If this formula is dimensionless, the dimensionless temperature layer S can be expressed as $S = \frac{d\theta_{a,z}}{dz} = \frac{X_0}{(T_{a,0}-T_0)}S = \frac{X_0}{\beta(T_{a,0}-T_0)}Sp$. Here, $\theta_{a,z}=(T_{a,z}-T_{a,0})/(T_{a,0}-T_0)$, $T_{a,0}$ is the initial temperature of the ambient fluid at the bottom (Z=0) (Gao, 2018).

Design of the water sampler

The deep-sea through-flow *in-situ* air-tight water sampler is mainly composed of a sampling channel, a trigger mechanism, a trigger drive system and an auxiliary mechanism. The sampling channel is mainly composed of sampling cavity, sampling inlet, sampling outlet, sampling valve, sampling pump, connecting pipe, etc., as shown in Figure 2.

The structure of the sampling channel as a whole continues the U-shaped design features of the first generation of water samplers in this subject. In this way, the space is more effectively used, and the sampling inlet and the sampling outlet are located on the same side, which is convenient for operation.

Results

Indirect displacement

As shown in Figure 3, when the sample inflow velocity is 0.1m/s, after the sample enters the sampling cavity from the sampling inlet located on the lower side of the cavity, the liquid front of the sample first sneaks along the wall to the left, and when it touches the left side A certain reverse flow is generated after the wall, and a certain layering phenomenon appears between the sample and the pre-filled deionized water.

When a portion of the sample begins to enter the upper sampling chamber, most of the sample in the lower sampling chamber continues to settle and raise the interface. Since the connecting channels between the sampling chambers are located on both sides of the sampling chamber, and the outlet of the sampling channel is located above the sampling chamber, the sample does not start to leave the sampling outlet until the deionized water in the lower sampling chamber is widely displaced, and the lower sampling chamber begins to leave. The deionized water in the lower sampling chamber can almost be successfully displaced.

After increasing the inlet flow rate, the displacement process in the sampling chamber presents different forms. After increasing the sample flow rate at the sampling inlet, the stratification between the sample and the pre-charged deionized water was less than before. The sample began to enter the upper sampling cavity from the lower sampling cavity very early, and the displacement rate was significantly improved, as shown in Figure 4.

For different displacement methods, considering the mixing of solutions, the effects of multiple and single displacement on displacement efficiency are discussed, and the displacement ratios of 0.5 and 0.75 are set as nodes. The double displacement with the displacement rate of 0.5 as the node and the triple displacement with the displacement rate of 0.5 and 0.75 as the nodes were set separately and compared with the single displacement effect.

It can be seen from Figure 5 that when the displacement starts from the node with a displacement rate of 0.5 and a node with a displacement rate of 0.75, the mixed solution will still appear layered, but the layered effect is not as obvious as that of a single displacement.

It can be seen from Figure 6 that the use of multiple displacement and single displacement will produce different displacement effects. When the inlet velocity of the sampling channel is 0.044m/s, the method of multiple displacement is adopted. At the middle and late stages of the displacement, the attenuation of the displacement curve is delayed, and the displacement effect is improved. When triple displacement is selected, the triple displacement will decrease relative to the

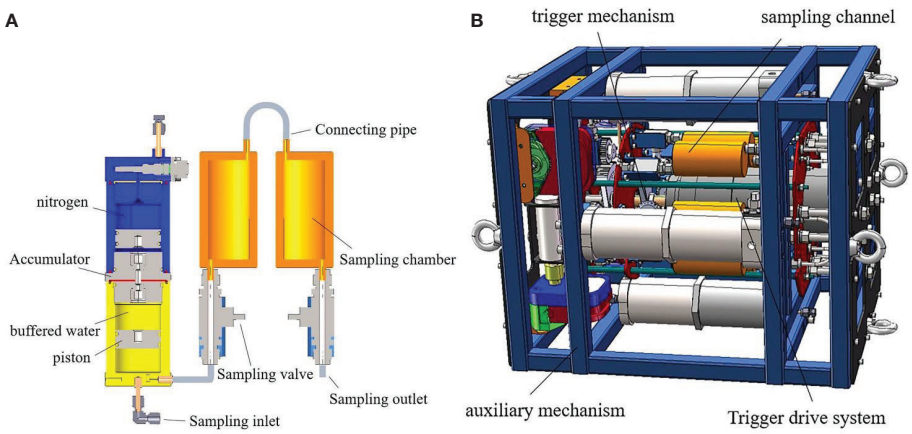

FIGURE 2
Model of the water sampler, **(A)** Sampling channel, **(B)** Overall design of the water sampler.

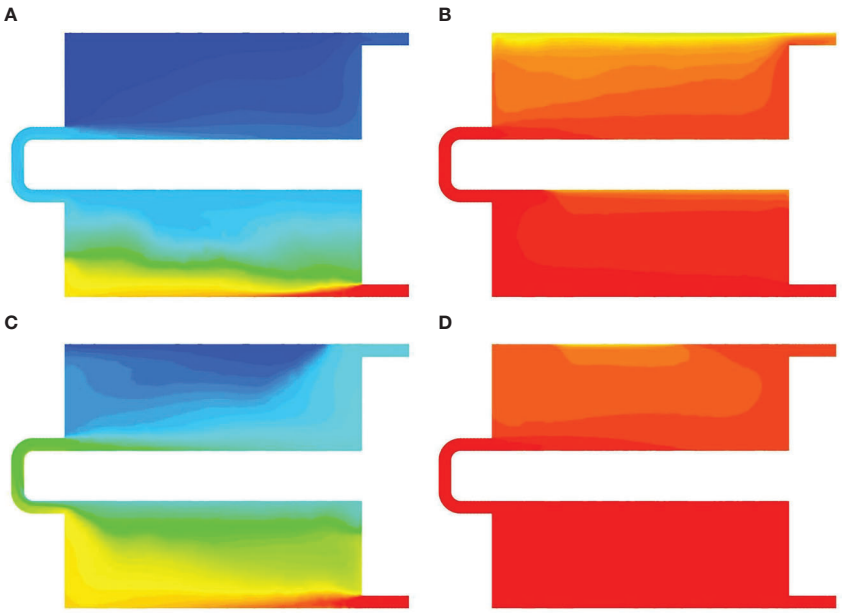

FIGURE 3
The concentration distribution of the two components in the sampling chamber, **(A, B)** The sample inflow velocity is 0.1m/s, **(C, D)** The sample inflow velocity is 0.2m/s.

double displacement after the start of the triple displacement, but it is still ahead of the single displacement.

When the sample inlet flow rate is 0.1m/s, the situation is different from that at low flow rate. When multiple displacements are used, the displacement curve decays earlier, and when single displacement is used, the displacement maintains a linear increase for a longer time, and the displacement effect is better, and the displacement effect is the worst in triple displacements.

When the sampling inlet velocity is 0.2m/s, the difference between the displacement effects of single and multiple displacement is small, and the displacement effect of single displacement is slightly ahead of that of double and triple displacement.

It can be seen that at low speed, multiple displacements can improve the displacement effect, and the number of times is appropriate, and too many times will weaken the lifting effect to a certain extent. In the high-speed sampling state, a single displacement method should be adopted to avoid the occurrence of displacement discontinuities as much as possible to ensure the best displacement effect.

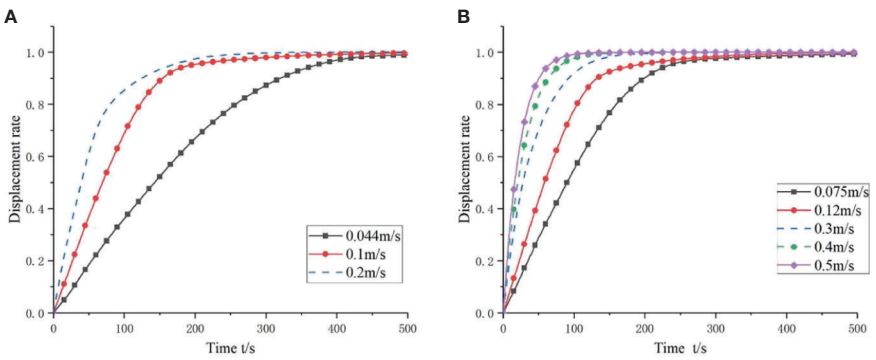

FIGURE 4
Displacement process diagram of each inflow rate, **(A)** Low speed, **(B)** High speed.

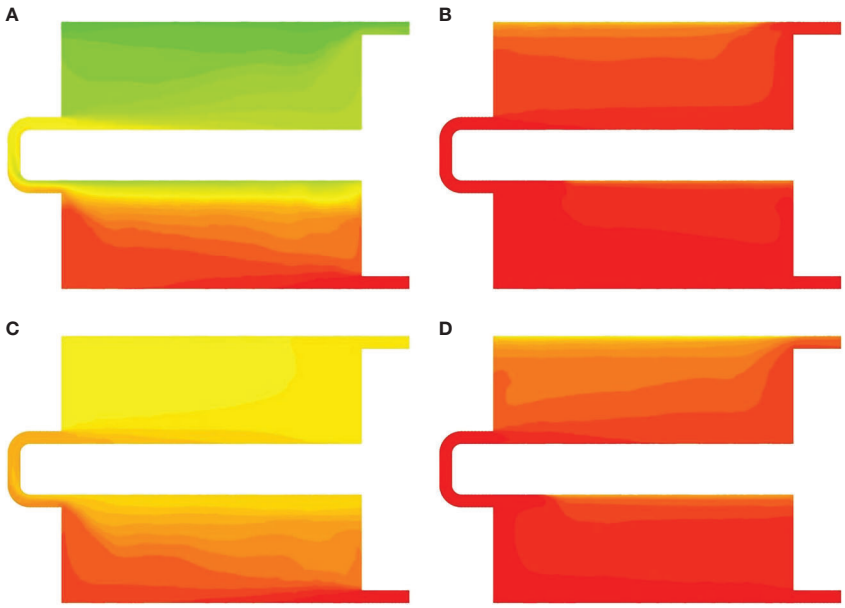

FIGURE 5
The concentration distribution of the solution when the sample inflow velocity is 0.1m/s, **(A, B)** The double displacement, **(C, D)** The triple displacement.

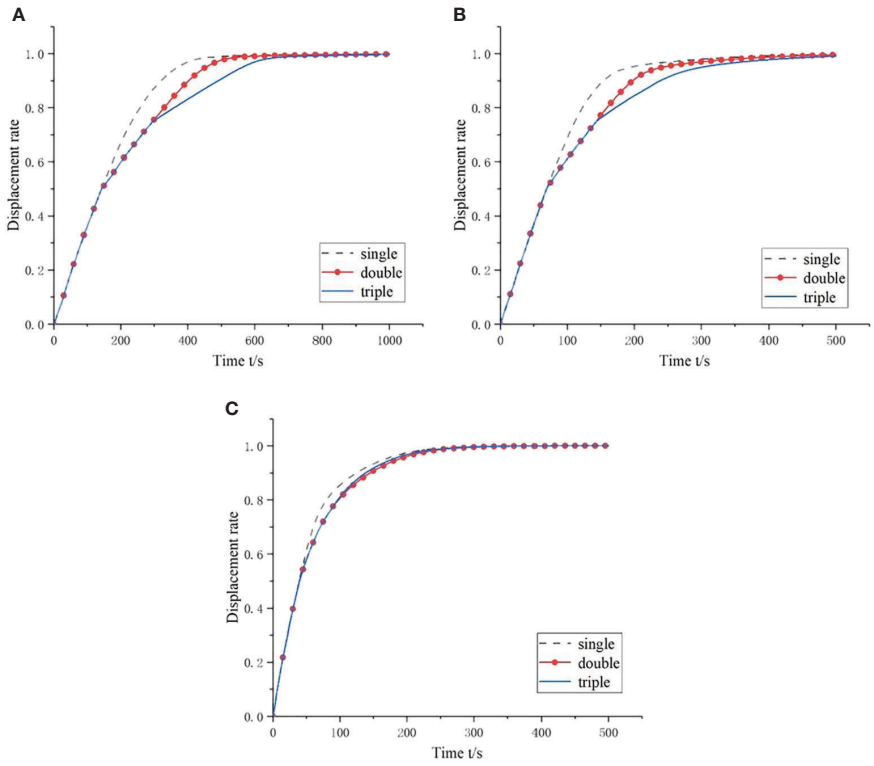

FIGURE 6
The diagram of the indirect displacement process, **(A)** 0.044m/s, **(B)** 0.1m/s, **(C)** 0.2m/s.

Results for different Coanda distances

According to this characteristic, the displacement calculation of the sampling cavity with different distances between the sampling port and the upper and lower walls is carried out. According to Figure 7, The results confirm that the design of making the sampling port as close as possible to the wall of the sampling cavity helps to strengthen the plane jet to improve the displacement efficiency to a certain extent.

The shape and diameter of the sampling inlet

In addition, different jet inlet shapes and diameters are also calculated.

In the case of using a circular sampling inlet, 5 sampling inlet diameter parameters were set from 5 mm to 7 mm. The diameter of the sampling inlet is also considered. Rectangular, square, and triangular sampling inlets are used in contrast to circular inlets. Among them, the sampling inlets of triangle and rectangle are also set in different orientations.

It can be seen from Figure 7 that the influence of the diameter of the inlet and outlet of the sampling channel on the displacement rate is basically the same as that of the inlet flow rate.

The results in Figure 7 show that the displacement efficiency can be slightly improved by using the rectangular sampling inlet and outlet. Although the displacement efficiency of the circular sampling inlet and outlet is low, considering the sealing, fit and overall design, the circular inlet and outlet are usually still used in most cases.

Stratification of liquid density and temperature

As shown in Figures 8 and 9, when the low Reynolds number jet acts, the vertical mixing dominates. With the increase of the Reynolds number, the negatively buoyant jet increases, the lateral mixing gradually dominates, and the entrainment and mixing phenomena become more and more obvious. The area of mixing is getting larger, but in the stable displacement area and the non-displacement area, the streamlines are relatively regular, and the stratification of temperature and density is relatively uniform.

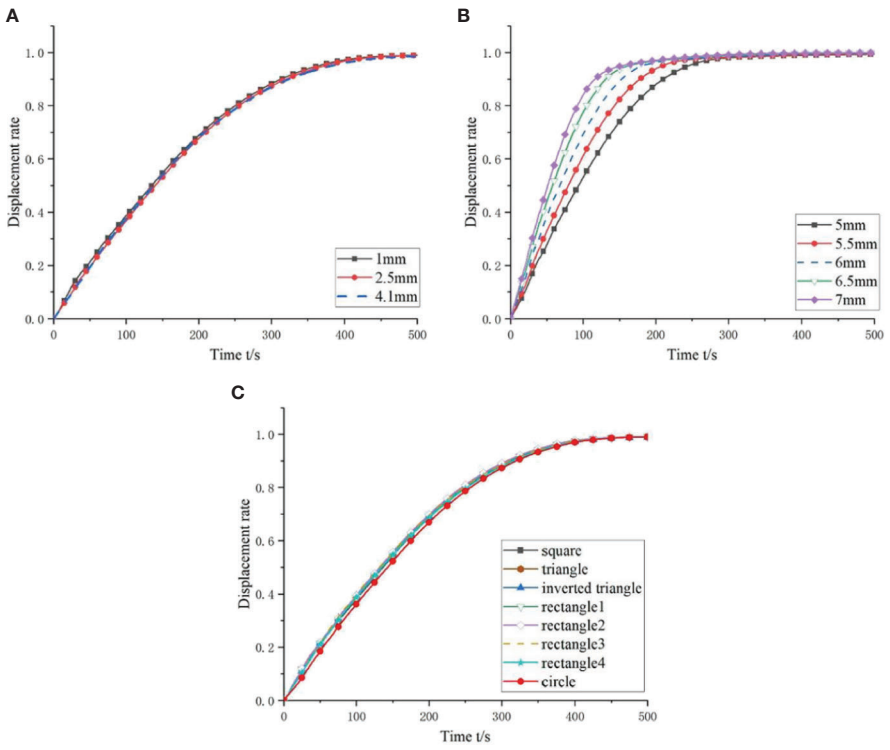

FIGURE 7
Displacement effect diagram of sampling cavity with different parameters, **(A)** Coanda distances, **(B)** Sampling chamber inlet diameters, **(C)** Sampling inlet shapes.

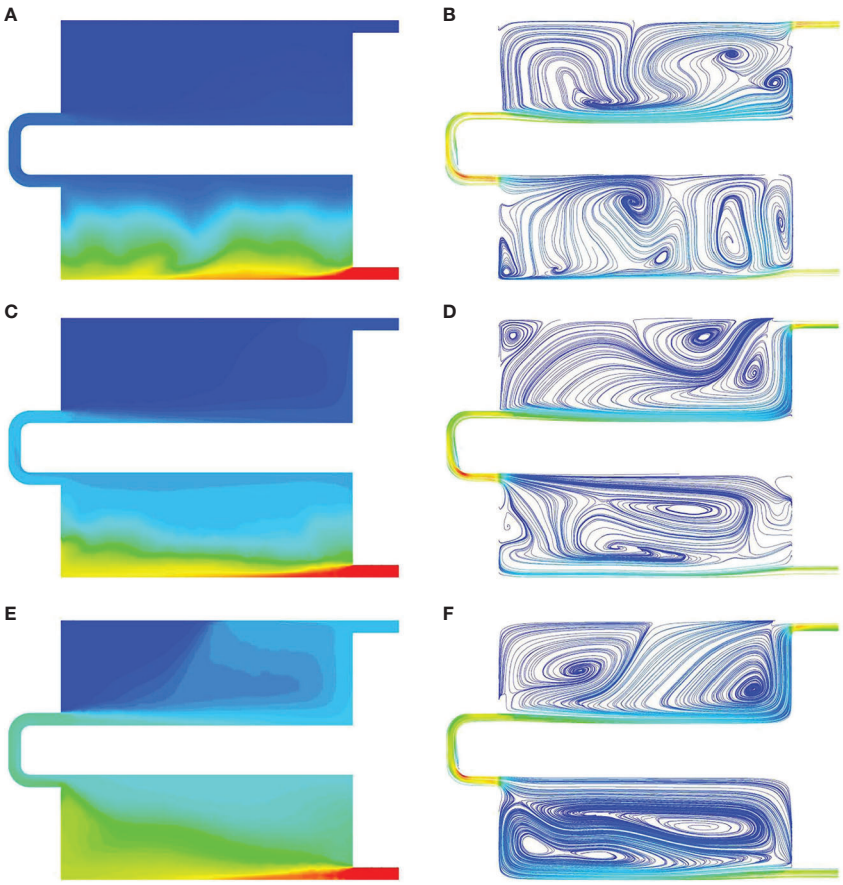

FIGURE 8
Density stratification and velocity distribution, **(A)** Density stratification at 0.044m/s, **(B)** Velocity distribution at 0.044m/s, **(C)** Density stratification at 0.1m/s, **(D)** Velocity distribution at 0.1m/s, **(E)** Density stratification at 0.2m/s, **(F)** Velocity distribution at 0.2m/s.

As shown in Figures 10 and 11, The samples are divided into light liquid layer, medium liquid layer, heavy liquid layer and low temperature layer, thermocline layer and high temperature layer according to the density and temperature. As the extraction speed increases, the jet becomes stronger with the increase of Reynolds number, the thickness of the thermocline and medium liquid layer gradually increase, and the liquid mixing area becomes larger.

Prototype test

We went to the South China Sea for sea trials in June 2022 with Southern Marine Science and Engineering Guangdong Laboratory (Guangzhou) and Guangzhou Marine Geological Survey (GMGS). The Ocean Geology No. 6 scientific research vessel of GMGS set off from Sanya on June 10, and ended its operation and docked in Dongguan on June 27. During this period, we went to the methane seepage area of the South China Sea and the 3,000-meter-deep waters. The actual operation depth was 1,399 meters in the methane seepage area and 3,021 meters in the 3,000-meter-deep waters.

During this sea trial, the water sampler was fixed to the rear of the deep-sea mobile platform. The water sampler is powered by the deep-sea mobile platform. The deep-sea mobile platform is controlled by the upper computer software on board. In addition to this water sampler, the sediment sampler and pore water sampler of the same project are also carried on the deep-sea mobile platform. The deep-sea mobile platform is hoisted from the rear deck by a winch and lowered to the deep sea for operation. At the end of the operation, it is winched from the seabed to the rear deck. as shown in Figure 12.

The basic parameters of the work location visited this time are described in Table 1.

At the end of the subsea operation, the deep-sea mobile platform was brought back on board, the sampling valve of the water sampler was opened, and the water samples in the sampling chamber was removed from the sampling chamber

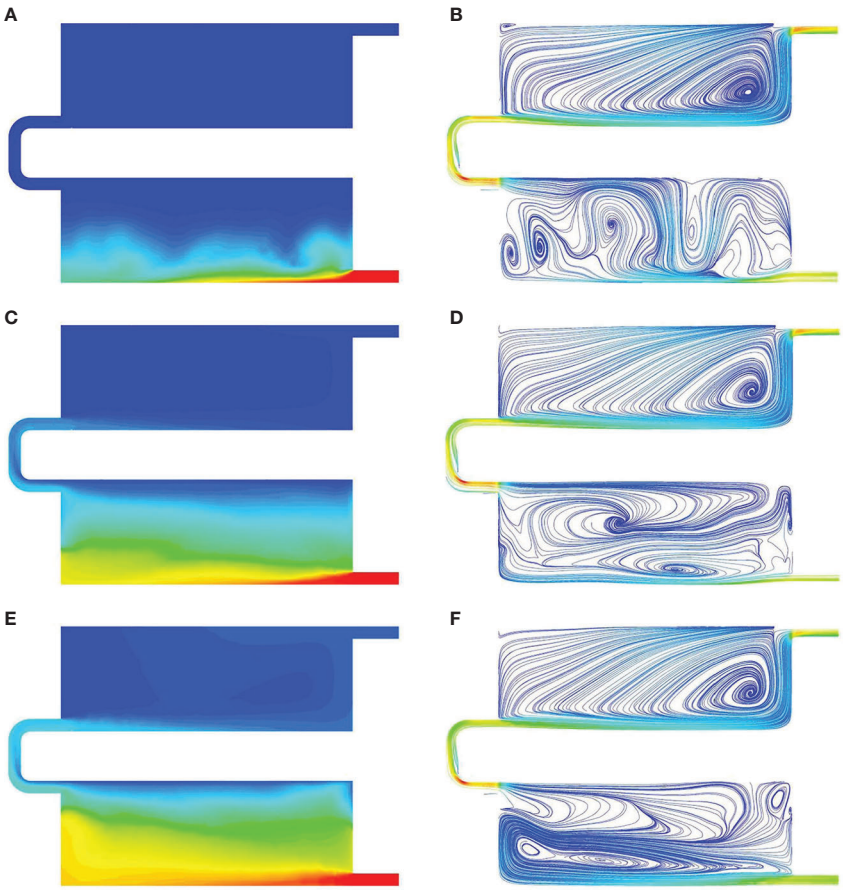

FIGURE 9
Temperature stratification and velocity distribution, **(A)** Temperature stratification at 0.044m/s, **(B)** Velocity distribution at 0.044m/s, **(C)** Temperature stratification at 0.1m/s, **(D)** Velocity distribution at 0.1m/s, **(E)** Temperature stratification at 0.2m/s, **(F)** Velocity distribution at 0.2m/s.

with the air compressor. In the 3000-meter sea area, the water extraction volumes of the four sampling channels are shown in Table 2, respectively.

We measured the bottom water sample from the 3000-meter seafloor with a refractometer, and the result showed a salinity of 34.8‰, which compared with the temperature salt deep sensor data carried by the deep sea mobile platform, and the sample purity reached 100%. The measurement results have been verified by experts on board and are accurate. In the end, the whole sea trial process passed the acceptance of experts in the industry, and the experts affirmed the whole sea trial process.

Discussion

After a series of numerical simulation calculations, combined with sea test verification, we have achieved a lot of research results. In fact, the jet theory is closely related to the displacement results. The displacement process is actually a very complex fluid motion process. The displacement process is affected by many factors, and the unpredictability of the deep sea environment and the interference of other unknown factors have caused a lot of instability in the displacement sampling process. During the whole sea trial process, we went through hardships and finally succeeded in the methane leakage area and the 3000-meter area.

The CFD method is recognized as an effective method for calculating fluid motion in today's academia. Through research, we found that if the sampling rate is low, an appropriate increase in the number of displacements can improve the displacement effect, but it should not be increased excessively. In high-speed sampling, a single displacement method should be used as much as possible. According to the theory of clinging wall jets, the inner wall of the sampling inlet and outlet is close to the inner wall of the sampling cavity, which helps to improve the sampling efficiency. The rectangular sampling inlet and outlet design helps to improve the displacement efficiency.

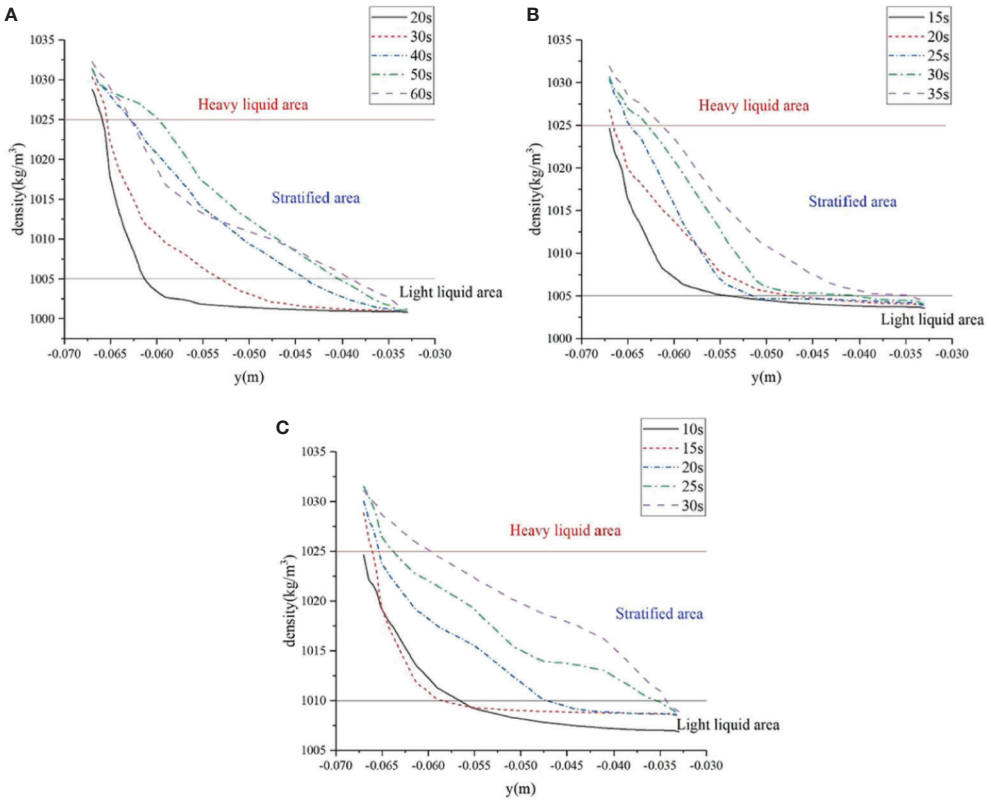

FIGURE 10
The density distribution curve of the central axis of the sampling cavity, **(A)** 0.044m/s, **(B)** 0.1m/s, **(C)** 0.2m/s.

During jetting, a mixing phenomenon occurs during the injection of one stream into another and leads to stratification of the liquid in the cavity. With the increase of pumping speed and jet intensity, the mixing area of sample liquid and light liquid becomes larger.

Fan et al. (2010) designed a new type of deep-sea pH detection electrode cavity with a three-dimensional structure according to the principle of hyperpycnal flow. The upper and lower water outlets are arranged in the cavity, and the high-efficiency displacement between the heavy liquid and the light liquid in the detection electrode cavity is realized by gravity layering. The relationship between the displacement performance of the pH detection electrode cavity and the Reynolds number and density difference was analyzed. The displacement effect of the triangular prism structure is better than that of the cylindrical structure. Compared with the water sampler used in this project, the overall displacement efficiency of the equipment is not high. The equipment has not been tested in the deep sea environment, and the interference of the deep sea environment cannot be excluded. The sea trial results of this topic are more reliable. And the sea trial results of this topic show that the displacement effect is better. The research results of displacement efficiency in this topic are more in-depth. Only cylindrical and triangular prismatic sampling cavities have been compared in their study. The research on the relationship between cavity structure and displacement efficiency needs to be further deepened. More shape variable parameters can be set.

Many institutions have conducted research on the sealing performance of deep-sea water samplers, such as the work of Niu and Yang (2012). Their work proved that the airtight water sampler developed at Zhejiang University has good sealing performance. A new gas-tight isobaric sampler for the collection of hydrothermal fluids venting at the seafloor has been designed by Seewald et al. (2002). This adjustable fill rate design can effectively reduce the entry of external seawater. External seawater pollution can indeed be reduced by this design, but from the experimental results, compared with the water sampler in this topic, the displacement sampling mechanism adopted in this topic has a more thorough inhibition of pollution. And their electronic control parts are more complicated to design and more expensive to produce.

Zhejiang University is one of the earliest institutions to carry out deep-sea sampling technology research in China. Wang et al. (2010) studied the fatigue life of PEEK poppet of deep-sea hydrothermal fluid sampling valve. These studies provide a reference for the analysis of fatigue life of components of other

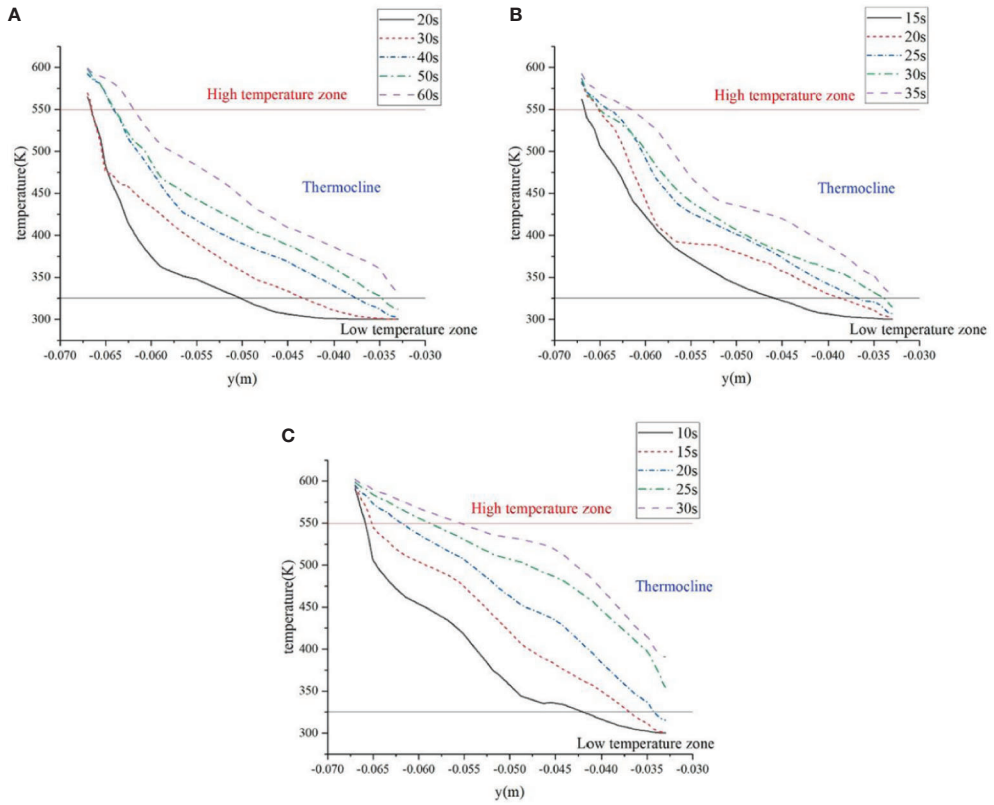

FIGURE 11
The temperature distribution curve of the central axis of the sampling chamber, **(A)** 0.044m/s, **(B)** 0.1m/s, **(C)** 0.2m/s.

materials under similar working conditions. A remotely operated serial sampler for collecting gas-tight fluid samples was developed at State Key Laboratory of Fluid Power Transmission and Control, Zhejiang University (Wu et al., 2015). The sampler has two modes of operation, either remotely controlled with equipment on the seafloor, or independently controlled as a stand-alone device. Afterwards, a new gas-tight pair sampler was designed by them for the collection of gas-tight fluid samples from the hadal zone (Wu et al., 2018). The water sampler was field tested in the Mariana Trench, and 3L of water samples were successfully obtained. Compared with the water sampler of this topic, the operation depth of their water sampler is deeper, the electric control system is designed to be more precise, sealing and pressure holding capacity is stronger. However, the flow-through structure similar to the water sampler in this project has not been used on their water sampler. The anti - pollution ability of the water sampler in this project is stronger.

Liu (2019) designed a driving device based on explosive bolts. An underwater anti-pollution isolation device is also designed. However, such a design method will result in a complex structure and high triggering cost. Jin (2019) proposed a sampling cylinder structure with sewage collection function, and the cylinder was divided into several parts with different pistons. However, the design still suffers from structural complexity. The anti-pollution ability of the water sampler in this project is better than that. A high-throughput deep-sea pressure-compensated sampling device was designed in Shandong Academy of Sciences (Li et al., 2018). This design is mainly for the sampling needs of deep-sea plankton. According to the results of numerical calculation, this device meets the needs of good sealing and pressure retention. The water sampler of our project is mainly designed for the sampling of chemical composition in seawater, and also for the analysis of microorganisms in seawater. A deep sea pressure compensator is designed in CRRC SMD (Shanghai) Ltd (Yu et al., 2020). They carried out the force analysis of the pressure compensator, and also designed a set of experimental test system. The structure of the sealing block is also an important factor affecting the sealing effect of the sampler. The China Ship Research Center has optimized the structure of the wedge block and simulated the sealing ring (Wu et al., 2021). However, their theoretical and simulation studies lack experimental support. And although this kind of sealing structure is simple, it lacks reliability in the deep

sea environment. Their research mainly focuses on pollution prevention and sealing pressure preservation.

In addition to deep sea water, some institutions are also studying surface water sampling devices. An *in-situ* hydrophore for the bottom water oil sampler was designed in Shandong Key Laboratory of Marine Environment Monitoring Technology (Hou et al., 2015). But this kind of water collector can only operate in the water environment of 0~100 meters. Its operating environment is relatively limited, and it is difficult to adapt to deep-sea sampling. Some organizations also analyze the water flow inside the water sampler to improve the water collector. Xin et al. (2018) from Dalian University of Technology used CFD to simulate the internal water flow in a stratified water sampler under ice. On this basis, the analysis and calculation are carried out, and the theoretical basis for improving the sub-ice water sampler is obtained. It can be seen that CFD has become an important method to study the water flow inside the water sampler. From a marine biology and chemistry perspective, trace elements in seawater are critical to our understanding of marine life and the environment. Merwe et al. (2019) from the University of Tasmania have developed a water sampler that can observe the concentration of Fe in seawater throughout the seasonal cycle. However, this kind of water collector has only been tested in seawater with a depth of 100 meters, and its operating ability in the deep sea cannot be guaranteed. In the later stage, we can try to design a water sampler with similar functions that can operate in the deep sea. The current deep-sea samplers often have a single function defect. In this regard, Li et al. (2019) of Yantai University designed a modular deep-sea sampling equipment, which uses the combination of a manipulator and a modular tool library to switch sampling tools. Such a design greatly improves the sampling efficiency, but tends to increase the cumbersomeness of deep-sea operations.

TABLE 1 Basic parameters of the work location.

	Depth	Longitude	latitude
Methane seepage zone	1399m	110°28′	16°43′
3000 meters sea area	3021m	113°26′	17°19′

At present, there are few studies on the thermal insulation of deep-sea samplers. Insulation is also a topic that cannot be ignored for deep-sea sampling. Changes in water temperature have an effect on the flow characteristics of water samples, especially on the mixing characteristics between liquids. In the field of biochemistry, water temperature also affects the activity of microorganisms in a sample. In the future, the research on

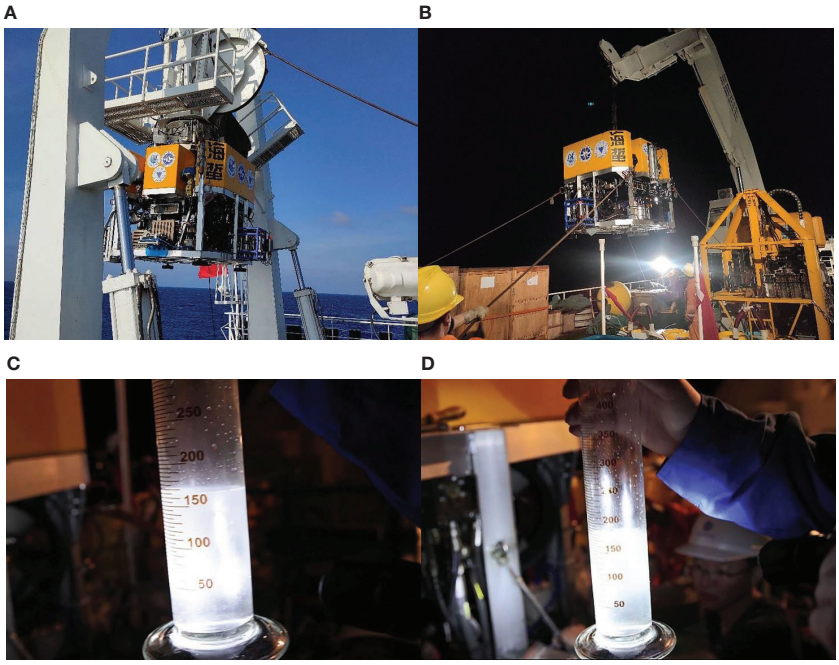

FIGURE 12
Prototype test and sampling process, **(A)** The arrangement of the water sampler, **(B)** The recovery of the water sampler, **(C)** Water extraction of channel 2, **(D)** Water extraction of channel 3.

TABLE 2 The water extraction volumes of the four sampling channels.

Channel 1	Channel 2	Channel 3	Channel 4
150ml	160ml	160ml	150ml

underwater insulation is likely to become an important direction in the field of deep-sea sampling.

Conclusion

In order to explore the influence of factors such as indirect displacement, shape and diameter of sampling inlet, Coanda distance, sampling rate and other factors on the displacement effect, the method of numerical simulation combined with synthesis was adopted. In addition, the stratification of the liquid density and temperature in the cavity with different sampling rates is also discussed. Based on the above theoretical research combined with the sea trials in the South China Sea, the following conclusions are drawn.

(1) The displacement phenomenon is mainly affected by the jet flow. The main factors affecting the jet phenomenon are the Reynolds number and the density Froude number. When the sample enters the sampling chamber from the inlet on the lower side of the sampling chamber, when the liquid front of the sample contacts the inner wall of the chamber, a reverse flow occurs, and a layering phenomenon occurs with the pre-filled water. During the displacement process, the liquid interface continued to rise, until the pre-stored water in the lower sampling chamber was widely displaced, and the sample began to leave the sampling outlet, and the pre-filled water in the lower sampling chamber could basically be successfully displaced. After increasing the sampling inlet flow rate, the sample water began to enter the upper sampling cavity from the lower sampling cavity very early, and the displacement rate was significantly improved.

(2) With the displacement rate of 0.5 and 0.75 bit nodes, compared with single displacement, when the inlet velocity of the sampling channel is 0.044m/s, using the method of multiple displacement, the attenuation of the displacement curve is delayed, and the displacement effect improve. When the sampling inlet velocity is 0.1m/s and 0.2m/s, the effect of single flooding is ahead of that of multiple flooding. Therefore, in low-speed sampling, multiple displacements can improve the displacement effect. In high-speed sampling, single displacement is appropriate, and the occurrence of displacement discontinuities should be avoided.

(3) The displacement calculation is carried out for different distances between the sampling inlet and the upper and lower walls of the sampling cavity. The results show that, according to the principle of clinging wall jets, making the sampling inlet as close as possible to and close to the inner wall of the sampling cavity can strengthen the jet to improve the displacement efficiency.

(4) The influence of sampling inlet and outlet diameter on displacement efficiency is basically consistent with the trend of inlet flow rate. The rectangular sampling inlet and outlet can slightly improve the displacement efficiency. In comparison, the circular sampling inlet and outlet have the lowest displacement efficiency. However, considering the overall design, sealing and coordination of the mechanism, the circular sampling inlet and outlet are still the choice in most cases.

(5) When the sample enters the sampling chamber, it will be entrained and mixed with the pre-filled water. Impairing the entrainment and mixing of the liquid in the sampling cavity during the sampling process is the focus of displacement. The velocity of the liquid in the cavity on the vertical section is semi-Gaussian distribution. In low Reynolds number jets, vertical admixture dominates. With the increase of the Reynolds number, the negatively buoyant jet becomes stronger, the lateral mixing begins to dominate, the entrainment and mixing phenomena increase, and the mixing area increases. But in the displacement stable zone, the stratification is relatively uniform. With the increase of the sampling inlet velocity, the jet flow becomes stronger with the increase of the Reynolds number, the thickness of the mid-liquid layer and the thermocline gradually increases, and the liquid mixing area increases.

Data availability statement

The original contributions presented in the study are included in the article/supplementary material. Further inquiries can be directed to the corresponding author.

Author contributions

HH was in charge of the whole project. YF wrote the manuscript and participated in the sea trials. DC and YD provided the platform and support for the sea trial. All authors contributed to the article and approved the submitted version.

Funding

Key Special Project for Introduced Talents Team of Southern Marine Science and Engineering Guangdong Laboratory (Guangzhou) (GML2019ZD0506) from Southern Marine Science and Engineering Guangdong Laboratory (Guangzhou), 511458; Research on Integrated Technology of Deep-sea in-situ

Filtration and Fidelity Sampling (2021Szvup013) from Shenzhen Research Institute of Dalian Maritime University

Acknowledgments

We are grateful to Professor Jiawang Chen and his students for their help in the experiment. I would also like to thank Guangzhou Marine Geological Survey (GMGS) for their help, and the support of Key Special Project for Introduced Talents Team of Southern Marine Science and Engineering Guangdong Laboratory (Guangzhou) (GML2019ZD0506) from Southern Marine Science and Engineering Guangdong Laboratory (Guangzhou), 511458, and Research on Integrated Technology of Deep-sea *in-situ* Filtration and Fidelity Sampling (2021Szvup013) from Shenzhen Research Institute of Dalian Maritime University.

Conflict of interest

The authors declare that the research was conducted in the absence of any commercial or financial relationships that could be construed as a potential conflict of interest.

Publisher's note

All claims expressed in this article are solely those of the authors and do not necessarily represent those of their affiliated organizations, or those of the publisher, the editors and the reviewers. Any product that may be evaluated in this article, or claim that may be made by its manufacturer, is not guaranteed or endorsed by the publisher.

References

Burridge, H. C., Hunt, G. R., and He, Z. (2017). From free jets to clinging wall jets: The influence of a horizontal boundary on a horizontally forced buoyant jet. *Phys. Rev. Fluids* 2 (2), 1–20. doi: 10.1103/PhysRevFluids.2.023501

Edgcomb, V. P., Taylor, C., Pachiadaki, M. G., Honjo, S., Engstrom, I., and Yakimov, M. (2016). Comparison of niskin vs. *in situ* approaches for analysis of gene expression in deep Mediterranean Sea water samples. *Deep Sea Res. Part II.* 129, 213–222. doi: 10.1016/J.DSR2.2014.10.020

Fan, W., Pan, H. C., and Chen, Y. (2010). Mechanism of high-performance liquid-liquid displacement for deep-sea sensor chamber. *J. Mech. Eng.* 46 (4), 143–149. doi: 10.3901/JME.2010.04.143

Gao, W. F. (2018). *A study on the turbulence generation mechanism of transitional fountains in linearly stratified fluid and its application. [dissertation/doctoral thesis]* (Kunming: Yunnan Normal University).

Hou, G. L., Wu, B. W., Chu, D. Z., He, J., Wang, X. P., and Liu, Y. (2015). Design of the in-situ hydrophore for the bottom water oil samples. *Ocean Technol.* 34 (5), 53–57. doi: CNKI:SUN:HYJS.0.2015-05-010

Jin, H. J. (2019). *Design and research of pressure-retaining pollution-preventing sampler at deep-sea. [dissertation/master's thesis]* (Zhoushan: Zhejiang University).

Junichi, M., Akiko, M., Yohei, M., Naoya, E., Saki, T., Jun-Ichiro, I., et al. (2017). WHATS-3: An improved flow-through multi-bottle fluid sampler for deep-Sea geofluid research. *Front. Earth Sci.* 5. doi: 10.3389/feart.2017.00045

Li, Q. (2021). *Study on the flow behavior of fountains and the mixing characteristics in a thermally stratified water tank. [dissertation/doctoral thesis]* (Kunming: Yunnan Normal University).

Li, L., Chai, Y. S., Yin, S. M., Liu, X. K., Wang, Q., Liu, Y. H., et al. (2019). Structural design and analysis of a modular deep-sea sampling device. *J. Yantai Univ. (Natural Sci. Eng. Edition)* 32 (4), 357–361. doi: 10.13951/j.cnki.37-1213/n.2019.04.010

Li, X. F., Jiang, Q. L., Gai, Z. P., Wang, L., Song, W. J., and Wang, J. Y. (2018). Design and performance research on deep-sea plankton sampler with concentrated and gas-tight function. *Chin. Hydraulics Pneumatics* 8, 27–32. doi: 10.11832/j.issn.1000-4858.2018.08.006

Liu, H. (2019). *Research on structure design and sealing technology of full-ocean-depth pressure-retaining water sampler. [dissertation/master's thesis]* (Zhoushan: Zhejiang University).

Liu, G. H., Lu, C., Zhao, H. Y., Liu, J. Y., Liu, Z. R., He, Z., et al. (2018). Design improvement and Sea test about *In situ* pore water sampler system for deep-Sea sediments. *Adv. Geosci.* 8 (1), 141–151. doi: 10.12677/ag.2018.81015

Merwe, P., Trull, T. W., Goodwin, T., Jansn, P., and Bowie, A. (2019). The autonomous clean environmental (ACE) sampler: A trace-metal clean seawater sampler suitable for open-ocean time-series applications. *Limnol. Oceanogr. Methods* 17 (9), 490–504. doi: 10.1002/lom3.10327

Niu, W. D., and Yang, F. (2012). Experimental research on the tightness of a gas-tight sampler in high-pressure chamber. *Dev. Innovation Machinery Electrical.* 25 (3), 132–134. doi: 10.3969/j.issn.1002-6673.2012.03.053

Okamura, K., Noguchi, T., Hatta, M., Sunamura, M., Suzue, T., Kimoto, H., et al. (2013). Development of a 128-channel multi-water-sampling system for underwater platforms and its application to chemical and biological monitoring. *Methods Oceanogr.* 8, 75–90. doi: 10.1016/j.mio.2014.02.001

Pokharel, P., and Acharya, S. (2021). Dynamics of circular and rectangular jets in crossflow. *Comput. Fluids* 230, 105111. doi: 10.1016/j.compfluid.2021.105111

Saegusa, S., Tsunogai, U., Nakagawa, F., and Kaneko, S. (2006). Development of a multibottle gas-tight fluid sampler WHATS II for Japanese submersibles/ROVs. *Geofluids* 6 (3), 234–240. doi: 10.1111/j.1468-8123.2006.00143.x

Sattley, W. M., Burchell, B. M., Conrad, S. D., and Madigan, M. T. (2017). Design, construction, and application of an inexpensive, high-resolution water sampler. *Water* 9 (8), 578. doi: 10.3390/w9080578

Seewald, J. S., Doherty, K. W., Hammar, T. R., and Liberatore, S. P. (2002). A new gas-tight isobaric sampler for hydrothermal fluids. *Deep Sea Res. Part I.* 49 (1), 189–196. doi: 10.1016/S0967-0637(01)00046-2

Wang, H. Z., Qin, H. W., Yang, C. J., and Chen, Y. (2010). Fatigue life of PEEK poppet for deep-sea hydrothermal fluid sampling valve. *J. Zhejiang Univ. (Eng. Sci.)* 44 (1), 14–18. doi: 10.3785/j.issn.1008-973X.2010.01.003

Wu, S. H., Liu, T. Q., Bian, R. G., and Zhang, Z. (2021). Research on the form of wedge seals of deep-sea sediment samplers. *J. Ship Mechanics* 25 (5), 652–658. doi: 10.3969/j.issn.1007-7294.2021.05.014

Wu, S. J., Wang, S., and Yang, C. J. (2018). Collection of gas-tight water samples from the bottom of the challenger deep. *J. Atmos. Oceanic Technol.* 35 (4), 837–844. doi: 10.1175/JTECH-D-17-0170.1

Wu, S. J., Yang, C. J., Ding, K., and Tan, C. Y. (2015). A remotely operated serial sampler for collecting gas-tight fluid samples. *China Ocean Eng.* 29 (5), 783–792. doi: 10.1007/s13344-015-0055-6

Xin, Y. J., Guo, L., Guo, T., Di, Y. J., and Li, Z. J. (2018). Numerical simulation and optimum design of stratified water harvester under ice. *J. Eng. Heilongjiang University* 9 (1), 78–83. doi: 10.13524/j.2095-008x.2018.01.014

Yu, C. Z. (1993). *Turbulent jet* (Beijing: Higher Education Press).

Yu, H. M., Liu, K. A., and Luo, L. B. (2020). Design of pressure compensator for deep-sea equipment. *Hydraulics Pneumatics Seals* 40 (5), 51–53. doi: 10.3969/j.issn.1008-0813.2020.05.014

frontiers | Frontiers in Marine Science

TYPE Original Research
PUBLISHED 23 January 2023
DOI 10.3389/fmars.2023.1090940

OPEN ACCESS

EDITED BY
Yuan Lin,
Zhejiang University, China

REVIEWED BY
Xiaolei Liu,
Ocean University of China, China
Xing Zheng,
Harbin Engineering University, China
Jiangong Wei,
Guangzhou Marine Geological Survey, China

*CORRESPONDENCE
Xiuqing Yang
yxqself@163.com

SPECIALTY SECTION
This article was submitted to Ocean Observation, a section of the journal Frontiers in Marine Science

RECEIVED 06 November 2022
ACCEPTED 09 January 2023
PUBLISHED 23 January 2023

CITATION
Guo L, Yang X, Xue G, Wang C, Fei Z, Zhang S, Liu Y, Lu K and Yang Y (2023) Development and application of a 6000-meter double decelerating lander. *Front. Mar. Sci.* 10:1090940. doi: 10.3389/fmars.2023.1090940

Development and application of a 6000-meter double decelerating lander

Lei Guo[1], Xiuqing Yang[2*], Gang Xue[1], Cheng Wang[1], Zihang Fei[3], Shaotong Zhang[4], Yanjun Liu[1], Kai Lu[5] and Yuan Yang[5]

[1]Institute of Marine Science and Technology, Shandong University, Qingdao, China, [2]College of Oceanic and Atmospheric Sciences, Ocean University of China, Qingdao, China, [3]College of Environmental Science and Engineering, Ocean University of China, Qingdao, China, [4]Frontiers Science Center for Deep Ocean Multispheres and Earth System, Key Laboratory for Submarine Geosciences and Prospecting Techniques (Ministry of Education), College of Marine Geosciences, Ocean University of China, Qingdao, China, [5]Qingdao Institute of Marine Geology, China Geological Survey, Qingdao, China

The deep-sea lander is an important equipment for *in-situ* detection and monitoring. It is of great significance to understand the benthic boundary layer's physical, chemical, and ecological environment. A 6000-meter double decelerating lander was created to meet the deployment requirements of underwater detection and monitoring, allowing for long-term *in-situ* monitoring of several benthic boundary layer components. Protection of the installed ocean bottom seismometer (OBS) is required due to the lander's and OBS's different impact resistances. The double decelerating unit enables the OBS to avoid colliding with the seabed when the lander lands and then collides with the seabed at a slow speed rather than the speed at which the lander falls, which is intended to safeguard OBS from damage. To ensure a safe deployment, the lander's static analysis and simulation were performed using ANSYS, and the motion characteristics of the application process were derived. Numerous data have been obtained after the lander's successful application in the South China Sea. The lander provides an investigation approach for marine science and geochemistry, complementing a technical approach to marine environmental investigations.

KEYWORDS

lander, double decelerating, *in-situ* monitoring, numerical simulation, field application

1 Introduction

There is an increasing requirement for the deep-sea exploration technology and equipment due to the scientific study at the hadal zone, which has a depth rating of 6000 to 11000 meters (Jamieson et al., 2009). The Benthic lander, an autonomous, unmanned marine exploration device, has been widely used since the early last century due to its simple structure, operation, and low cost (Hardy et al., 2013). It lands freely on the sea floor without any cable attached (Person et al., 2006). The lander may install specialized monitoring equipment to conduct long-term *in-situ* deep-sea observations and carry exploration-related

payloads (Wu et al., 2011). In addition, deep-sea landers can conduct *in-situ* tests with on-board instruments.

The benthic lander is an unpowered autonomous landing device. The substantial ballasts are attached to the underside of the lander when it is deployed, and due to the increased gravity, the lander sinks to the ocean floor. An acoustic order is issued to open the acoustic releaser when the lander is retrieved, causing the ballasts to separate from the lander. The lander then uses buoyancy to float to the water's surface (Yu et al., 2017). After that, the lander is found by GPS or radio beacon (Yu et al., 2022).

The development of benthic landers originated in the 1970s, and the FVR and MANOP landers developed by the US are the earliest benthic landers in the world (Berelson et al., 1987; Rowe et al., 1997). As the challenges in deployment and data collecting, early lander uses were uncommon. The "BOLAS" benthic lander, created by the Netherlands Institute of Oceanography, was often used to track how much oxygen seabed sediments consumed (Tahey et al., 1996; Witbaard et al., 2000; Duineveld et al., 2001). In the 21st century, with the development of low-power electronic devices and batteries, the development and application of landers have grown rapidly. At the beginning of the 21st century, the UK designed the BENBO lander to study benthic organisms on the surface of deep-sea sediments (Black et al., 2001). The Netherlands Institute of Oceanography successfully created "ALBEX," a multipurpose *in situ* observation benthic lander based on "BOLAS," and several applications have been made (Lavaleye et al., 2009; Oevelen et al., 2009). The working depth of landers developed in recent years has reached 6000 to 11000 m, such as "HADEEP" (Jamieson et al., 2009), "Tianya" (Chen et al., 2017), and so on. "HADEEP", a lander for photographing and capturing creatures in the hadal zone, was jointly developed by the UK and Japan (Jamieson et al., 2009). The "HADEEP" has been deployed and successfully recovered in areas such as Mariana Trench, Japan Trench, and Tonga Trench; simultaneously, many new species have been discovered during the application (Hardy et al., 2013; Turchik et al., 2015). In 2017, the "Tianya" abyss lander was developed successfully (Chen et al., 2017). To ensure a successful recovery, buoyant material was used to provide buoyancy for the "Tianya" (Chen et al., 2020). All of the aforementioned landers have triangle- or quadrilateral-shaped frames, and their bottom legs are all attached with circular footpads. Their thinness makes the round foot pads prone to settling in the silt, making floating the frame more challenging (Yu et al., 2022). The lander's deployment cannot be guaranteed due to the triangular or quadrilateral frame, making the lander readily capsize while bottoming out. Additionally, it is challenging to safeguard the equipment on board the landers. OBS is the most often exposed equipment (Ocean Bottom Seismometer), which requires additional protection. Traditional OBS is protected by buffer springs when the OBS collides with the seabed (Podolskiy et al., 2021; Schlindwein et al., 2022). When coupled with the lander, the OBS is often put at the bottom of the lander without any additional buffers. OBS can only rely on its strength to endure impact when the lander lands, which can easily cause OBS damage. Landers and buildings that safeguard other gadgets must thus be developed further.

Based on this, this study offers a self-developed 6000-meter twin decelerating lander for deep-sea environmental monitoring to suit the scientific research and technical demands in deep-sea exploration. In particular, the twofold decelerating structure ensures that the OBS progressively hits the seafloor after the lander lands rather than colliding with it. To ensure a safe deployment, the static analysis and simulation of the equipment were completed using ANSYS, and the motion characteristics of the equipment application process were determined. Finally, this paper introduces the application of landers in the South China Sea, and a series of data has been collected. The lander provides an investigation approach for marine science and geochemistry, complementing a technical approach to marine environmental investigations. In particular, the developed lander provides a viable means for simultaneous *in-situ* monitoring and deployment of OBS.

2 The 6000-meter double decelerating lander

The 6000-meter twin decelerating lander was created to guarantee the effective deployment of numerous seabed monitoring devices. Compared to the conventional lander, the new apparatus can decelerate, protecting the important sensors doubly. The physical equipment and its primary technical parameters are provided in Table 1, and its overall technological level is at an advanced worldwide rank.

TABLE 1 Technical indexes of 6000-meter double decelerating lander.

Item	Parameter and technical index
Size & Weight	2250×1800×1800 mm; 545 kg (without ballast)
Maximum working water depth	6000 m
Usage environment	-5~40°C, Continuous working time ≥1 year
Material	Titanium alloy, TA2
Buoyant body	Outer diameter 1800 mm; Internal diameter 1600 mm; Height 500 mm; Glass microsphere with a density of 0.6 g/cm^3
Glass floats	Ø430 mm; Glass thickness 14 mm
Acoustic releasers	Maximum working water depth 12000 m; Continuous working time 2 years; Load capacity 2500 kg
Monitorable parameters	Temperature; Pressure; Salinity; Turbidity; Hydrophone; Eh; Reserved for other sensor interfaces

2.1 Equipment configuration

The schematic and physical diagram of the new lander is presented in Figure 1. It comprises a deep-sea landing platform and a marine multi-parameter monitoring unit. A lander frame, a buoyant body, eight glass floats, a ballast, two acoustic releasers, an iridium beacon, a flash beacon, and an Ultra-Short Baseline (USBL) make up the deep-sea lander platform. The marine multi-parameter monitoring unit consists of a CTD, a Hydrophone, a lamp, a camera, an attitude indicator, and a battery tank, as shown in Figure 2A.

The new lander's construction and instrument configuration are optimized based on the conventional lander. The lander's frame is constructed from titanium alloy. The communication instrument layer, monitoring instrument layer, buoyancy layer, OBS installation layer, and ballast installation layer are stacked sequentially from top to bottom of the lander, as seen in Figure 2B. The combination of a buoyancy component and a glass floating ball to create a deep-sea floating unit is used for the new lander in order to improve the lander architecture, heighten the equipment floating center, and lengthen the distance between the barycenter and the buoyancy center. Considering hydrodynamic conditions and the lander frame, the Buoyancy component, made of a hollow glass microsphere with a density of 0.6 g/cm^3, is designed as a ring. Each glass float weighs 17.2 kg in the air and can provide 26 kg of buoyancy in water.

2.2 Release unit and recovery method

According to Figure 2C, the release unit comprises an acoustic releaser, a connecting mechanism, ballast, and other components. The major purpose of the release unit is to convert the tool into a gravity-based apparatus so that the lander may rapidly descend to the ocean floor. The ballast is consistently released in response to an auditory signal, enabling the lander to ascend swiftly to the water's surface.

Two acoustic releasers in parallel coupling to release ballast are designed to improve the success rate of recovery. The acoustic releaser is mounted at the top of the frame without obstruction, allowing stable reception of control signals from the sea surface. The releaser has a 2.5 t effective load capacity. A ballast system is fitted at the frame's base. The ballast is intended to make handling and installation easier and lessen the lander's tendency to sink in the silt. The integrated ballast's design also makes it easier to retrieve the lander without any bumps from the sediments.

The cable is attached to the ballast hooks at the two legs through the connecting bar, which is controlled by two releasers, according to the connection technique for the ballast. When the acoustic release is secured, the cable is tightened; however, when any of the acoustic releases are unlocked, the connecting rod detaches, and the cable slackens. The fixed locations at the frame's legs allow for the rotation of the hooks around them. The hook holds the ballast in place when the cable is tight; when the cable is free, the hook will open, and the ballast will be discarded.

2.3 Double decelerating structure and method

In order to protect some special sensors, such as OBS, the function of double decelerating is added to the lander. Despite being delicate, the OBS must make touch with the seafloor surface in order to function. A unique design is designed for the deployment of OBS in order to prevent harm to the OBS device when the lander reaches the bottom.

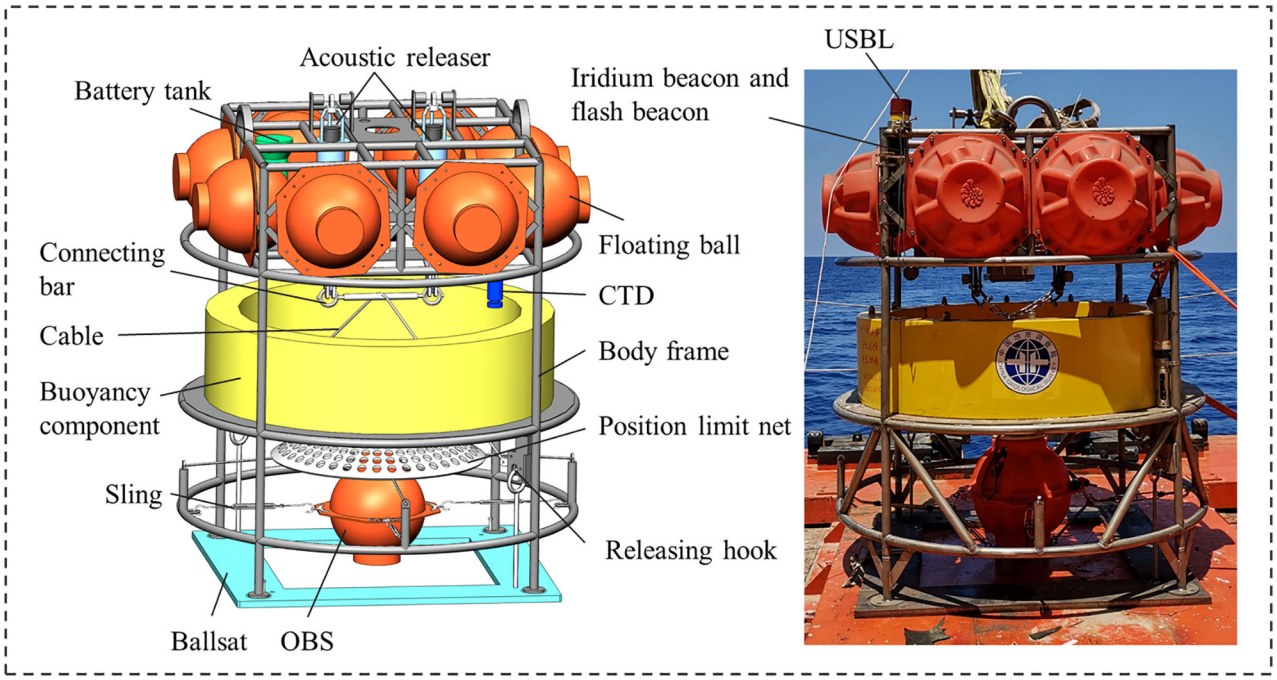

FIGURE 1
The 6000-meter Double Decelerating Lander.

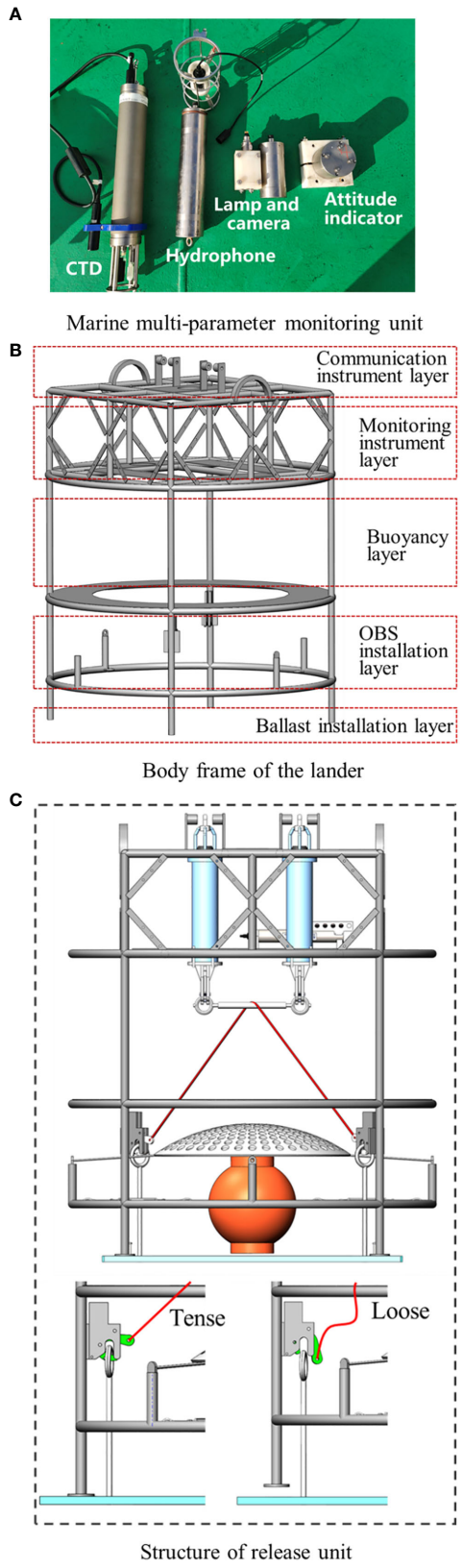

FIGURE 2
Parts of the lander. **(A)** Marine multi-parameter monitoring unit; **(B)** Body frame of the lander; **(C)** Structure of release unit.

The OBS is positioned on the lower portion of the lander, as depicted in Figure 3, and a flexible cable connects it to the bracket. The OBS is subjected to higher fluid resistance as the lander descends, as seen in Figure 3, which causes the cable to be tensioned and the OBS to move upward concerning the lander. After the lander lands, the OBS descends slowly by gravity. During the descent, there will be no impact to ensure that the OBS is not destroyed. In addition, the cable connecting the OBS should not be too long to minimize mutual cable entanglement, which might prohibit the releaser from releasing the ballast and prevent the OBS from clashing with other devices when going up. With the design of the limit net, the OBS will not cross the limit net, avoiding the collision between OBS and other devices.

3 Static analysis

The force applied to the lander by the different instruments must not be more than the strength of the frame material to ensure the lander's safe operation. As a result, the ANSYS performs the static analysis of the lander frame.

The analysis follows these steps, as shown in Figure 4: (a) The Static Structural of the ANSYS workbench is selected. Set the material to Titanium Alloy when importing the framework model; (b) Set the connection type at each welding point of the bracket to Bonded, not allowing relative sliding or separation between surfaces or lines of the parts; (c) Tetrahedrons are selected for meshing. For automated grid refinement, set Relevance Center to Fine. Set the smoothing to a high value, consider the nodes nearby, and smooth the grid's iterative processing. Set the Span Angle Center to Fine to fine-tune the edge mesh such that the span angle varies from 12° to 36°. Only Sizing and Contact Sizing are introduced during the scaffold analysis. The grid is formed when the configuration is complete; (d) Apply loads in the setup after meshing. Four outriggers are set as fixed points, and 5000N is applied to two lugs, respectively. According to the predicted component weight, additional forces are applied at the installation location, as illustrated in Figure 5; (e) Start to solve, including Equivalent Stress, Equivalent Strain, and Maximum Strain.

The static analysis of the lander frame is shown in Figure 6. According to the analysis's findings, the battery cabin's support plate is under maximum stress of 177.49 MPa, which is significantly less than the 373 MPa yield strength of TA2 titanium alloy. The battery compartment support plate also experiences the most strain. The lander frame can only deform a maximum of 5.8 mm, which falls within the acceptable deformation limit. According to the findings of the static study, the lander frame's design is sound and can accommodate several pieces of equipment.

4 Simulation analysis and calculation of lander

The lander is affected by gravity and current resistance in the water. Fluent software performs the hydrodynamic study of the

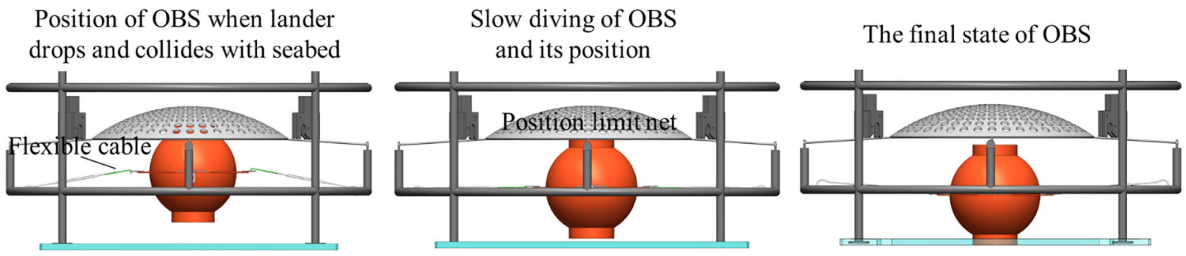

FIGURE 3
The working process of the double decelerating structure. OBS moves upwards as the lander drops and collides with the seabed, and cables tighten; OBS descent gradually slows after the lander lands; The lander collides with the seabed at an acceptable speed.

lander, including examining the lander's dive, increasing speed, and double decelerating to determine its operational condition.

4.1 Numerical simulation scheme

The hydrodynamic analysis of the lander is carried out by Fluent software, and the numerical simulation flowchart is shown in Figure 4. The steps are as follows: (a) Model establishment. The lander's three-dimensional model is imported into ICEM, and the Repair Geometry function is used to correct the model tolerance. To ensure model fidelity, Build Topology's tolerance is set to 0.002. The topology is chosen in Build Body. To construct the Body, select every bounding Surface, then assign the Body to the flow field. To establish the boundary conditions, choose to Create/Modify the Surface and give each bounding surface a name; (b) Meshing. To fine-tune the mesh, the Scale factor is set to 0.1 in Global Mesh Setup. The grid near the device is tight, and the grid distant from it is sparse thanks to variable mesh size choices, which can increase the accuracy and speed of calculations. Tetrahedral meshes without structures enable the model's spatial discretization. After the mesh is created, Smooth Elements Globally does the mesh smoothing; (c) Boundary conditions setting: Import the 3D mesh file into Fluent. In the General module, select Solver Type as Pressure-Based, and set Solver Time as Steady. Set the realizable k-epsilon model as the viscous model in Models. In Materials, create a fluid medium called water-liquid. Associate the body with water-liquid under cell zone conditions. The wall boundary condition in Boundary Conditions is symmetrical, while the equipment boundary condition is the wall. Set the lander's weight or buoyancy appropriately, activate gravity, and set the inlet boundary condition to Velocity Inlet with the Velocity Magnitude set to 0 m/s. This allows the lander to fall or float in the water freely; (d) Solver setting. The SIMPLE approach is used for the pressure-velocity coupling solution. Least Squares Cell Based, Second Order, Second Order Upwind, and Momentum processing are utilized for the spatial discretization of gradient, pressure, and momentum. The terms "Turbulent Kinetic Energy" and "Turbulent Dissipation Rate" are both Upwind First Order; (e) Example solution. When solving, the number of iteration steps is set to 10000.

4.2 Analysis of lander diving and rising

When the lander is launched, it will be moved horizontally by ocean currents. The lander's landing speed should be as quick as possible to guarantee a minimal horizontal displacement and that

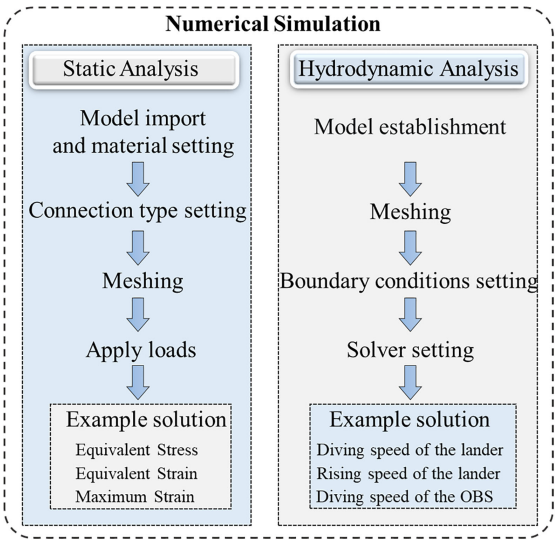

FIGURE 4
Numerical simulation flowcharts.

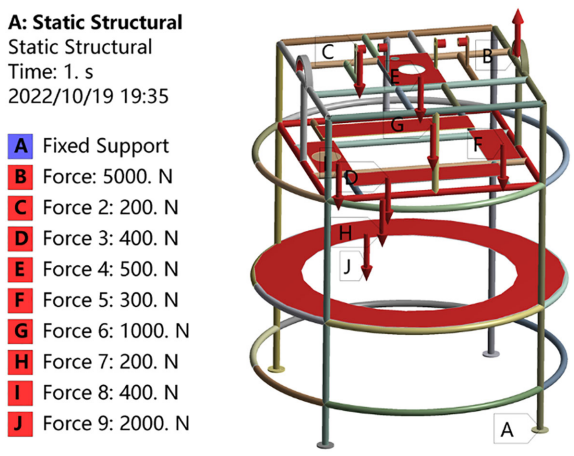

FIGURE 5
Load distribution.

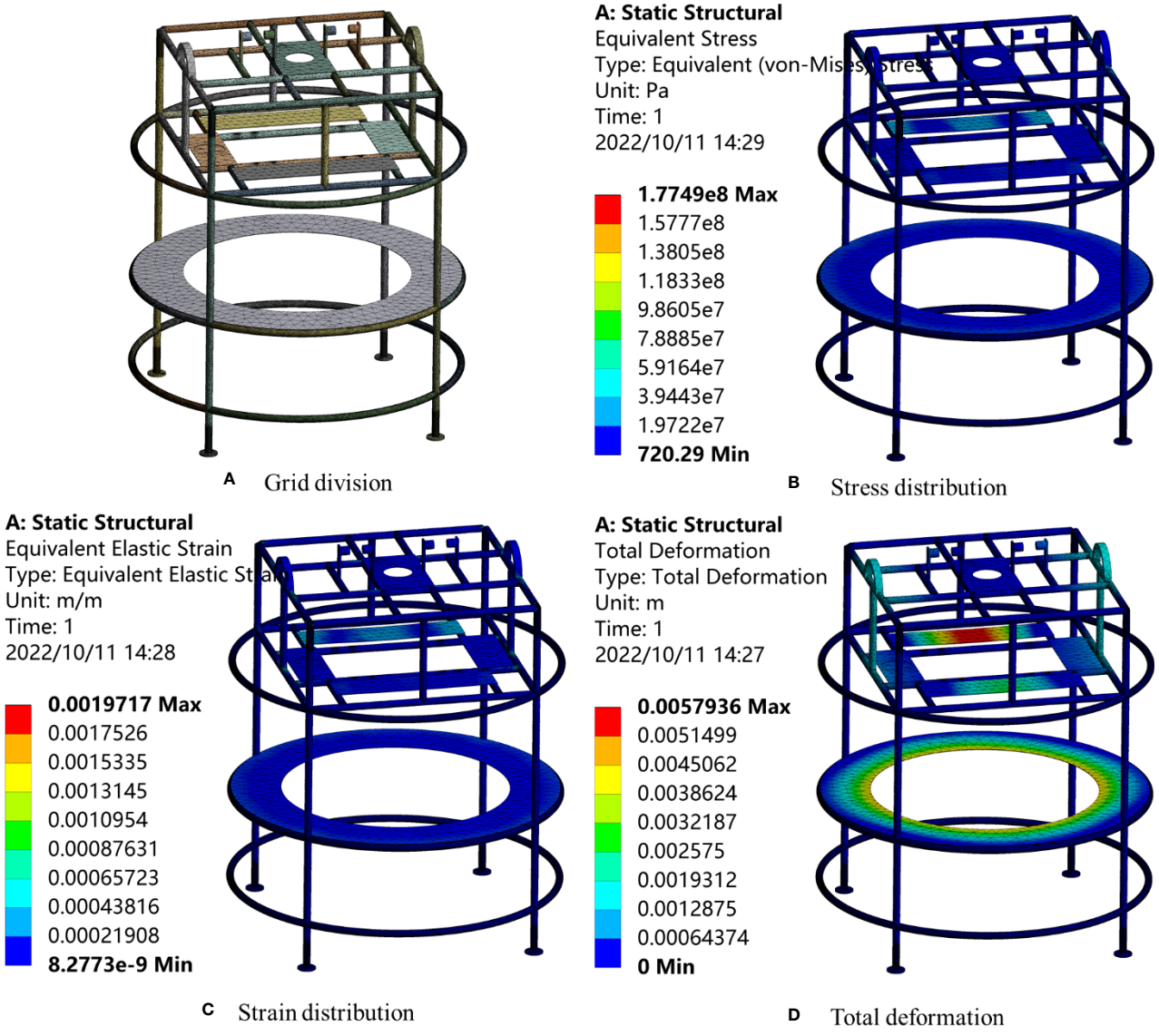

FIGURE 6
Static analysis of lander frame. **(A)** Grid division; **(B)** Stress distribution; **(C)** Strain distribution; **(D)** Total deformation.

the lander's landing position matches the preset location. On the other side, if the speed is too high, the lander damages itself as it rests on the seafloor and hits bottom. In order to ensure the safety of the lander, according to Li et al. (2013), the landing speed at 0.8 ~ 1.2 m/s is recommended.

Rough accounting of the various components of the lander, as shown in Table 2.

Furthermore, a ballast of 305.34 kg in the water is installed when the lander is deployed. According to this formula

$$F - \frac{1}{2} C_d \rho v^2 S = 0 \tag{1}$$

Where, F = force; C_d = fluid resistance coefficient; ρ= density of water; v = speed; S = the cross-sectional area of the lander. After calculation can be obtained:

$$(305.34 - 154.83) \times 9.8 - \frac{1}{2} \times 1.2 \times 1000 \times v_{\text{dive}}^2 \times \frac{\pi}{4} \times 1.8^2 = 0, \tag{2}$$

$$v_{\text{dive}} = 0.982 m/s$$

$$154.83 \times 9.8 - \frac{1}{2} \times 1.2 \times 1000 \times v_{\text{rise}}^2 \times \frac{\pi}{4} \times 1.8^2 = 0, \tag{3}$$

$$v_{\text{rise}} = 0.997 m/s$$

Import the meshed model into FLUENT as illustrated in Figure 7. The lander's overall weight is set to 150 kg for the simulation of its fall, which is the weight remaining after deducting its buoyancy, and its upward buoyancy is set to 155 kg for floating. According to the simulation results, the lander's constant diving speed and rising speed in the water are both about 1 m/s, and the results are shown in Figure 8.

TABLE 2 Lander weight and buoyancy estimation.

Item	Weight in the air (kg)	Weight in the water (kg)
Titanium alloy frame	95.38	74.09
8 glass floats	137.6	Provide buoyancy of 208 kg
Buoyancy component	162	Provide buoyancy of 98 kg
2 acoustic releasers	56	40
Acoustic acquisition monitor	3.5	2
Attitude indicator	1	0.34
CTD	10	5
Lamp and camera	0.91	0.38
Iridium beacon	3.64	2.56
Battery tank	43.7	11.8
OBS	30	5
ADCP	15	7
Other sensors	5	3
Sum	563.73	Buoyancy 154.83

The lander can travel at a maximum speed of 0.982 m/s when it strikes the bottom and 0.997 m/s when it reaches the water's surface. For around 102 minutes, the lander descends to a water depth of 6000 m. For approximately 100 minutes, the lander rises to the sea's surface. The simulation and calculation outcomes are nearly identical.

4.3 Simulation of double decelerating

The sensing instrument of OBS is all installed in a glass ball placed in a plastic shell. Therefore, the impact resistance of OBS is weak. On the other hand, in addition to the internal sensor balance, OBS must be in close touch with the seabed to correctly transform ground motion impulses into electrical signals and collect them. The gathered signal could be inaccurate if there is inadequate coupling between OBS and the seafloor. As a result, OBS cannot move too slowly when it touches the seafloor, or the coupling between OBS and the seafloor would be weak. OBS's deployment experience indicates that a speed of 0.5 to 0.8 m/s can guarantee a good connection between the device and the seafloor.

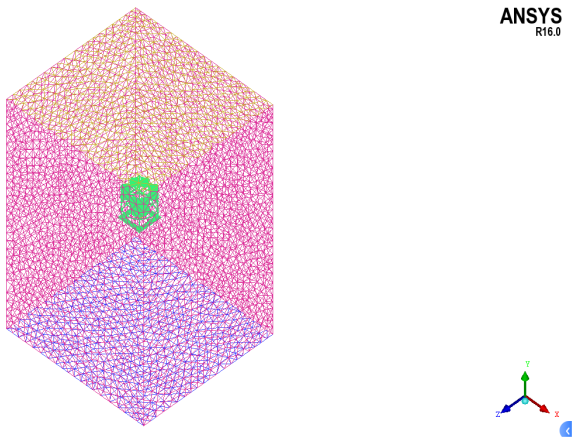

FIGURE 7
Simulation grid division.

The traditional OBS deployment method is to fix the ball on the steel frame, and there will be a buffer spring between the OBS and the steel frame, as demonstrated in Figure 9. When the OBS is deployed, throw the steel-framed OBS into the water, where it will fall under gravity at a speed of 1 to 1.5 m/s. When an OBS with a steel frame strikes the seafloor, the steel frame's speed decreases to 0 m/s from its diving speed. As it moves and compresses the spring, the OBS will continue to shield itself from harm. Although the descending speed of 1 to 1.5 m/s may guarantee that the lander's landing spot is near the predetermined area, it will also result in OBS damage, mainly if the landing site's sediment is complex or the landing site is rock.

When the OBS is mounted on the lander, the steel structure beneath it is no longer attached. The OBS is susceptible to damage when it collides with the seafloor directly without any protection. The lander's fall speed, which can assure a safe landing, is roughly 1 m/s, according to the findings of section 4.2. However, OBS might sustain damage if it strikes the seafloor at a speed of 1 m/s since the material's strength differs from the lander's. Therefore, to achieve the safe deployment of OBS, the lander is designed with the unit of decelerating landing, as described in Section 2.3.

The local simulation of the OBS installation layer is performed to verify the double decelerating's effectiveness. The simulation results show that when the lander is descending, the descent speed is 1 m/s. The OBS sphere's bottom lines up with the bottom of the lander when it is tightly attached to the frame. The OBS collides with the seafloor as the lander sinks to the bottom, and as it does so, its velocity drops from 1 m/s to 0, creating an impact force. The OBS is attached to the lander frame in this arrangement by a flexible cable moving upward relative to it when the water uplift

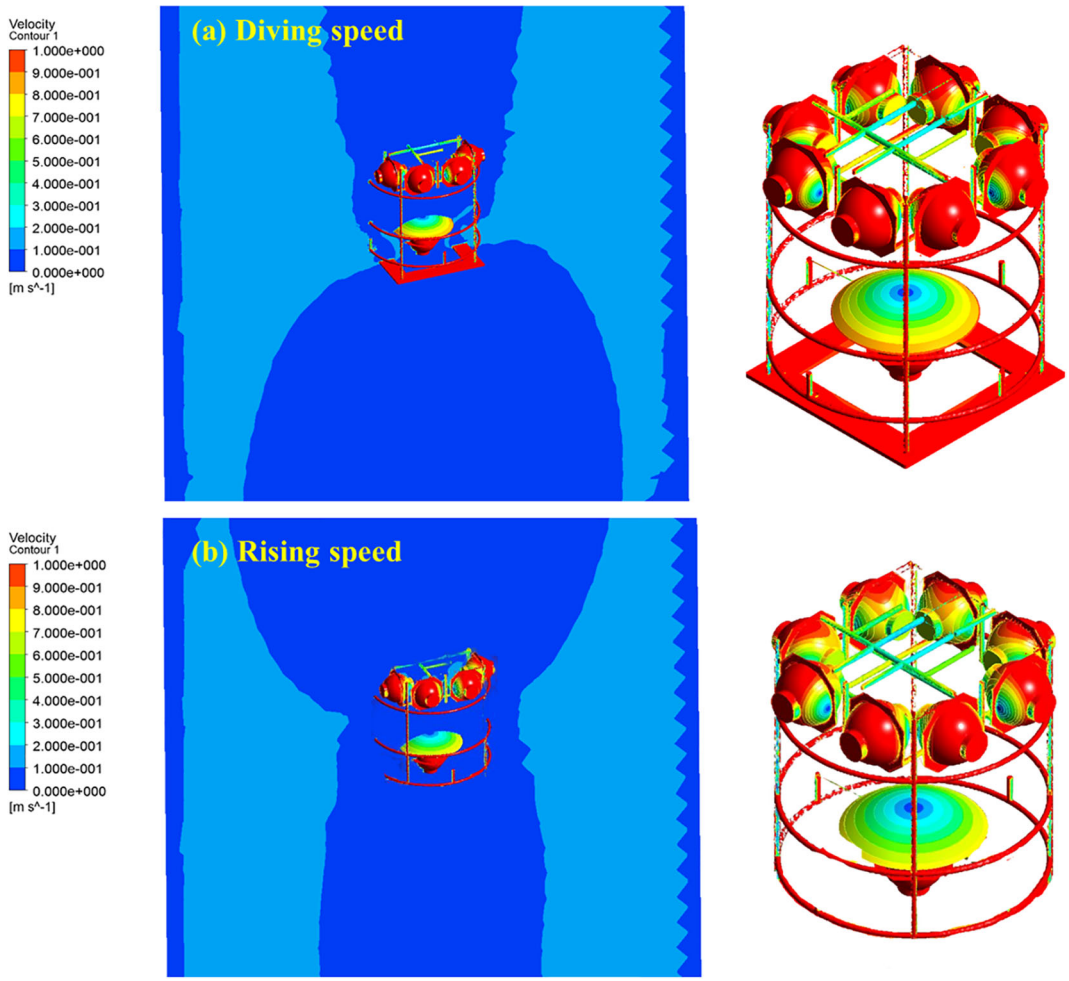

FIGURE 8
Simulation results of lander diving and rising speed. **(A)** Diving speed; **(B)** Rising speed.

force acts on it. Restricted by the length of the cable and the limiting net, the OBS stabilized after an upward displacement of 160 mm, as shown in Figure 8A and Figure 10, and then diving at 1 m/s with the lander. As illustrated in Figure 11, OBS's speed steadily reduces once the lander stops moving because of its gravity until it makes contact with the seafloor surface at a speed of 0.55 m/s. During the OBS deployment, there is no impact force, ensuring the safe placement of OBS balls.

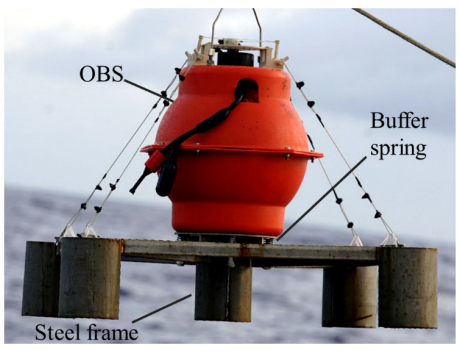

FIGURE 9
Traditional OBS structure (accessedhttp://oil.igg.cas.cn/gb2019/hddzy/hddzyobs/, 2019).

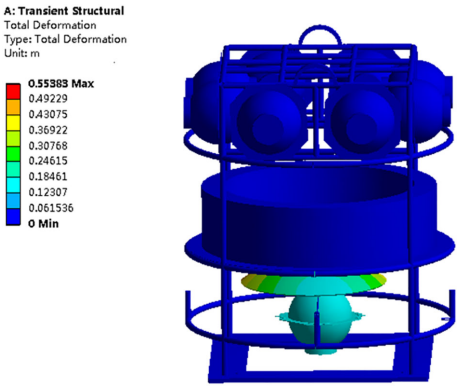

FIGURE 10
Simulation of the double decelerating landing of the lander.

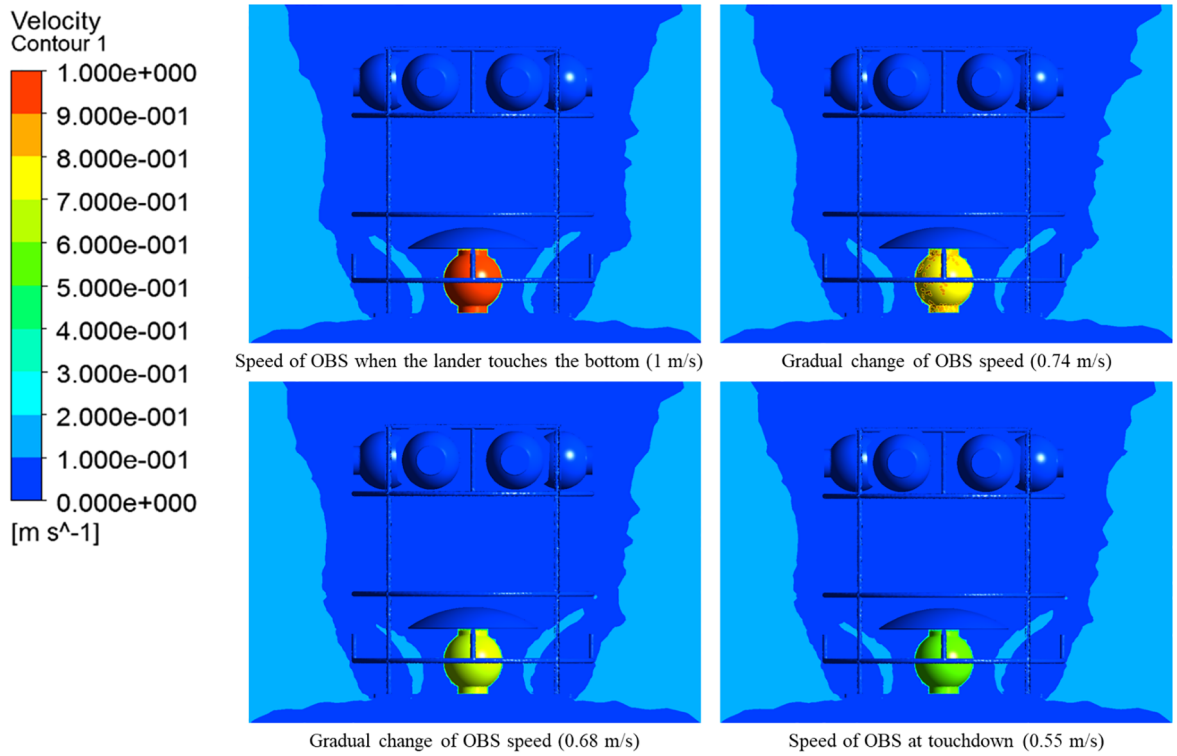

FIGURE 11
Simulation results of OBS speed when it contacts with the seabed.

5 Field application

Two field applications of the lander were carried out, as shown in Figure 12. In one of the actual applications, the lander functioned at a depth of 2,240 m for 75 hours. In a second application, the lander submerged for 45 hours at a depth of 1,790 meters. Two successful applications have proved that the characteristics and technical indicators of the lander are adequate. The lander's acoustic communication capabilities, free landing and surfacing, and acquisition performance in deep water were evaluated in a field application. In both applications, the monitoring equipment successfully obtained deep-sea *in-situ* data. The application site is shown in Figure 13.

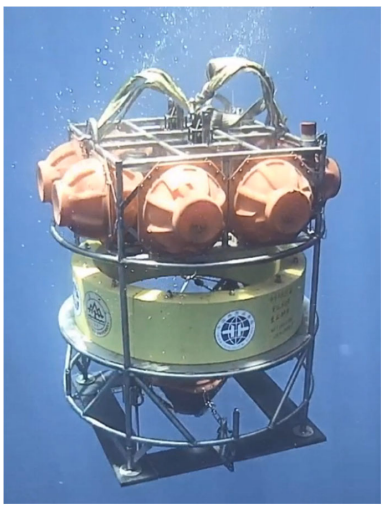

FIGURE 12
Underwater photography of lander.

Before the sea trial, all sensors on the lander were calibrated, and the lander underwent Special detection and general testing, including compressive strength testing, sealing testing, self-testing, and electromagnetic compatibility testing. In the field application, the operation phases consist of lander inspection, equipment assembly and testing, lander deployment, underwater operations, and lander retrieval.

Seafloor temperature, salinity, Eh, turbidity, underwater acoustic environment, and OBS data were successfully monitored in both field applications, which the corresponding data is not displayed because of confidentiality. As depicted in Figure 14, the attitude of the lander is steady during a dive, with little fluctuation in azimuth, pitch, and roll angles. The cylindrical chamber in the center of the lander promotes the flow of water from bottom to top (top-down when rising) and preserves the lander's attitude stability during deployment or recovery. In Section 4.2, the diving and rising velocities of the lander are calculated to be 0.982 m/s and 0.997 m/s, respectively. As illustrated in Figure 15, the lander measured diving and ascending speeds of 0.925 m/s and 0.9335 m/s, respectively, commensurate with the design speed. The difference between the actual speed and the calculated speed may be due to the simple formulas used in the calculation, and the numerical settings for parameters also need to be improved.

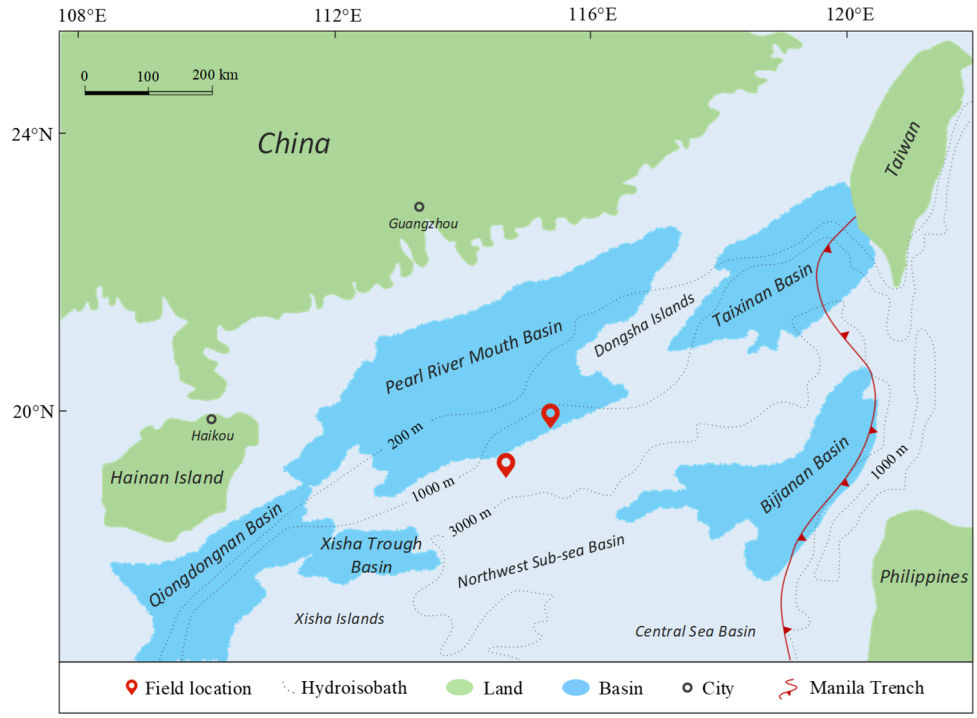

FIGURE 13
Overview of field application location and surrounding area (modified from Cui et al., 2022).

After two applications in the deep-sea, it shows that the lander can be used under deep-sea circumstances. The lander deployment and recovery are stable, and the *in-situ* monitoring task can be successfully completed, indicating that the lander design is successful.

6 Conclusions

A new double decelerating lander was successfully developed. The lander's design meets the installation and working requirements of various instrumentation devices, especially the design of double decelerating achieve the safe deployment of OBS and other equipment that must be in contact with the seabed. Optimizing the release structure improves the success rate of decoupling release counterweight. Simulation research demonstrates that the structural strength of the lander is sufficient, and the motion parameters of the lander during deployment and recovery are determined. Two field applications were successfully carried out, and various *in-situ* data in the deep sea were obtained, achieving the goal of long-term *in-situ* monitoring. The simulation results and field applications prove that the diving

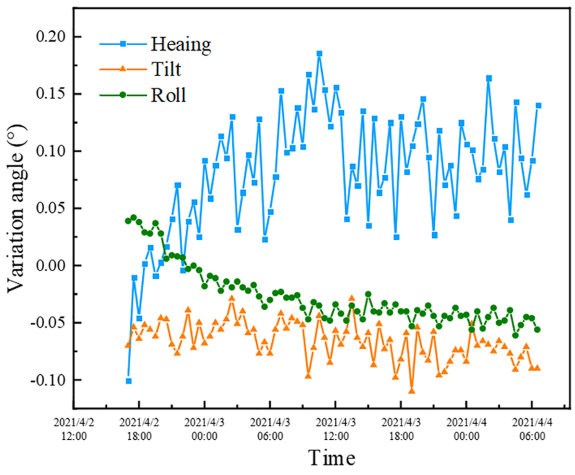

FIGURE 14
Attitude change of lander during diving.

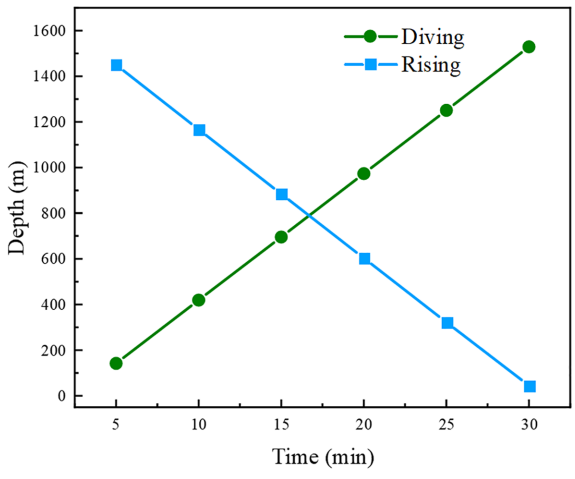

FIGURE 15
The depth change of the lander during the diving and rising.

speed of the developed lander meets the design and safety requirements, and can also protect the OBS device. A feasible technical means for deep-sea *in-situ* monitoring have been proposed, and the double decelerating lander has also expanded the technical system of marine environmental investigation.

Data availability statement

The original contributions presented in the study are included in the article/Supplementary Material. Further inquiries can be directed to the corresponding author.

Author contributions

LG and XY: Methodology, Formal analysis, Writing - Original Draft, Writing - Review & Editing. GX: Review & Editing. CW, ZF, and SZ: Formal analysis. YL: Visualization. KL and YY: Supervision. All authors contributed to the article and approved the submitted version.

Funding

This research was funded by the National Natural Science Foundation of China (NSFC) (No.U2006213) and Laoshan Laboratory (No. LSKJ202203505).

Conflict of interest

The authors declare that the research was conducted in the absence of any commercial or financial relationships that could be construed as a potential conflict of interest.

Publisher's note

All claims expressed in this article are solely those of the authors and do not necessarily represent those of their affiliated organizations, or those of the publisher, the editors and the reviewers. Any product that may be evaluated in this article, or claim that may be made by its manufacturer, is not guaranteed or endorsed by the publisher.

References

Berelson, W. M., Buchholtz, M. R., Hammond, D. E., and Santschi, P. H. (1987). Radon fluxes measured with the MANOP bottom lander. *Deep Sea Res. Part A Oceanographic Res. Papers* 34 (7), 1209–1228. doi: 10.1016/0198-0149(87)90072-0

Black, K. S., Fones, G. R., Peppe, O. C., Kennedy, H. A., and Bentaleb, I. (2001). An autonomous benthic lander: Preliminary observations from the UK BENBO thematic programme. *Continental Shelf Res.* 21 (8-10), 859–877. doi: 10.1016/S0278-4343(00)00116-3

Chen, Z., Li, J., Li, X., Chen, S., Dasgupta, S., Bai, S., et al. (2020). Characteristics and implications of isoprenoid and hydroxy tetraether lipids in hadal sediments of Mariana and yap trenches. *Chem. Geol.* 551, 119742. doi: 10.1016/j.chemgeo.2020.119742

Chen, J., Zhang, Q. F., and Li, J. (2017). Research on the application of the hadal lander technology in the Mariana trench. *J. Ocean Technol.* 36 (1), 63–69.

Cui, Y., Guo, L., Liu, T., Yang, Z., Ling, X., Yang, X., et al. (2022). Development and application of the 3000 m-level multi-parameter CPTu in-situ integrated test system. *Mar. Geores Geotechnol.* 1-12. doi: 10.1080/1064119X.2022.2053008

Duineveld, G., Lavaleye, M., Berghuis, E., and De Wilde, P. (2001). Activity and composition of the benthic fauna in the whittard canyon and the adjacent continental slope (NE Atlantic). *Oceanol. Acta* 24 (1), 69–83. doi: 10.1016/S0399-1784(00)01129-4

Hardy, K., Cameron, J., Herbst, L., Bulman, T., and Pausch, S. (2013). "Hadal landers: the DEEPSEA CHALLENGE ocean trench free vehicles," in *2013 OCEANS-San Diego* (San Diego: IEEE), 1–10.

Jamieson, A. J., Fujii, T., Solan, M., and Priede, I. G. (2009). HADEEP: Free-falling landers to the deepest places on earth. *Mar. Technol. Soc. J.* 43 (5), 151–160. doi: 10.4031/MTSJ.43.5.17

Lavaleye, M., Duineveld, G., Lundälv, T., White, M., Guihen, D., Kiriakoulakis, K., et al. (2009). Cold-water corals on the tisler reef: Preliminary observations on the dynamic reef environment. *Oceanography* 22 (1), 76–84. doi: 10.5670/oceanog.2009.08

Li, J., Xu, J., and Liu, Z. (2013). Applications of tripods to deep-Sea observation. *Adv. Earth Sci.* 28 (5), 559–565.

Oevelen, D. V., Duineveld, G., Lavaleye, M., Mienis, F., Soetaert, K., and Heip, C. H. (2009). The cold-water coral community as hotspot of carbon cycling on continental margins: A food-web analysis from rockall bank (northeast Atlantic). *Limnol. Oceanography* 54 (6), 1829–1844. doi: 10.4319/lo.2009.54.6.1829

Person, R., Aoustin, Y., Blandin, J., Marvaldi, J., and Rolin, J. F. (2006). From bottom landers to observatory networks. *Ann. Geophysics* 49 (2-3), 581–593. doi: 10.4401/ag-3122

Podolskiy, E. A., Murai, Y., Kanna, N., and Sugiyama, S. (2021). Ocean-bottom seismology of glacial earthquakes: The concept, lessons learned, and mind the sediments. *Seismol. Res. Lett.* 92 (5), 2850–2865. doi: 10.1785/0220200465

Rowe, G. T., Boland, G. S., Briones, E. G. E., Cruz-Kaegi, M. E., Newton, A., Piepenburg, D., et al. (1997). Sediment community biomass and respiration in the northeast water polynya, Greenland: a numerical simulation of benthic lander and spade core data. *J. Mar. Syst.* 10 (1-4), 497–515. doi: 10.1016/S0924-7963(96)00065-6

Schlindwein, V., Kirk, H., Hiller, M., Scholz, J. R., and Schmidt-Aursch, M. (2022). *GAKKELDEEP: DEPAS ocean-bottom seismometer operations at the gakkel ridge in 2018-2019.*

Tahey, T. M., Duineveld, G. C. A., DeWilde, P. A. W. J., Berghuis, E. M., and Kok, A. (1996). Sediment O-2 demand, density and biomass of the benthos and phytopigments along the northwestern Adriatic coast: The extent of po enrichment. *Oceanol. Acta* 19 (2), 117–130.

Turchik, A. J., Berkenpas, E. J., Henning, B. S., Shepard, C. M.IEEE (2015). "The deep ocean dropcam: A highly deployable benthic survey tool," in *In OCEANS 2015-MTS/IEEE Washington*, 1–8.

Witbaard, R., Duineveld, G. C. A., van der Weele, J. A., Berghuis, E. M., and Reyss, J. P. (2000). The benthic response to the seasonal deposition of phytopigments at the porcupine abyssal plain in the north East Atlantic. *J. Sea Res.* 43 (1), 15–31. doi: 10.1016/S1385-1101(99)00040-4

Wu, H., Tan, C., Jin, B., Yang, C., and Chen, Y. (2011). Design of an energy supplying device for equipments for in-situ detection of deep-sea hydrothermal fluid. *Mar. Sci.* 35 (02), 82–85.

Yu, X., Yan, Z., Zhu, M., Li, D., Jiang, Z., and Cui, S. (2017). Review of seabed landers for monitoring solute fluxes in deep sea. *Mar. Sci.* 41 (06), 150–161.

Yu, Z., Zhang, C., Chen, J., and Ren, Z. (2022). Dynamic analysis of bottom subsidence of benthic lander. *J. Mar. Sci. Eng.* 10 (6), 824. doi: 10.3390/jmse10060824

frontiers | Frontiers in Marine Science

TYPE Original Research
PUBLISHED 27 January 2023
DOI 10.3389/fmars.2023.1091523

OPEN ACCESS

EDITED BY
Yuan Lin,
Zhejiang University, China

REVIEWED BY
Haocai Huang,
Zhejiang University, China
Zhenzhong Chu,
University of Shanghai for Science and Technology, China
Wang Honghui,
Ocean University of China, China

*CORRESPONDENCE
Yanjun Liu
lyj111yjslw@163.com

SPECIALTY SECTION
This article was submitted to Ocean Observation, a section of the journal Frontiers in Marine Science

RECEIVED 07 November 2022
ACCEPTED 09 January 2023
PUBLISHED 27 January 2023

CITATION
Xue G, Bai F, Guo L, Ren P and Liu Y (2023) Research on the effects of complex terrain on the hydrodynamic performance of a deep-sea fishlike exploring and sampling robot moving near the sea bottom. *Front. Mar. Sci.* 10:1091523. doi: 10.3389/fmars.2023.1091523

Research on the effects of complex terrain on the hydrodynamic performance of a deep-sea fishlike exploring and sampling robot moving near the sea bottom

Gang Xue[1,2,3], Fagang Bai[1,2], Lei Guo[1], Pingshun Ren[1,2] and Yanjun Liu[1,2]*

[1]Institute of Marine Science and Technology, Shandong University, Qingdao, China, [2]School of Mechanical Engineering, Key Laboratory of High-Efficiency and Clean Mechanical Manufacture of Ministry of Education, National Demonstration Center for Experimental Mechanical Engineering Education, Shandong University, Jinan, China, [3]Key Laboratory of Ocean Observation Technology, Ministry of Natural Resources, People's Republic of China, Tianjin, China

Deep-sea exploring and sampling technologies have become frontier topics. Generally, the movable exploring mode near the seabed with low disturbance is an important way to improve the measurement accuracy and expand the measurement range. Inspired by fish, the fishlike propulsion method has the characteristics of low disturbance and high flexibility, which is very suitable for near-seabed detection under complex terrain conditions. However, the swimming mechanism and surrounding flow field evolution law of the robotic fish under the constraints of complex terrain are still unclear. In this paper, the confined terrain space is constructed with an undulating seabed and a narrow channel, and the hydrodynamic changing law and flow field evolution law of the autonomous swimming process of the fishlike swimmer in the confined space are analyzed. Moreover, the influence mechanism of the terrain on the motion performance of the robotic fish is revealed, and the optimal motion mode of the robotic fish under a complex terrain constraint is discussed. The results show that the propulsion force, Froude efficiency, and swimming stability of the robotic fish vary with the distance from the bottom under the undulating seabed condition lightly. When the distance from the bottom exceeds a certain value, it can be considered that the undulating seabed no longer affects the swimmer. Furthermore, when the robotic fish swims through a narrow channel with certain width, the swimming performance obviously varies with the distance from the boundary surface. During swimming in the confined terrain space, the propulsion force and swimming stability of robotic fish will decrease. In order to maintain the forward speed, the robotic fish should improve the tail-beat

frequency in real time. However, considering the swimming stability, the tail-beat frequency is not the larger the better. The relevant conclusions of this paper could provide theoretical support for the development of low-disturbance bionic exploring and sampling platforms for deep-sea resources and environments.

KEYWORDS

fishlike robot, hydrodynamic analysis, deep-sea exploring and sampling, swimming near the wall, CFD simulation

1 Introduction

In terms of marine scientific research, seafloor sample analysis in the laboratory (He et al., 2020) and *in situ* seafloor analysis (Takahashi et al., 2020) are important ways to obtain environmental, geological, and biological information about the seabed sediment. The heavy *in situ* equipment represented by deep-sea landers (Wei et al., 2020) and the light mobile equipment represented by underwater robots (Whitt et al., 2020) are the main seafloor detection and sampling tools. Because of the flexible motion ability and the extensive operational range, underwater robots have attracted increasing interest in both science area and technology area (Dhongdi, 2022).

In practice, underwater robots have been widely used in deep-sea exploration and sampling. Fossum et al. (2021) have developed an autonomous underwater vehicle (AUV) for detection and sampling of the Arctic front characterized by strong lateral gradients in temperature and salinity and the AUV-augmented ship-based sampling. Feng et al. (2021) have developed an AUV to detect and track the thermocline, which had an important influence on marine fisheries, and achieved coverage observation of a highly dynamic water column containing multiple thermoclines. In order to achieve autonomous discovery and intense sampling of high chlorophyll-a concentration areas, Zhang et al. (2022) have proposed an online path-planning method with heterogeneous strategies and low-communication cooperation for the adaptive sampling of multiple AUVs. Jiang et al. (2022) have proposed to construct a movable laboratory that includes a mothership and several full-ocean-depth autonomous and remotely operated vehicles to obtain samples in the hadal trenches. Yoerger et al. (2021) have developed an AUV to address the specific unmet needs for observing and sampling a variety of phenomena in the ocean, including environment and biodiversity. However, the abovementioned devices are driven by underwater screw propellers, which will severely disturb the water body and sediment. The water body and the sediment within the target area will easily mix with each other, and the sample purity and the detection accuracy will be seriously affected.

Fortunately, the swimming method of fish inspired the development of new concept underwater robots, and the fishlike propulsion mode could greatly lessen the effect of underwater robot movement on the *in situ* environment. Li et al. (2021) have developed a self-powered soft robot for deep-sea exploration by the dielectric elastomer material, which has been actuated successfully in the Mariana Trench. Wang et al. (Wang et al., 2022) have designed and manufactured a high-frequency swing robotic fish based on the electromagnetic driving mechanism to achieve fast swimming. Zhong et al. (2018) have developed a robotic fish with a wire-driven caudal fin and a pair of two-degree of freedom (DOF) pectoral fins, whose swimming speed can be 0.66 body length per second and turning radius can be 0.25 body length per second. Dong et al. (2022) have proposed a robotic fish driven by the soft actuator consisting of stacked soft polyvinyl chloride (PVC) gel to achieve high-flexibility swimming. Moreover, Wang et al. (2021) have designed a novel multilink gliding fish robot to build a reliable information collection system for the Internet of Underwater Things (IoUT), which could enable smart ocean in the future.

In order to increase the motion stability and the control accuracy of the robotic fish in the detection and sampling process, the hydrodynamic characteristics of the fishlike swimming motion should be analyzed to provide the dynamic model for the motion control. Ghommem et al. (2020) have simulated thrust forces, lateral forces, and vorticity patterns in the wake of a swimming deformable fishlike body to reveal the existence of an optimal lateral oscillation amplitude that produces positive thrust. Xue et al. (2020) have studied the evolvement rule of the fluid field around the fishlike model from starting to cruising and the hydrodynamic effect to find that the superposition of vortices could benefit the swimming performance. Ogata et al. (2017) have simulated the swimming processes of fishlike swimmers at various Reynolds numbers (*Re*) and analyzed several data sets of flow field using Q-criterion isosurfaces to build a prediction model for the terminal swimming speed at different *Re*. Hang et al. (2022) have designed a self-propelled two-link model to analyze the effects of both active and passive body bending on the swimming performance of robotic fish, and the results showed that speed and efficiency could be improved simultaneously when fish actively bend their bodies in a fashion that exploited passive hydrodynamics. Xing et al. (2022) have proposed a novel bionic pectoral fin and experimentally studied its hydrodynamic performance, and the results indicated that the hydrodynamic performance was closely related to the motion equation parameters including the amplitude, frequency, and phase difference. Li et al. (2021) have discussed the hydrodynamic characteristics and flow field structure of fish schools in various vertical patterns to find that the thrust and swimming efficiency of individuals can be improved. Macias et al. (2020) have emphasized the importance of the vortex wake for the formation of thrust during fish swimming. The Q-criterion was employed in their work for vortex identification to address the hydrodynamic characteristics of a swimming fish, and the

relationship between the hydrodynamic force coefficient and the vortex wake was analyzed. However, the research on hydrodynamic characteristics is mostly about the robotic fish swimming in the open flow field without boundaries. During the detection and sampling process, the robotic fish must move close to the seabed, which constitutes a restricted space for robotic fish to swim. The restricted space will affect the hydrodynamic characteristics and further affect the motion stability and the control accuracy.

Windsor et al. (2010) have proven that the characteristic changes in the form of the flow field occurred when the fish was near the plane wall, and the fish was able to sense the changes using a lateral line. The phenomenon has inspired to develop a distributed pressure sensory system (Xu and Mohseni, 2016). Quinn et al. (2014) have conducted force measurements and particle image velocimetry on flexible rectangular panels to imitate the flexible swimming mode of fish, and the results showed that panels produced more thrust near the ground. Xie et al. (2022) have investigated the hydrodynamics of a three-dimensional (3D) flapping caudal fin in ground effect to find that the caudal fin flapping near the ground has an effect of improving thrust and efficiency. Ma et al. (2021) have studied the influence of ground effect on the performance of robotic fish propelled by oscillating paired pectoral fins to find that the average thrust increased with the decreasing distance between the robotic fish and the bottom. The above studies all concentrated on the object of caudal fin, pectoral fin, and flexible plate, and the constraint boundaries were all single plane. The swimming performance of the entire fish or robotic fish has not been adequately studied. Additionally, deep-sea bottom topography is incredibly complex with features including undulating terrain, narrow channels, and other flow field boundary conditions. It is yet unclear how these complex deep-sea bottom topographic features affect the hydrodynamics of robotic fish.

This work focuses on the hydrodynamic characteristics of a fishlike swimmer under the constraint conditions of an undulating terrain and a trench terrain. Through the hydrodynamic force calculation and flow field visualization, the influence mechanism of the complicated terrain on the swimming performance is demonstrated, and the optimal motion mode of robotic fish adapting to a complex terrain condition is discussed. The rest of this paper is organized as follows. In the section *Model*, the geometry model and motion model of the fishlike swimmer are established, and the step boundary and the double-wall boundary are established to simulate the undulating terrain and the trench terrain, respectively. In the section *Method*, the numerical model to simulate the self-propelled fishlike swimmer moving in the restricted space is established, the simulation accuracy is discussed, and several cases are conducted with various tail-beat frequencies of the fishlike swimmer. In the section *Results and Discussion*, the hydrodynamic force and flow field are visualized, and the effects of the terrain on the hydrodynamic characteristics and swimming performance are discussed. In the section *Conclusion*, the work is concluded. The findings of this work will clarify the influence mechanism of complicated terrain conditions on the hydrodynamic characteristics of the fishlike swimmer, provide a theoretical bases for the motion control, and do favor in improving the motion stability and the control accuracy of robotic fish when detecting and sampling near the seabed.

2 Model

2.1 Geometry and kinematic laws for the fishlike swimmer

2.1.1 Geometrical model of the fishlike swimmer

After long-term evolution, the fish has developed complicated and varied movement patterns, which can be categorized into Body and/or Caudal Fin (BCF) mode and Median and/or Paired Fin (MPF) mode based on the motion parts (Wang et al., 2022). Most fish conduct BCF mode to achieve high swimming speed and excellent propulsion efficiency. In addition, according to the relative position that the propulsion force-generating part occupied compared to the overall length of the fish body, the BCF mode can be further divided into four categories, Anguilliform, Subcarangiform, Carangiform, and Thunniform (Hoar et al., 1983).

The Carangiform fish was taken as the biomimetic object of this study, whose head swing range is fairly small, the length of the caudal fin and swinging trunk occupied nearly half of the entire body, and the pectoral fins could do favor in propulsion. The total length L_b of the fishlike swimmer includes a head length L_1, a trunk length L_2, and a tail length L_3. The 3D dimension of the geometrical model is $L_b \times W_b \times H_b$, as shown in Figure 1.

2.1.2 Morphological kinematic model

Fish has a flexible body and can swim with a variety of fluctuating motion principles, which is the key point of excellent swimming performance (Wang et al., 2022). As a result, when describing the fluctuating motion model of the fish body, flexibility must be taken into consideration. In the swimming process, the motion trajectory of the fish body's midline can be precisely described by the traveling wave equation with a steadily rising amplitude (Cui et al., 2018).

The kinematic model specified by previous research (Xue et al., 2020) was adopted to describe the body's deforming motion of the Carangiform swimmer to minimize the head yaw amplitude. The length of the entire body was used in dimensionless processing. Meanwhile, a time function (Curatolo and Teresi, 2016) was introduced to simulate the whole deformation process from a static state to a steady pace to deal with the starting divergence problem in the simulation. The optimized kinematic model of the swimmer's midline can be expressed as follows:

$$y(x,t) = A\left[\frac{s}{s-1}\frac{x}{L_b} - \frac{4}{5(s-1)}\right]^{\epsilon} \sin\left(k\frac{x}{L_b} - 2\pi ft\right)\left(1 - e^{-\frac{t}{t_s}}\right)L_b \qquad (1)$$
$$s \geq 3, \epsilon \geq 1, 0 \leq x \leq L_b$$

where x represents the displacement along the direction from the head to the tail, y represents the lateral undulation value of the midline in the body frame, t is the swimming time, f is the tail-beat frequency, $k=2\pi/\lambda$ is the wave number, and λ is the wavelength. In addition, A and ε control the oscillating amplitude, and s describes the initial oscillating position at the body.

Assuming that the fishlike swimmer moves in a straight line along a set direction, without steering motion, and the fluctuation amplitude and period are constant. The body-caudal fin fluctuation of the fishlike swimmer can be regarded as periodic motion. The

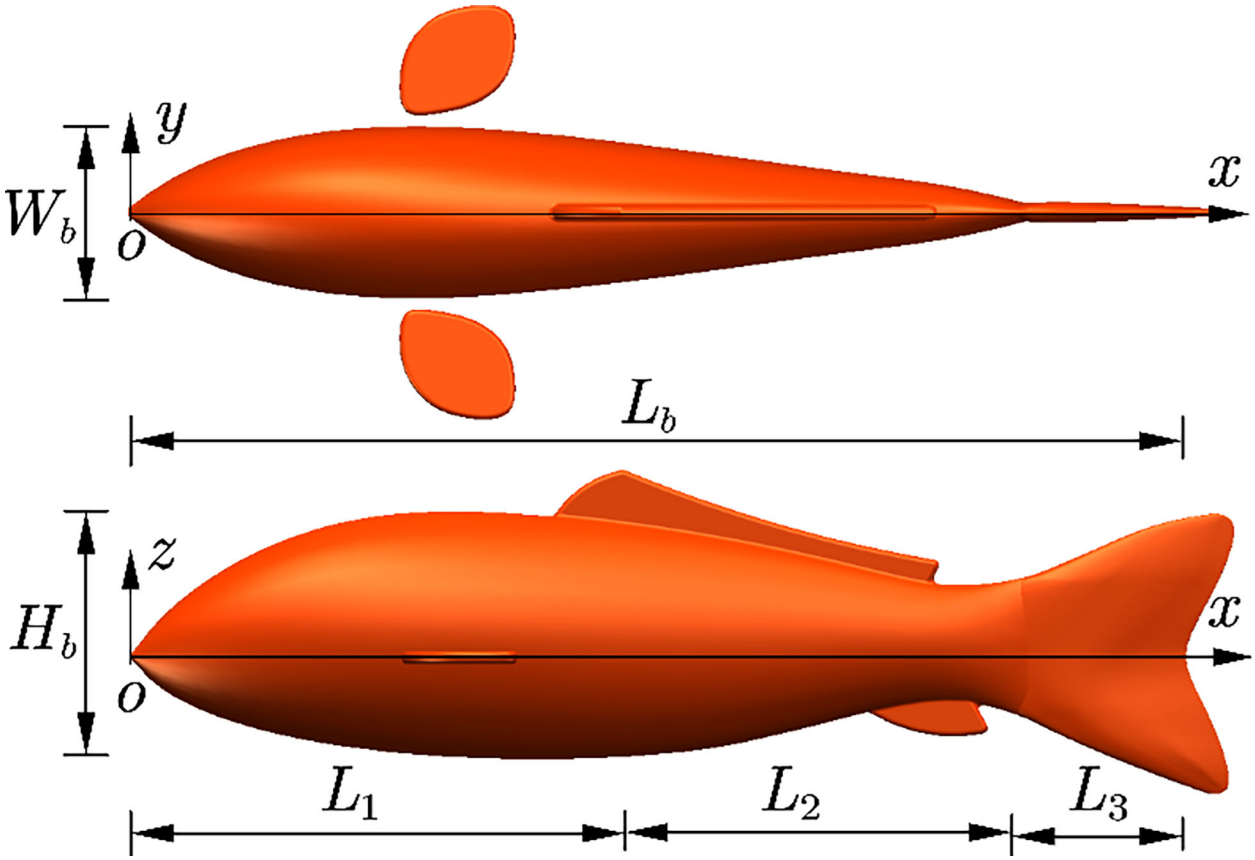

FIGURE 1
3D geometrical model of the fishlike swimmer. 3D, three-dimensional.

fluctuation curves of the midline in one tail-beat cycle are depicted in Figure 2, where λ=0.95 , A=0.1 , s=5 , and ϵ=3 .

The hydrodynamic force generated by the pectoral fins of the swimmer is the key factor to achieve the motion in three dimensions. Although it is not the focus of this study, in order to simulate the swimming process more realistically, the effect of the pectoral fin on swimming was taken into consideration. The left and right pectoral fins were simply defined as simultaneous oscillations with equal angles. The oscillation equation of pectoral fins in the x–z plane can be defined as follows.

$$\theta(t) = \theta_{max}\sin(2\pi ft + \varphi)\left(1 - e^{-\frac{t}{t_s}}\right) \tag{2}$$

where $\theta(t)$ represents the angular oscillation of the pectoral fins, θ_{max} is the maximum oscillation amplitude, and φ is the phase difference between the fluctuating motion of the body and oscillation of the fins.

2.2 Models of complex terrain

2.2.1 Undulating seabed boundary

When a robotic fish performs exploration and sampling near the seabed, the uneven seafloor surface constitutes the boundary of the motion space. The complex topography of the seafloor will significantly affect the flow field close to the seabed (Rogers et al., 2018) and further affect the swimming performance of the robotic fish. Compared to the size of the robotic fish, the scale of the terrain, such as a submarine mountain, cliff, and cave, is relatively large (Lecours et al., 2016). The effects on hydrodynamics caused by large-scale terrains change smoothly, which has little impact on the motion stability of the robotic fish. However, the structural characteristics, such as a small-scale undulation and a local bulge, have an obvious and sudden impact on the swimming performance, which should be taken into consideration.

The topography of the seafloor is intricately layered. In order to facilitate the quantitative description of the topography changes, the local undulation feature of the seabed was simplified using the stepped surface to describe the height change of the seabed. The height of the fish body H_b was used to nondimensionalize the distance H between the fish belly and the seafloor surface. The process of the robotic fish that swam near the stepped surface was simulated. As the robotic fish swam, the value of H decreased gradually, as shown in Figure 3. The impact of the seabed boundary modification on the swimming performance was examined. In this process, the values of H changed in the sequence as $5H_b$, $2.5H_b$, $1.25H_b$, and $0.25H_b$. Ahead of the comparison, the fishlike swimmer should reach to a steady speed to eliminate the influence of the starting process. Thus, the robotic fish swam a significant distance in the area where H was equal to $5H_b$. In addition, the swimming distance was $3L_b$ at the condition where H was equal to $2.5H_b$, $1.25H_b$, or $0.25H_b$.

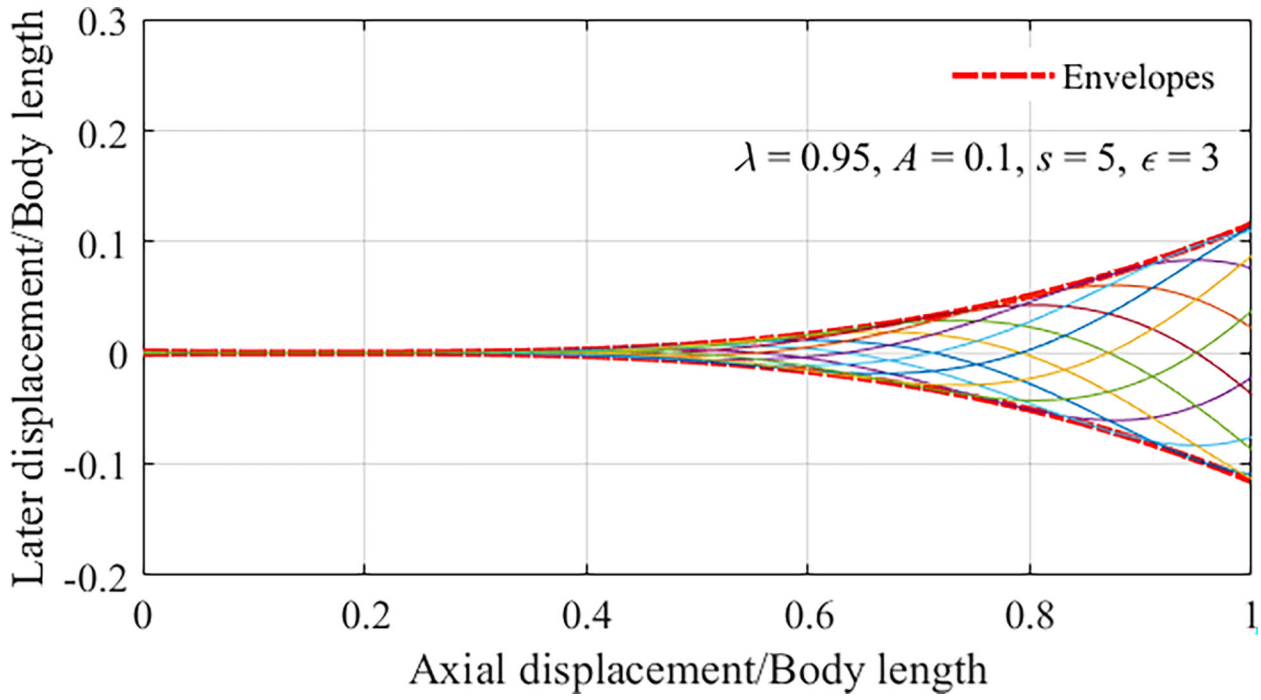

FIGURE 2
Midlines of the fish for different instants in one tail-beat cycle.

2.2.2 The narrow channel

The fishlike propulsion mode has shown excellent mobility and flexibility, which makes fish or robotic fish swim in narrow channels easily. The flow field changes resulting from the two vertical boundary surfaces of narrow channels should be given enough attention when the robotic fish conducts underwater exploration and sampling (Ćatipović et al., 2019). Under the condition that the channel width is narrow, the impact of the boundary surfaces on the hydrodynamic

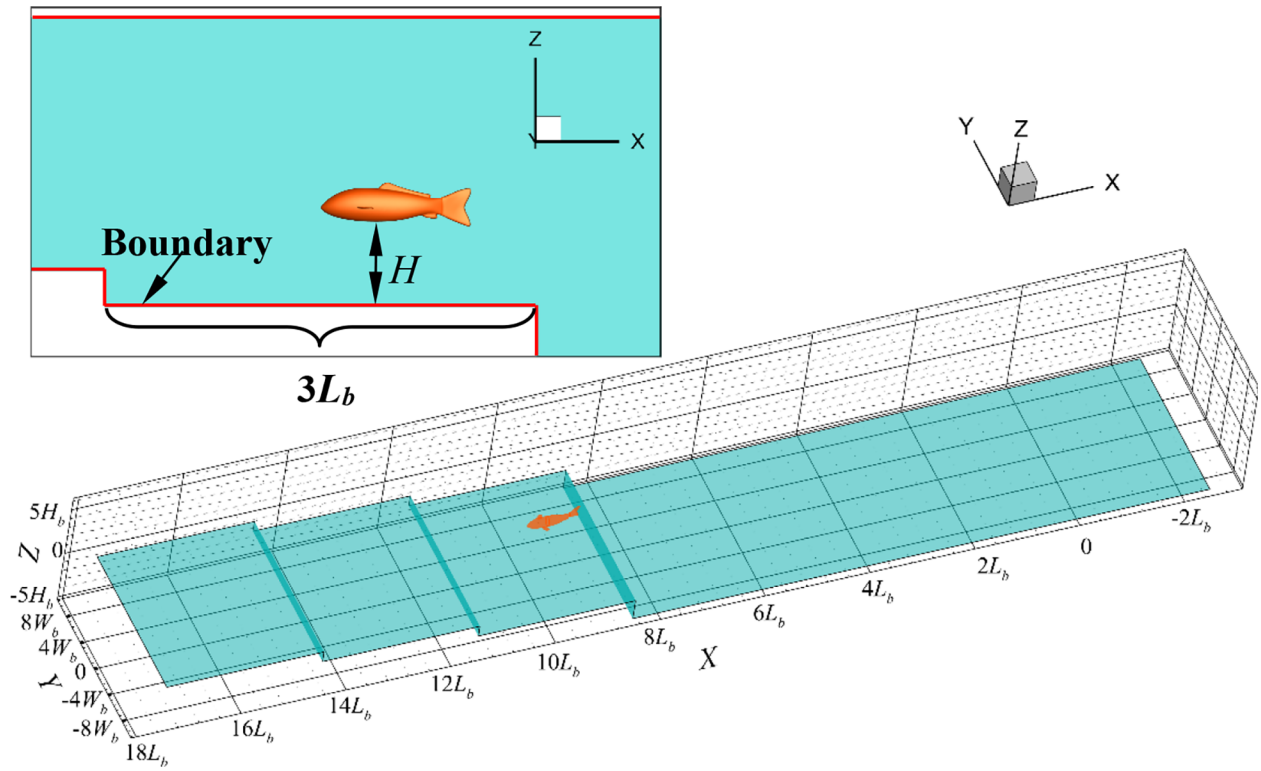

FIGURE 3
The undulating seabed boundary model.

characteristics of the swimmer is clear enough, which will affect the swimming performance. Especially during the processes of the swimmer entering the narrow channel from the open water and swimming from the narrow channel into the open water, the boundary conditions of the flow field change dramatically, which will disturb the motion state of the robotic fish. Then, the seabed exploration and sampling process will become unstable.

Similarly, the structure of the narrow channel was simplified. The two vertical boundary surfaces of the narrow-channel model were both set as plane, and the distance W from one side of the swimmer to the near narrow-channel boundary was nondimensionalized by the body width W_b, as shown in Figure 4. The continuous process of the swimmer moving into the narrow channel from the open water, passing the narrow channel, and subsequently moving out of the narrow channel to the open water was numerically simulated. The impact of the boundary on the motion stability of the swimmer was analyzed. In this process, the values of W changed in sequence as $10W_b$, $5W_b$, $1W_b$, and $10W_b$. Before moving into the narrow channel, the robotic fish swam a suitable distance in the area where W was equal to $10W_b$ before entering the narrow channel. The swimming distance was $3L_b$ at the condition where W was equal to $5W_b$ or $1W_b$. The included angle between the transition connection surface and the boundary surface is 45 degrees.

3 Method

3.1 Computational methodology

3.1.1 Numerical implementation

According to the above definition of kinematics, the rolling and pitching DOFs of the swimmer can be ignored when swimming in 3D space. Thus, the fishlike swimmer can achieve three translational DOFs (forward translation x, lateral translation y, and vertical translation z) and one rotational DOF (yaw angle ψ) in the global frame $OXYZ$ as shown in Figure 5. The generalized location X, velocity V, force F vectors, and the mass matrix M of the swimmer's center of mass (COM) can be defined as follows:

$$\boldsymbol{X}=\begin{pmatrix}x\\y\\z\\\psi\end{pmatrix},\boldsymbol{V}=\begin{pmatrix}u\\v\\w\\r\end{pmatrix},\boldsymbol{F}=\begin{pmatrix}F_h^x\\F_h^y\\F_h^z\\M_h^z\end{pmatrix},\boldsymbol{M}=\begin{pmatrix}m&0&0&0\\0&m&0&0\\0&0&m&0\\0&0&0&I_z\end{pmatrix} \tag{3}$$

where u, v, w, and r are the generalized velocity components corresponding to the generalized location, F_h is the force component in the corresponding directions, M_h is the moment component in the z-direction, m is the mass of the swimmer that has a density of $\rho_b=\rho$, and I_z is the moment of inertia to the COM. The 4-DOF motion of the self-propelled swimmer can be described as follows:

$$\boldsymbol{F}=\boldsymbol{M}_T\frac{d\boldsymbol{V}}{dt} \tag{4}$$

where M_T is the generalized total mass matrix, $M_T=M+M_A$, and M_A is the generalized added mass matrix. The generalized instantaneous fluid force F can be calculated directly by the numerical simulation. The swimmer's generalized location X and generalized velocity V of each time step Δt can be calculated from the force value and motion state at the previous time step in the numerical simulation.

The trapezoidal rule was used for numerical integration, such that the generalized variables at time $(t+\Delta t)$ in the calculation process can be expressed as follows:

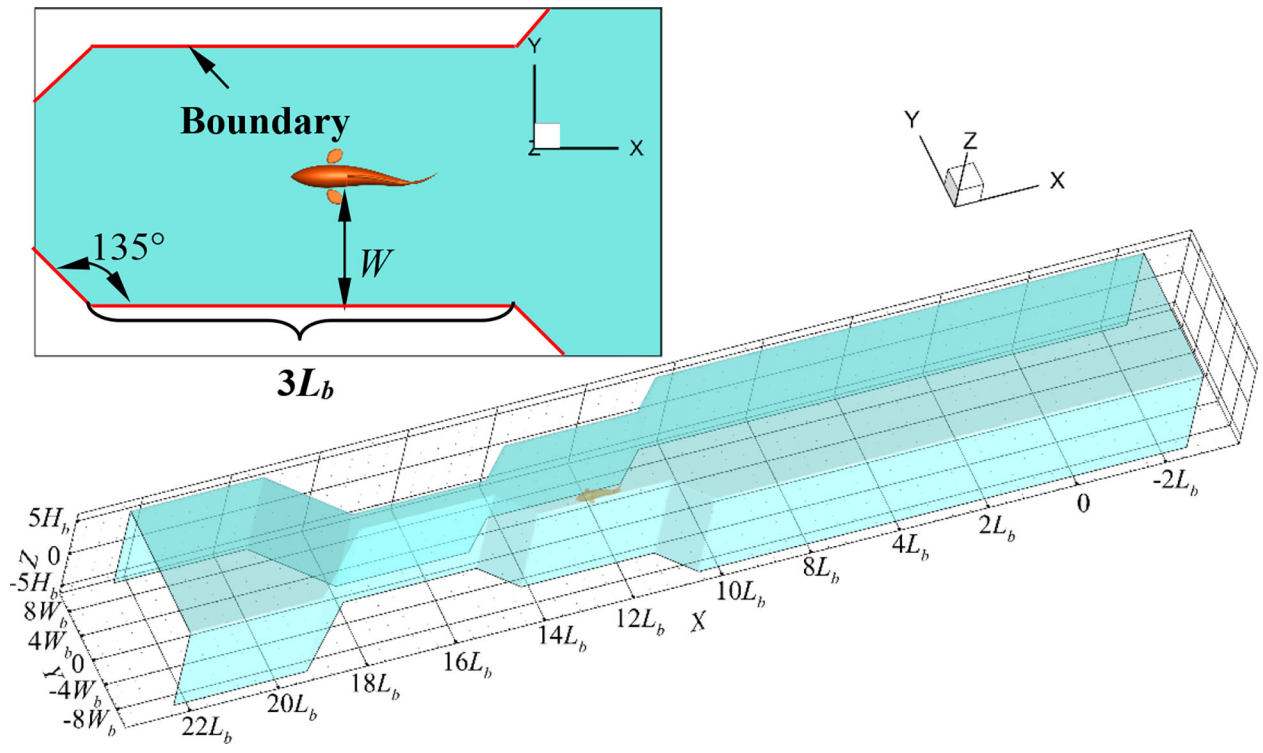

FIGURE 4
The narrow-channel boundary model.

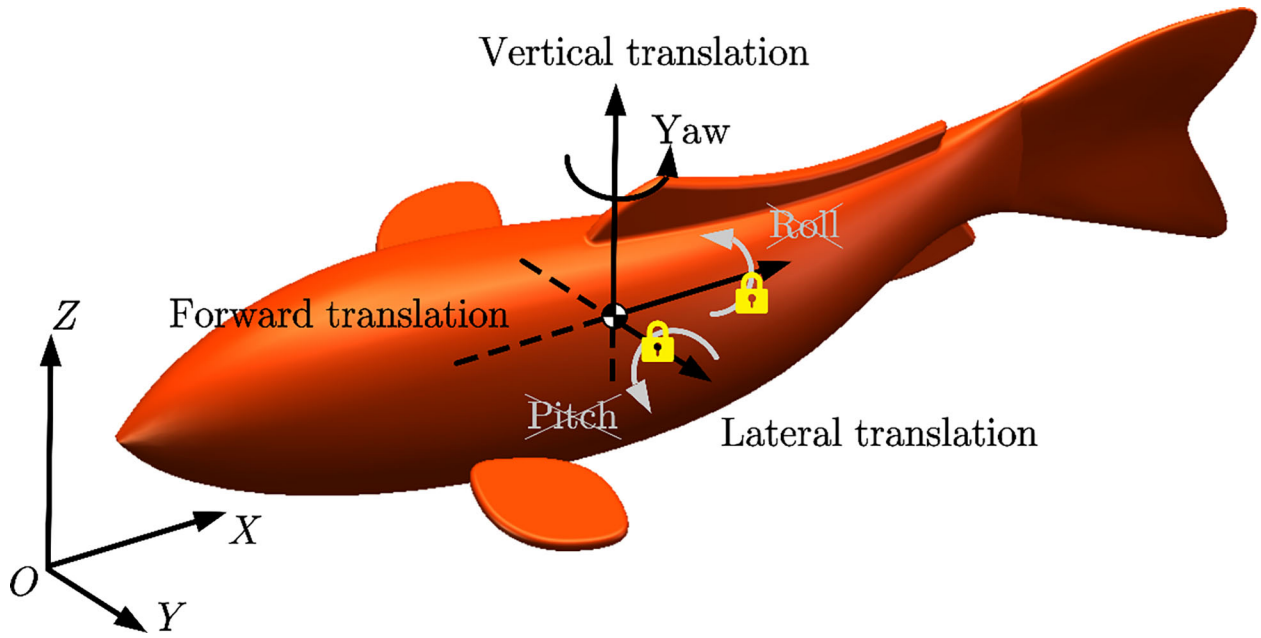

FIGURE 5
Sketch of the world frame *OXYZ* and the DOFs of the swimmer. DOFs, degree of freedoms.

$$\begin{cases} \boldsymbol{V}(t+\Delta t) = \boldsymbol{V}(t) + \boldsymbol{M}_T^{-1}\frac{\boldsymbol{F}(t+\Delta t)+\boldsymbol{F}(t)}{2}\Delta t \\ \boldsymbol{X}(t+\Delta t) = \boldsymbol{X}(t) + \frac{\boldsymbol{V}(t+\Delta t)+\boldsymbol{V}(t)}{2}\Delta t \end{cases} \tag{5}$$

3.1.2 Evaluation of the swimming performance

In this work, the variation of swimming efficiency and dimensionless hydrodynamic coefficients were used to evaluate the swimming performance of the fishlike swimmer under complex terrain changes.

Although there has been much discussion and controversy about the calculation method of the fishlike swimming efficiency (Schultz and Webb, 2002), the Froude efficiency was often adopted to quantify the swimming efficiency in most studies. Froude efficiency was a relatively reasonable parameter that indicated the proportion of the useful power to the total power, as follows (Borazjani and Sotiropoulos, 2008):

$$\eta = \frac{\bar{T}U_s}{\bar{T}U_s + \bar{P}_y} \tag{6}$$

where $\bar{T}$is the average thrust, U_s is the steady swimming speed, and $\bar{P}_y$is the average power loss due to the lateral undulations. In order to obtain the Froude efficiency of the fishlike swimmer in the steady swimming process, the instantaneous thrust and lateral power should be clarified first.

In the numerical simulation, the fishlike swimmer swam along the x direction of the computational domain, from static state to steady motion until the thrust was approximately equal to the drag, which was a continuous process. The fluid force $\boldsymbol{F}$ along the x direction can be computed by integrating the pressure force and viscous force on the fish body (Borazjani and Sotiropoulos, 2008), as follows:

$$F(t) = \int_s (pn_x - \tau_{xj}n_j)dS \tag{7}$$

where p and τ are the pressure and viscous stress tensor, respectively, n_j is the j–th component of the unit normal vector on dS, n_x is the unit vector along the x direction, and S is the surface area of the swimmer's body. To separate the contributions of thrust $T(t)$ and drag $D(t)$, the instantaneous net force $F(t)$ can be decomposed as follows (Li et al., 2019):

$$T(t) = 0.5F(t) + 0.5\int_s (|pn_x| + |\tau_{xj}n_j|)dS \tag{8}$$

$$-D(t) = 0.5F(t) - 0.5\int_s (|pn_x| + |\tau_{xj}n_j|)dS \tag{9}$$

Moreover, the nondimensional thrust (C_T) and drag (C_D) coefficients along the x direction can be calculated as follows:

$$C_T = \frac{T(t)}{0.5\rho U_s^2 L_b^2} \tag{10}$$

$$C_D = \frac{D(t)}{0.5\rho U_s^2 L_b^2} \tag{11}$$

The swimming power loss due to lateral undulations of the body can be calculated as follows:

$$P_y = \int_s (pn_y - \tau_{yj}n_j)u_y dS \tag{12}$$

where u_y is the lateral component of the body motion velocity.

The nondimensional lateral power loss coefficients can be defined as follows:

$$C_P = \frac{P_y}{0.5\rho U_s^3 L_b^2} \tag{13}$$

The effects of terrain change on the Froude efficiency and hydrodynamic coefficients were discussed in the following part.

3.1.3 Governing equations

The swimming process can be regarded as the research on the hydrodynamics and external flow field of a moving and undulating body in which the domain was occupied with an incompressible viscous fluid. The time-averaged continuity equation and the Reynolds-averaged Navier–Stokes (RANS) equations of incompressibility in the 3D Cartesian coordinate system can be used as the governing equations of the computational domain (Malalasekera and Versteeg, 2007), as follows:

$$\begin{cases} \nabla \cdot \mathbf{U} = 0 \\ \frac{\partial U}{\partial t} + \nabla \cdot (U\mathbf{U}) + \nabla \cdot \left(\overline{u'\mathbf{u}'}\right) = -\frac{1}{\rho}\frac{\partial P}{\partial x} + \nu \nabla^2 U + f_1 \\ \frac{\partial V}{\partial t} + \nabla \cdot (V\mathbf{U}) + \nabla \cdot \left(\overline{v'\mathbf{u}'}\right) = -\frac{1}{\rho}\frac{\partial P}{\partial y} + \nu \nabla^2 V + f_2 \\ \frac{\partial W}{\partial t} + \nabla \cdot (W\mathbf{U}) + \nabla \cdot \left(\overline{w'\mathbf{u}'}\right) = -\frac{1}{\rho}\frac{\partial P}{\partial z} + \nabla^2 W + f_3 \end{cases} \tag{14}$$

where $\mathbf{U}$ is the average velocity vector (U, V, W), u' is the pulsation velocity vector (u', v', w'), P represents the average pressure, ρ is the density of the fluid, and f_i are the components of body force in different directions. The instantaneous velocity vector u (u, v, w)=U+u'.

3.2 Preparation and verification of the numerical simulation

In this study, the commercial software ANSYS Fluent was used for the numerical solution of the governing equations with fluid-motion interaction. The computational domain was discretized by meshes using the commercial software Fluent Meshing. In particular, the compiled user-defined function (UDF) programs were written to realize the deformation and self-propelled motion of the fishlike swimmer. The flow field was visualized by the commercial software Tecplot, and the data-processing work was realized by the commercial software MATLAB. The numerical simulation was carried out on the desktop workstation configured with 64-Core 128-Processor Intel(R) Xeon(R) Platinum 8375 CPU @2.80GHz and 256GB RAM. Additionally, it should be noted that the validation of the numerical simulation was carried out in the case where the robotic fish swam in a rectangular tank, rather than the above complex terrain model, to reduce the computing resources. In the simulation with the complex terrain model, the discretization method of the computational domain, the partition scale of the grid, and the calculation settings were the same as the validated process. When the difference of the mean swimming speed value between the two consecutive motion cycles was less than 5%, the motion state can be regarded as steady swimming.

3.2.1 Computational domain discretization and calculation setup

The computational domain of the verification work to simulate the self-propelled motion of the fishlike swimmer was a large enough cubic tank full of fresh water, whose size is $11L_b \times 20W_b \times 11H_b$. The dynamic mesh technology based on the arbitrary Lagrangian–Eulerian (ALE) method was used in this study. However, it was difficult to deal with the complex self-propelled motion of the swimmer with body undulating and pectoral fins oscillating only using the dynamic mesh technology; the problem of negative volume mesh occurred frequently. Then, the overlapping grid technology was used to deal with that problem effectively (Li et al., 2012; Horne and Mahesh, 2019). Therefore, two sets of meshes were established: the poly-hexahedral global mesh was set as the background mesh and the triangular body-fixed mesh was set as the component mesh. The full tank was configured as the background mesh, and the swimmer was completely covered in the component mesh where the deformation of the swimmer was included. The dynamic mesh technology with diffusion smoothing method and remeshing method was used to deal with the large deformation of the component mesh, and the overset moving setup on the background mesh was used to define the relative motion between the swimmer and the global coordinate system.

The boundary conditions and meshes of the simulation domain are shown in Figure 6. Surface 1 was set to a velocity inlet with the velocity magnitude of 0 m/s to keep the water still, and surface 2 was set to a pressure outlet with the gauge pressure of 0 Pa. Surface 3 and surface 4 were no-slip walls, and the overset setup was imposed on surface 5.

The pressure-based solver, absolute velocity formulation, and transient time model were taken into utilization. The k–ω *SST* (shear stress transport) turbulence model with low *Re* adaptation was adopted to solve Eq. 14. The k–ω *SST* model was of relatively low computational cost and accurate calculation, which had good adaptability to the simulation of the boundary layer and free shear flow (Macias et al., 2020). In solution methods, the least-squares cell-based scheme was used for the gradient evaluation, the second-order discretization was used for the pressure term, and the second-order upwind scheme was used for the momentum term. Moreover, both the turbulent kinetic energy and turbulent dissipation rate were second-order upwind scheme; the transient formulation is first-order implicit type.

3.2.2 Independence validation and generalized added mass

In order to validate the independence of the mesh size to the simulation results, both the background mesh and component mesh of the computational domain were divided into five levels, as Coarse, Coarser, Normal, Finer, and Fine. Regardless of the mesh level, the local maximum size of the background mesh was four times its local minimum size, and the local maximum size of the component mesh was three times its local minimum size. The local minimum size of the five background meshes was 0.075 L_b, 0.0625 L_b, 0.05 L_b, 0.0375 L_b, and 0.025 L_b, and the local minimum size of the five component meshes was 0.015 L_b, 0.0125 L_b, 0.01 L_b, 0.0075 L_b, and 0.005 L_b. The minimum orthogonal quality of all meshes was required to be not less than 0.3. The tail-beat frequency f of 2.0Hz and other morphological kinematic parameters remained unchanged in the simulation with various meshes. The steady nondimensional forward velocity U_s/L_b was specified as the evaluation variable to verify the independence. Moreover, the maximum time step Δt_{max} was determined by the

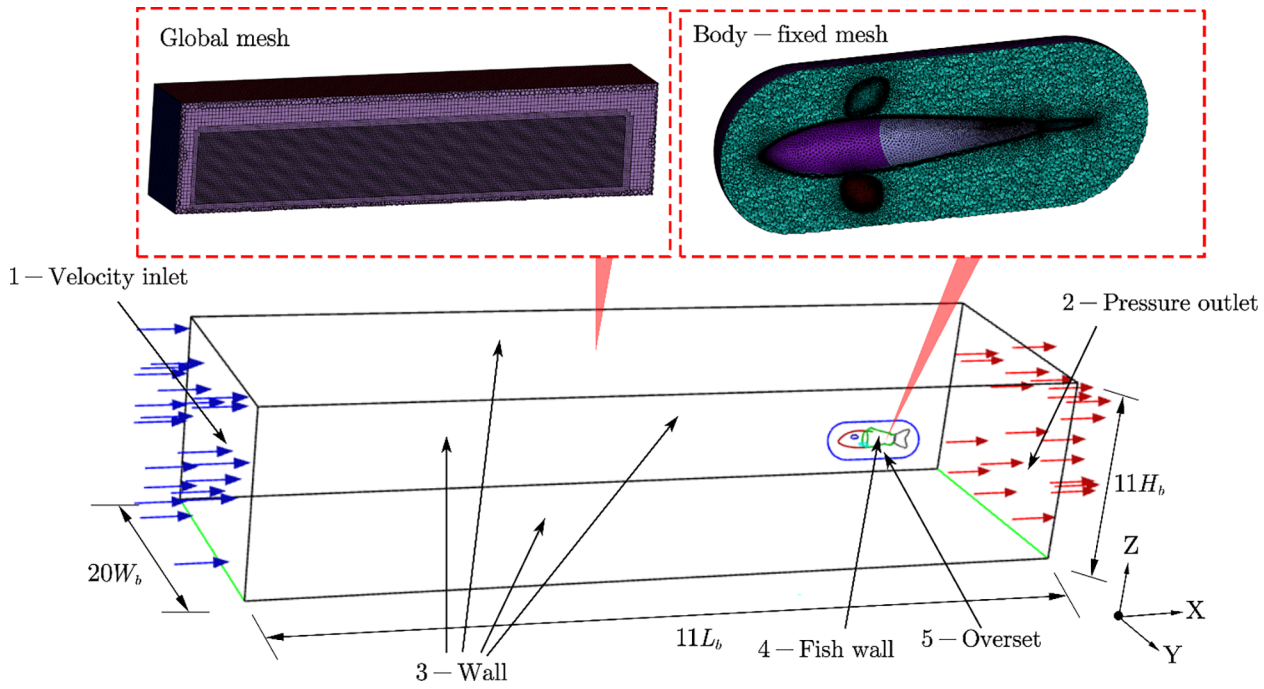

FIGURE 6
Meshes and boundary conditions.

minimum mesh size and the maximum deforming velocity of the body. Similarly, five levels of the time step, $T/80$, $T/100$, $T/200$, $T/400$, and $T/500$, were divided to validate the independence of the time step, where $T = 1/f$. The validation results are shown in Figure 7.

It was clear that the forward velocity that remained almost unchanged are reaching Normal-level mesh according to Figure 7A. The excessive rough mesh would cause serious instability in simulation results when mesh deforming, and excessive fine mesh would lead to not only the waste of computing resources but also limitation in accuracy improvement. Thus, the Normal-level mesh was selected for the time-step independence validation and swimming process simulation. As shown in Figure 7B, the forward velocity did not respond significantly to the change of time-step level, and the time step $T/100$ was selected for the swimming process simulation.

In order to calculate the generalized added mass, the motions of the swimmer along various directions were defined as low-speed and small-amplitude sine oscillating movements of a rigid body.

$$v_i = A_i \sin \omega_i t \tag{15}$$

where the subscript i =1,2,3 represents the translational mode in three directions of Cartesian coordinate system, i=4 represents the rotational mode around the z direction, A_i is the amplitude of motion

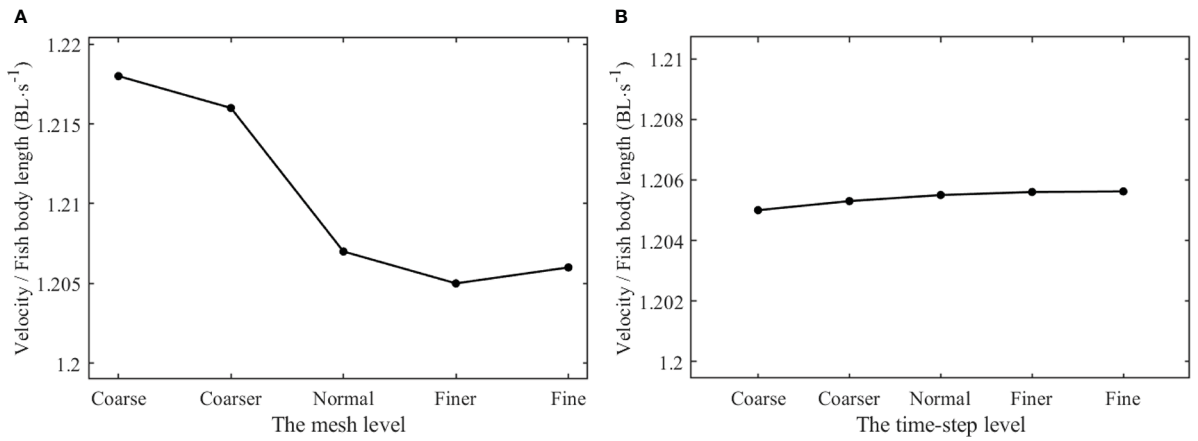

FIGURE 7
The values of nondimensional steady velocity for independence validation. **(A)** Independence validation of the mesh size **(B)** Independence validation of the time step.

velocity, and ω_i is the motion frequency. In this paper, A_i=0.01 m/s and ω_i = 0.5 rad/s. The generalized hydrodynamic force of the swimmer was decomposed into the generalized viscous force and inertia force attributed to velocity and acceleration, respectively (Li et al., 2010). The overset mesh technology was also used to simulate these motions as Eq. 15, and the hydrodynamics F_h and M_h were recorded. The generalized force on the swimmer should be entirely supplied by the acceleration when the instantaneous speed was zero. Thus, the added mass can be obtained by dividing the hydrodynamic force in each direction by the corresponding acceleration with a zero instantaneous speed. The result of the generalized added mass matrix was calculated as follows:

$$\boldsymbol{M}_A = \begin{pmatrix} 0.113m & 0 & 0 & 0 \\ 0 & 2.91m & 0 & 0 \\ 0 & 0 & 0.645m & 0 \\ 0 & 0 & 0 & 1.27I_z \end{pmatrix} \tag{16}$$

The completed dynamic equation of the robotic fish system can be established by combining Eq. 4 with Eq. 16.

3.3 Swimming process simulation

In the numerical simulation, the swimming motions of the fishlike swimmer at three tail-beat frequencies (1.0Hz, 1.5Hz, 2.0Hz) in an undulating terrain and a narrow channel were simulated. In terms of the simulation domain, the maximum width was $20W_b$ and the maximum height was $11H_b$, and in these circumstances, the fish body can be regarded to be free swimming without effect of the up-down and left-right boundary based on the validation results. When the robotic fish swam forward gradually along the x direction, the changing topography would gradually affect the hydrodynamic characteristics and swimming performance of the swimmer.

4 Results and discussion

4.1 Effects of complex terrain on the swimming performance

4.1.1 Forward speed

The forward swimming speeds of the fishlike swimmer are depicted in Figures 8A and 9A with changes in the tail-beat frequency f, the dimensionless height H, and the dimensionless distance W. The unit BL·s^{-1} used to describe the forward speed means the body length per second. The swimmer with different tail-beat frequencies swam across various terrain conditions, but the changing pattern of the forward speed was consistent. From the starting static state to a steady swimming condition, the forward speed gradually rose until reaching an asymptotic stable value. The forward speed rose as the tail-beat frequency rose, and the instantaneous speed fluctuated periodically, matching the tail-beat period.

Furthermore, the average forward speeds at different tail-beat frequencies, dimensionless height H, and dimensionless distance W were calculated. The effects of the above dimensionless distance parameters on the average forward velocity are described in Figures 8B and 9B. As shown in Figure 8B, when the dimensionless distance H was larger than 1.25H_b, the average forward speed varied little at different tail-beat frequencies. When the value of H was 0.25H_b, the average forward speed had a relatively small reduction approximately 0.3%–0.8% compared with that of the value of 1.25 H_b at different tail-beat frequencies. Figure 9B demonstrated that when the dimensionless distance W was larger than 5W_b, the average forward velocity had almost no change under different tail-beat frequencies. When the value of W reached 1W_b, corresponding to the three tail-beating frequencies of 1, 1.5, and 2.0 Hz, the average forward speed decreased by 1.82%, 2.41%, and 3.11%, respectively, compared with that of the value of 5W_b. When the value of W got back to 10W_b, the average forward speed increased synchronously. As a result, it was believed that the swimming boundary's bottom had

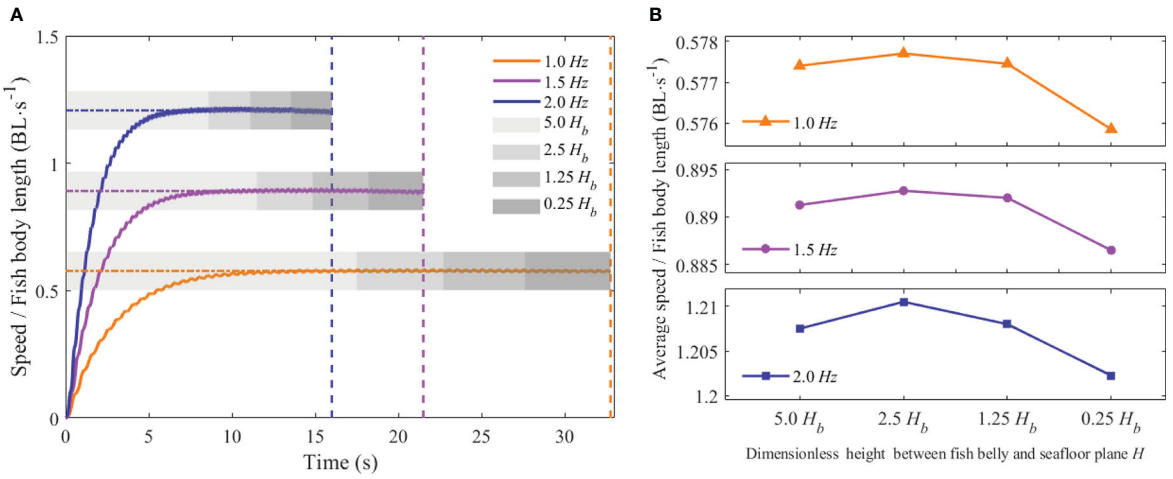

FIGURE 8
Forward speed of the swimmer at different values of f and H **(A)** Instantaneous forward speed **(B)** Average forward speed.

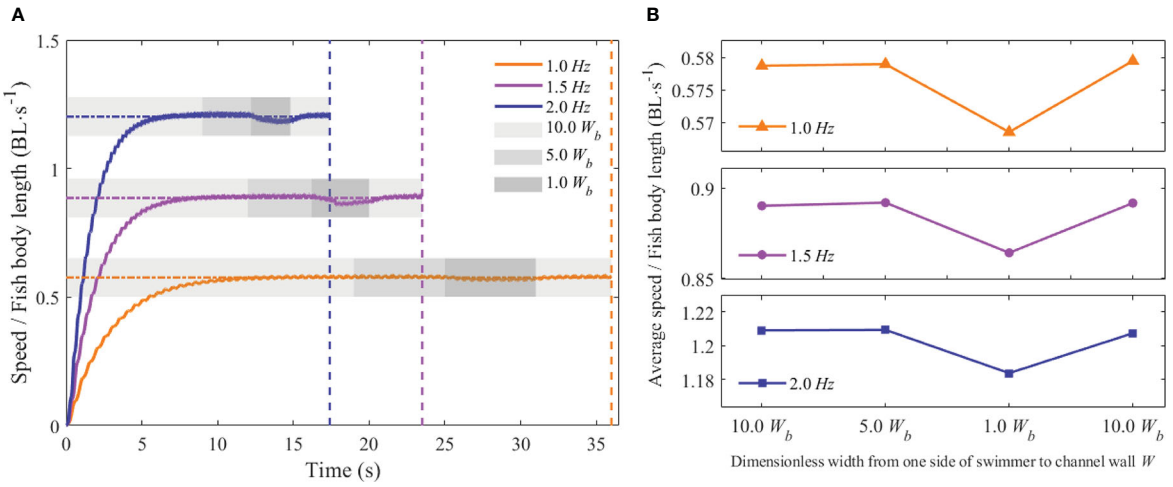

FIGURE 9
Forward speed of the swimmer at different values of *f* and *W*. **(A)** Instantaneous forward speed **(B)** Average forward speed.

little influence on the swimmer's swimming speed, but the forward speed would be slowed when the swimmer passed through the narrow channel. The higher the tail-beat frequency, the larger the decline.

4.1.2 Froude efficiency and hydrodynamic coefficients

A previous study (Takahashi et al., 2020) has shown that the Carangiform kinematic mode of self-propelled constant-speed swimming was inefficient at low *Re*. The model specified in this work guaranteed that the swimmer maintained a high *Re* at all tail-beat frequencies, exceeding 10,000. Figure 10 shows the change of Froude efficiency with dimensionless distance under various swing frequencies. Although there is a considerable variation in Froude efficiency under various swing frequencies, the distance parameter did not appear to have a major impact on it. The efficiency was maintained at a nearly constant value for each motion mode. It was worth mentioning that Froude efficiency appeared to increase with frequency. In order to further verify this point, the Strouhal number (*St*) based on tail-beat frequency *f*, tail-beat amplitude *A*, and steady forward speed U_s was calculated according to Eq. 17, and it characterized the swimmer's undulation performance. The values are 0.176, 0.171, and 0.165, respectively, under tail-beat frequencies of 1.0, 1.5, and 2.0 Hz. The results discovered that *St* gradually decreased as frequency increased. In fact, the swimmer at higher *St* indicated quicker lateral undulations, resulting in a higher lateral power loss and lesser efficiency, and which was consistent with the findings of this work.

$$St = \frac{fA}{U_s} \tag{17}$$

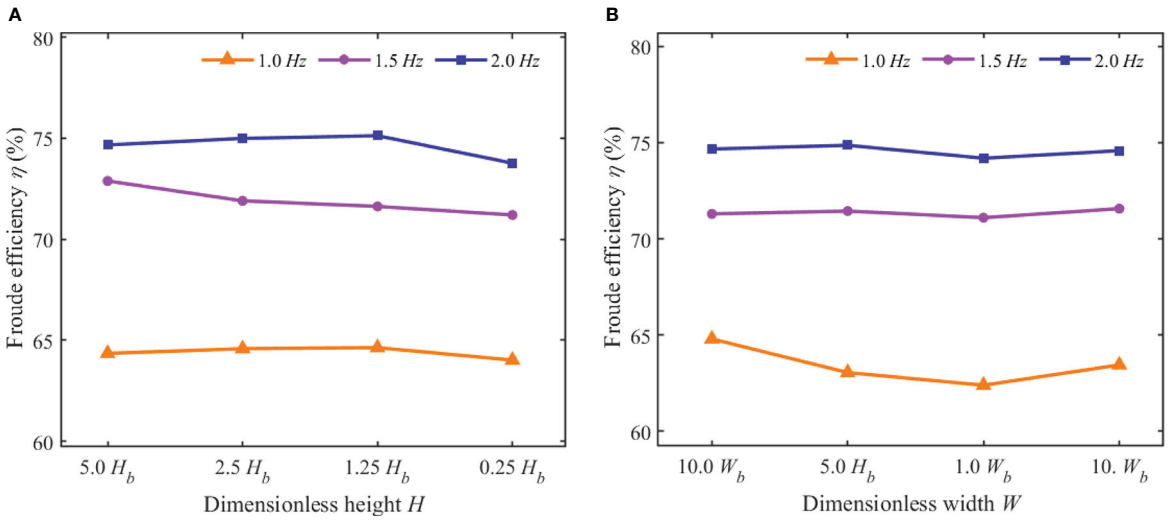

FIGURE 10
Froude efficiency of the swimmer at different values of *f*, *H*, and *W*. **(A)** Froude efficiency at different values of *f* and *H* **(B)** Froude efficiency at different values of *f* and *W*.

Several typical cycles in 2 s of instantaneous hydrodynamic coefficients, at different tail-beat frequencies for H=5.0H_b and W=10.0W_b , are presented in Figure 11. Throughout the whole swimming process, the swimmer needed various time lengths with different tail-beat frequencies because a lower tail-beat frequency motion took a longer time to reach a stable speed. Thus, the "a" in the horizontal axis of Figure 11 denoted the specific starting time after the swimmer reached a constant swimming speed at each tail-beat frequency. As can be observed in Figure 11, at each frequency, the thrust coefficient and drag coefficient changed on a regular basis, with the average values being about the same during an entire cycle. It indicated that the thrust forces and drag forces acting on the swimmer were almost the same, and the swimmer reached a stable swimming state. The fluctuation of the thrust coefficient was negligible compared to the drag coefficient. Moreover, the lateral fluctuation power that fluctuated around zero was likewise consistent with the expected value, since the swimmer merely swam in a straight line.

The influence of the dimensionless distance parameter on the periodic stability of the hydrodynamic coefficient was another point of concern. The standard deviation of the hydrodynamic coefficient across successive time periods was used to assess that impact. Figures 12A, B show the effect of the changed H and W on the thrust coefficient, drag coefficient, and lateral fluctuation power coefficient at different tail-beat frequencies. The standard deviations of the three hydrodynamic coefficients had similar overall fluctuation patterns. As illustrated in Figure 12A, when H was more than 1.25H_b, the standard deviation remained rather steady. However, when H hit 0.25H_b, the standard deviation increased. As illustrated in Figure 12B, the standard deviation of the three hydrodynamic coefficients tended to grow when the value of W decreased. When the value of W was reduced to 1.0W_b, the standard deviation increased, then dropped when the value of W returned to 10.0W_b. It indicated that although terrain changes had a limited impact on swimmers' hydrodynamic coefficients, the surface had a large disturbance effect on swimmers' hydrodynamic coefficients and force when approaching the bottom of the swimming boundary or passing through a narrow channel.

4.2 Evolution of the pressure field

In order to explore the influence mechanism of the complex terrain to Froude efficiency and hydrodynamic coefficients of the

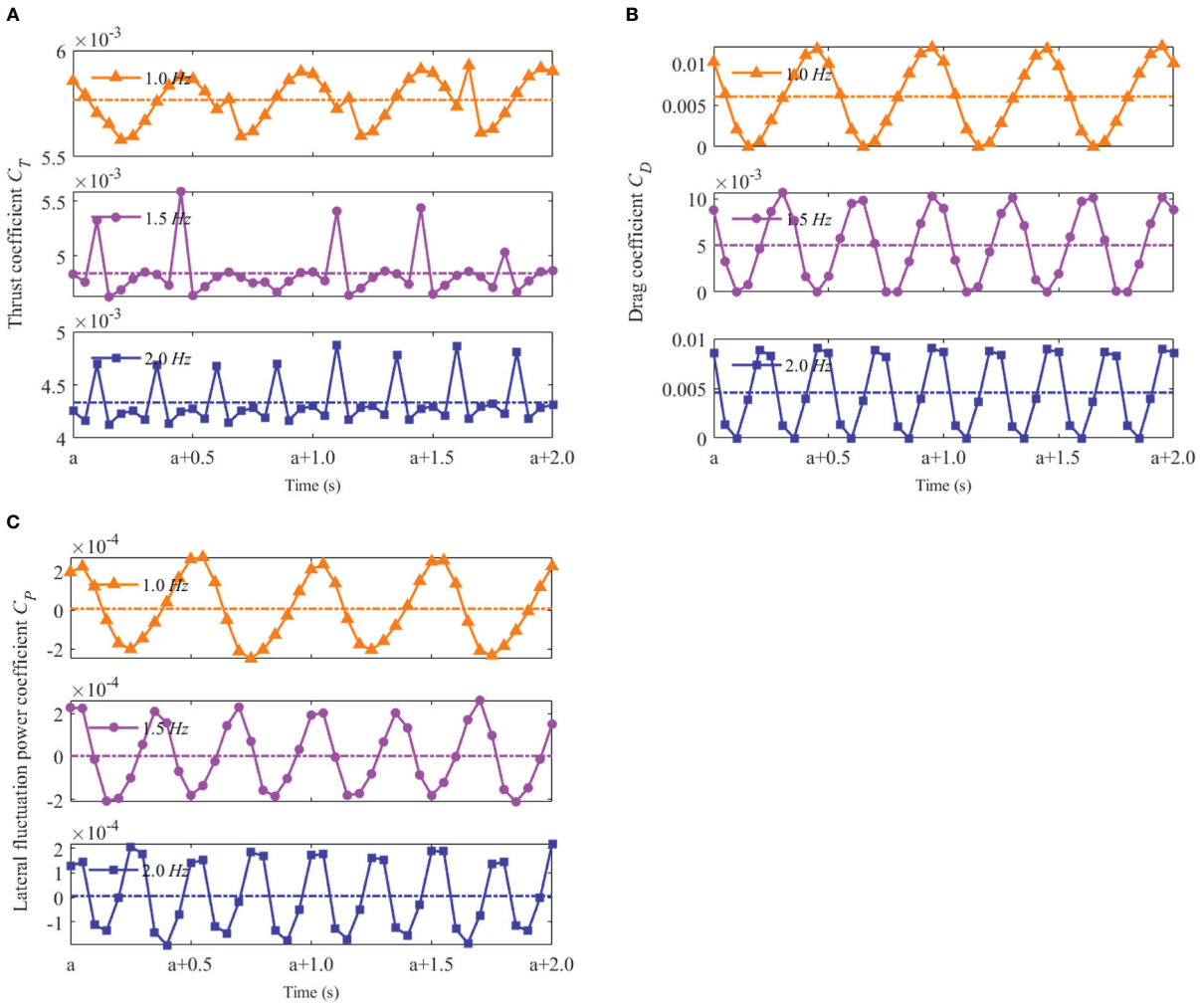

FIGURE 11
Hydrodynamic coefficients of the swimmer at different tail-beat frequencies f **(A)** Thrust coefficient C_T**(B)** Drag coefficient C_D **(C)** Lateral fluctuation power coefficient C_P.

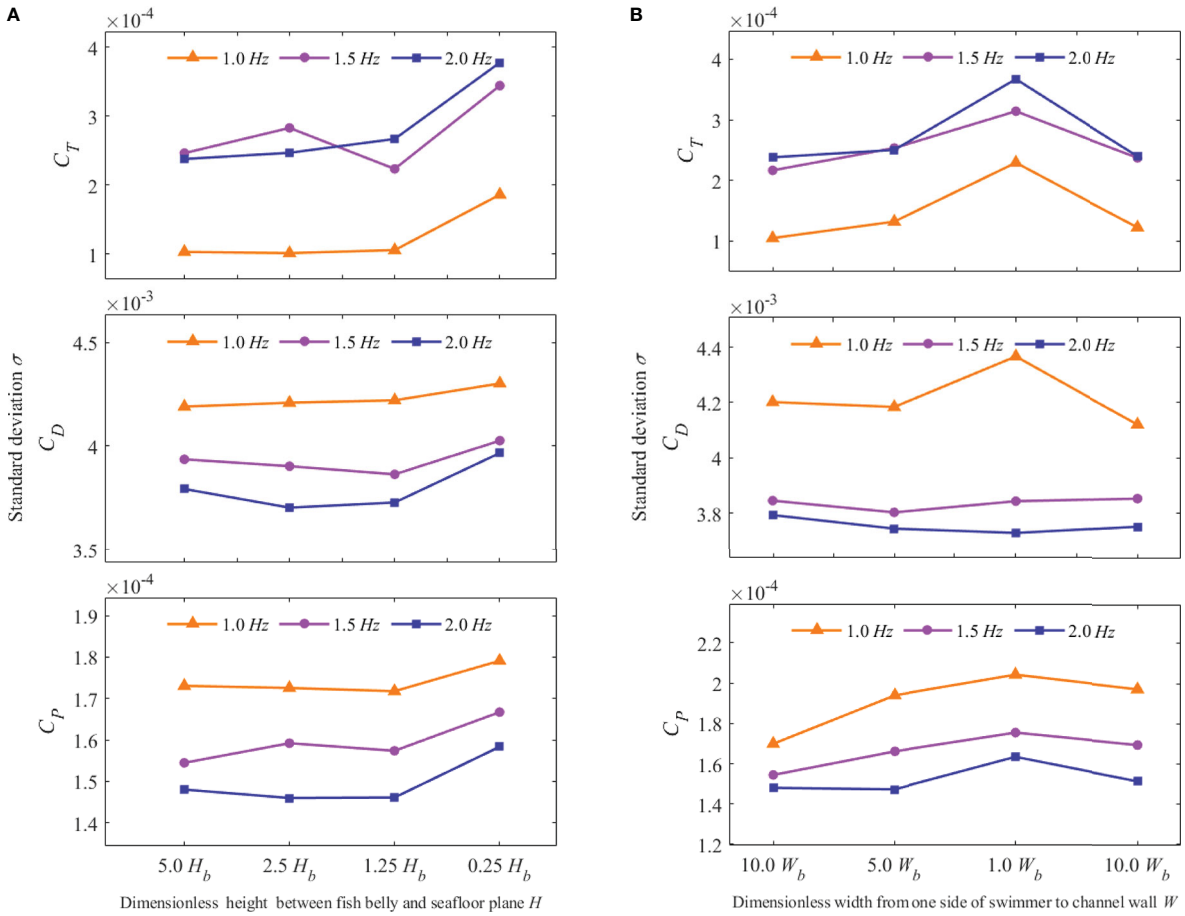

FIGURE 12
Hydrodynamic coefficient standard deviation of the swimmer at different values of *f*, *H*, and *W*. **(A)** Hydrodynamic coefficient standard deviation at different values of *f* and *H* **(B)** Hydrodynamic coefficient standard deviation at different values of *f* and *W*.

fishlike swimmer, the pressure field of the research domain was visualized by the pressure isosurface, as shown in Figure 13. The light color surface represents the relative pressure value 10 Pa, and the dark color surface represents the relative pressure value -10 Pa.

In Figure 13, there was a high-pressure area near the head part of the fishlike swimmer and a low-pressure area at the middle part. These two pressure areas would generate drag force on the swimmer. Moreover, at the tail part, the high-pressure area and low-pressure area appeared in pairs, which would generate thrust force and lateral force.

In the open water, the evolution of the pressure isosurface was stable, and the swimming mode was the only factor to affect the Froude efficiency and hydrodynamic coefficients. When a boundary surface appeared near the bottom of the swimmer, a part of the pressure area was blocked out by the boundary surface, and the force generated by the pressure difference would decrease. Then, the swimming process would be less efficient and the hydrodynamic coefficients would become smaller. Moreover, when the boundary surface appeared on both sides of the swimmer, more pressure areas would be blocked out, and the propulsion efficiency would be further reduced. That was the reason that the average forward speed had a small reduction under the undulating seabed boundary condition and a relatively large reduction under the narrow-channel boundary condition, as shown in Figures 8 and 9. Furthermore, two boundary surfaces at both sides of the swimmer would make the evolution of pressure field more complex, the standard deviation of hydrodynamic coefficients would increase, and the swimming stability would decrease, which was consistent with the results in Figure 12.

Thus, if the distance between the fish belly and the seafloor surface was large, perhaps larger than $0.25H_b$, there was no need to worry about the impact on forward speed. But the swimmer should improve tail-beat frequency to keep a steady speed when passing through a narrow channel, especially for the condition where the distance from one side of the swimmer to the near boundary was smaller than $1W_b$.

4.3 Evolution of the vortex distribution

On the other hand, the wake vortex contains the secret of highly efficient swimming of the fishlike swimmer (Harvey et al., 2022). The isosurface of Q-criterion has been used extensively as standard recognition of vortex (Ren et al., 2022). The evolution of the vortex distribution around the swimmer was visualized by the Q-criterion isosurface whose value was equal to 0.1, as shown in Figure 14.

In Figure 14, the vortex rings appeared in pairs after the swimmer to form the reverse Kaman vortex street. Then, the reverse Kaman vortex street would induce a jet effect to generate a positive force and

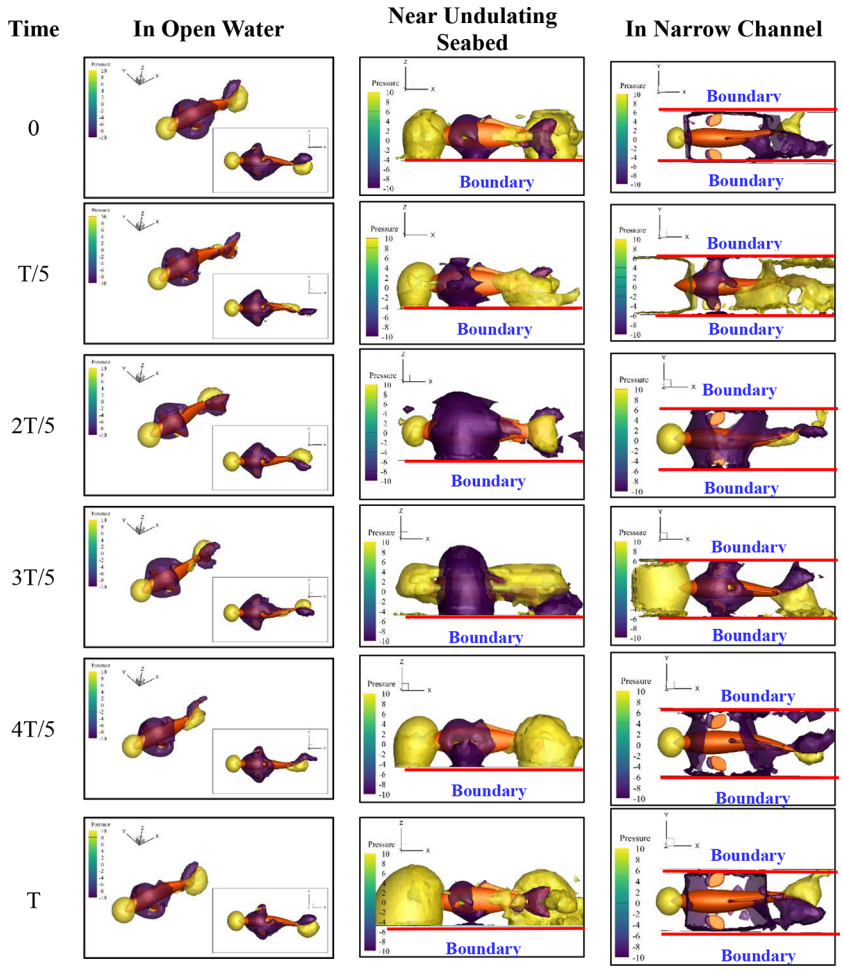

FIGURE 13
Pressure field of the research domain.

the force was applied to the swimmer to make the swimmer get high Froude efficiency. Thus, the fishlike swimming mode had a higher propulsion efficiency than the propeller-driven mode.

In the open water, the wake vortex evolved freely and gradually dissipated under the viscosity effect of the water. The positive force induced by the reverse Kaman vortex street was large, and the additional efficiency was high. Meanwhile, in the evolution process, the vortex ring diffused to the rear on both sides of the robotic fish, not above or below the swimmer. The height of the vortex ring near the tail was almost equal to that of the fish body. Thus, under the undulating seabed condition, the boundary surface near the bottom of the swimmer had little effect on the swimming efficiency. However, when the boundary surfaces were at both sides of the swimmer, like the narrow-channel condition, the wake vortex would hit the boundary surface and dissipate rapidly. Almost no jet effect was induced, and the additional efficiency was small. That was the reason that Froude efficiency had little reduction under the undulating seabed boundary condition and a relatively large reduction under the narrow-channel boundary condition, especially when the tail-beat frequency was 1.0 Hz, as shown in Figure 10.

When the robotic fish swam near the undulating seabed, the evolution of the vortex distribution would not be seriously affected, and it was recommended to keep the tail-beat frequency unchanged. But when the robotic fish passed through the narrow channel, a large tail-beat frequency was needed to get enough thrust force.

5 Conclusion

In this paper, the swimming processes of robotic fish under an undulating seabed condition and a narrow-channel condition were studied. The forward speed, Froude efficiency, and hydrodynamic coefficients were calculated to evaluate the influence of complex terrain on the swimming performance. Moreover, the evolution processes of the pressure field and vortex distribution were visualized to discuss the influence mechanism. The key points of this paper can be summarized as follows:

1) The influence of the undulating seabed condition on the swimming performance of robotic fish was small, but the change in the swimming stability should be given sufficient attention when robotic fish swam near the undulating seabed with the distance about $0.25H_b$.
2) The influence of the narrow-channel condition on the swimming performance was obvious because the boundary surface at both sides of the swimmer restricted the pressure

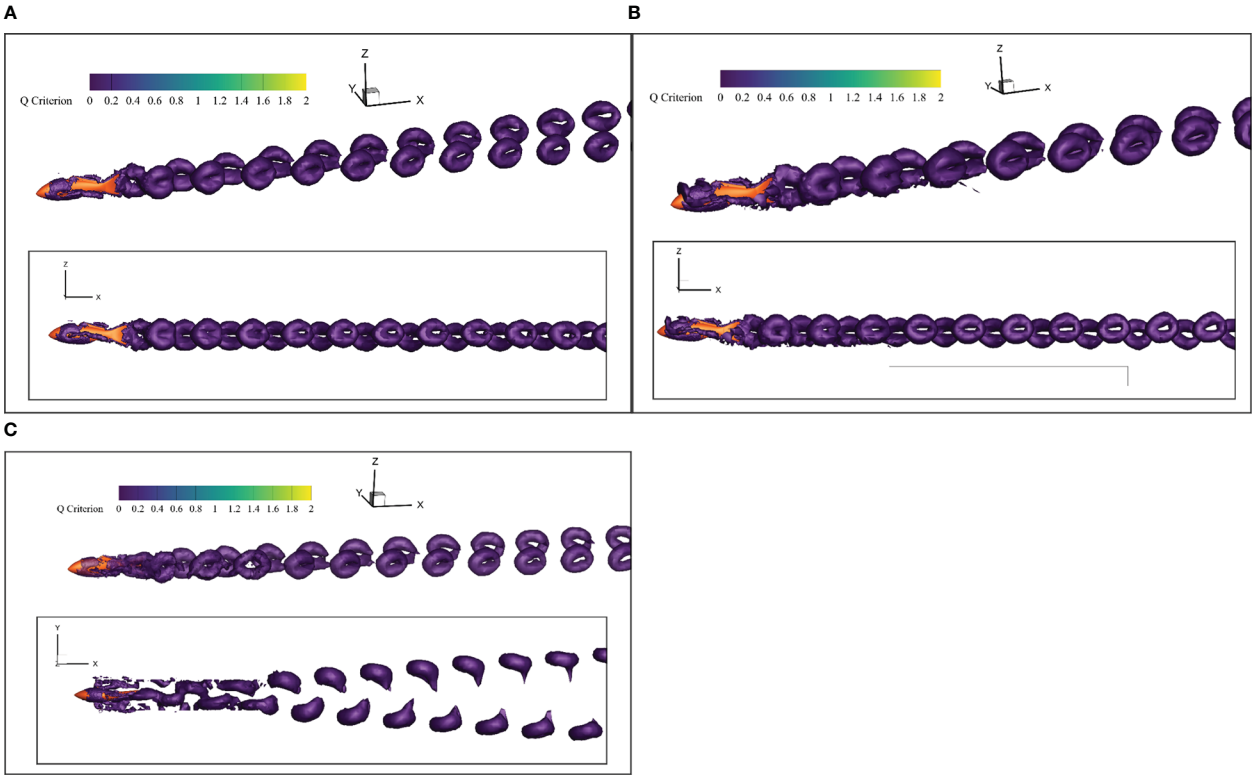

FIGURE 14
Vortex distribution of the research domain. **(A)** In Open Water **(B)** Near Undulating Seabed **(C)** In Narrow Channel.

field evolution and the vortex distribution evolution seriously. When robotic fish swam through a narrow channel at a certain tail-beat frequency, the forward speed and Froude efficiency decreased, and the swimming stability got worse.

3) In order to keep a good motion performance of the fishlike swimming mode when passing through a narrow channel, it was recommended to improve the tail-beat frequency. However, considering the swimming stability, the tail-beat frequency was not the larger the better.

In the future, the development of a physical robotic fish is expected. Various sensors should be integrated to record the force and motion state when the robotic fish conducts exploring and sampling in the deep sea. Experimental data will be helpful for further research on swimming performance optimization of the robotic fish and for the development of a low-disturbance bionic exploring and sampling platform.

Data availability statement

The raw data supporting the conclusions of this article will be made available by the authors, without undue reservation.

Author contributions

Conceptualization, GX; methodology, GX and FB; software and algorithm, FB; validation and analysis, GX and FB; visualization, FB and PR; investigation, PR; data curation, PR; writing-original draft preparation, GX and FB; writing-review and editing, GX and FB; supervision, YL; project administration, LG and YL; funding acquisition, LG and YL. All authors contributed to the article and approved the submitted version.

Funding

The research was supported by the National Natural Science Foundation of China (NO.52001186), the Natural Science Foundation of Shandong Province (NO.ZR2020QE292), the Open Fund Project of Key Laboratory of Ocean Observation Technology (NO. 2021klootA01), and the Science and Technology Innovation Project of Laoshan Laboratory (NO.LSKJ202203505), hereby thanks.

Conflict of interest

The authors declare that the research was conducted in the absence of any commercial or financial relationships that could be construed as a potential conflict of interest.

Publisher's note

All claims expressed in this article are solely those of the authors and do not necessarily represent those of their affiliated organizations, or those of the publisher, the editors and the reviewers. Any product that may be evaluated in this article, or claim that may be made by its manufacturer, is not guaranteed or endorsed by the publisher.

References

Ćatipović, I., Uščumlić, J., and Ćustić, L. (2019). Optimization of a subsea pipeline route profile with the elimination of free spans. *J. Pipeline Syst. Eng. Pract.* 10 (2), 04019007. doi: 10.1061/(ASCE)PS.1949-1204.0000375

Borazjani, I., and Sotiropoulos, F. (2008). Numerical investigation of the hydrodynamics of carangiform swimming in the transitional and inertial flow regimes. *J. Exp. Biol.* 211 (10), 1541–1558. doi: 10.1242/jeb.015644

Cui, Z., Yang, Z., Shen, L., and Jiang, H. Z. (2018). Complex modal analysis of the movements of swimming fish propelled by body and/or caudal fin. *Wave motion* 78, 83–97. doi: 10.1016/j.wavemoti.2018.01.001

Curatolo, M., and Teresi, L. (2016). Modeling and simulation of fish swimming with active muscles. *J. Theor. Biol.* 409, 18–26. doi: 10.1016/j.jtbi.2016.08.025

Dhongdi, S. C. (2022). Review of underwater mobile sensor network for ocean phenomena monitoring. *J. Network Comput. Appl.* 103418. doi: 10.1016/j.jnca.2022.103418

Dong, C., Zhu, Z., Li, Z., Shi, X., Cheng, S. J., and Fan, P. (2022). Design of fishtail structure based on oscillating mechanisms using PVC gel actuators. *Sensors Actuators A: Phys.* 341, 113588. doi: 10.1016/j.sna.2022.113588

Feng, H., Yu, J., Huang, Y., Qiao, J. A., Wang, Z. Y., Xie, Z. B., et al. (2021). Adaptive coverage sampling of thermocline with an autonomous underwater vehicle. *Ocean Eng.* 233, 109151. doi: 10.1016/j.oceaneng.2021.109151

Fossum, T. O., Norgren, P., Fer, I., Nilsen, F., Koenig, Z. C., and Ludvigsen, M. (2021). Adaptive sampling of surface fronts in the Arctic using an autonomous underwater vehicle. *IEEE J. Oceanic Eng.* 46 (4), 1155–1164. doi: 10.1109/JOE.2021.3070912

Ghommem, M., Bourantas, G., Wittek, A., Miller, K., and Hajj, M. R. (2020). Hydrodynamic modeling and performance analysis of bio-inspired swimming. *Ocean Eng.* 197, 106897. doi: 10.1016/j.oceaneng.2019.106897

Hang, H., Heydari, S., Costello, J. H., and Kanso, E. (2022). Active tail flexion in concert with passive hydrodynamic forces improves swimming speed and efficiency. *J. Fluid Mechanics* 932. doi: 10.1017/jfm.2021.984

Harvey, S. T., Muhawenimana, V., Müller, S., Wilson, C. A. M. E., and Denissenko, P. (2022). An inertial mechanism behind dynamic station holding by fish swinging in a vortex street. *Sci. Rep.* 12 (1), 1–9. doi: 10.1038/s41598-022-16181-8

He, S., Peng, Y., Jin, Y., Wan, B. Y., and Liu, G. P. (2020). Review and analysis of key techniques in marine sediment sampling. *Chin. J. Mechanical Eng.* 33 (1), 1–17. doi: 10.1186/s10033-020-00480-0

Hoar, W. S., Randall, D. J., and Donaldson, E. M. (1983). *Fish physiology* (Academic Press).

Horne, W. J., and Mahesh, K. (2019). A massively-parallel, unstructured overset method to simulate moving bodies in turbulent flows. *J. Comput. Phys.* 397, 108790. doi: 10.1016/j.jcp.2019.06.066

Jiang, Z., Lu, B., Wang, B. A., Cui, W. C., Zhang, J. F., Luo, R. L., et al. (2022). A prototype design and Sea trials of an 11,000 m autonomous and remotely-operated vehicle dream chaser. *J. Mar. Sci. Eng.* 10 (6), 812. doi: 10.3390/jmse10060812

Lecours, V., Dolan, M. F. J., Micallef, A., and Lucieer, V. L. (2016). A review of marine geomorphometry, the quantitative study of the seafloor. *Hydrology Earth System Sci.* 20 (8), 3207–3244. doi: 10.5194/hess-20-3207-2016

Li, G., Chen, X., Zhou, F., et al. (2021). Self-powered soft robot in the Mariana trench. *Nature* 591 (7848), 66–71. doi: 10.1038/s41586-020-03153-z

Li, X., Gu, J., Su, Z., Su, Z., and Yao, Z. Q. (2021). Hydrodynamic analysis of fish schools arranged in the vertical plane. *Phys. Fluids* 33 (12), 121905. doi: 10.1063/5.0073728

Li, S. M., Li, C., Xu, L. Y., Yang, W. J., and Chen, X. C. (2019). Numerical simulation and analysis of fish-like robots swarm[J]. *Appl. Sci.* 9 (8), 1652. doi: 10.3390/app9081652

Li, J., Lu, C., and Huang, X. (2010). Calculation of added mass of a vehicle running with cavity. *J. Hydrodynamics* 22 (3), 312–318. doi: 10.1016/S1001-6058(09)60060-3

Li, G., Müller, U. K., van Leeuwen, J. L., and Liu, H. (2012). Body dynamics and hydrodynamics of swimming fish larvae: A computational study. *J. Exp. Biol.* 215 (22), 4015–4033. doi: 10.1242/jeb.071837

Macias, M. M., Souza, I. F., Brasil, A. C. P., and Oliveira, T. F. (2020). Three-dimensional viscous wake flow in fish swimming-a CFD study. *Mechanics Res. Commun.* 107, 103547. doi: 10.1016/j.mechrescom.2020.103547

Malalasekera, W., and Versteeg, H. K. (2007). *An introduction to computational fluid dynamics :the finite volume method. 2nd ed. ed* Vol. 503 (Harlow, England: Pearson Education Ltd).

Ma, H. W., Ren, S., Wang, J. X., Ren, H., Liu, Y., and Bi, S. S. (2021). Research on the influence of ground effect on the performance of robotic fish propelled by oscillating paired pectoral fins. *Ind. Robot: Int. J. robotics Res. Appl.* 48 (1), 133–141. doi: 10.1108/IR-04-2020-0081

Ogata, Y., Azama, T., and Moriyama, Y. (2017). Numerical investigation of small fish accelerating impulsively to terminal speed. *J. Fluid Sci. Technol.* 12 (1), JFST0009–JFST0009. doi: 10.1299/jfst.2017jfst0009

Quinn, D. B., Lauder, G. V., and Smits, A. J. (2014). Flexible propulsors in ground effect. *Bioinspiration biomimetics* 9 (3), 036008. doi: 10.1088/1748-3182/9/3/036008

Ren, X. T., Guo, Y. L., Shen, S. Q., and Zhang, K. (2022). Large Eddy simulation of flow field in thermal vapor compressor. *Front. Energy Res.* 10, 1008927. doi: 10.3389/fenrg.2022.1008927

Rogers, J. S., Maticka, S. A., Chirayath, V., Woodson, C. B., Alonso, J. J., and Monismith, S. G. (2018). Connecting flow over complex terrain to hydrodynamic roughness on a coral reef. *J. Phys. Oceanography* 48 (7), 1567–1587. doi: 10.1175/JPO-D-18-0013.1

Schultz, W. W., and Webb, P. W. (2002). Power requirements of swimming: Do new methods resolve old questions? *Integr. Comp. Biol.* 42 (5), 1018–1025. doi: 10.1093/icb/42.5.1018

Takahashi, T., Yoshino, S., Takaya, Y., Nozaki, T., Ohki, K., Ohki, T., et al. (2020). Quantitative *in situ* mapping of elements in deep-sea hydrothermal vents using laser-induced breakdown spectroscopy and multivariate analysis. *Deep Sea Res. Part I: Oceanographic Res. Papers* 158, 103232. doi: 10.1016/j.dsr.2020.103232

Wang, C. C., Lu, J., Ding, X. L., Jiang, C. X., Yang, J. Y., and Shen, J. H. (2021). Design, modeling, control, and experiments for a fish-robot-based IoT platform to enable smart ocean. *IEEE Internet Things J.* 8 (11), 9317–9329. doi: 10.1109/JIOT.2021.3055953

Wang, Z., Wang, L. Y., Wang, T., and Zhang, B. (2022). Research and experiments on electromagnetic-driven multi-joint bionic fish. *Robotica* 40 (3), 720–746. doi: 10.1017/S0263574721000771

Wang, R., Wang, S., Wang, Y., Cheng, L., and Tan, M. (2022). Development and motion control of biomimetic underwater robots: A survey. *IEEE Trans. Systems Man Cybernetics: Syst.* 52 (2), 833–844. doi: 10.1109/TSMC.2020.3004862

Wei, Z. F., Li, W. L., Li, J., Chen, J., Xin, Y. Z., He, L. S., et al. (2020). Multiple *in situ* nucleic acid collections (MISNAC) from deep-sea waters. *Front. Mar. Sci.* 7, 81. doi: 10.3389/fmars.2020.00081

Whitt, C., Pearlman, J., Polagye, B., Caimi, F., Muller-Karger, F., Copping, A., et al. (2020). Future vision for autonomous ocean observations. *Front. Mar. Sci.* 697. doi: 10.3389/fmars.2020.00697

Windsor, S. P., Norris, S. E., Cameron, S. M., Mallinson, G. D., and Montgomery, J. C. (2010). The flow fields involved in hydrodynamic imaging by blind Mexican cave fish (Astyanax fasciatus). part II: Gliding parallel to a wall. *J. Exp. Biol.* 213 (22), 3832–3842. doi: 10.1242/jeb.040790

Xie, O., Yao, J., Fan, X. Z., Shen, C., and Zhang, C. B. (2022). Numerical and experimental study on the hydrodynamics of a three-dimensional flapping caudal fin in ground effect. *Ocean Eng.* 260, 112049. doi: 10.1016/j.oceaneng.2022.112049

Xing, C., Cao, Y., Cao, Y. H., Pan, G., and Huang, Q. G. (2022). Asymmetrical oscillating morphology hydrodynamic performance of a novel bionic pectoral fin. *J. Mar. Sci. Eng.* 10 (2), 289. doi: 10.3390/jmse10020289

Xu, Y., and Mohseni, K. (2016). A pressure sensory system inspired by the fish lateral line: Hydrodynamic force estimation and wall detection. *IEEE J. Oceanic Eng.* 42 (3), 532–543. doi: 10.1109/JOE.2016.2613440

Xue, G., Yanjun, L., Weiwei, S., Yifan, X., Fengxiang, G., and Zhitong, L. (2020). Evolvement rule and hydrodynamic effect of fluid field around fish-like model from starting to cruising. *Eng. Appl. Comput. Fluid Mechanics* 14 (1), 580–592. doi: 10.1080/19942060.2020.1734095

Yoerger, D. R., Govindarajan, A. F., Howland, J. C., Llopiz, J. K., Wiebe, P. H., Curran, M., et al. (2021). A hybrid underwater robot for multidisciplinary investigation of the ocean twilight zone. *Sci. Robotics* 6 (55), eabe1901. doi: 10.1126/scirobotics.abe1901

Zhang, J. X., Liu, M. Q., Zhang, S. L., Zheng, R. H., and Dong, S. L. (2022). Multi-AUV adaptive path planning and cooperative sampling for ocean scalar field estimation. *IEEE Trans. Instrumentation Measurement* 71, 1–14. doi: 10.1109/TIM.2022.3167784

Zhong, Y., Li, Z., and Du, R. (2018). Robot fish with two-DOF pectoral fins and a wire-driven caudal fin. *Advanced robotics* 32 (1), 25–36. doi: 10.1080/01691864.2017.1392344

Frontiers in Marine Science

Explores ocean-based solutions for emerging global challenges

The third most-cited marine and freshwater biology journal, advancing our understanding of marine systems and addressing global challenges including overfishing, pollution, and climate change.

Discover the latest Research Topics

See more →

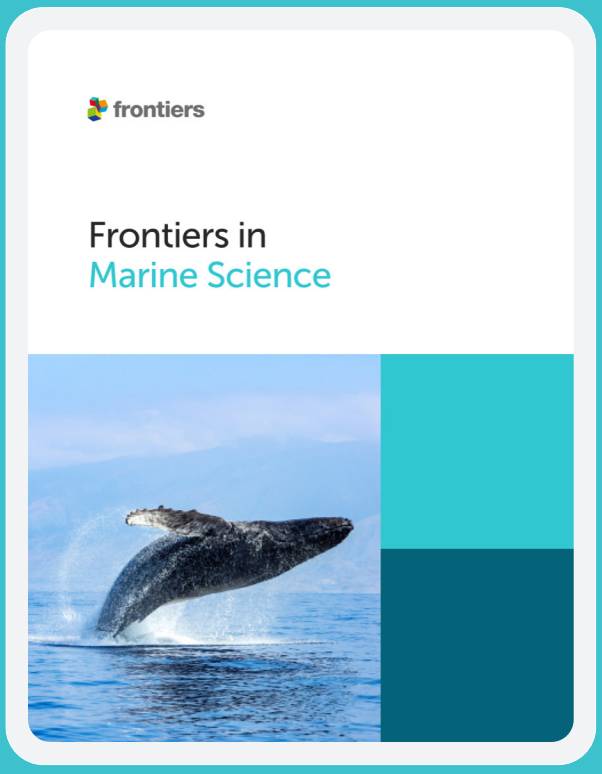

Frontiers

Avenue du Tribunal-Fédéral 34
1005 Lausanne, Switzerland
frontiersin.org

Contact us

+41 (0)21 510 17 00
frontiersin.org/about/contact